

## ABSTRACT

Title of dissertation: A Search for the Neutrinoless Double Beta Decay of Xenon-136 with Improved Sensitivity from Denoising

Clayton G. Davis, Doctor of Philosophy, 2014

Dissertation directed by: Professor Carter Hall  
Department of Physics

The EXO-200 detector is designed to search for the neutrinoless double beta decay of  $^{136}\text{Xe}$ .  $\beta\beta0\nu$  decay, if it occurs in nature, would demonstrate the fundamental nature of neutrino mass; set the mass scale of the neutrino sector; and demonstrate lepton number non-conservation. Since the  $\beta\beta0\nu$  decay produces a monoenergetic peak, the energy resolution of the detector is of fundamental importance for the sensitivity of the experiment.

The present work describes a new analysis technique which improves the energy resolution of EXO-200 through a combination of waveform denoising and weighting of waveform components based on their expected signal-to-noise ratio. With this method, the energy resolution of the detector is improved by 21% and the expected background in the  $2\sigma$  region of interest is reduced by 32%. Applying this technique to 99.8 kg\*years of exposure collected by EXO-200 between October 5, 2011 and September 1, 2013, we find no statistically significant evidence for the presence of  $\beta\beta0\nu$  in the data. We set a half-life limit  $T_{1/2} > 1.1 \cdot 10^{25}$  years at 90% confidence.

We also describe further improvements which could impact the energy resolution of EXO-200, and consider implications for the planned nEXO experiment.

A Search for the Neutrinoless Double Beta Decay of Xenon-136 with  
Improved Sensitivity from Denoising

by

Clayton G. Davis

Dissertation submitted to the Faculty of the Graduate School of the  
University of Maryland, College Park in partial fulfillment  
of the requirements for the degree of  
Doctor of Philosophy  
2014

Advisory Committee:

Professor Carter Hall, Chair/Advisor  
Professor Radu Balan, Dean's Representative  
Professor Elizabeth Beise  
Professor Rabindra Mohapatra  
Professor Peter Shawhan

© Copyright by  
Clayton G. Davis  
2014

## Dedication

For an endless supply of coffee, patience, support, and love, this work is dedicated to my wife Laura.

## Acknowledgments

Without the help of my colleagues, advisor, friends, family, and my wife, this thesis and the work it embodies would never have happened. Thanks go to them and to the EXO-200 collaboration, which has provided a supportive and stimulating environment for my work and learning over the past four years.

Particular thanks go to: David Auty, Phil Barbeau, Giorgio Gratta, Steve Herrin, Sam Homiller, Mike Jewell, Tessa Johnson, Tony Johnson, Caio Licciardi, Mike Marino, Dave Moore, Russell Neilson, Igor Ostrovskiy, J.J. Russell, Simon Slutsky, Erica Smith, Kevin O'Sullivan, Tony Waite, Josiah Walton, Liangjian Wen, Liang Yang, Yung-Ruey Yen, and of course my advisor Carter Hall. All of you have taught me to be the physicist I am today. Denoising has been a tremendously collaborative effort, and I am grateful that my last project with this collaboration has provided the chance to work with so many of you so closely.

My advisor Carter Hall has given me the freedom and support to try all kinds of crazy things in the EXO analysis, and I am grateful to him for his open-minded insight throughout. He has also been enormously helpful to me in finishing this dissertation on a very condensed schedule, taking much time from his own life to improve the quality of this work and its presentation; it could not have been what it is without so much of his help and guidance.

Finally, my friends, family, and wife have been extremely supportive of me throughout my time in graduate school. You have my deepest gratitude for everything you have done over the past five years and before. Thank you all.

# Contents

<b>List of Figures</b>	vii
<b>List of Abbreviations</b>	xvii
<b>1 Introduction</b>	1
<b>2 Theory of Neutrinoless Double-Beta Decay</b>	4
2.1 Two-Neutrino Double-Beta Decay . . . . .	5
2.2 Neutrinoless Double-Beta Decay . . . . .	8
2.3 Double-beta Decay Nuclear Matrix Calculations . . . . .	15
2.4 Neutrino Flavor Physics . . . . .	22
2.5 Particle Physics Constraints . . . . .	23
2.6 Nuclear Physics Constraints from $\beta\beta0\nu$ . . . . .	27
<b>3 The EXO-200 Detector</b>	34
3.1 Overview of the EXO-200 Detector . . . . .	34
3.2 Backgrounds to $\beta\beta0\nu$ Decay . . . . .	41
3.3 Passive Background Rejection . . . . .	47
3.4 Active Background Rejection . . . . .	57
3.5 Pulse Amplification and Waveform Readout . . . . .	59
3.6 Calibration Systems . . . . .	64
3.7 Summary . . . . .	68
<b>4 Denoising Theory and Implementation</b>	69
4.1 What is Denoising? . . . . .	70
4.2 Notational Conventions and External Input . . . . .	77
4.3 APD Noise Model: the Photon Perspective . . . . .	82
4.4 Bridge between Photons and Pulses . . . . .	89
4.5 Derivation of an Optimal Energy Estimator . . . . .	96
4.6 Matrix Formulation of Denoising . . . . .	104
4.7 Preconditioning of the Matrix Formulation . . . . .	110
4.8 Matrix Solver . . . . .	113
4.9 Computational Considerations . . . . .	115
4.10 Denoising in Practice . . . . .	121

4.11	Future Extensions to Denoising . . . . .	124
4.11.1	Anticorrelated Cluster Energies . . . . .	124
4.11.2	Wire Denoising . . . . .	127
4.12	Summary . . . . .	128
<b>5</b>	<b>Electronic Noise Measurements</b>	<b>129</b>
5.1	Mathematical Framework for Noise Correlations . . . . .	129
5.2	Time Windows of Constant Noise . . . . .	135
5.3	Algorithm for Measuring Noise . . . . .	146
5.4	Future Directions with Noise Measurement . . . . .	151
<b>6</b>	<b>The Lightmap</b>	<b>156</b>
6.1	A History of EXO-200 Lightmaps . . . . .	157
6.2	Four-Dimensional Lightmap . . . . .	160
6.3	Algorithm Details . . . . .	162
6.3.1	Event Selection . . . . .	163
6.3.2	Function Parametrization . . . . .	166
6.3.3	Convergence and Error Estimation . . . . .	170
6.4	Implementation for this Analysis . . . . .	173
6.5	Visualization . . . . .	175
6.6	Summary . . . . .	182
<b>7</b>	<b>EXO-200 Analysis and Results from Denoising</b>	<b>183</b>
7.1	Simulation . . . . .	183
7.1.1	Simulation of Particles using GEANT . . . . .	184
7.1.2	Digitization of Waveforms . . . . .	188
7.2	Cluster Reconstruction . . . . .	197
7.2.1	Pulse Finding . . . . .	199
7.2.2	Pulse Fitting . . . . .	203
7.2.3	Clustering Pulses into Deposit Sites . . . . .	205
7.3	Energy Corrections . . . . .	209
7.3.1	Charge Corrections . . . . .	209
7.3.2	Light Corrections . . . . .	213
7.3.3	Rotated Energy Calibration . . . . .	216
7.3.4	Measurement of Rotated Energy Resolution . . . . .	220
7.3.5	Cross-Checks on the Energy Calibration . . . . .	224
7.4	Fitting . . . . .	230
7.5	Results and Physics Reach . . . . .	243
7.6	Comparison to Results without Denoising . . . . .	248
7.6.1	Comparison of Energy Resolution and Calibration . . . . .	248
7.6.2	Comparison of Physics Results . . . . .	257
7.7	Summary . . . . .	274
<b>8</b>	<b>Conclusions and Future Plans</b>	<b>275</b>



# List of Figures

2.1	Feynman diagram for $\beta\beta2\nu$ decay. The reaction products are equivalent to two $\beta$ decays in succession, but this reaction can sometimes occur even if a single $\beta$ decay would be energetically forbidden. Figure from [1]. . . . .	5
2.2	Energy diagram of isotopes with atomic mass $A = 136$ . The energies $\Delta E$ are the binding energies of the atom, compared to the bare masses of the same nuclei. Values are from [3]. . . . .	7
2.3	Feynman diagram for $\beta\beta0\nu$ decay. A virtual neutrino mediates the exchange. This is only possible if $\bar{\nu}_R$ can flip its handedness to $\nu_L$ , and the interaction that induces this parity change also generates neutrino mass. Figure from [1]. . . . .	9
2.4	Even without any assumptions about the mechanism which leads to $\beta\beta0\nu$ decay, we can use that process to generate an effective neutrino mass as a higher-order process. Figure from [1]. . . . .	10
2.5	A selection of $\beta\beta0\nu$ half-life limits versus the publication year of the limit. Colors indicate which isotope is under study. Open circles indicate experiments which have not yet concluded data-taking. Data is from [12–68]. . . . .	14
2.6	Nuclear matrix element calculations for a variety of isotopes. The behavior is relatively stable from isotope to isotope due to the short-range interaction for $\beta\beta0\nu$ decay. The shaded regions represent ranges based on known biases of the various methods, as suggested by [72]. Figure from [72]. . . . .	18
2.7	The electron spectrum of Tritium ( ${}^3H$ ) $\beta$ decay. The endpoint contains only a small fraction of the total statistics. Figure from [82]. . .	26
2.8	The relationship between the effective Majorana mass $\langle m_{\beta\beta} \rangle$ and other fundamental neutrino quantities: the lightest neutrino mass eigenstate $m_{min}$ , the sum of mass eigenstates $M = \sum m_i$ , and the effective single-beta-decay neutrino mass $\langle m_\beta \rangle$ . Black (magenta) lines indicate the allowed region for the inverted (normal) hierarchy; red (blue) hatches indicate uncertainty for the inverted (normal) hierarchy due to the unknown CP-violating and Majorana phases $\delta$ , $\alpha_1$ , and $\alpha_2$ [86]. . . . .	29

3.1	A two-dimensional energy spectrum of scintillation and ionization from a testbed liquid xenon experiment under an electric field of 4 kV/cm. The spectrum is from a $^{207}\text{Bi}$ source with dominant gamma lines at 570 and 1064 keV. Figure reproduced from [97]. . . . .	35
3.2	Schematic of the inner EXO-200 TPC. Figure reproduced from [96]. . . . .	37
3.3	Anode collection wires (u-wires) and induction wires (v-wires) from EXO-200. (1) and (5) indicate the wire support frame; (2) indicates the wires themselves, constructed as gangs of three wires; (3) illustrates the attachment between wires and the support frame; (4) shows the return cables from the wires to the data acquisition system. Figure reproduced from [96]. . . . .	39
3.4	Representative $^{238}\text{U}$ spectra as the energy resolution of the detector changes. Red lines indicate the $2\sigma$ region of interest around the $Q$ -value. Normalization is arbitrary, but all spectra have the same normalization. Betas and gammas are assumed to have the same calibration here; alternative beta scales are considered in section 7.4.	44
3.5	Representative $^{232}\text{Th}$ spectra as the energy resolution of the detector changes. Red lines indicate the $2\sigma$ region of interest around the $Q$ -value. Normalization is arbitrary, but all spectra have the same normalization. Betas and gammas are assumed to have the same calibration here; alternative beta scales are considered in section 7.4.	46
3.6	Relative change in background rates expected in our $2\sigma$ region of interest as a function of the energy resolution. Rates are normalized to one at a $Q$ -value energy resolution of 1.6% $\sigma/E$ , the design goal of EXO-200. The three backgrounds shown, from $^{232}\text{Th}$ , $^{238}\text{U}$ , and $^{137}\text{Xe}$ , are currently our dominant backgrounds. Betas and gammas are assumed to have the same calibration here; alternative beta scales are considered in section 7.4. . . . .	48
3.7	X-ray attenuation lengths in xenon. Compton scattering, pair production, and photoelectric absorption are shown, along with their combined attenuation length; coherent (Rayleigh) scattering is omitted because it produces no observable energy deposit. The $Q$ -value of $^{136}\text{Xe} \beta\beta0\nu$ decay is indicated with a dashed black line. The vertical axis, in $\text{cm}^2/\text{g}$ , can be multiplied by the density of the xenon to derive an attenuation factor per unit length. Data from [104]. . . . .	50
3.8	Wire triplet, read as one channel. Figure from [96]. . . . .	52
3.9	APDs ganged together (bottom right). Wiring to the front-end electronics are visible as yellow “tape.” Figure from [96]. . . . .	53
3.10	A cutaway schematic image of the TPC and surrounding materials in the cleanroom. HFE-7000 refrigerant is contained between the cryostat and the LXe vessel. Figure from [96]. . . . .	54
3.11	Muon flux as a function of depth, in meters water equivalent. The WIPP site is indicated in relation to other underground science facilities. Figure from [107]. . . . .	56

3.12 An overview of the EXO-200 electronics and readout subsystems. The area inside the dashed line indicates cold subsystems inside the cryostat or TPC. Figure from [96]. . . . .	60
3.13 A cross-sectional schematic of an APD is shown in (a). The electric field as a function of depth is shown in (b). Figure from [108]. . . . .	61
3.14 A guide tube permits gamma sources to be inserted to known locations near the TPC. Green dots indicate a few of the locations where the source may conventionally be placed. Figure from [96]. . . . .	65
4.1 Detector energy resolution (without denoising) is strongly correlated with noise observed on the APDs. Noise data provided by Josiah Walton. . . . .	71
4.2 Coherent and incoherent noise power spectra for a sample set of APD channels without pulse shaping. The coherent noise power spectrum is measured by adding together waveforms from different channels and computing a power spectrum; the incoherent noise power spectrum is measured by computing power spectra for each channel individually and adding them together [114]. . . . .	72
4.3 APD waveforms from a single event. No energy deposit occurred during this event, so the waveforms represent pure electronic noise. The horizontal axis indicates time, and the vertical axis indicates channel number; colors ranging from blue to red indicate the baseline-subtracted waveform magnitude. Vertical streaks are indicative of correlations in noise across channels. . . . .	73
4.4 Shaped and unshaped APD waveforms. The normalization is shown to make the peak of the shaped waveform have a magnitude of one, and the time axis is shifted so that the unshaped waveform is a step function centered at $t = 0$ . . . . .	80
4.5 It is known that the parameters used for denoising in this analysis are not optimal. Here we use a scaling factor to adjust the parameter controlling the importance of Poisson noise. Data from run 3516 and 4544 are shown on the left and right, respectively; top plots show single-site resolution, bottom plots show multi-site resolution. We can see that an improvement of roughly 0.05 percentage points at 2615 keV could be achieved by moving from the expected optimum. It is not currently understood why scaling factors above the expected optimum yield further improvements to resolution. . . . .	123
5.1 Sum noise for all APD channels measured from charge injection runs, with environmental changes indicated which may correlate with observed changes in noise. Data provided by Josiah Walton. . . . .	136
5.2 Sum noise for each APD plane measured from charge injection runs, with environmental changes indicated which may correlate with observed changes in noise. Data provided by Josiah Walton. . . . .	138

5.3	Sum noise for each APD electronics board measured from charge injection runs, with environmental changes indicated which may correlate with observed changes in noise. Data provided by Josiah Walton.	139
5.4	Sum noise for each APD pie (6-7 channels) measured from charge injection runs, with environmental changes indicated which may correlate with observed changes in noise. Data provided by Josiah Walton.	140
5.5	Time trend of $\langle \tilde{N}_{192}^R[385]\tilde{N}_{193}^R[385] \rangle$ (black), $\langle \tilde{N}_{192}^R[385]\tilde{N}_{193}^I[385] \rangle$ (green), and $\langle \tilde{N}_{192}^I[385]\tilde{N}_{193}^I[385] \rangle$ (red) corresponding to the correlations between channels 192 and 193 at 188 kHz. Blue lines indicate tentative noise windows. This frequency is chosen because it is associated with a peak in the noise power spectrum, and the pair of channels is selected as a representative example for seeking changes in noise behavior. A restart of the front-end power supply at run 2700 is coincident with the reduction in correlated noise shown here, but the reason for this effect is not understood [128]. . . . .	141
5.6	Time trend of $\langle \tilde{N}_{202}^R[383]\tilde{N}_{203}^R[383] \rangle$ (black), $\langle \tilde{N}_{202}^R[383]\tilde{N}_{203}^I[383] \rangle$ (green), and $\langle \tilde{N}_{202}^I[383]\tilde{N}_{203}^I[383] \rangle$ (red) corresponding to the correlations between channels 202 and 203 at 187 kHz. Blue lines indicate tentative noise windows. This frequency is chosen because it is associated with a peak in the noise power spectrum, and the pair of channels is selected as a representative example for seeking changes in noise behavior. Installation of electronics board cooling fans is coincident with the reduction of noise around run 2900, with different installation times for different channels, but the reason this particular noise frequency is so strongly affected is not understood [128]. . . . .	142
5.7	Cumulative low-background livetime collected in EXO-200. Figure provided by David Auty. . . . .	146
5.8	The amplitude of the TEM injected pulses (“glitch” pulses) over time for channel 158. Figure provided by Sam Homiller. . . . .	152
6.1	Lightmap position-dependence $R(\vec{x})$ for selected APD gangs. . . . .	175
6.2	Lightmap position-dependence $R(\vec{x})$ for selected APD gangs. Here extreme anode positions are omitted to permit better contrast for the lightmap in the fiducial volume. . . . .	176
6.3	Functions $S(t)$ for selected channels. . . . .	177
6.4	Functions $S(t)$ for selected channels. . . . .	178
6.5	Functions $S(t)$ for selected channels. . . . .	179
7.1	The GEANT simulation includes large-scale features of the EXO-200 detector, including the outer and inner lead wall (black), outer and inner cryostat and TPC legs (red), and the TPC itself (brown). Components are assembled from simple geometrical shapes, and distant objects are only described coarsely [111]. . . . .	185

7.2	To ensure computational time is only spent on important details, detector components which are close to the liquid xenon are simulated in GEANT with greater accuracy than distant objects. The TPC contains the xenon, so it is simulated in detail [111]. . . . .	186
7.3	Energy spectra from $^{238}\text{U}$ in the TPC vessel for single-site (red) and multi-site (black) events. No energy smearing is performed; peak widths are due to energy loss outside of the liquid xenon [111]. . . . .	189
7.4	Energy spectra from $^{232}\text{Th}$ in the TPC vessel for single-site (red) and multi-site (black) events. No energy smearing is performed; peak widths are due to energy loss outside of the liquid xenon [111]. . . . .	190
7.5	The wire planes are modeled in only two dimensions; charge drifts along the field lines, which are arranged to terminate only on the u-wires [111]. . . . .	192
7.6	Weight potential of a u-wire channel consisting of three ganged wires. Electric field lines are superimposed [111]. . . . .	194
7.7	Weight potential of a v-wire channel consisting of three ganged wires. Electric field lines are superimposed [111]. . . . .	195
7.8	Comparison between simulated and observed waveforms on a u-wire (left) and v-wire (right) from $^{228}\text{Th}$ sources. The events are chosen to have similar energies so that the magnitudes match [111]. . . . .	196
7.9	Comparison between simulated and observed energy spectra (a) and standoff distance (b) in single-site $^{226}\text{Ra}$ events from a source located at position S5 [89]. . . . .	198
7.10	A u-wire waveform (left) and the output from operation of the matched filter (right). The red line on the right indicates our filtered pulse threshold; the matched filter output exceeds the threshold, so this waveform is determined to contain a pulse [112]. . . . .	201
7.11	A u-wire waveform composed of two pulses near in time is shown (top left); the matched filter (top right) correctly detects the presence of a pulse, but does not detect the presence of two distinct pulses. At bottom left, the waveform is unshaped; at bottom right the waveform is reshaped with shorter differentiation times, leading to easier detection [112]. . . . .	202
7.12	Fits to data for a u-wire (top left), v-wire (top right), and summed-APD waveform (bottom). The red model line indicates the time extent of the fit window [112]. . . . .	204
7.13	The purity charge correction is measured by fitting the 2615-keV $^{208}\text{Tl}$ gamma line as a function of Z-position [140]. . . . .	211
7.14	The expected grid correction of a u-wire as a function of Z-position. In this plot, $Z = 6$ mm represents the position of the u-wire plane and $Z = 12$ mm is the position of the v-wire plane [110]. . . . .	211
7.15	After applying all charge corrections, we find that the 2615-keV $^{208}\text{Tl}$ ionization peak is observed at the expected location for single-wire events; however, for two-wire events a residual bias is observed which also exhibits Z-dependence [140]. . . . .	212

7.16 A residual calibration offset and Z-dependent behavior is observed in the denoised scintillation measurements. The top plots show the relative peak position of the scintillation-only 2615-keV $^{208}\text{Tl}$ peak (one-wire and two-wire) and average alpha energy from $^{222}\text{Rn}$ versus Z (top left) and R (top right). The bottom plot shows the absolute denoised scintillation energy from the 2615-keV $^{208}\text{Tl}$ peak for one and two wires, with the measured correction function (equation 7.7) overlaid [140]. . . . .	214
7.17 Corrected scintillation versus charge energy are shown for a thorium run. The projection angle for the rotated energy measurement is illustrated at the 2615-keV peak; the projection onto a calibrated axis is shown. The dotted red line indicates the diagonal cut described in section 7.4. Figure provided by Liangjian Wen. . . . .	218
7.18 Charge-only, scintillation-only, and rotated energy spectra are shown from a thorium source run; the significant improvement in energy resolution with the rotated energy measurement is apparent, as are low-energy features which are washed out in the lower-resolution spectra. Figure provided by Liangjian Wen. . . . .	219
7.19 The time-averaged resolution functions (left) and relative resolution functions (right) for single-site (red) and multi-site (purple) denoised data. Shaded bands indicate uncertainties. Data provided by Caio Licciardi. . . . .	222
7.20 A typical monoenergetic gamma line, where the horizontal axis indicates ionization energy and the vertical axis indicates scintillation energy. We note that the ionization-only and scintillation-only resolutions are dominated by the length and angle of the island, which are dominated by xenon physics and the choice of electric field rather than the accuracy of the readouts in those channels. . . . .	223
7.21 Scintillation-only resolution over time, including: single-site denoised (blue), multi-site denoised (red), single-site undenoised (black solid), multi-site undenoised (hollow square). Although denoising does show some improvement in the scintillation-only resolution, it is quite modest; this is because the scintillation-only resolution is dominated by fluctuations in light yield. [140]. . . . .	223
7.22 The single-site (left) and multi-site (right) gamma line at 2.2 MeV from neutron capture on hydrogen can be used as a low-background cross-check on the resolution calibration. Here, data which is coincident with a muon veto is shown to include the expected neutron capture peak [140]. . . . .	225
7.23 The low-background potassium peak at 1461 keV is used as a cross-check on the single-site (left) and multi-site (right) energy calibrations. Fits also include the nearby 1332-keV cobalt peak [140]. . . . .	226

7.24	The residuals between calibrated and true peak positions for all sources is compared. Calibrations were obtained from the $^{137}\text{Cs}$ , $^{60}\text{Co}$ , and $^{232}\text{Th}$ peaks at 662, 1173, 1332, and 2615 keV. The peak from $^{226}\text{Ra}$ at 2448 keV is also shown, but was not used for calibration. Low-background calibration lines are neutron capture on hydrogen (2200 keV) and $^{40}\text{K}$ (1461 keV). Figure from [140]. . . . .	227
7.25	Time-dependence of the peak positions from all calibration campaigns. Error bars, when not visible, are smaller than the circle. Top row is the $^{60}\text{Co}$ peak at 1173 keV; middle row is the $^{60}\text{Co}$ peak at 1332 keV; bottom row is the $^{137}\text{Cs}$ peak at 662 keV. Thorium is not included because it is used to measure the time-dependence of the peak positions, so it is necessarily calibrated to a time-independent value. Figure from [140]. . . . .	228
7.26	Time-dependence of the energy resolution at the $^{208}\text{Tl}$ 2615 keV gamma line. Single-site (blue) and multi-site (red) energy resolutions are shown. The time-averaged energy resolutions ( $1.47\% \sigma/E$ for single-site, $1.59\% \sigma/E$ for multi-site, both at 2615 keV) are shown in blue and red dashed lines, respectively. Data provided by Liangjian Wen. . . . .	229
7.27	Here the X-Y orthogonal coordinates are shown along with the U-V coordinates that run orthogonal to the wire planes. The X-Y fiducial cuts applied to the data (dashed hexagon) do not include the entire active volume (solid hexagon); for the $\beta\beta0\nu$ search we find that aggressive fiducial cuts optimize our sensitivity, so very little active xenon is left unused. . . . .	232
7.28	Vetoing events coincident with muons can reduce our $1\sigma$ and $2\sigma$ event counts. Figure provided by David Auty. . . . .	233
7.29	The fit provides constraints on the beta-scale. Figure provided by Liangjian Wen. . . . .	239
7.30	Energy spectra with best-fit PDFs for single-site (top) and multi-site (bottom). Residuals between data and the combined PDFs are shown below the spectra. The last bin of the spectra is an overflow bin. The $2\sigma$ region of interest around the $Q$ -value is shown on the single-site spectrum. Insets for single-site and multi-site zoom around the $Q$ -value. The simultaneous standoff-distance fit is not shown [89].	241
7.31	The positions of events in the $1\sigma$ region of interest (red) and wider energy range 2325 – 2550 keV (black) are shown projected onto their X-Y (left) and $R^2$ -Z (right) coordinates. Lines indicate the fiducial volume. Figure provided by Dave Moore. . . . .	242
7.32	Profile scan of negative log-likelihood as a function of the number of fit $\beta\beta0\nu$ counts [89]. . . . .	242

7.33 Assuming that the background measurements of EXO-200 from this analysis are accurate, toy datasets are simulated. The top plot shows the probability distribution of our 90% confidence limit; we find that our median upper limit is 14.04 counts attributed to $\beta\beta0\nu$ , compared to our observed upper limit of 23.92 counts. The bottom plot shows the probability distribution of our ability to reject the null hypothesis (no $\beta\beta0\nu$ ) based on the negative log-likelihood; we find that the present dataset rejects the null hypothesis with probability less than 90%. Figures provided by Ryan Killick. . . . .	244
7.34 $\beta\beta0\nu$ constraints are shown from $^{136}\text{Xe}$ (horizontal) and $^{76}\text{Ge}$ (vertical). The four diagonal lines represent four recent matrix element computations [71, 145–147] and one recent phase-space factor [94] relating the two half-lives; tick marks along the diagonal represent the corresponding mass $\langle m_{\beta\beta} \rangle$ . 90% confidence limits and median 90% sensitivities are shown for the KamLand-Zen [13], GERDA [15], and EXO-200 experiments [89]; the claimed 2006 discovery by Klapdor-Kleingrothaus and Krivosheina is shown as a $1\sigma$ confidence interval [148]. . . . .	246
7.35 A comparison of the spectra before and after denoising for a set of representative thorium source runs (4758 and 4766). The thickness of the lines indicate Poisson error bars on the number of counts in a bin; smoothing is applied to the spectra to permit easier comparison of peaks. Important gamma lines are indicated. Around 500-600 keV threshold effects become significant, making comparison difficult. . . . .	249
7.36 A comparison of the spectra before and after denoising for a representative cobalt source run (4787 and 4788). The thickness of the lines indicate Poisson error bars on the number of counts in a bin; smoothing is applied to the spectra to permit easier comparison of peaks. The two gamma lines of $^{60}\text{Co}$ are indicated. . . . .	250
7.37 A comparison of the spectra before and after denoising for a representative cesium source run (4777-4781). The thickness of the lines indicate Poisson error bars on the number of counts in a bin; smoothing is applied to the spectra to permit easier comparison of peaks. The gamma line of $^{137}\text{Cs}$ is indicated. Threshold effects are significant at this energy and the calibration is extrapolated from higher-energy sources, but the spectra illustrate the fact that resolution improves dramatically at low energy. . . . .	251
7.38 The time-averaged resolution functions (top) and relative resolution functions (bottom) are compared for denoised and undenoised data. Bands indicate uncertainties. Data provided by Caio Licciardi. . . . .	252
7.39 Time dependence of the single-site energy resolution at 2615 keV with denoised (blue) and undenoised (red) scintillation. Time-averaged energy resolutions at this energy (1.47% denoised, 1.86% undenoised) are overlaid as dashed lines. Data provided by Mike Marino. . . . .	255

7.40 The non-linearity of the calibration is shown here for denoised (red) and undenoised (black) data in single-site (left) and multi-site (right). $R_{rec}$ is defined as the ratio between the observed peak position and the observed peak position of the 2615 keV $^{232}\text{Th}$ peak, and $R_{real}$ is defined as the true ratio between the peak position and 2615 keV; the vertical axis shows the relative difference between $R_{rec}$ and $R_{real}$ , which reflects how much non-linear correction the calibration must perform. The cesium, cobalt, and thorium peaks (662, 1173, 1332, and 2615 keV) are used to obtain a calibration; the radium line at 2448 keV and the neutron capture line from hydrogen at 2200 keV are shown as cross-checks [140]. . . . .	256
7.41 Denoised (red) and undenoised (blue) profile likelihood curves for $\beta\beta0\nu$ . . . . .	262
7.42 Denoised (red) and undenoised (blue) data counts are shown in 30 keV bins. The total best-fit PDF, where the $\beta\beta0\nu$ contribution is fixed to zero, is overlaid for denoised and undenoised data. Dashed lines indicate the $2\sigma$ region of interest. . . . .	264
7.43 Denoised (red) and undenoised (blue) single-site low-background data and pdfs in the energy window from 1200 to 1800 keV. The thick lines indicate the total single-site pdfs; thin lines indicate contributions from $^{40}\text{K}$ . Both fits are constrained to have no contribution from $\beta\beta0\nu$ . . . . .	265
7.44 Denoised (red) and undenoised (blue) multi-site low-background data and pdfs in the energy window from 1200 to 1800 keV. The thick lines indicate the total multi-site pdfs; thin lines indicate contributions from $^{40}\text{K}$ . Both fits are constrained to have no contribution from $\beta\beta0\nu$ . . . . .	266
7.45 Denoised (red) and undenoised (blue) multi-site low-background data and pdfs in the energy window from 1000 to 1600 keV. The thick lines indicate the total multi-site pdfs; thin lines indicate contributions from $^{60}\text{Co}$ . Both fits are constrained to have no contribution from $\beta\beta0\nu$ . . . . .	267
7.46 Denoised (red) and undenoised (blue) single-site low-background data and pdfs in the energy window from 2000 to 2600 keV. The thick lines indicate the total single-site pdfs; thin lines indicate contributions from isotopes in the $^{238}\text{U}$ decay chain. Dashed vertical lines indicate the $2\sigma$ region of interest around the $Q$ -value. Both fits are constrained to have no contribution from $\beta\beta0\nu$ . The uranium decay chain contributes 10.0 (8.9) mean expected counts in the $2\sigma$ region of interest for denoised (undenoised) data. . . . .	268
7.47 Denoised (red) and undenoised (blue) multi-site low-background data and pdfs in the energy window from 1600 to 2800 keV. The thick lines indicate the total multi-site pdfs; thin lines indicate contributions from isotopes in the $^{238}\text{U}$ decay chain. Both fits are constrained to have no contribution from $\beta\beta0\nu$ . . . . .	269

7.48 Denoised (red) and undenoised (blue) single-site low-background data and pdfs in the energy window from 2200 to 2800 keV. The thick lines indicate the total single-site pdfs; thin lines indicate contributions from isotopes in the $^{232}\text{Th}$ decay chain. Dashed vertical lines indicate the $2\sigma$ region of interest around the $Q$ -value. Both fits are constrained to have no contribution from $\beta\beta0\nu$ . The thorium decay chain contributes 18.7 (34.5) mean expected counts in the $2\sigma$ region of interest for denoised (undenoised) data. . . . .	270
7.49 Denoised (red) and undenoised (blue) multi-site low-background data and pdfs in the energy window from 2200 to 2800 keV. The thick lines indicate the total multi-site pdfs; thin lines indicate contributions from isotopes in the $^{232}\text{Th}$ decay chain. Both fits are constrained to have no contribution from $\beta\beta0\nu$ . . . . .	271
7.50 Denoised (red) and undenoised (blue) single-site PDF contributions from $^{137}\text{Xe}$ , where we constrain $\beta\beta0\nu$ to have no decays in both fits. . . . .	272
8.1 NEST simulation software has been used to estimate how the rotated energy resolution at 2615 keV (vertical axis) depends on the scintillation-only resolution at 2615 keV (horizontal axis); this theoretical estimate is shown in blue, as applicable to the EXO-200 detector with fixed electric field. Black points indicate measurements from thorium source runs without denoising; red points indicate measurements from thorium runs with denoising. Figure provided by Liangjian Wen using NEST software [118]. . . . .	276

## List of Abbreviations

EXO	Enriched Xenon Observatory
EXO-200	Current (200-kg) iteration of the EXO family of detectors
nEXO	Planned next-generation EXO detector
APD	Avalanche Photo-diode
ADC	Analog-Digital Converter, or one of its discrete output units
DAQ	Data Acquisition System
TPC	Time Projection Chamber
WIPP	Waste Isolation Pilot Plant
PDF	Probability Distribution Function
ROI	Region Of Interest (around 2457 keV)
$\beta\beta0\nu$	Neutrinoless double-beta decay
$\beta\beta2\nu$	Two-neutrino double-beta decay
FEC	Front-End Card
QRPA	Quasi-Random Phase Approximation
VUV	Vacuum Ultra-Violet

# Chapter 1: Introduction

The EXO-200 detector is designed to search for a hypothetical decay mode of  $^{136}\text{Xe}$  whereby two electrons and no neutrinos are emitted from the nucleus. This neutrinoless double-beta ( $\beta\beta0\nu$ ) decay, if it occurs, would have profound implications for nuclear and particle physics: it would set the absolute mass scale of the neutrino sector, provide clues to the mechanism which generates mass in the neutrino sector, and give the first observation of non-conservation of total lepton number.

EXO-200 contains roughly 110 kg of liquid xenon in its active volume. The xenon used by EXO is enriched to 80.6% in xenon-136, resulting in approximately  $3.9 \times 10^{26}$  atoms of  $^{136}\text{Xe}$  which can be monitored. The observation of  $\beta\beta0\nu$  decay would present itself as a peak in the energy spectrum at a Q-value of 2458 keV, so EXO-200 is designed to subject such a peak to as little background as possible

Background is controlled primarily by reducing the level of radioactivity of materials in and around the liquid xenon. All materials used in the construction of the EXO-200 detector were carefully screened to insure low concentration of radioactive isotopes, making EXO-200 one of the lowest-background detectors in the world.

After construction, background reduction must be performed by discrimination between  $\beta\beta0\nu$  and other processes. This can be performed primarily by exploiting the event topology and by refining the energy measurements. The event topology of  $\beta\beta0\nu$  consists of a highly localized energy deposit due to the short interaction length of  $\beta$  particles; in contrast, backgrounds will often produce diffuse energy deposits which can be rejected as candidate  $\beta\beta0\nu$  events.

Perhaps the most conceptually straightforward method of background reduction, however, is by precise energy estimation. An improved energy resolution assures us that  $\beta\beta0\nu$  candidate events must come from a narrower region of the energy spectrum and allows us to reject events outside of that region of interest (ROI). The EXO-200 detector observes energy in two forms, ionization (charge) and scintillation (light), and both are necessary to achieve excellent energy resolution. The scintillation measurement has a lower accuracy, so it is the limiting factor to the energy resolution of EXO-200.

In this work, we describe a new technique for improving the accuracy of the scintillation measurements of the EXO-200 detector through a detailed offline waveform analysis. This technique, identified throughout this work as “denoising”, consists of understanding the signal-to-noise ratio of the different components of our scintillation measurement. The signal-to-noise content of our scintillation measurements depends on both the proximity of a light sensor to the energy deposit and on the spectral shape of light pulses compared to waveform noise. An active noise reduction program is included in this effort, which in turn improves the signal-to-noise content of the scintillation measurements. An overall improvement in the EXO-200

energy resolution of more than 20% is achieved at the  $\beta\beta0\nu$  Q-value.

We provide an overview of the theoretical motivations for the search for  $\beta\beta0\nu$  decay in chapter 2. Chapter 3 describes the design of the EXO-200 detector, the expected background, and some of the techniques it is capable of using to reduce those backgrounds. Chapter 4 derives the mathematical framework of denoising and some practical considerations of its application; chapters 5 and 6 describe the measurements of electronic noise and light yield which are critical inputs to denoising. In chapter 7 we describe the components and results of the EXO-200 double beta decay search, including comparisons between results with and without denoising in sections 7.3.3 and 7.6. Conclusions and future outlook are contained in chapter 8.

# Chapter 2: Theory of Neutrinoless Double-Beta Decay

Toward the end of the 1990s neutrinos were conclusively proven to possess a non-zero mass. Subsequent effort has been directed toward understanding the absolute scale of neutrino mass spectrum and the nature of the interaction which causes it. Neutrinoless double-beta ( $\beta\beta0\nu$ ) decay, would provide a window onto both questions. This chapter presents the theoretical motivations for searching for  $\beta\beta0\nu$  decay. Section 2.1 describes the closely-related two-neutrino double-beta ( $\beta\beta2\nu$ ) decay which is allowed in the standard model. Section 2.2 defines  $\beta\beta0\nu$  decay and reasons for hypothesizing its occurrence. Considerations and challenges in nuclear physics are described in section 2.3. The parametrization of the neutrino sector is provided in section 2.4. Section 2.5 summarizes constraints on neutrino masses which can be obtained from observations of single- $\beta$  decay and cosmology, and section 2.6 describes in detail the considerations and challenges involved in searching for  $\beta\beta0\nu$  decay. The reader will obtain a general understanding of the state of the field before continuing on to the details of the EXO-200 detector in chapter 3.

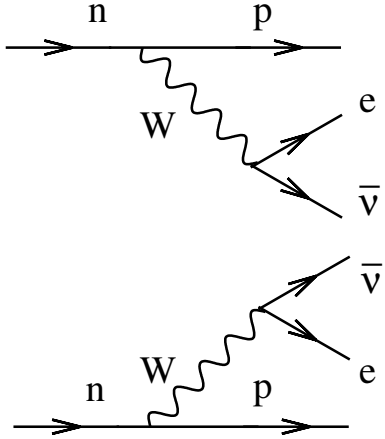


Figure 2.1: Feynman diagram for  $\beta\beta 2\nu$  decay. The reaction products are equivalent to two  $\beta$  decays in succession, but this reaction can sometimes occur even if a single  $\beta$  decay would be energetically forbidden. Figure from [1].

## 2.1 Two-Neutrino Double-Beta Decay

Standard-model two-neutrino double beta ( $\beta\beta 2\nu$ ) decay is the result of the particle interaction

$$2d \rightarrow 2u + 2e^- + 2\bar{\nu}_e \quad (2.1)$$

mediated by  $W^-$ -exchange, as depicted in Figure 2.1. It is effectively the simultaneous occurrence of two beta ( $\beta$ ) decays from the same nucleus.

Because  $\beta\beta 2\nu$  decay is a second-order weak interaction, it has a remarkably slow rate compared to most  $\beta$  decay processes. Although many nuclei are expected to decay by  $\beta\beta 2\nu$ , the process is thoroughly masked by conventional  $\beta$  decay in most of them. In most cases, we can only hope to detect  $\beta\beta 2\nu$  decay in isotopes where  $\beta$  decay is forbidden or highly suppressed.

An example of an isotope for which  $\beta$  decay is highly suppressed is  $^{48}_{20}\text{Ca}$ . The ground state of  $^{48}_{20}\text{Ca}$  has zero units of angular momentum, whereas its single- $\beta$  decay daughter product  $^{48}_{21}\text{Sc}$  has six units of total angular momentum in its ground state, and is thus highly suppressed by angular momentum conservation. In contrast,  $^{48}_{22}\text{Ti}$  has zero units of total angular momentum, making  $\beta\beta2\nu$  decay of  $^{48}_{20}\text{Ca}$  permitted by angular momentum and energy considerations, and as a result the  $\beta\beta2\nu$  decay mode of  $^{48}_{20}\text{Ca}$  dominates [2].

In the most promising  $\beta\beta2\nu$  candidates, single  $\beta$  decay is forbidden by energy conservation. It is well-known that nuclei minimize their energy by arranging similar nucleons to have overlapping wavefunctions [2]. Thus, isotopes with an even number of protons and an even number of neutrons will have less nucleon-pairing potential energy than an isotope with either an odd number of protons or an odd number of neutrons, which in turn will have less nucleon-pairing potential energy than an isotope with an odd number of protons and an odd number of neutrons.

The effect is illustrated by the nuclear energy level diagram shown in figure 2.2 for the  $A = 136$  isobar. Xenon, barium, cerium, and neodymium are even-even isotopes, and have systematically lower energies than the odd-odd isotopes iodine, cesium, lanthanum, and praseodymium. For this particular isobar, we can see that xenon is energetically forbidden from single- $\beta$  decaying to cesium because the odd-odd isotope of cesium has slightly more potential energy than the even-even isotope of xenon. As a result, the primary mode of decay of xenon-136 will be  $\beta\beta2\nu$  decay to barium-136. Similarly, cerium-136 can undergo double-electron capture (ECEC), electron capture with positron emission ( $\text{EC}\beta^+$ ), or double-positron emis-

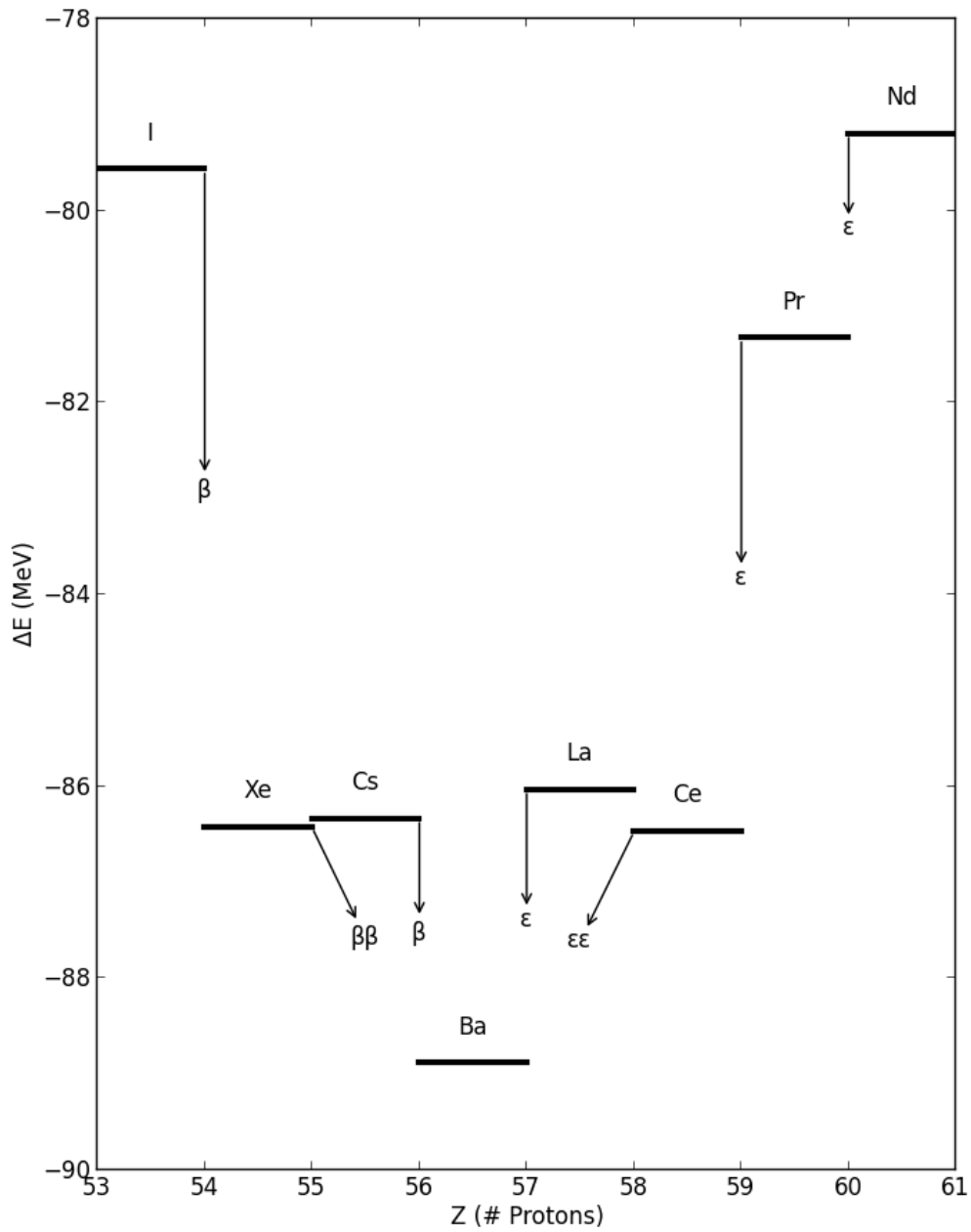


Figure 2.2: Energy diagram of isotopes with atomic mass  $A = 136$ . The energies  $\Delta E$  are the binding energies of the atom, compared to the bare masses of the same nuclei. Values are from [3].

sion ( $\beta^+\beta^+$ ); however, in practice the expected rates for these decays will be lower than the rates for  $\beta\beta2\nu$  decay, so we will not consider them further in this work.

## 2.2 Neutrinoless Double-Beta Decay

The detection and study of  $\beta\beta2\nu$  decay provides an opportunity to test a class of nuclear matrix element computations; however, the decay does not violate any fundamental symmetries and its existence is, in this sense, a mundane prediction of the Standard Model. The primary appeal of isotopes which undergo  $\beta\beta2\nu$  decay is the opportunity these isotopes provide to probe the nature of neutrinos through the related neutrinoless decay.

It had been suggested as early as 1937 that neutrinos could possess mass through a neutrino-antineutrino interaction, provided that the neutrino is its own antiparticle [4]. The theorized Majorana interaction comes from Lagrangian terms of the form (for each of three neutrino eigenstates)

$$\begin{aligned}\mathcal{L}_{Maj} = & -\frac{m_L}{2} (\overline{\Psi}_L^c \Psi_L + \overline{\Psi}_L \Psi_L^c) \\ & -\frac{m_R}{2} (\overline{\Psi}_R^c \Psi_R + \overline{\Psi}_R \Psi_R^c),\end{aligned}\tag{2.2}$$

where the superscript-*c* represents charge conjugation. (This is the reason that Majorana mass terms are only possible for a chargeless lepton.) The masses  $m_L$  and  $m_R$  may be chosen independently; since there has never been an observation of right-handed neutrinos or left-handed anti-neutrinos, it is possible that  $m_R = 0$  and that the fields  $\Psi_R$  and  $\Psi_R^c$  do not exist in nature [1].

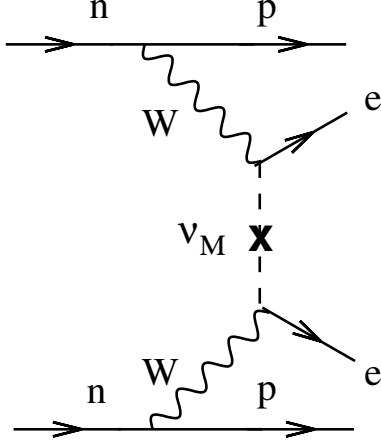


Figure 2.3: Feynman diagram for  $\beta\beta0\nu$  decay. A virtual neutrino mediates the exchange. This is only possible if  $\bar{\nu}_R$  can flip its handedness to  $\nu_L$ , and the interaction that induces this parity change also generates neutrino mass. Figure from [1].

If neutrinos do have Majorana mass interactions, then any isotope that undergoes  $\beta\beta2\nu$  decay can also undergo the related process  $2d \rightarrow 2u + 2e^-$ , depicted in Figure 2.3, in which the two outgoing neutrinos in  $\beta\beta2\nu$  decay are replaced by one virtual neutrino. This process is called neutrinoless double-beta ( $\beta\beta0\nu$ ) decay. We can interpret this as a mixing interaction between a left-handed neutrino and a right-handed antineutrino; this is only possible if neutrinos are Majorana particles.

The tree-level diagram for  $\beta\beta0\nu$  has one additional interaction vertex compared to  $\beta\beta2\nu$  decay, and as a result we would expect it to occur at an even slower rate. However, the more immediate consequence of  $\beta\beta0\nu$  decay is that lepton number conservation is violated. The lepton number changes by two units corresponding to the creation of two leptons with no balancing anti-leptons. Numerous theories have suggested other plausible modes of lepton number non-conservation [5, 6], but none have yet reported a positive result. In the conventional Standard Model with

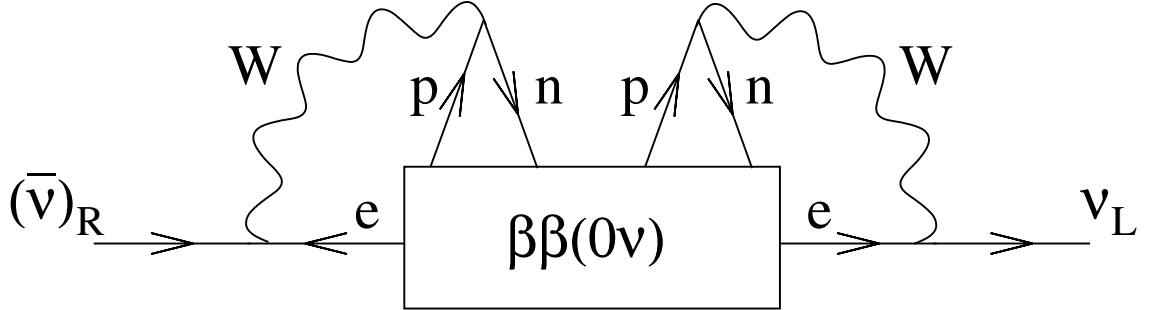


Figure 2.4: Even without any assumptions about the mechanism which leads to  $\beta\beta0\nu$  decay, we can use that process to generate an effective neutrino mass as a higher-order process. Figure from [1].

massless neutrinos, lepton number conservation is an accidental symmetry [7], but in a model with massive neutrinos there may no longer be any reason *a priori* to expect conservation of lepton number.

It is worth noting that the interaction term above assumes no mediating particles in the mass mechanism, whereas it is possible that  $\beta\beta0\nu$  could be mediated by some higher-order interaction terms. However, if  $\beta\beta0\nu$  decay is observed, it leads very generally to a conclusion that neutrinos have an *effective* Majorana mass interaction [8]. We can see this by embedding the  $\beta\beta0\nu$  process into a higher-order one, as shown in figure 2.4. Regardless of the details of how  $\beta\beta0\nu$  occurs, its existence would necessarily generate an effective neutrino mass as a higher-order process.

We have described so far only the theorized Majorana interaction of equation 2.2. However, it is also possible that neutrinos could have a Dirac mass term analogous to the other fermions. The full set of neutrino mass terms in the La-

grangian would then be:

$$\begin{aligned}\mathcal{L}_{Maj+Dirac} = & -\frac{m_L}{2} (\bar{\Psi}_L^c \Psi_L + \bar{\Psi}_L \Psi_L^c) \\ & -\frac{m_R}{2} (\bar{\Psi}_R^c \Psi_R + \bar{\Psi}_R \Psi_R^c) \\ & - m_D (\bar{\Psi}_L \Psi_R + \bar{\Psi}_R \Psi_L),\end{aligned}\quad (2.3)$$

where  $m_D$  is the new Dirac mass term. The three flavors observed in nature would result in three sets of these terms, one for each flavor, and nine possible mass terms in total [1].

For simplicity, we consider now the mass terms for a one-flavor system. We can rearrange the Lagrangian terms as:

$$\mathcal{L}_{Maj+Dirac} = -\frac{1}{2} \left( \overline{(n_L)^c} \mathcal{M} n_L + \overline{(n_L)} \mathcal{M} n_L^c \right), \text{ where} \quad (2.4a)$$

$$\mathcal{M} = \begin{pmatrix} m_L & m_D \\ m_D & m_R \end{pmatrix} \quad (2.4b)$$

$$n_L = \begin{pmatrix} \Psi_L \\ (\Psi_R)^c \end{pmatrix}. \quad (2.4c)$$

The matrix  $\mathcal{M}$  can, in all cases, be diagonalized by some unitary matrix, which means that there is always a basis in which two interaction terms are sufficient. In nearly all cases the eigenvalues will be distinct values, so the two eigenstates are non-degenerate. Both eigenstates in this case are their own antiparticles, so they are Majorana. The only exceptions to this are when  $m_L = m_R$  and  $m_D = 0$ , or

when  $m_L = m_R = 0$ . Both of those special cases lead to degenerate eigenspaces; in the former, the system is clearly purely Majorana from the beginning, and in the latter the system is purely Dirac. Thus we can see that even though it is possible to include a Dirac neutrino mass term, neutrinos will be Majorana particles unless  $m_L = m_R = 0$ . Similar results hold in the three-flavor case [1].

We have spoken of the possibility that the Majorana mass term comes from a tree-level Lagrangian term. However, this would be a surprising result. The Majorana fields would not have the same quantum number under the  $SU(2)_L \times SU(2)_R$  symmetry, meaning that either neutrinos would need to choose between the Majorana and Dirac terms or some larger symmetry would need to take the place of  $SU(2)_L \times SU(2)_R$ . It is viewed as more likely that neutrino mass is generated through an effective interaction. A natural mechanism to generate neutrino mass called the see-saw mechanism was developed around 1980 [9, 10]. In this scheme we presume that  $m_R \gg m_D \gg m_L$ . The Dirac term could come from the Higgs mechanism, so we expect  $m_D$  to occupy the 1 MeV energy range typical of other leptons and quarks. The large mass  $m_R$  of the right-handed neutrino  $\nu_R$  is meant to explain the absence of  $\nu_R$  and  $\overline{\nu}_R^c$  from all observations. When we take  $m_L = 0$

and diagonalize the single-flavor neutrino mass matrix  $\mathcal{M}$  we obtain:

$$\mathcal{M} = \begin{pmatrix} 0 & m_D \\ m_D & m_R \end{pmatrix} \quad (2.5)$$

$$\propto \begin{pmatrix} i & m_D/m_R \\ -im_D/m_R & 1 \end{pmatrix} \begin{pmatrix} -m_D^2/m_R & 0 \\ 0 & m_R \end{pmatrix} \begin{pmatrix} -i & im_D/m_R \\ m_D/m_R & 1 \end{pmatrix}. \quad (2.6)$$

In other words, if we presume that there is a Dirac neutrino mass similar to the masses of other leptons and a right-handed Majorana neutrino mass  $m_R \gg m_D$ , then in another basis a small left-handed Majorana neutrino mass  $m_D^2/m_R$  is generated. This is widely considered to be the most natural mechanism for explaining the lightness of the neutrinos observed in nature [1, 11].

A selection of  $\beta\beta0\nu$  half-life limits are shown in figure 2.5 for the  $^{76}\text{Ge}$ ,  $^{100}\text{Mo}$ ,  $^{130}\text{Te}$ , and  $^{136}\text{Xe}$  isotopes with the publication year of the result. Although some results did exist before 1980, after the see-saw mechanism described in [9, 10] was appreciated experimental interest in neutrinoless double-beta decay flourished, and we can see that for the last thirty years there has been steady progress in improving experimental sensitivity for many isotopes. The discovery of oscillation of atmospheric neutrinos ([69]) verified that neutrinos do have finite mass of some sort, adding to the motivation to search for the  $\beta\beta0\nu$  process. The following sections describe computational and experimental considerations associated with searches for  $\beta\beta0\nu$  decay.

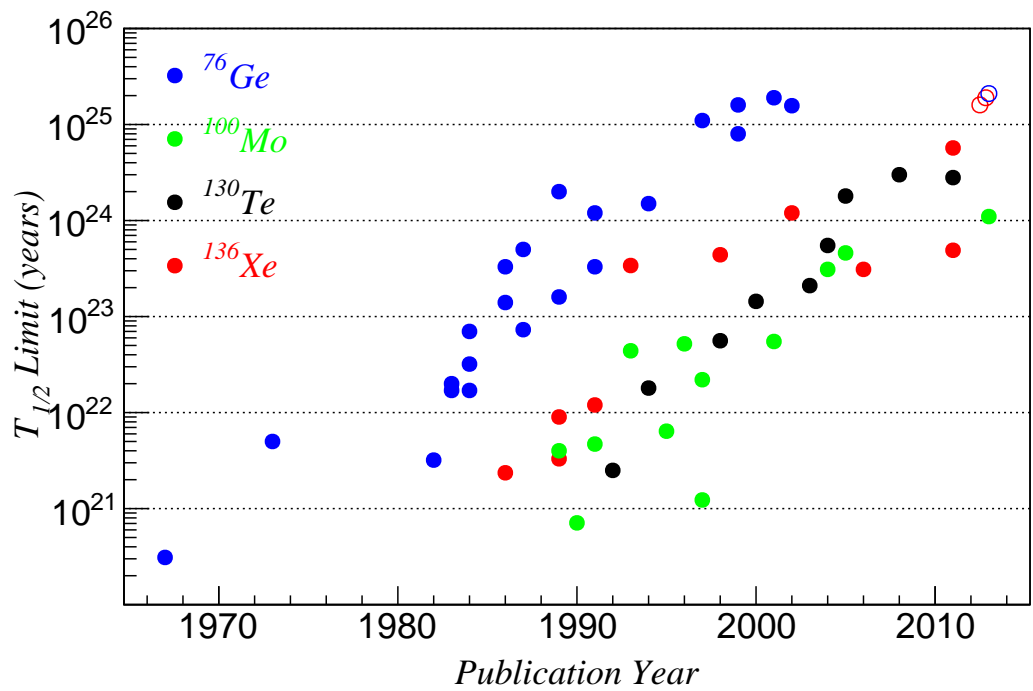


Figure 2.5: A selection of  $\beta\beta0\nu$  half-life limits versus the publication year of the limit. Colors indicate which isotope is under study. Open circles indicate experiments which have not yet concluded data-taking. Data is from [12–68].

## 2.3 Double-beta Decay Nuclear Matrix Calculations

If the dominant mechanism of  $\beta\beta0\nu$  decay is a tree level neutrino mass term as shown in figure 2.3, then the rate of  $\beta\beta0\nu$  decay will also reflect the magnitude of the neutrino mass parameters. To specify this relation precisely we need an understanding of the nuclear physics of the decaying isotope. This section will identify the relevant quantities which must be computed and provide a survey of the computational approaches to estimating them.

For a tree-level Majorana interaction we can write the partial half-life  $T_{1/2}^{0\nu}$  of an isotope which undergoes  $\beta\beta0\nu$  decay as

$$[T_{1/2}^{0\nu}]^{-1} = G_{0\nu}(Q_{\beta\beta}, Z) |M_{0\nu}|^2 \langle m_{\beta\beta} \rangle^2, \quad (2.7)$$

where  $G_{0\nu}(Q_{\beta\beta}, Z)$  is a phase-space factor coming from the range of possible output states,  $M_{0\nu}$  is a nuclear matrix element, and  $\langle m_{\beta\beta} \rangle$  is the effective  $\beta\beta0\nu$  neutrino mass which will be defined in section 2.6.

The two factors  $G_{0\nu}(Q_{\beta\beta}, Z)$  and  $M_{0\nu}$  may be computed by a variety of methods, and it is tempting to draw nuclear matrix elements and phase factors from different publications. However, this must be done carefully: scaling factors can be absorbed from one into the other, and if nuclear matrix elements and phase space factors are calculated using different conventions, the result of combining them will

not be correct.

For example, in early calculations, the nuclear matrix element and phase-space factor were generally computed in units of  $\text{fm}^{-1}$  and  $\text{yrs}^{-1}\text{fm}^2$ , respectively. Starting in the mid-1980s common practice shifted to multiply the nuclear matrix element by the nuclear radius  $R_0 \propto A^3$ , where  $A$  is the number of nucleons, and divide the phase-space factor by  $R_0^2$ , making the nuclear matrix element unitless and the phase-space factor have units of  $\text{yrs}^{-1}$ . With this convention care must be taken that the nuclear radius used in both calculations is the same, whereas for many years different authors might choose  $R_0 = 1.1A^3$  fm or  $R_0 = 1.2A^3$  fm without specifying that choice [70]. Modern practice is now that the value of  $R_0$  is explicitly specified in any matrix element or phase-space factor calculations. Another convention is whether the fourth power of the axial vector current  $g_A^4$  should be included with the phase space factor, nuclear matrix element, or separately as its own factor of equation 2.7, and again one must be careful to understand the chosen conventions before combining results from different sources [71].

The phase-space factor  $G_{0\nu}(Q_{\beta\beta}, Z)$  accounts for the phase space of the final state of  $\beta\beta0\nu$  decay. This includes two outgoing electrons and the final state nucleus. The mass of the outgoing nucleus is always much larger than the masses of the neutrinos, so nearly all momentum will be carried by the two electrons. Each contributes a phase space integral of the form  $\int_0^{p_{max}} d \cdot p E$ , which individually contribute a factor proportional to  $p_{max}^3$ . Considering the system in the rest frame of the initial state nucleus, the sum of the two electron momenta are constrained to be equal to zero, so the combined phase space integral for both electrons is proportional

to

$$\int_0^{p_{max}} dp_1 p_1 E_1 \int_0^{p_{max}} dp_2 p_2 E_2 \delta(p_2 - p_1) \propto p_{max}^5. \quad (2.8)$$

As a result, the phase space factor  $G_{0\nu}(Q_\beta\beta, Z)$  of  $\beta\beta0\nu$  decay will be proportional to  $Q^5$ , where  $Q$  is the total energy of the decay [11]. The strong dependence of  $G_{0\nu}(Q_\beta\beta, Z)$  on  $Q$  means that isotopes which have high  $Q$ -values will be expected to have shorter  $\beta\beta0\nu$  half-lives than isotopes with low  $Q$ -values, which is one reason that most  $\beta\beta0\nu$  searches focus on high- $Q$  isotopes.

Another important contribution to the phase space factor come from the electric potential of the atomic nucleus and its atomic electrons. The potential  $V(r)$  experienced by the escaping electron as a function radius is approximated by: [71]

$$V(r) = -Z\alpha\hbar c \cdot \begin{cases} 1/r & r \geq R_0 \\ (3 - (r/R_0)^2)/2R_0 & r < R_0, \end{cases} \quad (2.9)$$

where  $Z$  is the nuclear charge,  $\alpha$  is the fine structure constant,  $\hbar$  is Planck's constant,  $c$  is the speed of light, and  $R_0$  is the radius of the nucleus. Higher-order corrections include the change in nuclear charge due to the decay and the density of the electron cloud (which includes angular asymmetries). A modern treatment can be found in [71].

The nuclear matrix element  $M_{0\nu}$  describes the transition rate from the initial to the final nuclear state of the decay process. The transition may be treated as a

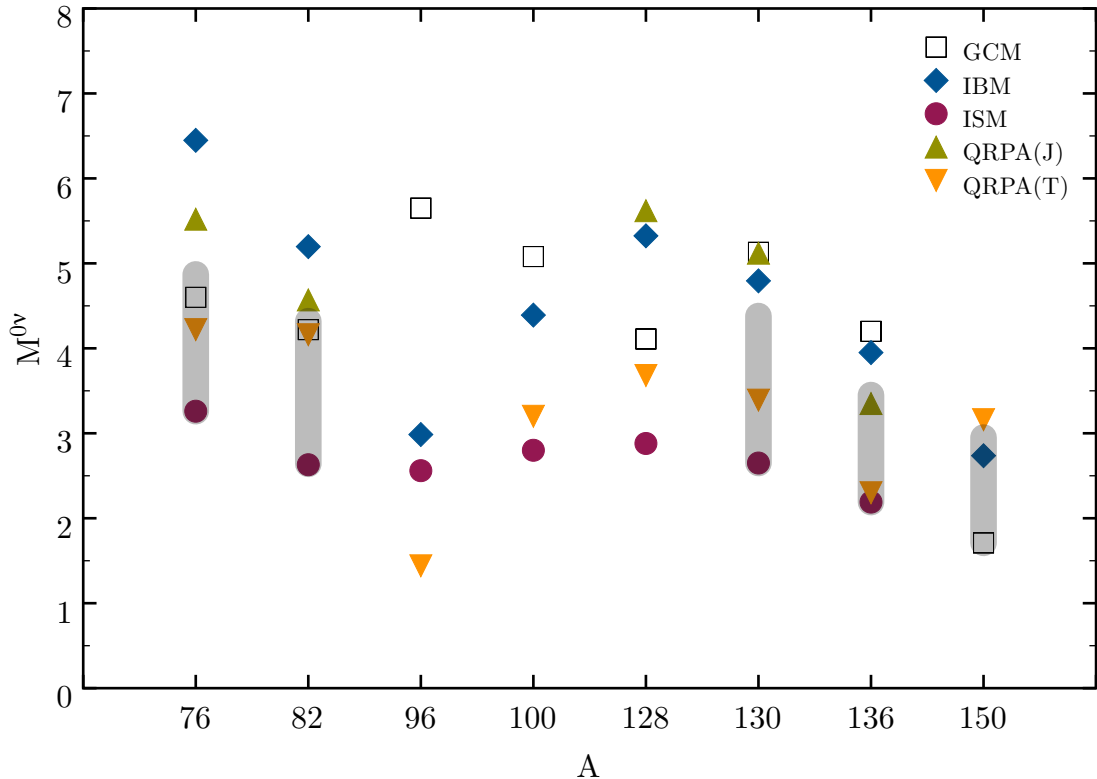


Figure 2.6: Nuclear matrix element calculations for a variety of isotopes. The behavior is relatively stable from isotope to isotope due to the short-range interaction for  $\beta\beta0\nu$  decay. The shaded regions represent ranges based on known biases of the various methods, as suggested by [72]. Figure from [72].

two-step process:

$$(Z, A) \rightarrow (Z + 1, A) + e^- + \bar{\nu}_e \\ \nu_e + (Z + 1, A) \rightarrow (Z + 2, A) + e^-, \quad (2.10)$$

where the intermediate state is a virtual state because it does not conserve energy.

Because the two converted protons must be near each other within the nucleus for the neutrino interaction to occur, the  $M_{0\nu}$  is not very sensitive to the variations in nuclear structure between elements; this is in contrast to the transition probability for  $\beta\beta 2\nu$ ,  $M_{2\nu}$ , for which the neutrons may be well-separated within the nucleus [73].

This similarity can be observed in figure 2.6.

To compute the nuclear matrix elements  $M_{0\nu}$ , two main approaches exist: the quasi-random phase approximation (QRPA) and the nuclear shell model. In the simpler random phase approximation (RPA), the transition from initial to intermediate state and from intermediate to final state are produced by operators of the form  $p^+ n$ , where  $p^+$  represents the proton creation operator and  $n$  represents the neutron annihilation operator. The goal is to make these operators more bosonic (and hence more amenable to treatment in a statistical fashion), and so these operators are diagonalized in a new basis which acts on pairs of nuclei and obeys bosonic commutation rules. QRPA is similar to RPA, but additionally takes into account the preference of like nuclei to pair together. This is accomplished at the cost of breaking nucleon number conservation in the operator, but nucleon number is still preserved on average, and the modification can have a significant impact on the

result [1].

The other common approach to nuclear matrix calculations, the nuclear shell model, attempts to capture more fully the dynamics of a nuclear system by including the full nucleon state space and using nucleon-pair (or higher-order) interactions which can be measured empirically from small nuclei. The disadvantage compared to QRPA is its enormous computational demands which make a full shell model treatment of relevant  $\beta\beta0\nu$  nuclei impossible at this point. However, it is possible to perform nuclear shell model calculations with a severely truncated state space, and for nuclei whose shape is close to spherical the results can be reasonable. As computational power increases it is likely that the shell model will overtake QRPA methods, but for now only a few large-scale shell model calculations of  $\beta\beta0\nu$  matrix elements have been undertaken [1].

One important component of both the shell model and QRPA techniques is feedback from experimental data. This can serve two purposes. The first is validation: because both approaches make significant approximations, the results of those approximations must generally be tested empirically to ensure they do not have adverse consequences for the accuracy of the result. Observables such as nuclear energy levels and emission spectra are commonplace; only recently, however, have precision decay rates for  $\beta\beta2\nu$  decay begun to appear in the literature [74]. Although there are many differences between the calculations of  $M_{2\nu}$  and  $M_{0\nu}$ , still it is currently the best source of validation for  $M_{0\nu}$  calculations available, so this can help researchers to improve their understanding of the appropriate approximations for double-beta decay matrix elements.

The other benefit of experimental data is that it can help to constrain input parameters to the calculations. In QRPA, a parameter called  $g_{pp}$  controls the strength of phonon-phonon interactions and needs to be fixed from experimental data; the double-beta matrix elements depend strongly on the value of this parameter, and precision observations of  $\beta\beta2\nu$  can be used to constrain its value [1, 73]. In the shell model, the extreme truncation of the single-particle state space results in a need to renormalize the axial vector current  $g_A$ , which requires a related observable to control that renormalization; precision observations of  $\beta\beta2\nu$  can be an appropriate method to constrain that value as well. One disadvantage to the use of  $\beta\beta2\nu$  decay rates to constrain parameters which are input to calculations is that the same observations can no longer be used to validate the approximations for double-beta decays [73]. A description of efforts to obtain new experimental data useful for nuclear theory can be found in [75].

When the results from modern shell model and QRPA calculations are compared, it is found that the results can differ by as much as a factor of 2-3 [1]. Provided that there is no systematic effect which impacts both methods similarly, this permits us to understand in a rough way the level of accuracy provided by these calculations. Progress in reducing these differences continues primarily by increasing the number of single-particle states that can be included, but it is clear that for the near term the search for  $\beta\beta0\nu$  will only be able to set rough limits on Majorana neutrino mass  $\langle m_{\beta\beta} \rangle$  of equation 2.7.

## 2.4 Neutrino Flavor Physics

Neutrinos are known to exist in three flavors, or eigenstates which are diagonal with respect to the lepton interaction terms of the Standard Model. These flavors are  $\nu_e$ ,  $\nu_\mu$ , and  $\nu_\tau$ ; they interact, respectively, with  $e$ ,  $\mu$ , and  $\tau$  leptons. We also expect there to be a basis in which the neutrino mass matrix is diagonalized, and these two bases are not the same. We call the mass eigenstates  $\nu_1$ ,  $\nu_2$ , and  $\nu_3$  with respective masses  $m_1$ ,  $m_2$ , and  $m_3$ . The unitary operator which translates between the two bases is specified by:

$$\begin{pmatrix} \nu_e \\ \nu_\mu \\ \nu_\tau \end{pmatrix} = \mathbf{U} \begin{pmatrix} \nu_1 \\ \nu_2 \\ \nu_3 \end{pmatrix} = \begin{pmatrix} U_{e1} & U_{e2} & U_{e3} \\ U_{\mu 1} & U_{\mu 2} & U_{\mu 3} \\ U_{\tau 1} & U_{\tau 2} & U_{\tau 3} \end{pmatrix} \begin{pmatrix} \nu_1 \\ \nu_2 \\ \nu_3 \end{pmatrix}. \quad (2.11)$$

These formalities are uninteresting if the neutrino sector is massless, since the mass eigenstates are degenerate. However, in the case where neutrinos are massive, we can see that neutrinos which are created in one flavor eigenstate will oscillate between the flavor eigenstates with a period which depends on the differences between masses, as is typical in an N-state quantum system. In the neutrino sector, we can more specifically state that the probability for a transition from flavor  $\alpha$  to flavor  $\beta$  will be: [76]

$$P_{\alpha\beta} = \delta_{\alpha\beta} - 4 \sum_{i=1}^2 \sum_{j=i+1}^3 \text{Re} [U_{\alpha i} U_{\beta i}^* U_{\alpha j}^* U_{\beta j}] \sin^2 \left( \frac{[m_i^2 - m_j^2] L}{4E} \right) \quad (2.12)$$

where  $L$  is the distance (or time, in  $c = 1$  units) between neutrino source and destination, and  $E$  is the relativistic energy of the emitted neutrinos.

The transition probability is sensitive to the masses of the neutrinos, but only in the form  $|m_i^2 - m_j^2|$ . These measurements have now been performed in a variety of neutrino oscillation experiments, and the best current constraints are  $|m_1^2 - m_2^2| = (7.50 \pm 0.20) \cdot 10^{-5} \text{eV}^2$  [77] and  $|m_2^2 - m_3^2| = 2.32_{-0.08}^{+0.12} \cdot 10^{-3} \text{eV}^2$  [78].

However, oscillation experiments cannot constrain the overall mass scale of neutrinos; they can only set a conservative lower limit that  $\max(m_2, m_3) \geq 0.048 \text{ eV}$  if we assume one of  $m_2$  or  $m_3$  is zero. Furthermore, they do not establish the sign of the difference. We can see that  $m_1$  and  $m_2$  are fairly close together, and  $m_3$  is significantly different; but we cannot see whether  $m_3$  is larger or smaller than the other two masses. We refer to the situation with  $m_1 \simeq m_2 \ll m_3$  as the normal hierarchy, and  $m_3 \ll m_1 \simeq m_2$  as the inverted hierarchy; the regime where  $m_1 \simeq m_2 \simeq m_3 \gg |m_1^2 - m_2^2|$  is called the degenerate region. Distinguishing between these three situations is one of the significant open questions in neutrino physics because of its impact on observable quantities.

## 2.5 Particle Physics Constraints

To produce more detailed constraints on neutrino physics, it is generally useful to provide a parametrization of the mixing matrix  $\mathbf{U}$  from equation 2.11. The standard

parametrization is:

$$\begin{aligned}
\mathbf{U} &= \begin{pmatrix} U_{e1} & U_{e2} & U_{e3} \\ U_{\mu 1} & U_{\mu 2} & U_{\mu 3} \\ U_{\tau 1} & U_{\tau 2} & U_{\tau 3} \end{pmatrix} \\
&= \begin{pmatrix} 1 & 0 & 0 \\ 0 & \cos(\theta_{23}) & \sin(\theta_{23}) \\ 0 & -\sin(\theta_{23}) & \cos(\theta_{23}) \end{pmatrix} \begin{pmatrix} \cos(\theta_{13}) & 0 & \sin(\theta_{13})e^{-i\delta} \\ 0 & 1 & 0 \\ -\sin(\theta_{13})e^{i\delta} & 0 & \cos(\theta_{13}) \end{pmatrix} \times \quad (2.13) \\
&\quad \begin{pmatrix} \cos(\theta_{12}) & \sin(\theta_{12}) & 0 \\ -\sin(\theta_{12}) & \cos(\theta_{12}) & 0 \\ 0 & 0 & 1 \end{pmatrix} \begin{pmatrix} e^{i\alpha_1/2} & 0 & 0 \\ 0 & e^{i\alpha_2/2} & 0 \\ 0 & 0 & 1 \end{pmatrix}.
\end{aligned}$$

Out of the six parameters used in defining this matrix, the only ones which have been measured are the three mixing angles  $\sin^2(2\theta_{12}) = 0.857^{+0.023}_{-0.025}$  [77],  $\sin^2(2\theta_{13}) = 0.089 \pm 0.010(\text{stat}) \pm 0.005(\text{sys})$  [79], and  $\sin^2(2\theta_{23}) > 0.95$  [80]. The Dirac phase  $\delta$  is in principle observable from oscillation experiments, but no current experiments have achieved the sensitivity necessary to accomplish this. The Majorana phases  $\alpha_1$  and  $\alpha_2$  cannot be extracted from neutrino oscillations [1].

The sum of the three mass eigenstates,  $M = \sum m_i$ , can be constrained by cosmological observations. This constraint, like all cosmologically-based constraints, is model-dependent; it relies on the expectation that low-mass, hot forms of dark matter similar to neutrinos promote the formation of large-scale structures in the early universe by allowing extremely remote regions of matter to remain in thermal

equilibrium. Recent results from Planck combined with WMAP and baryon acoustic oscillations have restricted  $M < 0.230$  eV with 95% confidence [81]. Considering the assertion in section 2.4 that the heaviest neutrino must have a mass no less than 0.048 eV, we can see that this cosmological constraint pushes  $M$  to within a factor of five of its lower limit. Taken at face value, the Planck measurement is the strongest existing constraint on the absolute mass scale of neutrinos.

Closer to home, the mass of neutrinos is also reflected in  $\beta$  decay,  $d \rightarrow u + e^- + \bar{\nu}_e$ . The total energy of the daughter products is known, and is shared between the electron and antineutrino; the minimum energy of the antineutrino is its rest mass, so by searching for the maximum energy of the electron we can simultaneously measure the rest mass of the neutrino. The electron anti-neutrino emitted from beta decay is a mixture of all three mass eigenstates; since no current or planned experiment has sufficiently good energy resolution to resolve the separate endpoints from the three neutrino masses, we can instead write an effective rest mass of an electron antineutrino as: [1]

$$\langle m_\beta \rangle^2 = \sum_i m_i^2 |U_{ei}|^2. \quad (2.14)$$

To measure  $\langle m_\beta \rangle$  we must observe the electron energy spectrum of beta decays at the endpoint, which is complicated by the fact that this portion of the electron spectrum contains only a small fraction of the total electron statistics. Tritium ( ${}^3H$ ) is commonly used for these experiments because it has a medium-length half-life of 12.3 years and an extremely low  $\beta$  decay endpoint energy of 18.6 keV, which

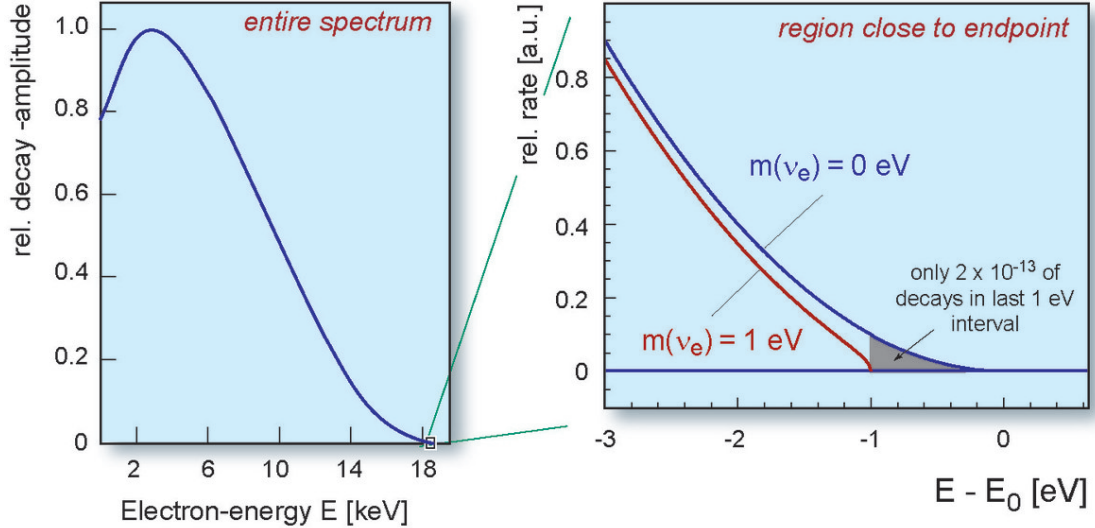


Figure 2.7: The electron spectrum of Tritium ( ${}^3H$ )  $\beta$  decay. The endpoint contains only a small fraction of the total statistics. Figure from [82].

maximizes the relative shift in endpoint energy due to  $\langle m_\beta \rangle$ . Figure 2.7 shows that for  $\langle m_\beta \rangle = 1$  eV in Tritium, experiments must observe a shift in the spectrum which affects only about one decay in  $5 \cdot 10^{12}$ , making this level of sensitivity extremely difficult to achieve. The best existing limit from  $\beta$  decay is  $\langle m_\beta \rangle < 2.05$  eV, with 95% confidence, from the Troitsk experiment which ran from 1994 to 2004 [83]. The KATRIN experiment hopes to achieve a sensitivity of 0.2 eV, and is expected to begin taking data in 2015 [84, 85].

## 2.6 Nuclear Physics Constraints from $\beta\beta0\nu$

As stated in equation 2.7, it is possible to relate the rate of  $\beta\beta0\nu$  decay to the effective Majorana neutrino mass  $\langle m_{\beta\beta} \rangle$  by:

$$[T_{1/2}^{0\nu}]^{-1} = G_{0\nu}(Q_{\beta\beta}, Z) |M_{0\nu}|^2 \langle m_{\beta\beta} \rangle^2, \quad (2.15)$$

where the phase-space factor  $G_{0\nu}(Q_{\beta\beta}, Z)$  and nuclear matrix element  $M_{0\nu}$  have been described in section 2.3. We can now proceed to relate the effective Majorana neutrino mass to the parametrization of section 2.4. We follow this relation with a discussion of the considerations which affect a  $\beta\beta0\nu$  decay search and a summary of the current state of the field.

The effective Majorana neutrino mass  $\langle m_{\beta\beta} \rangle$  comes from a combination of the three mass eigenvalues described in section 2.4. It takes the form:

$$\langle m_{\beta\beta} \rangle = \left| \sum_k m_k U_{ek}^2 \right|. \quad (2.16)$$

Unlike  $\langle m_\beta \rangle$ , which is an incoherent sum of strictly positive terms in equation 2.14, we can see that  $\langle m_{\beta\beta} \rangle$  is a coherent sum of terms, each of which may have arbitrary complex phase which may increase or decrease the result of equation 2.16. In other words it is possible, even if neutrinos do have Majorana mass, for  $\langle m_{\beta\beta} \rangle$  to be arbitrarily small if  $\mathbf{U}$  is tuned to produce cancellations between terms, specifically by tuning the Majorana phases and selecting the normal rather than inverted mass

hierarchy [86].

It is possible to relate the observables  $\langle m_{\beta\beta} \rangle$ ,  $\langle m_\beta \rangle$ , and  $M$  within the model for  $\mathbf{U}$  of equation 2.13. These relations are shown in figure 2.8; we recall from section 2.5 that beta spectrum measurements constrain  $\langle m_\beta \rangle < 2.05$  eV and cosmological observations constrain  $M < 0.230$  eV, both with 90% confidence. The strongest constraints on  $\langle m_{\beta\beta} \rangle$  from  $\beta\beta0\nu$  searches place  $\langle m_{\beta\beta} \rangle < 0.15 - 0.4$  eV, depending on the choice of matrix element calculations. We can see that if the cosmological limits are to be trusted, they provide the strongest constraints on the neutrino mass parameters; however, all three observables are complementary, and the wide range of experimental approaches means that systematic effects are unlikely to be shared by all three methods. The figure shows the relation between these parameters in blue for the normal hierarchy and red for the inverted hierarchy; we note that it is only for the normal hierarchy at equation 2.16 can lead to an extremely small  $\langle m_{\beta\beta} \rangle$ . In the case of the inverted hierarchy we can see  $\langle m_{\beta\beta} \rangle > 0.013$  eV, only an order of magnitude lower than the current limits.

The sensitivity of an experiment for measuring  $T_{1/2}^{0\nu}$  can be described by the approximate formula: [1]

$$T_{1/2}^{0\nu}(n_\sigma) = \frac{4.16 \cdot 10^{26} \text{ yrs}}{n_\sigma} \left( \frac{\epsilon a}{W} \right) \sqrt{\frac{Mt}{b\Delta E}}, \quad (2.17)$$

where  $M$  is the mass of material,  $a$  is the isotopic enrichment,  $W$  is the molecular mass of the material in atomic units, and  $t$  is the livetime of the experiment;  $\epsilon$  is the signal efficiency,  $b$  is the background rate (in counts per kg keV year, or some

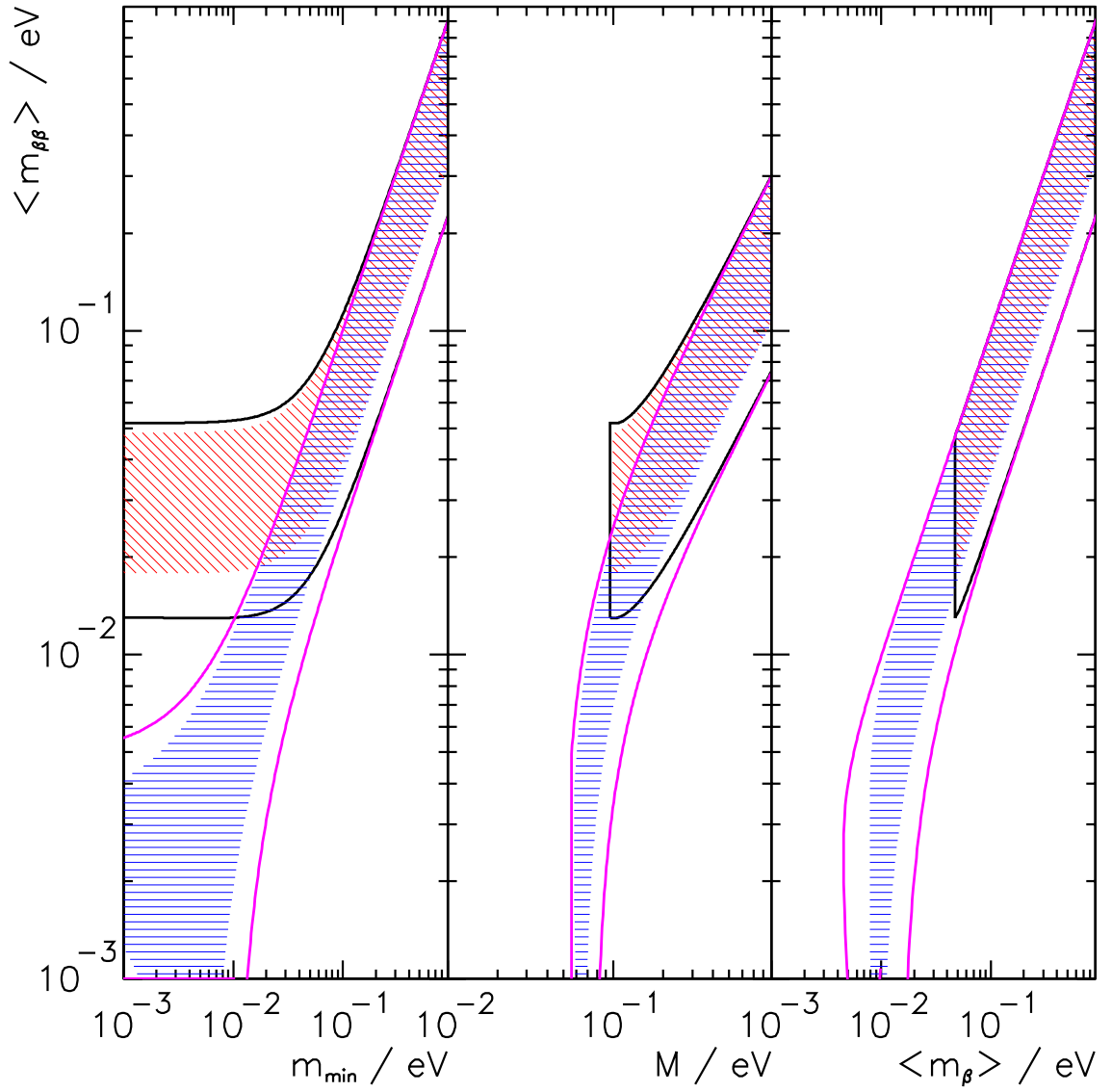


Figure 2.8: The relationship between the effective Majorana mass  $\langle m_{\beta\beta} \rangle$  and other fundamental neutrino quantities: the lightest neutrino mass eigenstate  $m_{\min}$ , the sum of mass eigenstates  $M = \sum m_i$ , and the effective single-beta-decay neutrino mass  $\langle m_\beta \rangle$ . Black (magenta) lines indicate the allowed region for the inverted (normal) hierarchy; red (blue) hatches indicate uncertainty for the inverted (normal) hierarchy due to the unknown CP-violating and Majorana phases  $\delta$ ,  $\alpha_1$ , and  $\alpha_2$  [86].

similar units), and  $\Delta E$  is the energy resolution of the detector at the  $Q$ -value; and  $n_\sigma$  is the desired confidence limit, in sigmas, where the standard 90% confidence limit will require  $n_\sigma = 1.64$ . The scaling of this equation is most accurate when the energy resolution is much smaller than the  $Q$ -value and the background is uniformly distributed in energy; however, when combined with phase factor and nuclear matrix element estimates it roughly allows us to compare the sensitivity of different  $\beta\beta0\nu$  experiments.

According to equation 2.17 we should prefer experiments for which:

- A large quantity of highly-enriched isotope can be obtained.
- Signal detection is highly efficient.
- Background contamination around the  $Q$ -value is small, and does not scale with detector mass.
- Good energy resolution can be achieved.

The leading experiments which are planned or currently searching for  $\beta\beta0\nu$  are as follows:

1. The leading search for  ${}^{76}\text{Ge}$  comes from the GERDA experiment at the Gran Sasso Laboratory in Italy. GERDA consists of an array of cryogenic germanium detectors with charge readout.  ${}^{76}\text{Ge}$  has a  $Q$ -value of only 2039 keV, giving it a lower phase factor than other popular materials. It also is expensive to grow large uniform crystals of germanium; this means that it is difficult for a germanium experiment to take advantage of self-shielding from external

radioactive backgrounds. However, its strongest advantage is its excellent energy resolution: GERDA has achieved an energy resolution at its  $Q$ -value of 1.1-1.7 keV ( $\sigma$ ) with its newer crystals [15].

2. The best results with  $^{130}\text{Te}$  have come from the CUORICINO experiment which ran at the Gran Sasso Laboratory in Italy. CUORICINO was a bolometric experiment: it cooled tellurium crystals to extremely low temperatures where the heat capacity becomes small, so that a decay inside the tellurium creates a measurable change in temperature. Similarly to  $^{76}\text{Ge}$ , it is expensive to grow large crystals of tellurium, so most tellurium experiments use an array of detectors.  $^{130}\text{Te}$  has a  $Q$ -value of 2528 keV, somewhat larger than that of  $^{76}\text{Ge}$ , but the energy resolution of the enriched crystals was 2.1-10.6 keV ( $\sigma$ ), depending on the crystal. CUORICINO stopped running in 2008 [20]; planned experiments in  $^{130}\text{Te}$  include CUORE [87] and SNO+ [88], both of which anticipate data-taking beginning in 2015.
3. The two leading experiments in  $^{136}\text{Xe}$  are KamLAND-Zen, located at the Kamioka Observatory, and EXO-200, located in the WIPP facility.  $^{136}\text{Xe}$  also has a  $Q$ -value of 2458 keV, giving it a higher phase-space factor than  $^{76}\text{Ge}$  but not  $^{130}\text{Te}$ . KamLAND-Zen dissolves its xenon in a liquid scintillator and observes only scintillation energy; it achieves an energy resolution of 103 keV ( $\sigma$ ), modest compared to the resolution achieved in tellurium and germanium, but its monolithic nature allows it to keep backgrounds low [13]. EXO-200 is a pure liquid xenon detector which observes both ionization and scintillation.

Isotope	$T_{1/2}^{0\nu}$ (years)	$M_{0\nu}$	$G_{0\nu}$ (yrs $^{-1}$ )	$\langle m_{\beta\beta} \rangle$ (eV)	Collaboration
$^{48}\text{Ca}$	$5.8 \cdot 10^{22}$	2.28	$2.48 \cdot 10^{-14}$	3.7	ELEGANT IV [90]
$^{76}\text{Ge}$	$2.1 \cdot 10^{25}$	5.98	$2.36 \cdot 10^{-15}$	0.24	GERDA [15]
$^{82}\text{Se}$	$3.6 \cdot 10^{23}$	4.84	$1.02 \cdot 10^{-14}$	1.1	NEMO-3 [91]
$^{96}\text{Zr}$	$9.2 \cdot 10^{21}$	2.89	$2.06 \cdot 10^{-14}$	8.0	NEMO-3 [92]
$^{100}\text{Mo}$	$1.1 \cdot 10^{24}$	4.31	$1.59 \cdot 10^{-14}$	0.56	NEMO-3 [27]
$^{116}\text{Cd}$	$1.6 \cdot 10^{22}$	3.16	$1.67 \cdot 10^{-14}$	6.1	NEMO-3 [91]
$^{130}\text{Te}$	$3.0 \cdot 10^{24}$	4.47	$1.42 \cdot 10^{-14}$	0.34	Cuoricino [21]
$^{136}\text{Xe}$	$1.1 \cdot 10^{25}$	3.67	$1.46 \cdot 10^{-14}$	0.22	EXO-200 [89]
$^{136}\text{Xe}$	$1.9 \cdot 10^{25}$	3.67	$1.46 \cdot 10^{-14}$	0.16	KamLAND-Zen [13]
$^{150}\text{Nd}$	$1.8 \cdot 10^{22}$	2.74	$6.30 \cdot 10^{-14}$	3.4	NEMO-3 [93]

Table 2.1: A listing of the strongest available  $\beta\beta0\nu$  limits; all half-life and mass limits are quoted at 90% confidence. Limits on  $\langle m_{\beta\beta} \rangle$  are obtained using phase space factors from [94] and matrix elements from [95], both chosen for the completeness of their tabulations. These sources explicitly factor out  $g_A$ ; we use  $g_A = 1.269$ . For  $^{136}\text{Xe}$ , both Kamland-Zen’s published results and the EXO-200 results described in this work are included in the table.

This, combined with analysis improvements described in the present work,

allows it to achieve a somewhat better energy resolution of 38 keV ( $\sigma$ ) [89].

Table 2.1 tabulates the most current  $T_{1/2}^{0\nu}$  limits in all  $\beta\beta0\nu$  isotopes for which  $\beta\beta0\nu$  limits have been published. Representative limits on  $\langle m_{\beta\beta} \rangle$  are also included; these come from one particular set of phase space factors and nuclear matrix element calculations performed using the interacting-boson model; this pair of sources for calculations is made because they include tabulations for a broad range of isotopes and permit comparisons across all available half-life limits [94, 95]. However, one should bear in mind that errors in the matrix elements propagate to errors in  $\langle m_{\beta\beta} \rangle$  of as much as a factor of two for each isotope. We can see that although there are a favored set of isotopes, active and successful programs exist in a wide range of isotopes, and no one isotope is ideal in all respects.

As the table indicates,  $^{136}\text{Xe}$  has provided some of the strongest constraints

on  $\langle m_{\beta\beta} \rangle$  in spite of its relatively modest energy resolution. The present work demonstrates significant improvements to the energy resolution observed by the EXO-200 detector in  ${}^{136}\text{Xe}$  which have been achieved through offline denoising of the scintillation signals. This denoising technique is applied to data from the detector, and results in a stronger limit on  $T_{1/2}^{0\nu}$  from EXO-200 than could be obtained from the same data without denoising. Chapter 7 presents recent results from EXO-200 which benefit from this denoising technique, as well as increased livetime and other improvements.

# Chapter 3: The EXO-200 Detector

This chapter describes the physical apparatus of the EXO-200 detector. Section 3.1 gives a broad overview of the detector. Section 3.2 identifies the dominant backgrounds for  $\beta\beta0\nu$  decay, and sections 3.3 and 3.4 describe methods used to mitigate these backgrounds. The pulse and waveform readout subsystems are described in section 3.5, where discussion of the scintillation readout will be particularly important for subsequent chapters. We conclude with a description of the calibration systems in section 3.6. Throughout, the reader is referred to the detailed description in [96] for more information.

## 3.1 Overview of the EXO-200 Detector

The EXO-200 detector is a cryogenic experiment containing 175 kg of liquid xenon enriched to 80.6% in  $^{136}\text{Xe}$ . Of those 175 kg of liquid xenon, 110 kg are contained within the “active” volume where the detector is fully sensitive to deposited energy from  $\beta\beta0\nu$  decay [96], and 94.7 kg are contained within the fiducial volume where the detector’s response is well-understood. This implies that  $3.39 \cdot 10^{26}$  atoms  $^{136}\text{Xe}$  which are for the search [89].

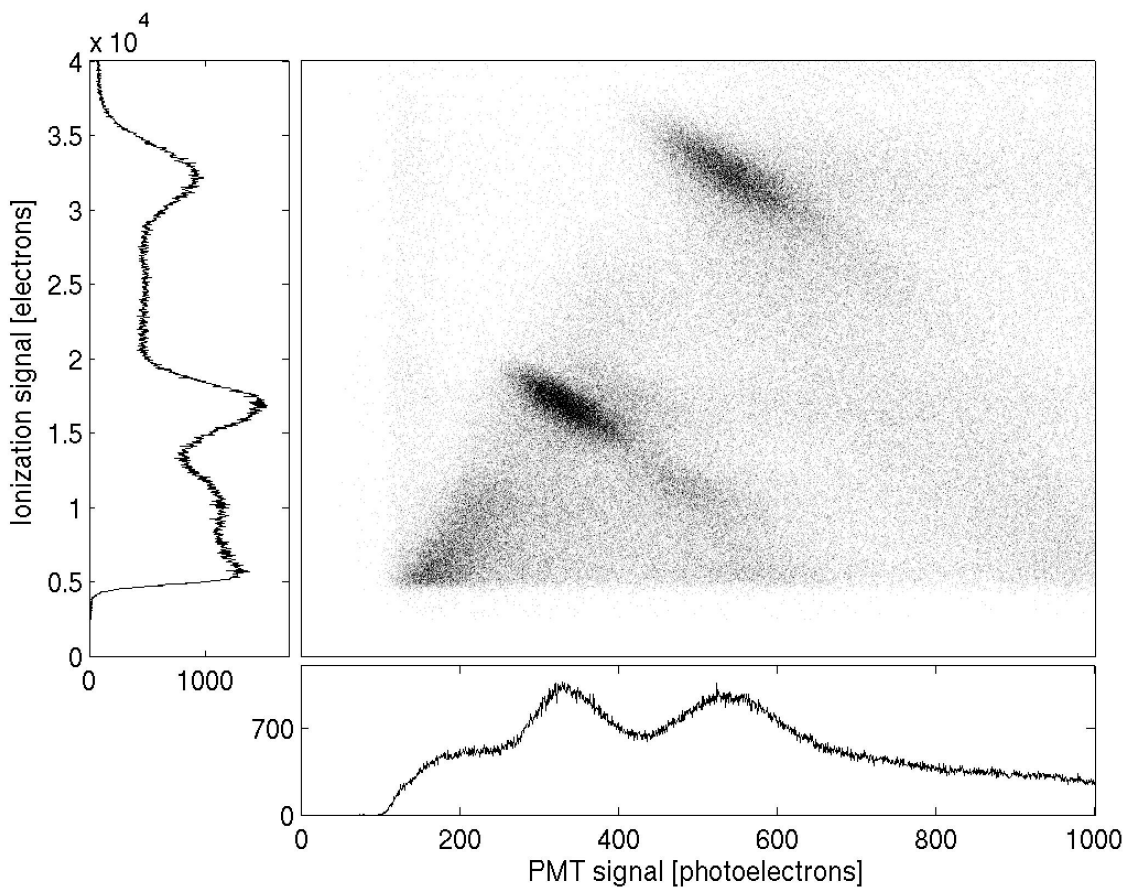


Figure 3.1: A two-dimensional energy spectrum of scintillation and ionization from a testbed liquid xenon experiment under an electric field of 4 kV/cm. The spectrum is from a  $^{207}\text{Bi}$  source with dominant gamma lines at 570 and 1064 keV. Figure reproduced from [97].

Energy deposits in xenon can be measured primarily in two ways: vacuum ultraviolet (VUV) scintillation photons are emitted from the de-excitation of xenon eximers, and xenon atoms are ionized to produce free electrons. It is well-known [97] that liquid noble element calorimeters show significant fluctuations in their separate production of scintillation photons and free electrons, but that these separate quantities are strongly anticorrelated. As a result, it is possible to achieve far better energy resolution if both light and charge are independently measured than if only one is detected. Figure 3.1 illustrates this phenomenon in a testbed liquid xenon experiment, where it is apparent that using light and charge simultaneously lets us observe narrower gamma lines than either would individually; the same is also true of beta and double-beta lines such as the  $\beta\beta0\nu$  decay we seek.

To observe free electrons we must impose an electric field on the xenon which drifts the electrons onto a collection anode. The EXO-200 detector is shaped as a cylinder, and the required electric field is produced by placing a cathode grid in the center of that cylinder and anode wires along each of the two endcaps of the detector; such a detector is called a time projection chamber, or TPC. The EXO TPC is shown in figure 3.2. Charge is collected on the anode wires and light is collected by avalanche photo-diodes (see section 3.5) mounted on the endcaps behind the anode wires; the time difference between the two signals indicates the initial position of the charge along the direction of the field. The anode wires are thin, so the u- and v-wire planes together have 91.8% optical transparency which does not interfere significantly with APD light collection [96].

The cathode is maintained at a voltage of  $-8$  kV below the anode wire voltage,

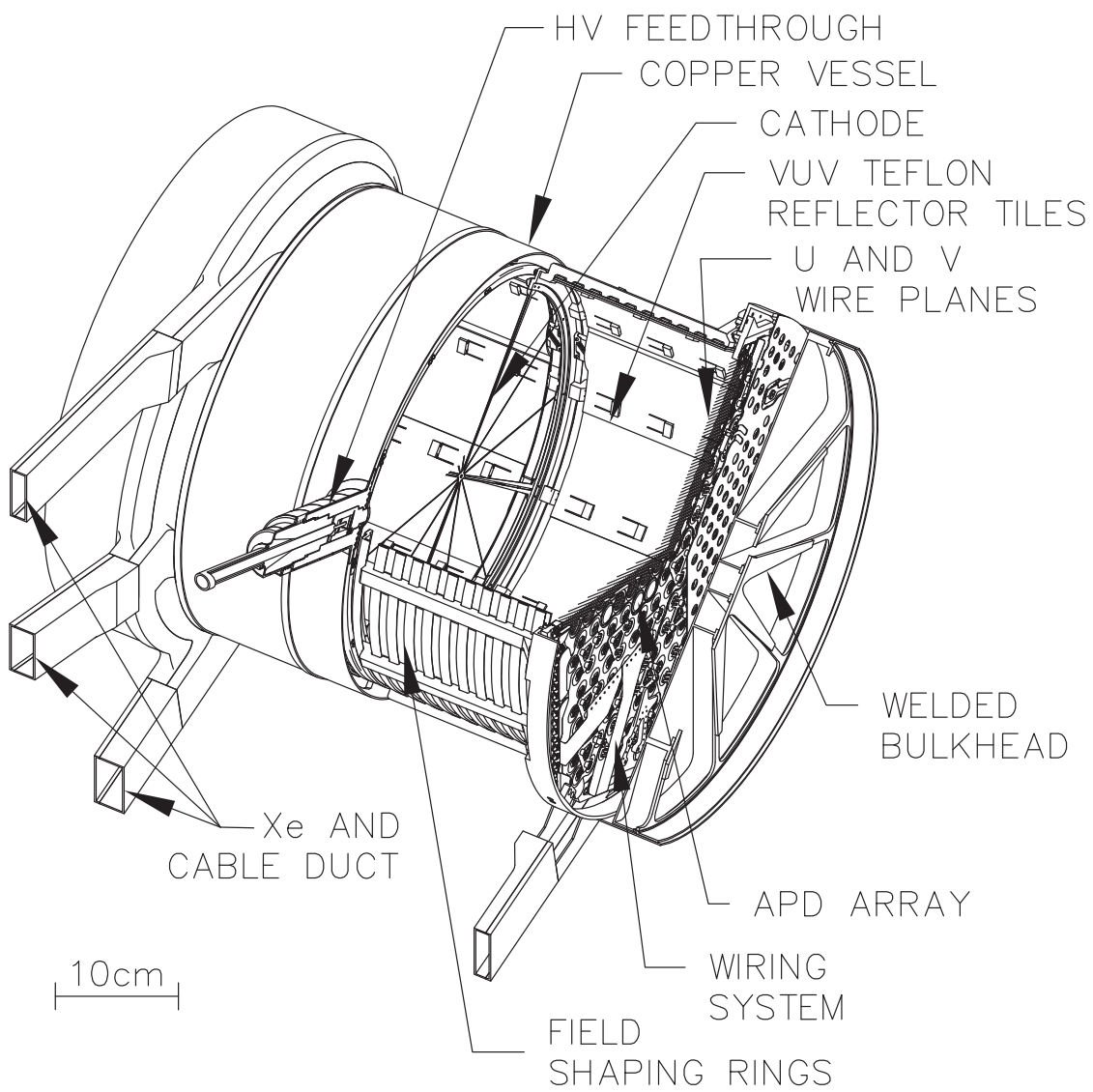


Figure 3.2: Schematic of the inner EXO-200 TPC. Figure reproduced from [96].

which is at virtual ground. Field shaping rings encircle the charge drift region to ensure that electric field lines are parallel and the magnitude of the electric field is constant in the bulk volume of xenon. (Near the edges, non-uniformities in the electric field are expected to exist; these are a continuing topic of research.) The cathode and APDs are separated by 20.4 cm. The bulk volume of xenon has an electric field of 374 V/cm.

Electrons in liquid xenon drift at a velocity of  $1.71 \text{ mm}/\mu\text{s}$  under an electric field of 374 V/cm. The maximum drift distance from the cathode to the anode is 198.4 mm, resulting in a maximum electron drift time of  $116 \mu\text{s}$ . Free electrons are not absorbed by xenon – as for other noble elements, xenon has a low electronegativity, so in pure xenon electrons drift unimpeded indefinitely. The EXO-200 liquid xenon has small quantities of electronegative impurities which could include oxygen or nitrogen. The exact nature of these impurities is unknown. To minimize the concentration of these impurities, the xenon is constantly circulated through a hot zirconium getter which extracts chemically active molecules and permits noble elements to pass through [96].

It is necessary to associate charge pulses with their corresponding scintillation pulses because they are separated by an unknown drift time of up to  $116 \mu\text{s}$ . This is easily done provided the typical time between events is much longer than  $116 \mu\text{s}$ , and the time difference serves as our measurement of the position of the energy deposit along the direction of the electric field. Our  $1 \mu\text{s}$  sampling rate permits us to reconstruct this position coordinate with an accuracy of 0.42 mm [74].

At the anode, there are two sets of parallel wire planes as shown in figure 3.3.

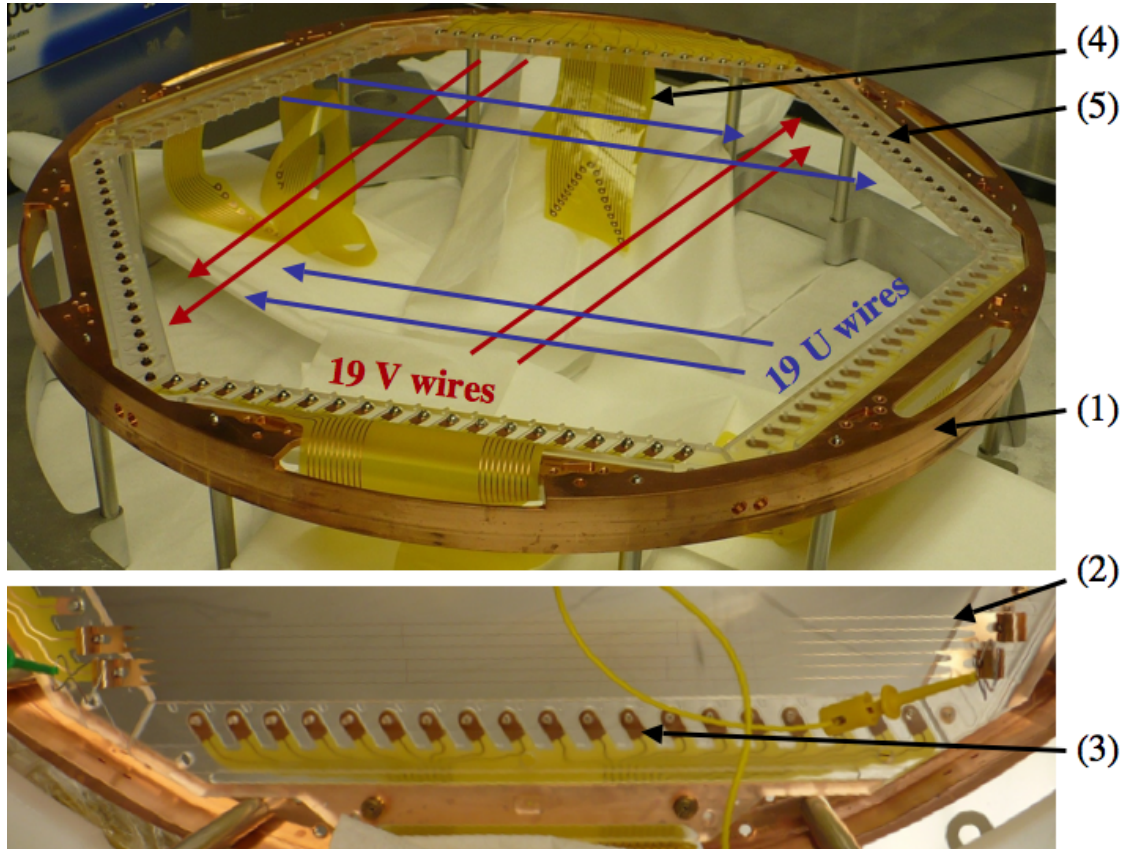


Figure 3.3: Anode collection wires (u-wires) and induction wires (v-wires) from EXO-200. (1) and (5) indicate the wire support frame; (2) indicates the wires themselves, constructed as gangs of three wires; (3) illustrates the attachment between wires and the support frame; (4) shows the return cables from the wires to the data acquisition system. Figure reproduced from [96].

The first (closer to the cathode) parallel wire plane is called the “v-wire” plane, and the second plane is called the “u-wire” plane. The voltages of the two wire planes are set so that no drift field lines terminate on the v-wires. Instead, all drift field lines penetrate through the v-wire plane and terminate on the u-wires. When charge is deposited in the liquid xenon and drifts toward the anode, it induces a bipolar current on the v-wires as it passes by, and then produces a unipolar current on the u-wires as it is collected. See section 3.5 for details on the wire readout and section 7.1.2 for illustrations of the expected pulse shapes.

The u- and v-wires are rotated sixty degrees relative to each other. Figure 3.3 indicates the orientation of the u-wires and v-wires, and figure 7.27 illustrates from top-down perspective the u-v coordinate system defined by the wires alongside the x-y coordinate system used in analysis. By detecting which wires observe a current pulse in both the u-wire and v-wire channels, it is possible to identify the two-dimensional location on the anode where the charge arrived. Channels in each plane are 9 mm wide; by taking advantage of signal sharing which sometimes occurs between u-wires and always occurs between v-wires, we are able to achieve position accuracy of 2.4 mm perpendicular to the u-wires and 1.2 mm perpendicular to the v-wires [74].

Energy which appears to come from a single location is called a charge deposit “cluster” or “site”, and events are classified according to the number of sites they produce (their “multiplicity”) as either single-site or multi-site. We will see in section 3.4 that this provides a powerful tool for background characterization and rejection.

This section has described how energy deposits in the liquid xenon are transformed into scintillation and charge, which are then observed by APDs and anode wires, respectively. These observations are sufficient for us to reconstruct the positions and magnitudes of energy deposits in the liquid xenon in all three coordinates.

## 3.2 Backgrounds to $\beta\beta0\nu$ Decay

$^{136}\text{Xe}$  has a relatively high  $Q$ -value compared to  $^{76}\text{Ge}$ ; in the neutrinoless mode the two emitted electrons will share 2456.7 keV [89]. This means that the sensitivity of  $T_{1/2}^{0\nu}$  to the mass of the neutrino is good in  $^{136}\text{Xe}$  compared to  $^{76}\text{Ge}$ , as was described in section 2.6; it also means that the energy spectrum around our  $Q$ -value will naturally be relatively free from most sources of background radiation. This section will identify the types of background which can be expected to affect our  $\beta\beta0\nu$  search; subsequent sections will describe methods of mitigating those backgrounds.

It is common for alpha decays to have energies well in excess of our  $Q$ -value. As a result, we might expect all alpha decays to be possible backgrounds to  $\beta\beta0\nu$ . However, alpha particles are stopped rapidly by even a small quantity of shielding, and as a result the only alpha decays which can be observed in the detector are those from sources which are dissolved into the xenon. Radon is the only alpha-emitting noble element, and in EXO-200 only  $^{222}\text{Rn}$  is sufficiently long-lived to diffuse into the xenon; as a result, we only expect  $^{222}\text{Rn}$  and its daughter products to contribute a significant quantity of alpha decays to the detector.

Cosmic rays produce high-energy muons; these are another source of high-

energy backgrounds. Observations using the EXO-200 detector have indicated that the vertical flux of muons  $\Phi_v$  is

$$\Phi_v = (4.01 \pm 0.04(\text{stat})^{+0.04}_{-0.05}(\text{sys})) \times 10^{-7} \frac{\text{Hz}}{\text{cm}^2\text{sr}} \quad (3.1)$$

which implies a depth of  $1481^{+8}_{-6}$  meters water-equivalent [98]. The depth and muon flux of WIPP relative to other underground facilities can be seen in figure 3.11. Muons which pass through the TPC will produce a streak of energy in the detector rather than discrete clusters; generally they will have sufficient energy to pass fully through the detector. We can expect that such an event will look substantially different from a  $\beta\beta0\nu$  event, and generally will deposit substantially more energy than our  $Q$ -value as well.

More interesting are the associated by-products from the nearby passage of such a high-energy particle through the EXO-200 shielding or the surrounding salt, called spallation products. Although high-energy muons can produce a range of fission products, the most significant spallation product of muons will be neutrons which can diffuse into the detector and activate materials there.  $^{134}\text{Xe}$  and  $^{136}\text{Xe}$  are both present in significant quantities in the TPC, and by activation can be converted into the radioactive isotopes  $^{135}\text{Xe}$  and  $^{137}\text{Xe}$  respectively.  $^{135}\text{Xe}$  has an endpoint decay energy of 1165 keV which is too small for it to be a background to  $\beta\beta0\nu$  decay, but  $^{137}\text{Xe}$  undergoes  $\beta$  decay with an endpoint energy of 4173 keV. We will see that indeed  $^{137}\text{Xe}$  is a significant source of background in our detector [89, 99].

Some sources of background are intrinsic to the  $\beta\beta0\nu$  search. Any isotope

which can undergo  $\beta\beta0\nu$  decay can also undergo  $\beta\beta2\nu$  decay, and the endpoint of the  $^{136}\text{Xe}$   $\beta\beta2\nu$  spectrum is necessarily at our  $Q$ -value. The only means of reducing background from  $\beta\beta2\nu$  is to improve the energy resolution of the detector so that fewer such decays can mimic  $\beta\beta0\nu$  decay. Fortunately with the energy resolution exhibited by the EXO-200 detector,  $\beta\beta2\nu$  is subdominant to other backgrounds by many orders of magnitude [89].

Similarly, it is hypothetically possible for neutrino absorption to stimulate a single- $\beta$  decay which would otherwise have been energetically forbidden; that isotope may then undergo a second single- $\beta$  decay with a  $Q$ -value greater than the  $Q$ -value of the  $\beta\beta0\nu$  decay, acting as a background for our search. For example, in  $^{136}\text{Xe}$  the reaction  $^{136}\text{Xe} + \nu_e \rightarrow ^{136}\text{Cs} + \text{gammas}$  can occur;  $^{136}\text{Cs}$  will then undergo single- $\beta$  decay with an endpoint energy of 2548 keV and half-life of 13.6 days. This energy is above the  $Q$ -value for  $^{136}\text{Xe}$   $\beta\beta0\nu$  decay. However, this process is expected to occur at quite a low rate, and estimates indicate that it will be a negligible background until  $^{136}\text{Xe}$  sensitivities reach  $T_{1/2}^{0\nu} \approx 10^{27}$  years [100, 101].

A gamma background which is particularly detrimental to EXO-200 comes from  $^{214}\text{Bi}$ , a member of the  $^{226}\text{Ra}$  decay chain.  $^{214}\text{Bi}$  emits a gamma at 2448 keV with a branching ratio of 1.548%, which with our energy resolution is indistinguishable from our  $Q$ -value.  $^{226}\text{Ra}$  has a half-life of 1600 years and generally will be supported by  $^{230}\text{Th}$  (75,000 years),  $^{234}\text{U}$  (250,000 years), and ultimately by  $^{238}\text{U}$  ( $4.5 \cdot 10^9$  years) which has a primordial abundance in the Earth's crust and most natural materials [102]. Figure 3.4 shows the  $^{238}\text{U}$  energy spectrum as the energy resolution improves; we can see that even with excellent resolution the 2448 keV

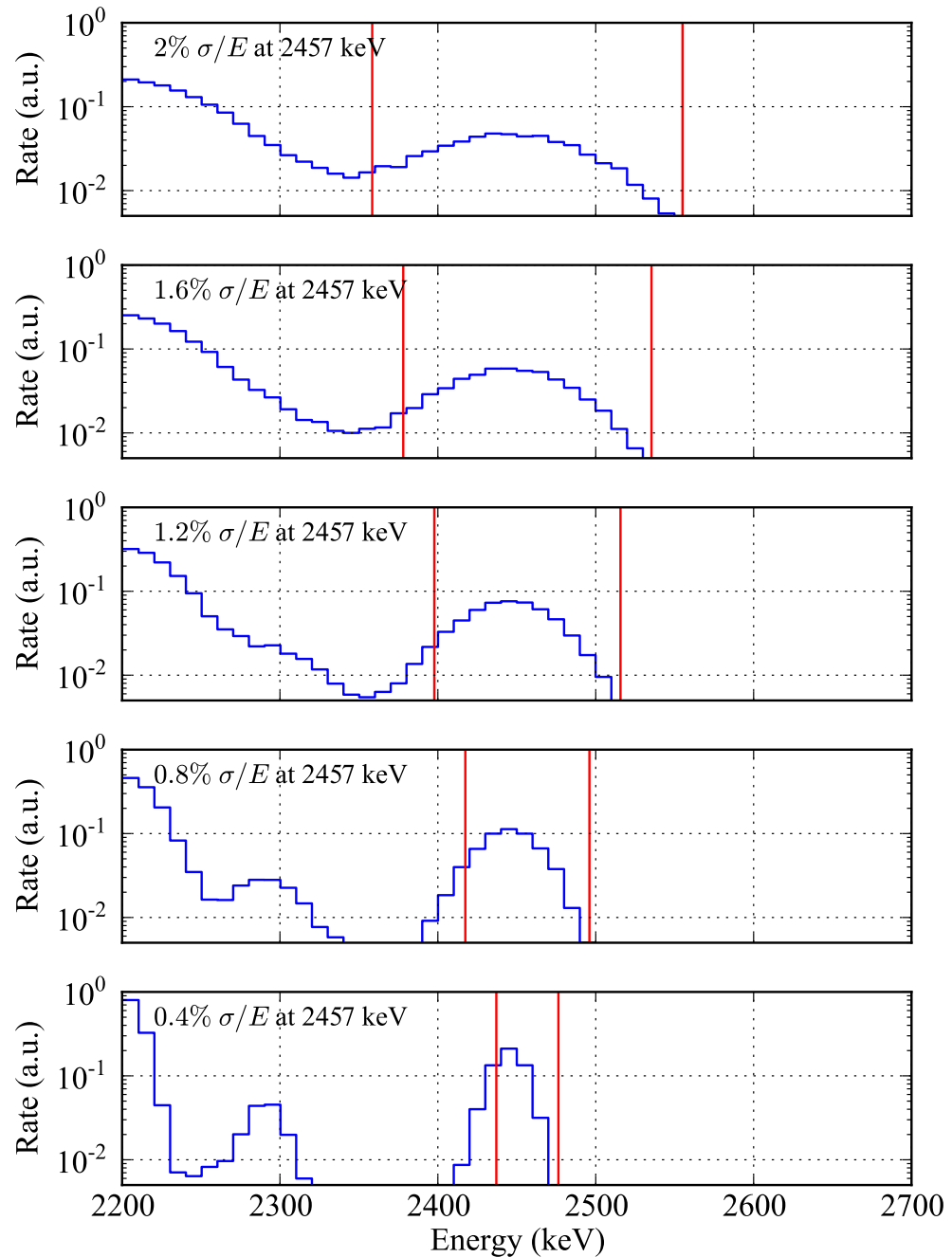


Figure 3.4: Representative  $^{238}\text{U}$  spectra as the energy resolution of the detector changes. Red lines indicate the  $2\sigma$  region of interest around the  $Q$ -value. Normalization is arbitrary, but all spectra have the same normalization. Betas and gammas are assumed to have the same calibration here; alternative beta scales are considered in section 7.4.

gamma line will be a problematic  $\beta\beta0\nu$  background.

Most other backgrounds to  $\beta\beta0\nu$  will be gamma decays from  $^{208}\text{Tl}$ , a member of the  $^{232}\text{Th}$  decay chain.  $^{208}\text{Tl}$  is produced from  $^{232}\text{Th}$  with a 35.94% branching ratio and emits a gamma at 2614.5 keV with a 99.74% branching ratio; with our  $Q$ -value of 2456.7 keV, the two energies are separated by 157.8 keV [102]. The energy resolution (in  $\sigma/E$  at our  $Q$ -value) of EXO-200 has historically been 1.5–2% at these energies [89], meaning that separation between the central values of the gamma lines will be  $3 - 4\sigma$ . (If betas and gammas have different calibrations then this number may vary; see section 7.4 for more information on the beta scale.)  $^{232}\text{Th}$  has a half-life of 14 billion years and a significant abundance in most natural materials; we expect it to contribute a significant fraction of our radioactive backgrounds, and as a result some events from the 2615 keV  $^{208}\text{Tl}$  line will leak across those  $3 - 4\sigma$  and act as backgrounds. Improving the energy resolution to 1.5% will reduce contamination from this gamma line.

The Compton edge is a well-known feature of gamma scattering spectra; it originates from gammas which enter a calorimeter, scatter once, and escape from the detector. The maximum energy which a gamma of incident energy  $E_{inc}$  can deposit in a single scatter is: [103]

$$E_{dep} = \frac{2E_{inc}^2}{m_e c^2 + 2E_{inc}}. \quad (3.2)$$

When the incident gamma has an energy of 2615 keV, the Compton edge will lie at 2382 keV, or only 74.5 keV below our  $Q$ -value. If our energy resolution is around

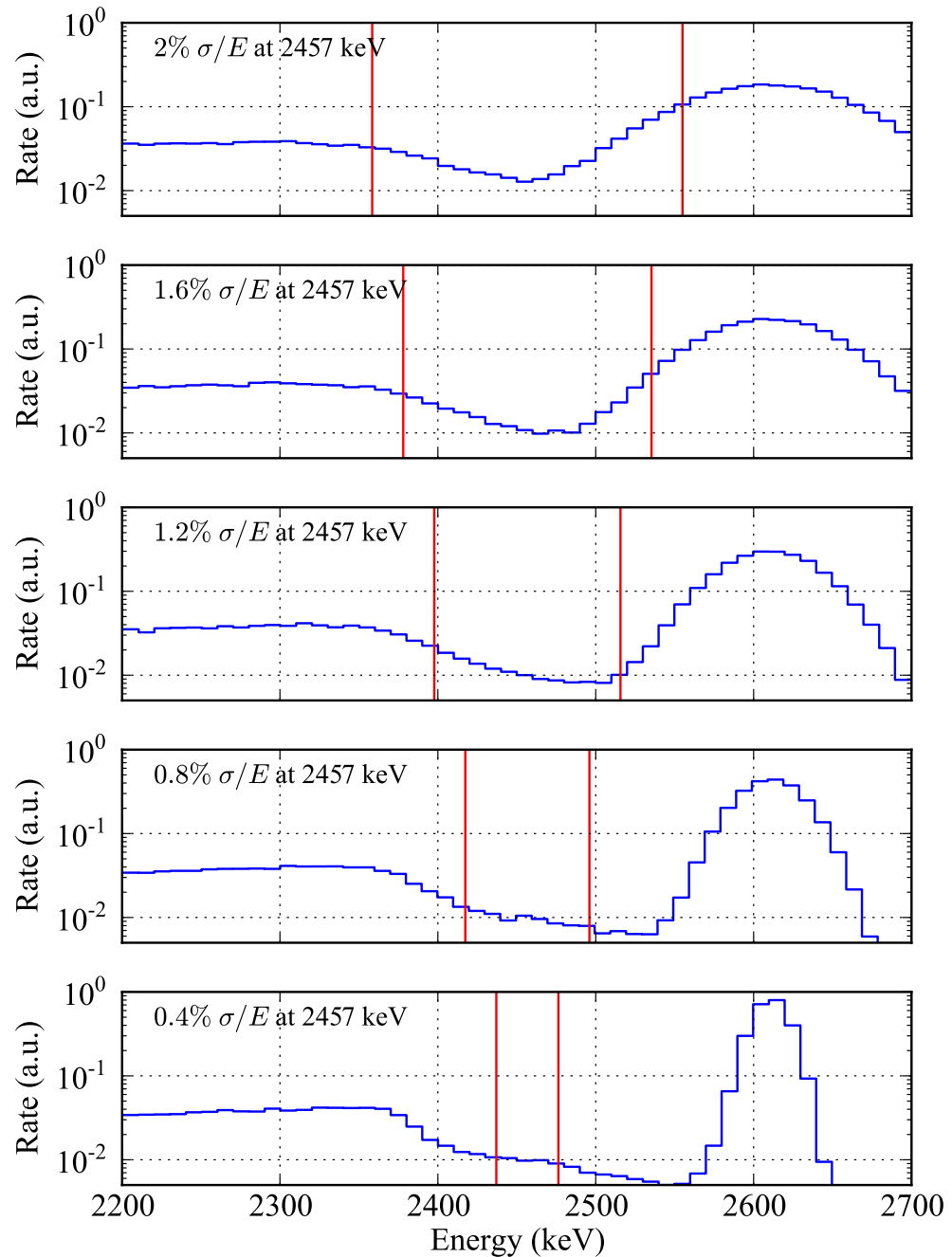


Figure 3.5: Representative  $^{232}\text{Th}$  spectra as the energy resolution of the detector changes. Red lines indicate the  $2\sigma$  region of interest around the  $Q$ -value. Normalization is arbitrary, but all spectra have the same normalization. Betas and gammas are assumed to have the same calibration here; alternative beta scales are considered in section 7.4.

$1.5 - 2\% \sigma/E$  at these energies, this separation is  $1.5 - 2\sigma$ . At energy resolutions which are better than about 1.4%, we find that the Compton edge begins to contribute more background to our  $2\sigma$  region of interest than the gamma line at 2615 keV; we can see this phenomenon from the energy spectra of figure 3.5.

Figure 3.6 summarizes the background rates from our three dominant backgrounds,  $^{232}\text{Th}$ ,  $^{238}\text{U}$ , and  $^{137}\text{Xe}$ , as they depend on the energy resolution of the detector. We can see that the background rates of  $^{232}\text{Th}$  and  $^{238}\text{U}$  do not vary smoothly with resolution due to the presence of gamma lines; by contrast, the spectrum of  $^{137}\text{Xe}$  is smooth and its background rates decrease linearly with resolution. The EXO-200 detector has a time-averaged resolution of 1.94%  $\sigma/E$  without the denoising technique described in this work, and 1.53%  $\sigma/E$  with denoising; we can see that this results in a significant reduction of backgrounds from  $^{232}\text{Th}$ . However, improvements in resolution will not decrease the backgrounds from  $^{238}\text{U}$  unless resolutions below 0.5%  $\sigma/E$  are reached, which is not feasible with the current detector. The following sections will identify some of the mechanisms beyond energy resolution which are used to further minimize these backgrounds.

### 3.3 Passive Background Rejection

We can distinguish between two classes of background rejection methods: passive methods, in which backgrounds are reduced by reducing the amount of background reaching the liquid xenon, and active methods, in which backgrounds are observed by the detector but discriminated from  $\beta\beta0\nu$  signal based on identifying character-

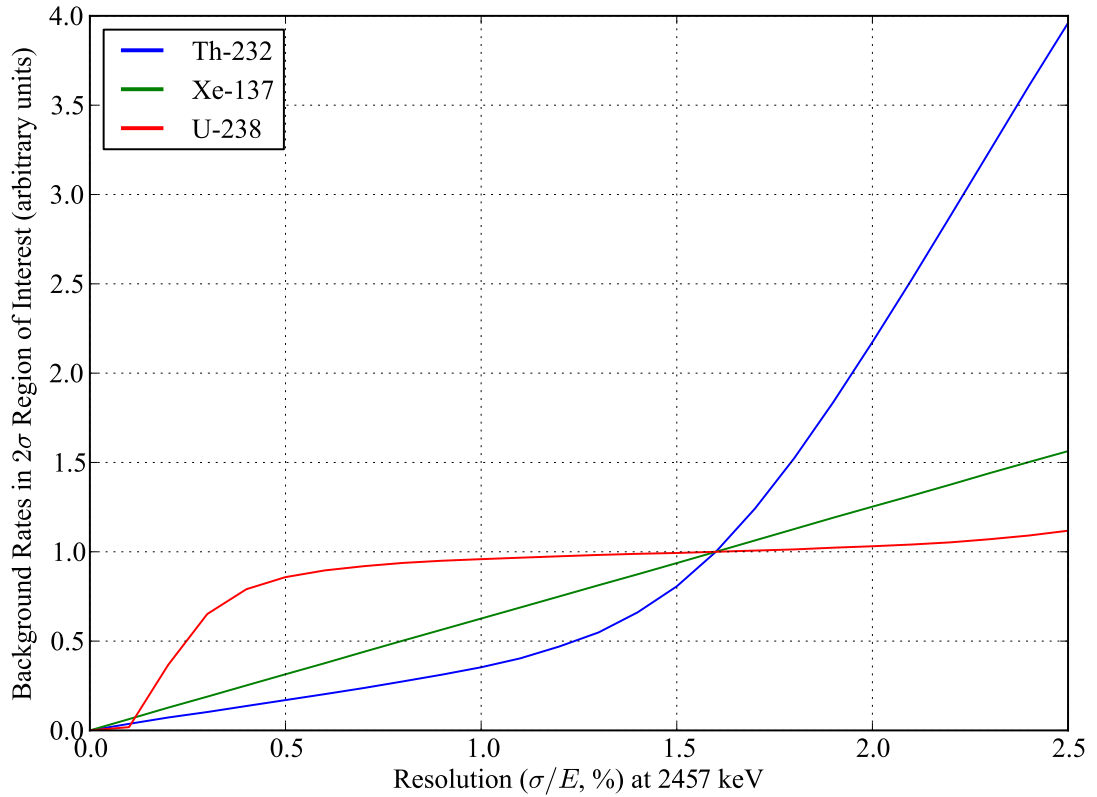


Figure 3.6: Relative change in background rates expected in our  $2\sigma$  region of interest as a function of the energy resolution. Rates are normalized to one at a  $Q$ -value energy resolution of 1.6%  $\sigma/E$ , the design goal of EXO-200. The three backgrounds shown, from  $^{232}\text{Th}$ ,  $^{238}\text{U}$ , and  $^{137}\text{Xe}$ , are currently our dominant backgrounds. Betas and gammas are assumed to have the same calibration here; alternative beta scales are considered in section 7.4.

istics. In this section, passive methods will be described; section 3.4 will describe the active methods of background rejection. The passive methods we will identify are exploiting the self-shielding properties of xenon, screening the materials for radioactivity, and putting the experiment deep underground.

The simplest method of reducing the presence of backgrounds is by exploiting the self-shielding properties of xenon. The xenon itself is extremely pure due to the ease of chemical purification. As a result most backgrounds will be external to the xenon. Since external gammas are weakly attenuated by dense materials such as liquid xenon, which has a density of  $3.0305 \pm 0.0077$  g/cm<sup>3</sup> [74], we can expect that the xenon near the center of the detector will be exposed to less background than the xenon near the TPC walls. This is one of the primary advantages of xenon as a source: it is possible to construct a large monolithic detector, maximizing the quantity of xenon which is shielded from the walls.

Figure 3.7 shows the attenuation lengths of gammas at a range of energies in xenon. Photoabsorption and pair production both convert the gamma entirely into short-ranged electron and positron carriers; Compton (incoherent) scattering results in a fractional energy deposition, with the rest remaining in the gamma which rebounds and continues on a deflected path. Enriched liquid xenon has a density of  $3.0305 \pm 0.0077$  g/cm<sup>3</sup> [74], which means that the minimal attenuation factor is 0.108/cm at an energy of 4.34 MeV. Unfortunately, this is similar to our  $Q$ -value at 2456.7 keV, where the attenuation factor is still only 0.116/cm, which means that self-shielding is minimally effective for  $\beta\beta0\nu$ . Nevertheless, there is some reduction in backgrounds deeper in the interior of the xenon, and lower-energy gammas are

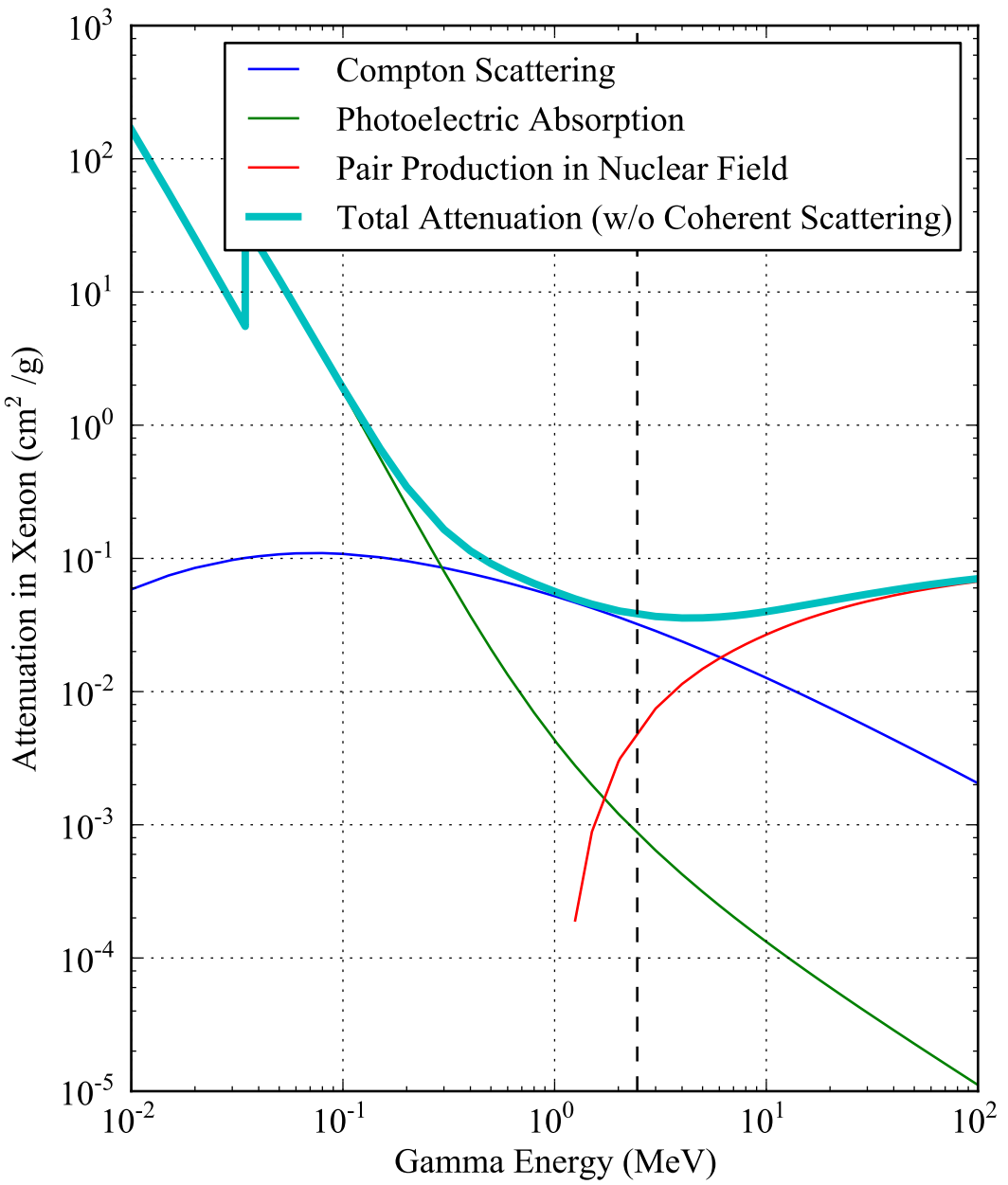


Figure 3.7: X-ray attenuation lengths in xenon. Compton scattering, pair production, and photoelectric absorption are shown, along with their combined attenuation length; coherent (Rayleigh) scattering is omitted because it produces no observable energy deposit. The  $Q$ -value of  $^{136}\text{Xe}$   $\beta\beta0\nu$  decay is indicated with a dashed black line. The vertical axis, in  $\text{cm}^2/\text{g}$ , can be multiplied by the density of the xenon to derive an attenuation factor per unit length. Data from [104].

attenuated more effectively [104].

To reduce the quantity of background around the detector, all materials near the xenon were carefully screened for radioactive contamination [105]. Backgrounds from  $^{40}\text{K}$ ,  $^{232}\text{Th}$ , and  $^{238}\text{U}$  were cataloged for all materials which have unshielded line-of-sight access to the detector system. Requirements for  $^{238}\text{U}$  are particularly stringent because its daughter products include the  $^{214}\text{Bi}$  background which cannot be resolved from  $\beta\beta0\nu$  decay. For the copper of the TPC vessel and the lead shielding around the detector apparatus, samples from a range of companies and mines were tested to locate an optimal choice of material source. For the wires which were placed into the TPC, a range of manufacturing methods were tested; improvements to a photo-etching scheme were identified which led to a reduction in background from these materials [96]. This thorough material screening research is one of the distinctive processes which has enabled EXO-200 to achieve its background goals. Details of the quantification of and constraints on material radioactivity can be found in [105].

Beyond selecting extremely clean materials, it is possible to reduce backgrounds by minimizing the mass of these external materials. Most notably, the EXO-200 copper TPC vessel is, in most places, only 1.37 mm thick. To maintain structural integrity, supporting structures are welded to the TPC where needed. The total mass of copper is less than 30 kg [96].

Some materials were dispensed with entirely. Typically, silicon APDs are encapsulated with ceramic to isolate them from water contamination and provide electrical insulation. However, this ceramic material would have contributed back-

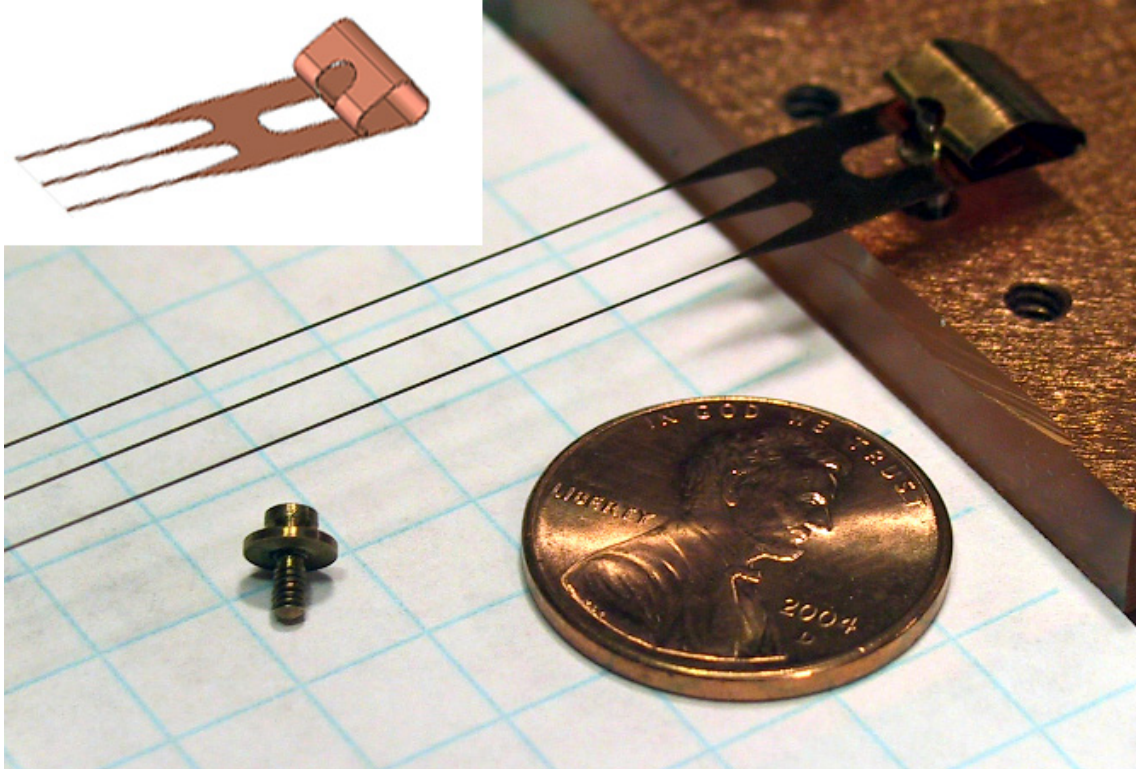


Figure 3.8: Wire triplet, read as one channel. Figure from [96].

grounds. Instead, the APDs were delivered “bare,” without any encapsulation, and protected from water by storing them in a dry-nitrogen container. Liquid xenon itself serves as an electrical insulator, ensuring the APDs would function properly during detector operations [106].

The cabling of the wires and APDs was also done with great care. The electrical amplifiers and digitizers contain many high-background plastics, metals, and other complex materials, so they were placed outside the lead shielding rather than close to the TPC. Wires connect the sensors in the TPC to these electronics; ordinarily such long wires would need to be shielded by coaxial cabling to minimize cross-talk noise. However, the coaxial cabling was expected to contribute a high



Figure 3.9: APDs ganged together (bottom right). Wiring to the front-end electronics are visible as yellow “tape.” Figure from [96].

quantity of radioactive background, and was omitted; instead wires are partially electrically shielded by surrounding them with inactive wires which reduce cross-talk noise. Furthermore, the total number of wires needed was reduced by ganging together triplets of u- and v-wires and groups of six or seven APDs into single channels. This reduced the fineness of event information available in analysis, but also reduced the quantity and complexity of material placed near the detector. The wire gangs are shown in figure 3.8; APD gangs cabling are visible in figure 3.9 [96].

The TPC is shielded by nested layers of clean material designed to prevent backgrounds from reaching the xenon. In the innermost layer, HFE-7000 refrigerant (see figure 3.10) is used to maintain the detector at liquid xenon temperatures and to shield from external gammas. However, the HFE-7000 has a significant quantity of hydrogen, which also makes it an excellent stopping agent for thermal neutrons.

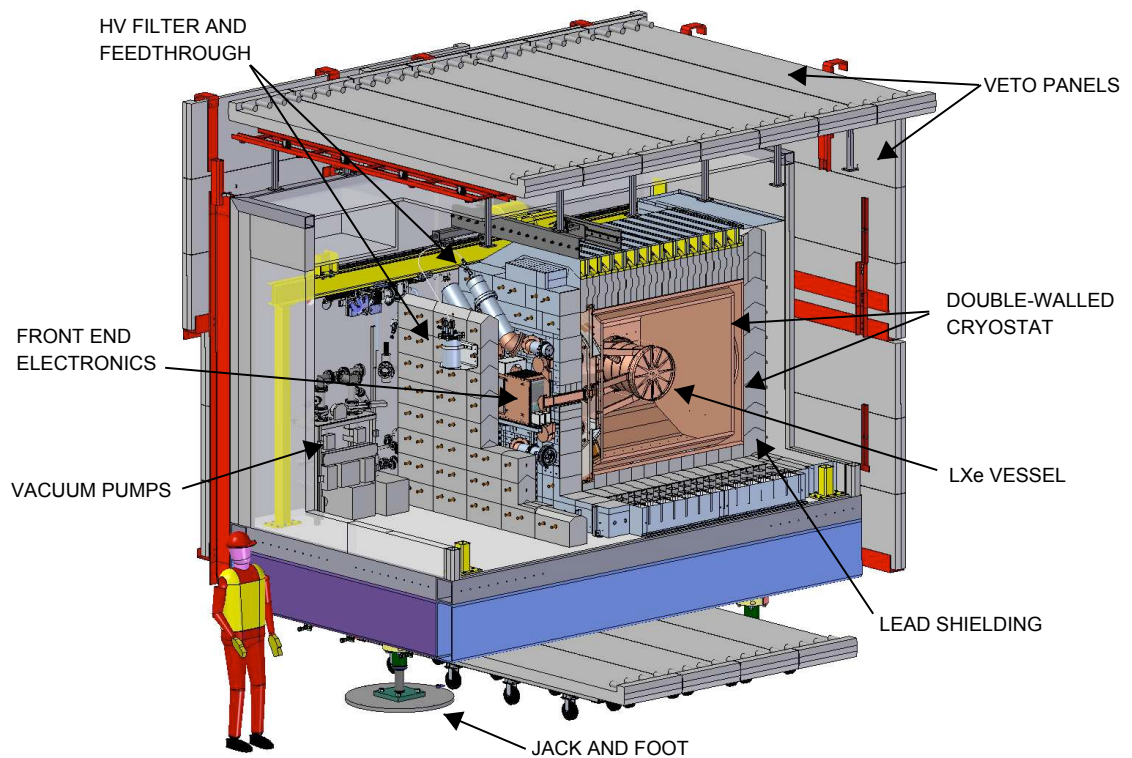


Figure 3.10: A cutaway schematic image of the TPC and surrounding materials in the cleanroom. HFE-7000 refrigerant is contained between the cryostat and the LXe vessel. Figure from [96].

The refrigerant layer is more than 50 cm thick, so most external neutrons thermalize, absorb onto hydrogen, and emit a 2.2 MeV gamma rather than reaching the TPC and producing  $^{137}\text{Xe}$  with its more harmful 4173 keV beta endpoint energy [96].

The following layer of shielding is copper cryostat, then lead, shown in figure 3.10. This is a common approach for low-background experiments due to the high density of lead, which enables it to stop gammas in a short distance. Lead bricks surround the detector on all sides; the bricks were designed with an interlocking shape to ensure no seams between bricks left a line-of-sight path from external sources into the TPC. In the front of the detector, where plumbing must enter and exit the detector through the first lead wall, a second lead wall is assembled with the purpose of blocking any line-of-sight paths into the TPC through the plumbing gaps of the first wall [96].

Outside of the lead shielding, restrictions on materials are less stringent; however, control over the presence of materials is still desired. The entire apparatus is contained inside a class-1000 cleanroom facility. The entire facility is located in the Waste Isolation Pilot Plant (WIPP) facility, a Department of Energy waste repository located in a salt formation near Carlsbad, NM. The overburden of the facility is  $1481_{-6}^{+8}$  meters water-equivalent [98]. Figure 3.11 shows the reduction in muon flux due to depth at the WIPP site and a selection of other underground science facilities.

These passive approaches have all been demonstrated to reduce the rate of backgrounds depositing energy in the liquid xenon. The following section will describe an active set of background-rejection approaches.

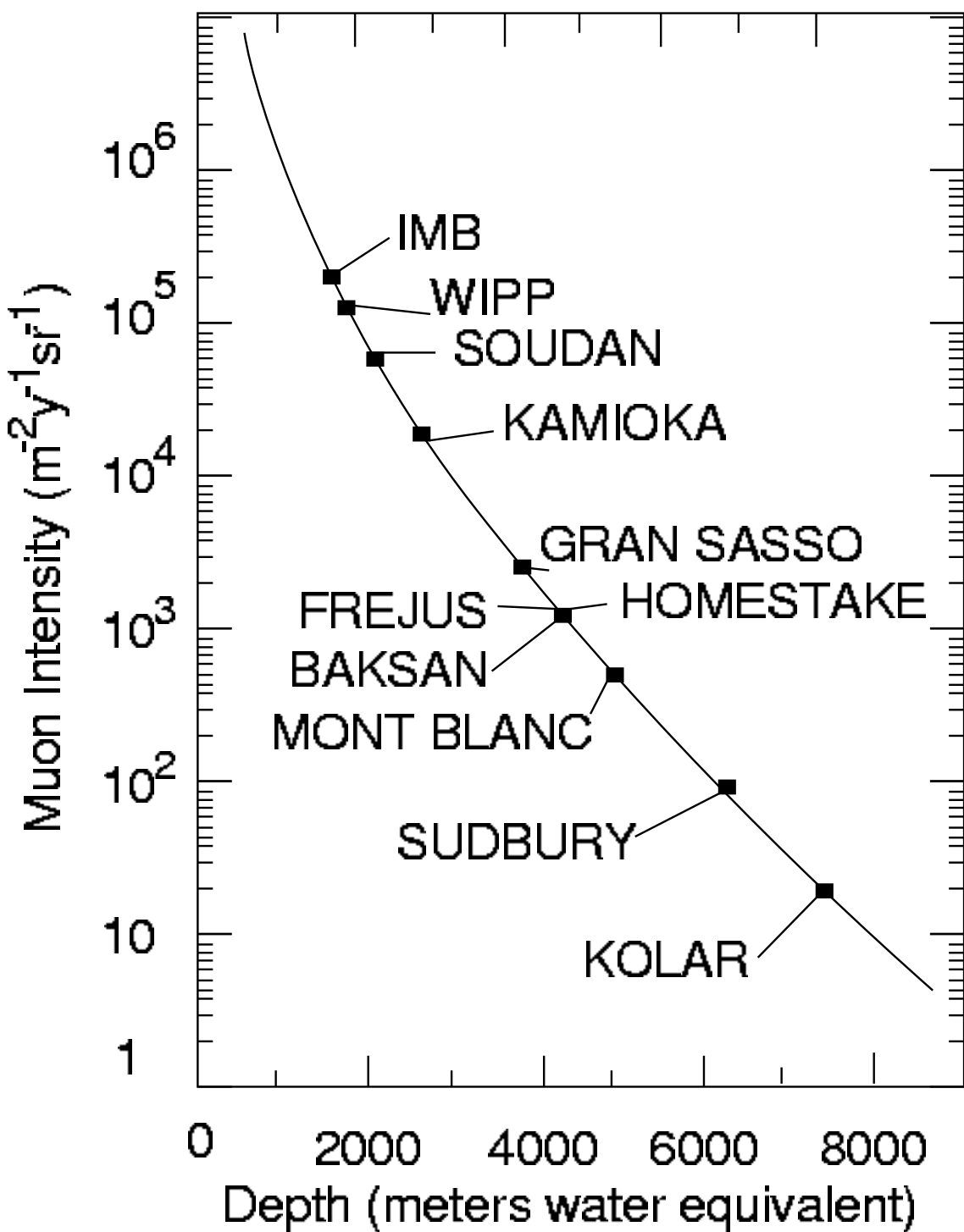


Figure 3.11: Muon flux as a function of depth, in meters water equivalent. The WIPP site is indicated in relation to other underground science facilities. Figure from [107].

## 3.4 Active Background Rejection

This section will describe the “active” forms of background reduction employed by the EXO-200 detector, in which events are observed but discriminated from  $\beta\beta0\nu$  events based on their characteristics. We neglect the energy resolution as a background rejection tool here, since section 3.2 has already described how the impact of certain backgrounds may be reduced by improvement to the energy resolution.

A number of cosmogenic backgrounds have been described: neutrons and fission products can be produced from muons penetrating down to the depth of the WIPP facility. To reject many of these events, it is sufficient to detect the passage of a muon anywhere near the detector. This is accomplished by a set of plastic scintillator veto panels surrounding the cleanroom on four of six sides. Muons are detected by coincident PMT hits on opposite sides of a single panel, with  $(96.0 \pm 0.5)\%$  efficiency for detecting muons which traverse the TPC [96]. Further reduction in the impact of muon-induced backgrounds is achieved by searching for muon tracks observed within the TPC itself, and also by applying a one-second coincident event cut as a catch-all for spallation products of muons which may decay multiple times in rapid succession.

Alpha decays within the xenon are another possible source of high-energy backgrounds. However, it is possible to discriminate alpha decays from beta and gamma decays based on the properties of their energy measurement. Alphas produce a far more dense energy deposit in liquid xenon than betas and gammas; the dense col-

lection of free electrons and ionized xenon has a higher rate of charge recombination than is observed with betas and gammas, which translates into a higher ratio of scintillation to ionization for alphas than for betas and gammas. This feature can be used to eliminate essentially all alpha backgrounds.

Discriminating between gamma, beta, and double-beta decays is more difficult. Betas from external backgrounds will not penetrate into the xenon due to their short attenuation lengths, so only dissolved beta emitters are backgrounds to  $\beta\beta0\nu$  decay; this constrains the number of plausible beta decays that must be considered. Gammas generally deposit their energy by ionizing atomic electrons of xenon, so in this way their behavior closely mimics that of betas. However, most gammas within our energy window (and particularly gammas near our  $Q$ -value) will be attenuated by Compton (incoherent) scattering, as can be seen in figure 3.7. By this process the gamma will deposit energy in more than one discrete location, which beta and double-beta decay will not do. We are generally able to resolve the positions of these energy deposits and classify the event as multi-site. More than half of external gamma backgrounds are classified as multi-site, whereas the fraction of  $\beta\beta0\nu$  events classified as multi-site due to bremsstrahlung is only 5% [74].

Finally, the liquid xenon itself is continuously purified and quite low in backgrounds, so most radioactive backgrounds in EXO-200 are external. We have noted that 94.7 kg of liquid xenon are treated as fiducial; the remaining quantity of roughly 15 kg of xenon which is in the active volume of the detector is used as an active veto shield, where any interaction which deposits energy in this volume disqualifies the entire event from use as a  $\beta\beta0\nu$  candidate. Moreover, the fits which will be described

in section 7.4 take into account the depth into the detector of an energetic deposit, giving events near the exterior greater likelihood of being an external background than events deep inside the xenon. These strategies give us some discriminating power against external backgrounds.

These are some of the basic techniques employed to reduce backgrounds in offline analysis, and the detector has been designed with the goal of facilitating their application. The EXO-200 detector currently has two and a half years of data with enriched xenon, and although improvements to the passive methods of background reduction cannot be applied to this existing dataset, it may be hoped that these active methods may be improved or extended through further analysis. These improvements could have the potential to reduce backgrounds below their current levels in offline analysis, making them a particularly attractive target now that EXO-200 has collected a significant dataset.

### 3.5 Pulse Amplification and Waveform Readout

This section will provide a brief overview of the EXO electronics and waveform readout. Particular attention is paid to subsystems which are relevant to the denoising algorithm described in chapter 4, including the APDs and front-end electronics. A schematic of the electronics and readout subsystems can be seen in figure 3.12.

The APDs are constructed from a silicon semiconductor which is doped and biased so that: [108]

1. Photons arriving at the active surface of the APD can deposit their energy by

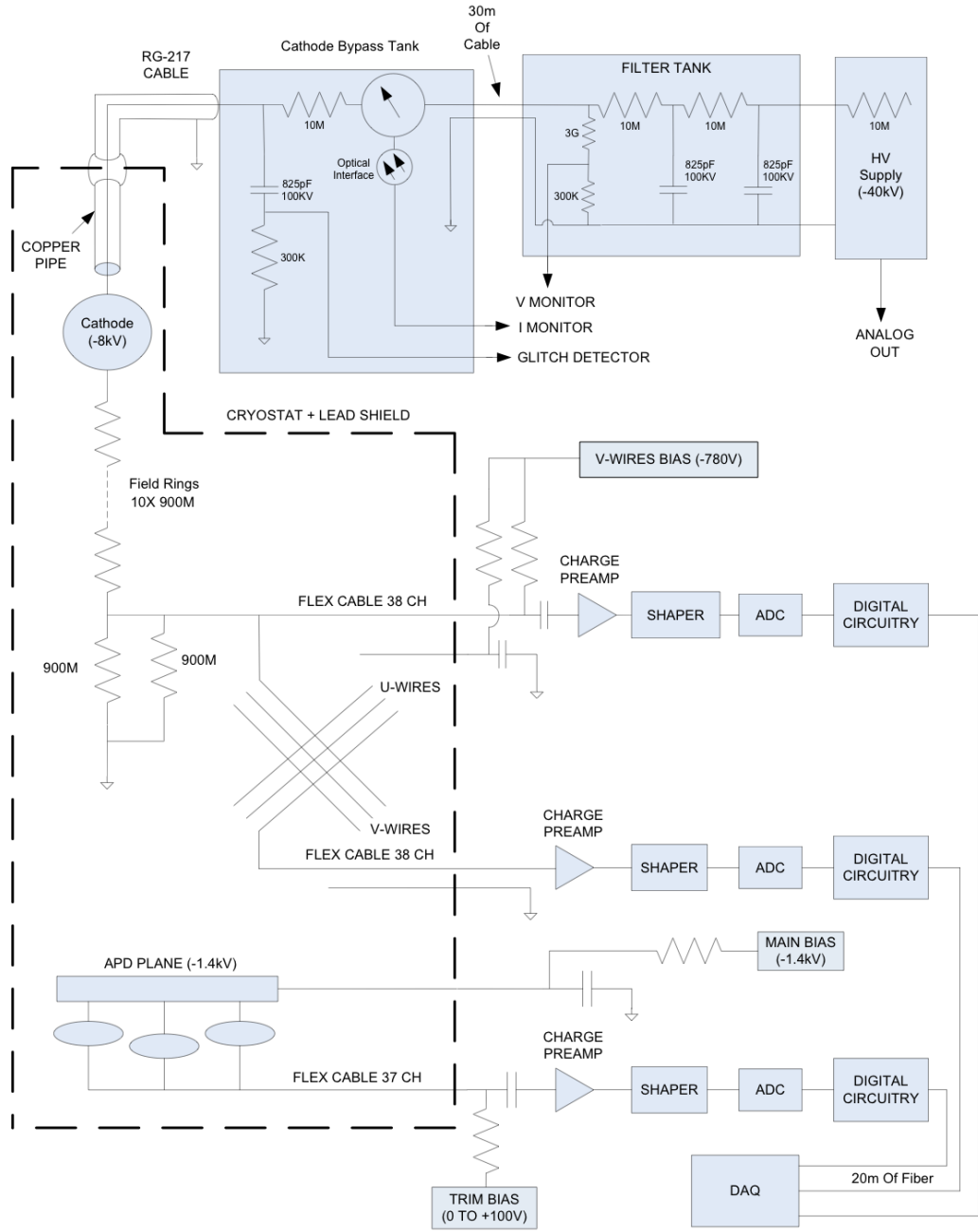


Figure 3.12: An overview of the EXO-200 electronics and readout subsystems. The area inside the dashed line indicates cold subsystems inside the cryostat or TPC. Figure from [96].

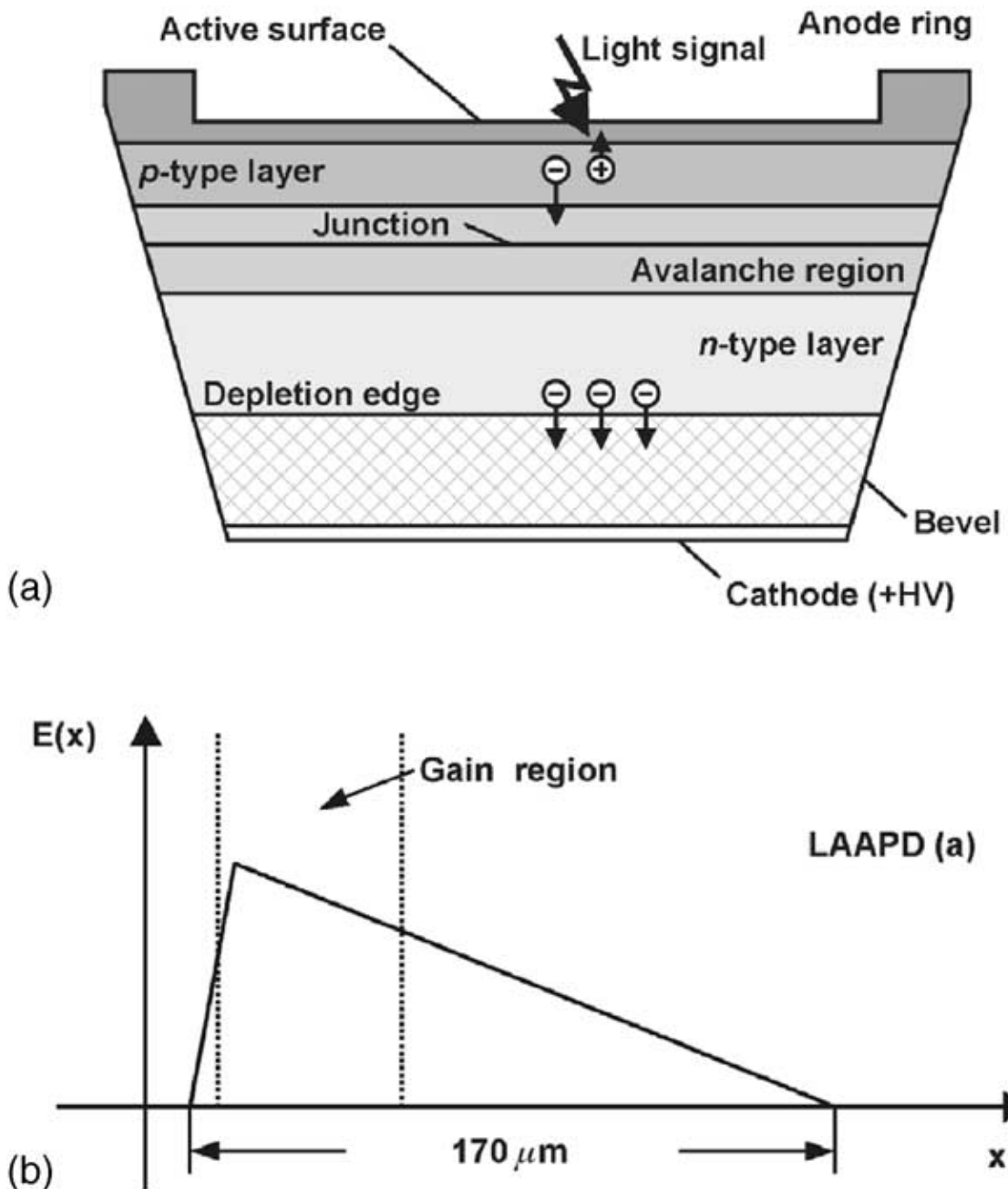


Figure 3.13: A cross-sectional schematic of an APD is shown in (a). The electric field as a function of depth is shown in (b). Figure from [108].

generating an electron-hole pair in the silicon semiconductor.

2. The electron-hole pair is drifted apart by an electric field. Here the electric field is low and the silicon is doped to be of p-type (electron-poor), ensuring a similar number of electron-hole pairs are produced by all photons before any amplification can occur.
3. The electron enters a high-field n-type (electron-rich) region of silicon, and liberates additional electron-hole pairs in an avalanche effect.
4. Electrons reach another p-type region of silicon, and then are collected on a cathode as an output current pulse.

These phases of the APD are illustrated in figure 3.13.

851 APDs were specially made for EXO-200; from those, 468 were selected for use based on their favorable noise and gain properties [106]. For each APD, the relative quantum efficiency and the bias voltage needed to ensure the product of gain and quantum efficiency equals one hundred were both measured. It is impossible to make the gain of all APDs perfectly uniform because of limitations in the configurability of the APD bias voltages in EXO-200: APDs are grouped into twelve pies, and the APD bias voltage within a pie is controlled by a single parameter [96]. To mitigate this effect, APDs were assigned to gangs and pies so that their products of gain and quantum efficiency could be set to one hundred as uniformly as possible [109]. We note that the current operating conditions of EXO-200 establish a higher operating gain of around 200 – 300. This may have the side effect of making the product of gain and quantum efficiency less uniform in each APD gang.

In the u-wires, charge is collected and delivered directly to the electronics as current. In the v-wires, no net charge is delivered, but transient currents are induced in such a way that the v-wire remains at a constant voltage; these transient currents produce a bipolar pulse, such that the integral (before shaping) is zero. We note that the pulse shape depends on the drift path of ionization in the liquid xenon – both sets of wires deliver a current signal which is induced from approaching charge before the charge deposits on the u-wires, and the path of the electrons can affect the time development and, in the case of the v-wires, the magnitude of that induced current. Furthermore, ions (being much more massive than electrons) drift much more slowly through liquid xenon. As a result, the pulse magnitude will depend on the point of origin of the electrons because from that location the ions will hold a net charge on the u- and v-wires which is released only on much longer timescales than we can observe with our electronics [110, 111].

The front-end electronics, located between the two lead walls in front of the detector at room temperature, consist of four stages: [96, 112]

1. A transimpedance amplifier which converts the current signals from the detector to voltage signals. This stage applies amplification and a differentiator with a long time constant (roughly  $60\mu\text{s}$  for wires and  $300\mu\text{s}$  for APDs).
2. Two differentiators and two integrators, to improve signal-to-noise ratio for real-time triggering. For the u-wires, each integrator has a time constant of  $1.5\mu\text{s}$  and each differentiator has a time constant of  $40\mu\text{s}$ ; for the APDs and v-wires, each integrator has a time constant of  $3\mu\text{s}$  and each differentiator has

a time constant of  $10\mu\text{s}$ . Some signal amplification is applied at this stage as well.

3. An analog-to-digital converter (ADC) converts voltage pulses into 12-bit digital waveforms. The full 12-bit scale is equivalent to 2.5V. Digitization is performed at a rate of 1MHz.
4. A triggering module reads the digitized waveforms and issues a trigger to the data acquisition (DAQ) when signals exceed programmable thresholds. The triggering module can also accept external requests for a “solicited” trigger.

In most cases, when a trigger is issued, the DAQ will write out 2048 samples (just over 2 ms) from all waveforms, centered on the first sample responsible for the trigger. In cases where the data rate is high, waveforms can be truncated to a length less than 2048 samples.

## 3.6 Calibration Systems

Energy resolution has been discussed as a general feature of the detector which can have a significant impact on the reduction of backgrounds. A significant factor in the resolution is the quality of the detector’s absolute energy scale calibration. This is particularly important because of the long lifetime of the experiment. If the calibration of the detector drifts over time, and this drift is not corrected, this will be perceived in the cumulative low-background spectrum as a smearing out of energy peaks, worsening the effective resolution. This section will describe some

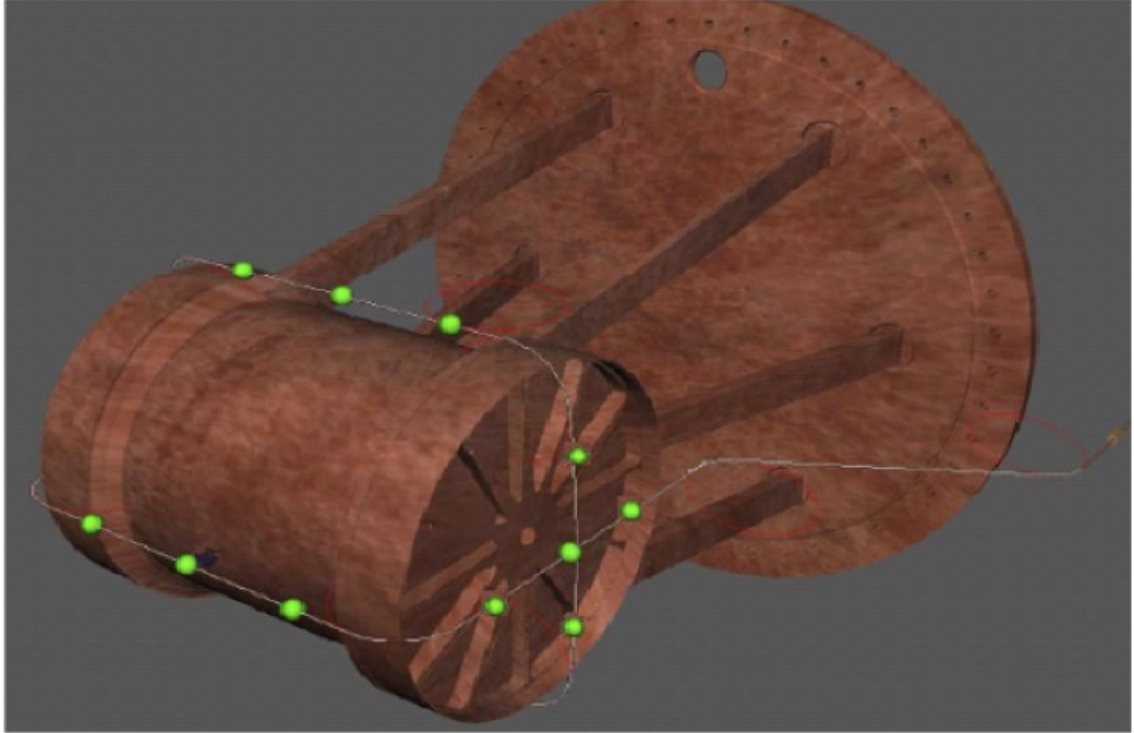


Figure 3.14: A guide tube permits gamma sources to be inserted to known locations near the TPC. Green dots indicate a few of the locations where the source may conventionally be placed. Figure from [96].

of the techniques used to produce an accurate time-dependent calibration for the energy scale.

The most critical type of calibration comes from external gamma sources. The EXO experiment was constructed with a guide tube passing through the HFE-7000 refrigerant and wrapping loosely around the TPC, as shown in figure 3.14. Currently available to the experiment are sources containing  $^{228}\text{Th}$  (primary gamma line at 2615 keV),  $^{60}\text{Co}$  (simultaneous emission of gammas at 1173 and 1332 keV), and  $^{137}\text{Cs}$  (gamma line at 662 keV); additionally, a new  $^{226}\text{Ra}$  source became available in the summer of 2013 (numerous gammas, including 2448 keV). The  $^{228}\text{Th}$  and

$^{60}\text{Co}$  sources are available in weak and strong strengths, where the strong strength is chosen to produce a data rate that is still low enough that charge-light association can usually be done unambiguously. Together these sources allow us to observe the detector response to external gammas with known energies, permitting energy calibrations, energy resolution measurements, and verification of Monte Carlo simulations.

All of these sources have been used periodically (roughly every three months) in calibration campaigns intended to permit a full characterization of the detector response across a wide energy range at a particular moment. Additionally, the  $^{228}\text{Th}$  source has been deployed regularly, typically three times every week for 2 – 3 hours, for the entire history of the dataset. The richness of the accumulated  $^{228}\text{Th}$  source dataset, along with the benefit that it contains a relatively clean high-energy gamma line, make it particularly convenient to work with. It will play a prominent role in the generation of our lightmap described in chapter 6.

Other calibrations are also performed on the detector, and may in some instances supplement the information provided by the source data. To perform direct calibrations of the APDs, one APD mount contains a light diffuser rather than an APD device; the diffuser can be illuminated by a laser through optical fibers [96]. The APDs can be calibrated by pulsing the laser while varying the voltages of the APDs to adjust their gain, and in this way it is possible to measure the gain of the APDs *in situ*. A laser system was available at the beginning of the dataset used in this work; however, there were certain deficiencies to the laser system which made its data difficult to use, and as a result a new and more accurate laser system was

commissioned in August 2012. Laser data in some form has been collected roughly once per week for much of the time containing this dataset. Composing the laser data into a coherent history of the APD gains is an ongoing project, but it has been possible to use APD gain information from specific moments to inform the APD noise model described in section 4.3.

Just as it is possible and desirable to learn the gain of the APDs separately from other components using laser runs, it is also desirable to learn the relative gain of the electronics amplifiers separately from other detector function. This is accomplished using “internal calibrations”: simultaneously with software triggers solicited by the data acquisition, a switched capacitor injects charge into the input of the electronics cards of individual or groups of channels [113]. The resulting waveform is then read normally, and the size of the output pulse reflects the gain of the electronics. This system is employed approximately daily on all channels; it provides an excellent measure of relative changes in the electronics gains over time. However, the absolute gains cannot be extracted accurately from this data due to variances in the capacitors, and must be obtained by other means.

To measure the absolute gains of the electronics, the front-end cards must be physically removed from their enclosures; when this is done, it is possible to use a more accurately calibrated capacitor to make an absolute gain measurement in the same style as the internal calibrations. These “external calibrations” can be performed in two flavors: manual, in which a capacitor calibrated to 1% is used to inject charge, and automatic, in which the calibration is automatically performed at a much faster rate but accuracy is limited to 2 – 3%. Due to the inconvenience

of removing electronics cards from their enclosures, this process has only been performed once in February 2011. Both styles of external calibration were performed on the u-wire channels. Less demanding needs for resolution on the v-wires and APD channels were foreseen, so only the less accurate automatic calibration was performed on those channels. The data from these runs has not been fully analyzed, but may be revived in future analyses to permit a better calibrations of the subsequent internal calibrations which were taken. A few electronics boards have been swapped since February 2011; channels on those boards will no longer have an absolute calibration available after the board swap, so it may be advisable to perform an additional external calibration [110].

### 3.7 Summary

This chapter has described some of the key characteristics of the construction and operation of the EXO-200 detector. Background reduction has been a theme throughout – EXO-200 has employed both passive and active methods to reject background and improve its sensitivity to  $\beta\beta0\nu$  decay. Energy resolution has also been described as a key element in background rejection because the  $2\sigma$  region of interest shrinks linearly with energy resolution, so with sufficiently precise energy measurements the rates of most backgrounds will decrease. Chapter 4 will discuss a new scheme to extract more accurate energy measurements from the APD channels, thereby improving our overall energy resolution and the sensitivity of our  $\beta\beta0\nu$  half-life limit.

# Chapter 4: Denoising Theory and Implementation

We have shown in section 3.2 that if it is possible to improve the energy resolution of EXO-200 then backgrounds, particularly from  $^{232}\text{Th}$  and  $^{137}\text{Xe}$ , can be reduced. The energy resolution of EXO-200 is limited by its scintillation energy resolution, so any attempt to improve the energy resolution should focus on improved extraction of APD pulse magnitudes. In this chapter we present a new technique for extracting optimal scintillation energy measurements based on an improved model of the pulses and noise on APD waveforms. The estimator derived in this chapter is optimal partly due to its ability to operate in the presence of noise; we therefore describe it throughout as a “denoising” technique, though at no point are denoised waveforms produced.

We begin with a general overview in section 4.1 of what qualitative methods of noise reduction a denoising technique may hope to apply and why they are necessary for our APDs. Notational conventions and some crucial input parameters are listed in section 4.2. Section 4.3 presents a detailed physics model of the fluctua-

tions in observed pulse magnitude, and section 4.4 connects that physics model to observable output of the APD channels. The optimal energy estimator is presented in section 4.5 with a derivation. Sections 4.6-4.9 translate the optimal energy estimator into a usable form and describe the computational steps needed to apply it to data. Differences between the optimal version of denoising presented in this chapter and the version used for the present physics analysis are shown in section 4.10. We finish in section 4.11 by identifying some extensions to the denoising technique presented here which may prove interesting for future analyses.

## 4.1 What is Denoising?

Before the investigations described in this work, scintillation energy was not measured from individual APD channels. Instead, two summed waveforms were constructed: a sum of all waveforms from APDs on the North plane, and a sum of all waveforms from APDs on the South plane. This simplified the construction of a position-dependent correction function, or lightmap. (For more details on why this is so, see section 6.1.) However, when we sum waveforms together we discard information; this section shows that the information which is thrown away is in fact critical to improving our scintillation energy measurements.

Energy resolution is a critical factor in the strength of the EXO-200 experiment. Figure 4.1 shows the energy resolution trend which was observed before denoising was developed. We can see that there was a long period of worsening resolution from March 2012 to February 2013, when the single-site energy resolution

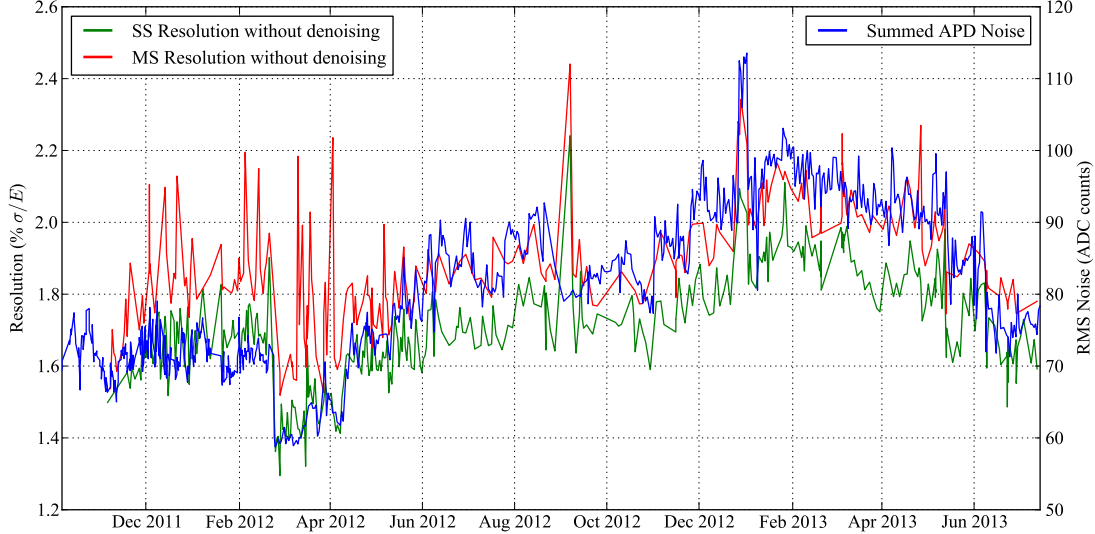


Figure 4.1: Detector energy resolution (without denoising) is strongly correlated with noise observed on the APDs. Noise data provided by Josiah Walton.

changed from 1.4% to 1.9%  $\sigma/E$  at our  $Q$ -value, followed by a period of improvement to 1.6% in July 2013. There has always been interest in ways to improve the energy resolution, but the upward trend gave greater urgency to understand the observed fluctuations, reverse them, and find a way to counter the effect in offline analysis for existing data.

A search began for environmental changes which could be correlated to the worsening energy resolution. In addition to the energy resolution trend, figure 4.1 overlays a trend of the root-mean-square noise on the sum of APD waveforms, and we can immediately see that the overall energy resolution is closely tied to electronic noise on the summed APD channels.

The design goal of EXO-200 was for individual APD channels to have root-mean-square noise levels of 2000 electrons, and this goal was met [114]. However,

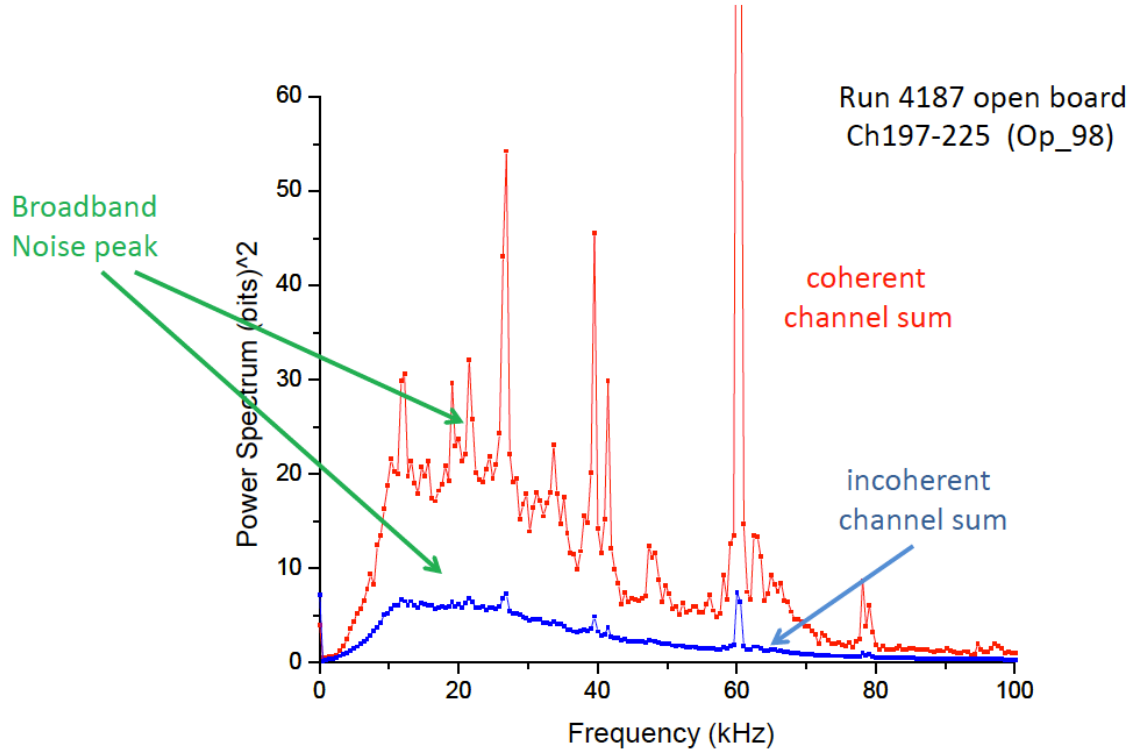


Figure 4.2: Coherent and incoherent noise power spectra for a sample set of APD channels without pulse shaping. The coherent noise power spectrum is measured by adding together waveforms from different channels and computing a power spectrum; the incoherent noise power spectrum is measured by computing power spectra for each channel individually and adding them together [114].

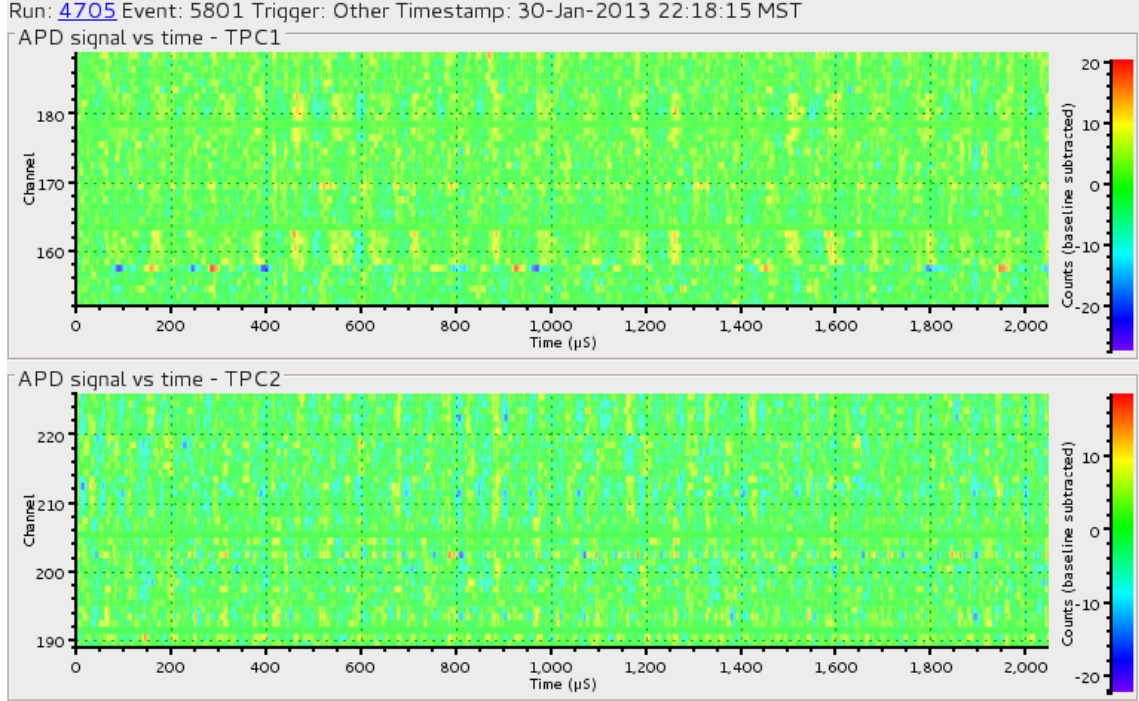


Figure 4.3: APD waveforms from a single event. No energy deposit occurred during this event, so the waveforms represent pure electronic noise. The horizontal axis indicates time, and the vertical axis indicates channel number; colors ranging from blue to red indicate the baseline-subtracted waveform magnitude. Vertical streaks are indicative of correlations in noise across channels.

rather than observing the noise on summed APD channels increase proportionally to the square root of the number of channels, the summed APD noise is roughly two to three times higher than projected. Figure 4.2 compares the power spectrum of the summed APD waveforms to the sum of power spectra of individual APD waveforms; the power spectrum of the sum is 2-3 times higher than the sum of power spectra. These observations indicate that the phases of the noise frequency components on different channels are positively correlated, leading to a worse impact on energy resolution than the same level of uncorrelated noise would give.

Electronics Board	APD Channels
0	158-163, 176-182
3	189-195, 202-207
4	208-213, 220-225
5	196-201, 214-219
6	170-175, 183-188
9	152-157, 164-169

Table 4.1: Electronics boards and their corresponding channels, as defined during the time range from February 2012 to this writing. Although electronics board numbers are different at other times, their corresponding channel numbers do not change.

The correlations in noise across channels are visible even by eye. Figure 4.3 shows a single noise event from the detector taken on January 30, 2013, when noise levels were near their highest. The horizontal axis represents time, the vertical axis represents channel number, and color indicates the magnitude of the baseline-subtracted waveform. If noise on different channels were uncorrelated, we should see no relation between the noise on different horizontal rows (channels) of the plot. Instead, vertical streaks can be seen which indicate noise which is in phase across multiple channels. Table 4.1 identifies the channel numbers corresponding to each electronics board, and we can see that the correlations are strongest for channels on the same board.

The observation that noise is correlated across channels has provided an important clue to the origin of the noise, and investigations led to the discovery that switching power supplies and a switched voltage regulator introduce noise into the electronics; these are magnified by a ground loop in the electronics and a pre-amplifier design which is not optimized to reject noise in its power supply. Efforts are underway to address these issues in hardware [115, 116].

The observation that coherent APD electronic noise is the limiting factor in our energy resolution also implies that we can mitigate this noise in offline analysis. Although the correlations in noise initially worsen our energy resolution due to their linear scaling with the number of channels, knowledge of these correlations permits us to take advantage of the redundancy in the noise and reduce its overall magnitude. By observing that the majority of our APD noise is correlated, we have learned that we can eliminate the majority of our APD noise in offline analysis and improve the quality of data which has already been taken. Efforts to denoise the data in this way have been made by many members of the EXO collaboration; here we describe the success of one of these denoising approaches.

Although the previous discussion emphasizes the electronic noise which induces time variations in our energy resolution, we note that this is not the only source of noise in APD waveforms. The types of noise which are considered in the present work are:

- Electronic noise. More generally, we consider collectively additive noise which is uncorrelated with pulses. APD dark current is another possible source of such noise.
- Fluctuations in photon collection efficiency.
- Fluctuations in APD gain.

The last two are sometimes collectively described as Poissonian noise because they each introduce a variance term which is roughly linear in the energy of the event.

We note that the electronic noise scales linearly with the number of channels used, in the case where it is dominated by coherent noise; by contrast, Poissonian noise decreases proportionally to the square root of the number of channels used, in the case where all channels are expected to have similar mean photon collection and gain. Thus, there are competing forces to form our energy estimates from a small number of channels to minimize the electronic noise and from a large number of channels to minimize the Poissonian noise. Finding the optimal balance between these two extremes is one of the challenges of denoising.

The energy estimator which we derive in this chapter is an optimal linear estimator, and we do not attempt to control how it produces its estimates. However, we still can identify a number of qualitative approaches to reducing the noise levels in the scintillation channel. We refer to “passive” approaches as those in which components of our waveforms are weighted based on their relative signal-to-noise content. “Active” approaches, by contrast, are classified as those which attempt to improve the signal-to-noise content of the waveforms. We identify the following three types of denoising:

### **Frequency weighting**

On a given channel waveform, weight more heavily the frequency components which contain larger signal-to-noise ratio. This passive denoising scheme requires knowledge of the power spectra of the pulse signal and the noise.

### **Channel weighting**

Different channels may have differing levels of noise, so some may generally

have lower signal-to-noise ratios. More importantly, though, the pulse magnitude on a given channel depends strongly on the proximity of the APD gang to the source of scintillation within the detector. This passive denoising scheme therefore consists of weighting more heavily the channels which have larger expected pulse magnitudes, as determined on an event-by-event basis.

### Noise cancellation

This active form of denoising consists of using correlations between noise on multiple channels to produce a better estimate of the noise component of waveforms than each waveform taken independently could provide. To accomplish this, we require detailed information about the pairwise noise correlations across channels at each frequency.

Section 4.2 specifies the mathematical framework for denoising. This framework is general enough to include all of the features described in this section.

## 4.2 Notational Conventions and External Input

In this section, we first establish a set of notational conventions which clarify the mathematics of this chapter. We then describe the overarching framework in which denoising takes place, taking care that the framework is general enough to include all of the qualitative features described in section 4.1.

Throughout this chapter we use the following notational conventions:

- $i, j$  represents indices over APD channels (or equivalently, APD gangs).

- $a, b, c$  represents indices of scintillation clusters in an event; a scintillation cluster is a set of simultaneous energy deposits which may occur at multiple locations.
- $\tau$  represents the time indices of a discrete-time waveform;  $t_a$  represents the calendar time of a scintillation deposit  $a$ .
- $f, g$  represents the frequency indices of Fourier-transformed waveforms.
- $\delta_{ij}$  is the Kronecker delta, equal to 1 if  $i = j$  and 0 otherwise.
- For a waveform  $*[\tau]$ , we represent the discrete Fourier transform of that waveform with  $\tilde{*}[f]$ , where the particular convention used to evaluate the Fourier transform is not significant.
- For a Fourier-transformed waveform  $\tilde{*}[f]$ , we denote the real and imaginary parts of that waveform by  $\tilde{*}^R[f]$  and  $\tilde{*}^I[f]$ , respectively.
- For an unknown parameter  $p$ , the symbol  $\hat{p}$  identifies an estimator for  $p$ .
- For an expression  $f(\cdot)$  containing random variables,  $\langle f(\cdot) \rangle$  is the expectation value of  $f(\cdot)$ . Here the expectation value is meant in a frequentist sense: if we could repeat the experiment of generating the same number of initial photons in the same places,  $\langle f(\cdot) \rangle$  would be the average value of  $f(\cdot)$  from many trials of this hypothetical experiment. The expectation value of  $f(\cdot)$  conditional on the value of some random variable  $X$  is written  $\langle f(\cdot) | X \rangle$ .
- When a bare index appears on both sides of an equation, the equation holds

for all possible values of that index; for example,  $f_i(\cdot) = g_i(\cdot)$  would mean that for all possible indices  $i$  the equation holds.

- Einstein notation is not used; all summations are written explicitly.
- All energies are in units of 2615 keV (the energy of the  $^{208}\text{Tl}$  gamma line). This energy scale is natural for us because the lightmap of chapter 6 is measured with events from that gamma line.

We describe the data as a collection of discretely sampled waveforms,  $X_i[\tau]$ . We assume that all pulse times and shapes are already known, and only their magnitudes need to be extracted; so we can model the waveforms by

$$X_i[\tau] = \sum_a M_{ia} Y_{ia}[\tau] + N_i[\tau] + b_i, \quad (4.1)$$

where  $Y_{ia}[\tau]$  is the template function of the pulse caused by scintillation cluster  $a$  on channel  $i$ ,  $M_{ia}$  is the unknown magnitude of that pulse, and  $N_i[\tau]$  and  $b_i$  represent the electronic noise and baseline, respectively, of the channel.

To break the degeneracy between  $M$  and  $Y$  we must fix the magnitude of the template function  $Y$ . We choose to require that the function  $Y$  has a baseline of zero and a peak magnitude of one, as illustrated in figure 4.4.

The magnitude of a pulse is a random variable which depends on both the energy of the scintillation cluster and on random fluctuations detailed in section 4.3.

We assume that the expected magnitude  $\langle M_{ia} \rangle$  of a pulse on channel  $i$  from a single-site 2615-keV deposit is known, and is characterized as a function  $L_i(\vec{x}_a, t_a)$  of the

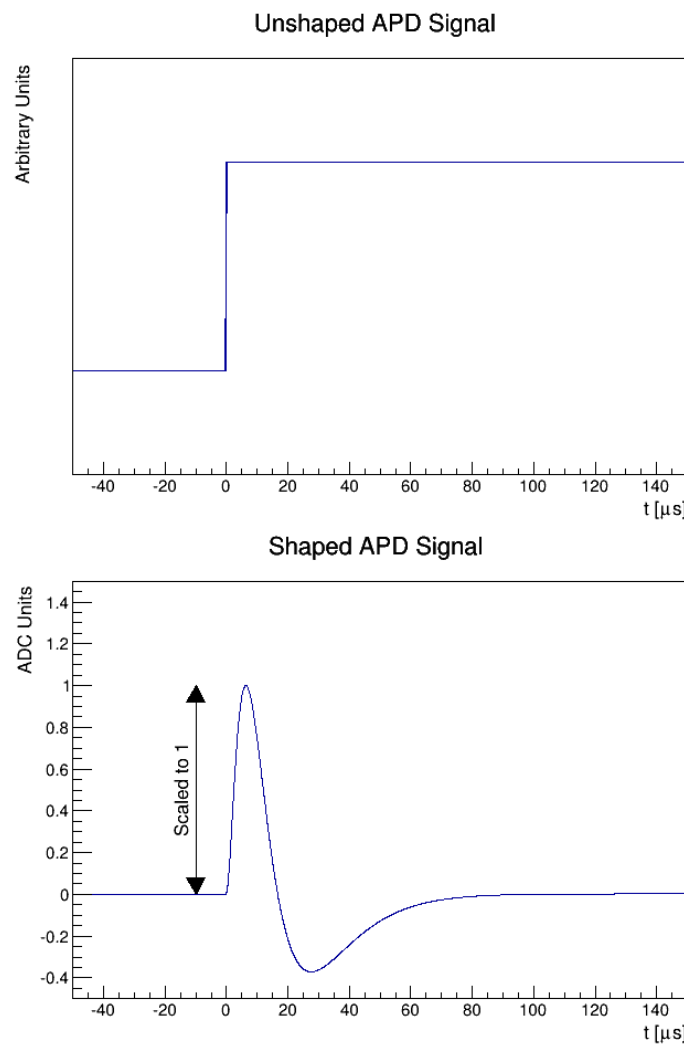


Figure 4.4: Shaped and unshaped APD waveforms. The normalization is shown to make the peak of the shaped waveform have a magnitude of one, and the time axis is shifted so that the unshaped waveform is a step function centered at  $t = 0$ .

deposit position  $\vec{x}_a$  and calendar time  $t_a$ . We can thereby characterize the expected yields  $M_{ia}$  from a scintillation cluster with energy  $E_a$  (in units of 2615 keV) as:

$$\langle M_{ia} \rangle = L_i(\vec{x}_a, t_a) E_a. \quad (4.2)$$

The exact methods for measuring  $L_i(\vec{x}, t)$  is described in chapter 6.

In cases where a multi-site scintillation cluster deposits energy in multiple locations, we use the charge information to estimate the energy deposited in each location; the estimated lightmap yield  $L_i^{MS}$  from a multi-site scintillation cluster is a weighted sum:

$$L_i^{MS}(\vec{x}_1, \dots, \vec{x}_{n_{max}}, t) = \frac{\sum_n E_n^{charge} L_i(\vec{x}_n, t)}{\sum_n E_n^{charge}}, \quad (4.3)$$

where the index  $n$  ranges over the charge clusters associated with this scintillation cluster. For notational simplicity, we still write the expected yield on a channel  $i$  from a multi-site scintillation cluster as  $L_i(\vec{x}, t)$ ; in practice it is always clear how to compute the expected yields for any scintillation cluster from this function.

The electronic noise correlations are simplest in frequency space, so we take the Fourier transform of equation 4.1 and drop the zero-frequency component (which only serves as a measure of the baseline  $b_i$ ) to obtain

$$\tilde{X}_i[f] = \sum_a M_{ia} \tilde{Y}_{ia}[f] + \tilde{N}_i[f]. \quad (4.4)$$

We characterize the electronic noise by its second moments. It is computationally

useful to decompose complex-valued numbers into their rectangular coordinates, so our characterization of the electronic noise should include the expectation values of:

$$\left\langle \tilde{N}_i^R[f] \tilde{N}_j^R[f] \right\rangle \quad (4.5a)$$

$$\left\langle \tilde{N}_i^R[f] \tilde{N}_j^I[f] \right\rangle \quad (4.5b)$$

$$\left\langle \tilde{N}_i^I[f] \tilde{N}_j^R[f] \right\rangle \quad (4.5c)$$

$$\left\langle \tilde{N}_i^I[f] \tilde{N}_j^I[f] \right\rangle, \quad (4.5d)$$

for all pairs  $i, j$  of APD channels and all non-zero frequency components  $f$ . Correlations between noise in different frequencies,  $\left\langle \tilde{N}_i[f] \tilde{N}_j[g] \right\rangle$  where  $f \neq g$ , are always equal to zero. The measurement of these correlations is described in chapter 5; this chapter simply presumes that they are known.

### 4.3 APD Noise Model: the Photon Perspective

In this section we describe a model for the Poissonian noise which comes from fluctuations in photon collection and APD gain. The model is constructed from a physical understanding of the APDs, and includes a step-by-step breakdown of where noise is introduced at each stage of the light collection process. For reference, the reader is referred to section 3.5 which describes the readout process, including the operation of APDs.

We define  $P_a^{(0)}$  to be the initial number of photons generated by scintillation

cluster  $a$ ; this parameter is an unknown non-random parameter. Subsequent steps in the readout process result in  $P_{ia}^{(n)}$  quanta (photons, electron-hole pairs, or electrons) on channel  $i$ , where  $n$  indicates the step of the readout process; this quantity is a function of  $P_a^{(0)}$  and also incorporates the randomness of photon collection and gain fluctuations, so  $P_{ia}^{(n)}$  is a random parameter whose distribution reflects the unknown non-random parameter  $P_a^{(0)}$ . We now describe the readout stages.

First, each APD gang  $i$  has some number  $P_{ia}^{(1)}$  of photons which reach its active surface. The mean fraction of photons reaching a particular gang  $i$  from position  $\vec{x}_a$  is written  $f_i(\vec{x}_a)$  and is assumed to be known; however, the initial paths of the optical photons emitted from the source, their trajectories through the xenon, and their success in reflecting off of teflon surfaces are all random, so  $P_{ia}^{(1)}$  is a Poisson-distributed random variable with mean  $f_i(\vec{x}_a)P_a^{(0)}$ . A typical  $\beta\beta0\nu$  event may deposit up to  $\sim 1000$  photons on a nearby APD gang, resulting in roughly 3% uncertainty from photon statistics; for a deposit in the bulk of the xenon, individual APD gangs may collect only one-tenth of this number of photons, resulting in closer to 10% uncertainty due to photon statistics on the nearest APD gang. Thus, we find that the noise on a single APD channel due to photon collection fluctuations may be quite significant.

Additionally, the numbers of photons reaching different gangs are not uncorrelated; since a photon which reaches gang  $i$  cannot deposit on a different gang  $j$ ,  $P_{ia}^{(1)}$  and  $P_{ja}^{(1)}$  are anticorrelated for different gangs  $i \neq j$ . This process is described by a multinomial distribution. Explicitly, the expectation values of our multinomial

distribution are known to be: [117]

$$\left\langle P_{ia}^{(1)} \right\rangle = f_i(\vec{x}_a) P_a^{(0)} \quad (4.6a)$$

$$\left\langle P_{ia}^{(1)} P_{jb}^{(1)} \right\rangle = \left\langle P_{ia}^{(1)} \right\rangle \left\langle P_{jb}^{(1)} \right\rangle + [f_i(\vec{x}_a) \delta_{ij} - f_i(\vec{x}_a) f_j(\vec{x}_a)] P_a^{(0)} \delta_{ab} \quad (4.6b)$$

(As a detail, we should note that the multinomial distribution is an incorrect model in one important respect: a photon may reflect off of teflon one or more times on its way to the APD. Photons incident on the teflon may be absorbed, which would lead to a reflection efficiency which is less than one. Furthermore, it is possible that teflon is mildly fluorescent at the wavelength of our scintillation, leading to an increase in reflection efficiency. Combining the variances which come from each segment on a photon's trajectory and the variances from fluctuations in the reflection efficiency of teflon can be done with the conditional variance formula [117], but we currently have no estimate of the number of reflections a photon undergoes. The consequence is that we probably mis-estimate the variance of  $P_{ia}^{(1)}$ .)

Next, photons which arrive at the active surface of an APD must convert to electron-hole pairs in the silicon semiconductor layer of the APD; see section 3.5 for details. The energy required to produce one electron-hole pair in silicon is 3.66 eV, so each incident photon produces roughly 1.9 electron-hole pairs. We define  $P_{ia}^{(2)}$  to be the number of electron-hole pairs actually produced from  $P_{ia}^{(1)}$  incident photons. The Fano factor for electrons produced in silicon is roughly 0.1, meaning that in addition to the uncertainty in  $P_{ia}^{(1)}$  which we have already characterized, there is an additional uncorrelated variance in  $P_{ia}^{(2)}$  equal to  $0.1 \left\langle P_{ia}^{(2)} \right\rangle$  [106]. The correlations

in the parameters  $P_{ia}^{(2)}$  are therefore:

$$\left\langle P_{ia}^{(2)} \middle| P_{ia}^{(1)} \right\rangle = 1.9 \cdot P_{ia}^{(1)} \quad (4.7a)$$

$$\left\langle P_{ia}^{(2)} P_{jb}^{(2)} \middle| P_{ia}^{(1)}, P_{jb}^{(1)} \right\rangle = (1.9)^2 \cdot P_{ia}^{(1)} P_{jb}^{(1)} + 0.1 \cdot 1.9 \cdot P_{ia}^{(1)} \delta_{ij} \delta_{ab} \quad (4.7b)$$

Electron-hole pairs are then amplified by an avalanche process inside the APDs. The magnitude of this gain is APD-dependent, generally on the order of  $200 - 300$ , and can be identified by a time-dependent quantity  $G_i^D(t)$  (where  $D$  stands for diode); we call the number of output electrons  $P_{ia}^{(3)}$ . In addition to amplification of existing noise in  $P_{ia}^{(2)}$ , two additional source of noise are introduced:

- First, there is statistical variance in the amplification experienced by each electron due to the randomness of the avalanche process. This variance is dependent on many factors, including the gain, and scales linearly with the number of electrons; we define the variance on the gain experienced by a single electron on channel  $i$  as  $\sigma_{G_i}^2(t)$ . From [106],  $\sigma_{G_i}^2(t)$  is approximately equal to  $(G_i^D(t))^2$  when  $G_i^D(t) = 100$ ; as a result, we approximate

$$\sigma_{G_i}^2(t) \approx (G_i^D(t))^2. \quad (4.8)$$

- Second, there are gain non-uniformities in the diode volume, which contribute variance proportional to the square of the number of initial electron-hole pairs; we identify the proportionality constant as  $\sigma_{NU}^2$ , which may depend on time and APD gang. The magnitude of this uncertainty is not well-known, but

may be significant. In particular, the ganging together of APDs means that a single channel is a sum of pulses which have been exposed to six or seven different gain factors from the different APDs in that gang; the diameter of an APD gang is 58 mm [96], and gain non-uniformity is expected to be a significant factor when photons deposit preferentially on one portion of that area. Our current code base treats  $\sigma_{NU}^2$  as zero; however, future analyses will likely attempt to estimate it, and the derivation which follows retains it as an aid to that anticipated work.

These fluctuations are not correlated across channels, so their variances are multiplied by  $\delta_{ij}\delta_{ab}$  to ensure they only contribute to variance terms and not covariance terms. The correlations in the parameters  $P_{ia}^{(3)}$  are therefore:

$$\left\langle P_{ia}^{(3)} \middle| P_{ia}^{(2)} \right\rangle = G_i^D(t_a)P_{ia}^{(2)} \quad (4.9a)$$

$$\left\langle P_{ia}^{(3)} P_{jb}^{(3)} \middle| P_{ia}^{(2)}, P_{jb}^{(2)} \right\rangle = G_i^D(t_a)G_j^D(t_b)P_{ia}^{(2)}P_{jb}^{(2)} + \left[ P_{ia}^{(2)}\sigma_{G_i}^2(t_a) + \left(P_{ia}^{(2)}\right)^2\sigma_{NU}^2 \right] \delta_{ij}\delta_{ab} \quad (4.9b)$$

Finally, there is amplification  $G_i^E(t)$  associated with the electronics of the APDs which is dependent on time and channel. This includes preamplifier gain, shaper gain, gain associated with the shaping times, and conversion from voltage to ADC counts. We assume that this gain does not suffer any fluctuations, so no new variance is produced. The output from this amplification is a waveform in ADC counts, so we can link it to the magnitude variable  $M_{ia}$  of equation 4.4 by stating

that:

$$\left\langle M_{ia} \middle| P_{ia}^{(3)} \right\rangle = G_i^E(t_a) P_{ia}^{(3)} \quad (4.10a)$$

$$\left\langle M_{ia} M_{jb} \middle| P_{ia}^{(3)}, P_{jb}^{(3)} \right\rangle = G_i^E(t_a) G_j^E(t_b) P_{ia}^{(3)} P_{jb}^{(3)}. \quad (4.10b)$$

Although we assume that no noise correlated with pulses is introduced during this stage, there is electronic noise  $N_i[\tau]$  introduced at this stage which has been described above and is uncorrelated with the pulses. Additionally, the APDs can contribute noise in the form of a dark current which is uncorrelated with pulses; this is inseparable from the electronic noise, and so we absorb it into our description of  $N_i[\tau]$ .

Equations 4.6, 4.7, 4.9, and 4.10 collectively chart the mean and variance of the APD pulse magnitudes at each step of readout and amplification. We can eliminate the intermediate terms  $P_{ia}^{(1)}$ ,  $P_{ia}^{(2)}$ , and  $P_{ia}^{(3)}$  by substitution and obtain a full description for the first and second moments of the pulse magnitudes  $M_{ia}$ ,  $M_{jb}$  depending only on the unknown numbers of emitted photons  $P_a^{(0)}$ ,  $P_b^{(0)}$  and not on

any random variables:

$$\langle M_{ia} \rangle = 1.9 \cdot G_i(t_a) f_i(\vec{x}_a) P_a^{(0)} \quad (4.11a)$$

$$\langle M_{ia} M_{jb} \rangle = (1.9)^2 \cdot G_i(t_a) G_j(t_b) f_i(\vec{x}_a) f_j(\vec{x}_b) P_a^{(0)} P_b^{(0)}$$

$$- (1.9)^2 \cdot G_i(t_a) G_j(t_a) f_i(\vec{x}_a) f_j(\vec{x}_a) P_a^{(0)} \delta_{ab} \quad (4.11b)$$

$$+ 1.9 \cdot (G_i^E(t_a))^2 f_i(\vec{x}_a) P_a^{(0)} \left[ [(0.1 + 1.9) + 1.9 \cdot f_i(\vec{x}_1) (P_a^{(0)} - 1)] \sigma_{NU}^2 \right. \\ \left. + (1.9 + 0.1) (G_i^D(t_a))^2 + \sigma_{G_i}^2(t_a) \right] \delta_{ij} \delta_{ab},$$

where for notational convenience we have defined  $G_i(t) = G_i^E(t) G_i^D(t)$  as the product of the electronic and APD gains.

A simple substitution is possible by the property of conditional expectations, which states that the expectation value of a random value  $X$  is the same as the result from taking an expectation value of  $X$  conditional on  $Y$  followed by an expectation value of the result: [117]

$$\langle X \rangle = \langle \langle X | Y \rangle \rangle. \quad (4.12)$$

The choice throughout to convey second moments of random variables with expectation values, as  $\langle XY \rangle$ , rather than with covariances as  $\text{cov}(X, Y)$ , is for the simplicity this provides; had we chosen to use covariances, combining these separate results would have required the use of the conditional covariance formula: [117]

$$\text{cov}(X, Y) = \langle \text{cov}(X, Y | Z) \rangle + \text{cov}(\langle X | Z \rangle, \langle Y | Z \rangle). \quad (4.13)$$

So, simplicity has been gained by avoiding a description of the model in terms of covariances.

Equations 4.11 fully characterize the first and second moments of the random variables  $M_{ia}$ , which are the magnitudes of the observed pulses. This is a key step in building a full model of the APD noise. However, the expressions for these first and second moments are in terms of some parameters which are not directly observable. In particular, we do not have the ability to directly measure the function  $f_i(\vec{x})$  which describes the average fraction of photons which arrive on channel  $i$  from an initial position  $\vec{x}$ . In section 4.4 we restate equations 4.11 in terms of quantities which are directly observable so that it is usable in practice.

## 4.4 Bridge between Photons and Pulses

We have characterized in equation 4.11 the first and second moments of the random variables  $M_{ia}$ . However, that characterization is phrased in terms of quantities which are not observable, so its practical utility is limited. In this section we transform equation 4.11 into a form which is usable in practice, and identify where we obtain the key parameters which it contains.

The main part of equation 4.11 which we are unable to access experimentally is  $f_i(\vec{x})$ , the mean fraction of photons originating from position  $\vec{x}$  which arrive at APD channel  $i$ . However, we do have observations of a related quantity: in equation 4.2 we make use of a lightmap function  $L_i(\vec{x}, t)$  which identifies the average magnitude (in ADC counts) of a pulse on channel  $i$  produced from a 2615-keV energy deposit

at position  $\vec{x}$  and calendar time  $t$  (where 2615 keV is selected because we measure it from the 2615-keV  $^{208}\text{Tl}$  gamma line of our thorium source calibrations). Chapter 6 describes how this lightmap function is measured from data; here we simply note that, because  $L_i(\vec{x}, t)$  relates deposited energy to measured pulse sizes without reference to the number of photons internally created, it is possible to measure it directly from data.

Additionally, we must relate the quantity of energy deposited to the number of photons produced. This is not directly measurable in the EXO-200 detector, so we must rely on simulation to estimate it; however, in section 4.5 we find that this relation has a very small impact on our energy estimator, so it need not be precise. Simulations using NEST [118] which have been performed within the EXO group by Liangjian Wen at our bulk electric field of 376 V/cm indicate that we can expect 82,000 photons from a 2615-keV gamma deposit. We identify this ratio between photons generated and energy deposited with the parameter  $c \approx 82,000$ , and express the average relation between energy and photon yield in EXO-200 by

$$P_a^{(0)} = c \cdot E_a, \quad (4.14)$$

where  $E_a$  is the energy of scintillation cluster  $a$  in units of 2615 keV.

Equation 4.14 is treated here as exact, but this may not be so. It is likely that photon yield does not scale linearly with energy; additionally, there are fluctuations in the number of photons produced for a particular energy deposit, and we are not treating  $P_a^{(0)}$  as a random variable depending on  $E$ . The essential point here is that

the scintillation “energy” which we measure with the APD waveforms is a direct reflection of the number of photons  $P_a^{(0)}$ , and only indirectly reflects the true scintillation cluster energy  $E_a$ . Similarly, the ionization energy measurement which is made with the u-wires is a direct reflection of the number of free electrons generated, and only indirectly reflects the true deposit energy. The purpose of the energy calibration, described in section 7.3, is to combine our estimates of scintillation energy (proportional to the number of photons) and ionization energy (proportional to the number of free electrons) into a single estimate of the true deposited energy, taking into account any non-linearities in either component. We find it convenient to report the scintillation energy as  $P_a^{(0)}/c$  rather than the true number of photons  $P_a^{(0)}$ , so the reported scintillation energy is roughly comparable to the true amount of deposited energy; but our goal is still only to measure (a quantity proportional to) the number of photons created. In the derivations of this chapter we refer to  $E_a$  as the energy of scintillation cluster  $a$ , but it is the scintillation energy, not the true deposited energy, which we mean by this variable.

We can now combine equations 4.2, 4.11a, and 4.14 to relate  $f_i(\vec{x})$  and  $L_i(\vec{x}, t)$ :

$$L_i(\vec{x}, t) = 1.9 \cdot c f_i(\vec{x}) G_i(t). \quad (4.15)$$

We use this relation and equation 4.14 to eliminate  $f_i(\vec{x})$  from equation 4.11 and

restate the moments of the pulse magnitudes  $M_{ia}$  as:

$$\langle M_{ia} \rangle = L_i(\vec{x}_a, t_a) E_a \quad (4.16a)$$

$$\langle M_{ia} M_{jb} \rangle = L_i(\vec{x}_a, t_a) L_j(\vec{x}_b, t_b) E_a E_b$$

$$- L_i(\vec{x}_a, t_a) L_j(\vec{x}_a, t_a) E_a \delta_{ab} / c \quad (4.16b)$$

$$+ L_i(\vec{x}_a, t_a) E_a \left[ [(0.1 + 1.9)G_i(t_a) + L_i(\vec{x}_a, t_a)(E_a - 1/c)] \frac{\sigma_{NU}^2}{(G_i^D(t_a))^2} \right. \\ \left. + (0.1 + 1.9)G_i(t_a) + \frac{G_i^E(t_a)}{G_i^D(t_a)} \sigma_{G_i}^2(t_a) \right] \delta_{ij} \delta_{ab}.$$

To simplify the notation, let us define a new function:

$$q(i, a) := L_i(\vec{x}_a, t_a) E_a \left[ [(0.1 + 1.9)G_i(t_a) + L_i(\vec{x}_a, t_a)(E_a - 1/c)] \frac{\sigma_{NU}^2}{(G_i^D(t_a))^2} \right. \\ \left. + (0.1 + 1.9)G_i(t_a) + \frac{G_i^E(t_a)}{G_i^D(t_a)} \sigma_{G_i}^2(t_a) \right] \quad (4.17)$$

which we note should be strictly positive if measured correctly (because all gains and lightmap values should be strictly positive, and all variances are non-negative).

Using this shorthand, we re-write the expectation values of equation 4.16 in the more compact form:

$$\langle M_{ia} \rangle = L_i(\vec{x}_a, t_a) E_a \quad (4.18a)$$

$$\langle M_{ia} M_{jb} \rangle = L_i(\vec{x}_a, t_a) L_j(\vec{x}_b, t_b) E_a E_b \\ - L_i(\vec{x}_a, t_a) L_j(\vec{x}_a, t_a) E_a \delta_{ab} / c \\ + q(i, a) \delta_{ij} \delta_{ab}. \quad (4.18b)$$

We will see in equation 6.1 that the lightmap  $L_i(\vec{x}, t)$  is treated as a separable function,  $L_i(\vec{x}, t) = R_i(\vec{x})S_i(t)$ . The right hand side of equation 4.15 has factors which depend strictly on either position or time, but not both; so we can separate the position-dependent and time-dependent factor from both sides and state:

$$R_i(\vec{x}) \propto f_i(\vec{x}) \quad (4.19a)$$

$$S_i(t) \propto G_i(t). \quad (4.19b)$$

So, we can use the lightmap to understand the time-dependent behavior of the product of electronic and APD gain,  $G_i(t)$ , for each channel; but we cannot use it to set the absolute scale, nor can we use it to understand separately  $G_i^E(t)$  and  $G_i^D(t)$ .

Measurements of  $G_i^E(t)$  are possible from internal charge injection runs, as described in section 3.6. However, using these runs in a uniform way is difficult. Internal charge injection runs are only useful for understanding relative changes in the electronic gain over time, and an external charge injection run is needed to set an absolute scale for the gain. The only APD external charge injection runs were taken in February 2011, and have not been analyzed since that time; also, since that time some APD electronics boards have been replaced, resetting the scale of the internal charge injection runs. For the present analysis, the charge injection runs are not used to fix  $G_i^E(t)$ .

However, we can still derive an estimate for the electronic gain which is sufficient for the present analysis. The electronic gain comes entirely from known electronic components; based on these electronic components, the preamplifier has

a gain of  $1/(5 \text{ pF})$ , shapers have a combined 21.2, and the digitizer digitizes 12 bits (4096 ADC counts) for a 2.5 volt pulse. Combining these factors, we use a time-independent estimate:

$$G_i^E(t) = 1.1 \cdot 10^{-3} \text{ ADC/e}^- . \quad (4.20)$$

Future work should include a more careful study of the charge injection runs to improve this estimate, but we use this value to perform the present analysis. A consequence of this choice is that all time-dependence of  $S_i(t)$  must be absorbed into  $G_i^D(t)$ , so we can strengthen equation 4.19b to:

$$S_i(t) \propto G_i^D(t) . \quad (4.21)$$

We also have independent measurements of the APD gains  $G_i^D(t)$  available from laser calibration runs. These special runs allow a laser to shine into the detector from a fixed point and with a stable amplitude while the bias voltages on the APDs are varied from an effective unity gain to our standard voltage settings. Using these measurements, we are able to measure  $G_i^D(t)$  at weekly intervals from September 2012 to the present time. Before September 2012, some less-reliable laser data is available, but results from that data are not readily available as of this writing.

It would be possible, and should be a goal for future improvements, to make use of this full range of laser data. However, the laser data provides a less uniform history of APD gains over the full data-taking window of EXO-200 from September

2011 to November 2013, and it is much easier to track time-dependent behavior from thorium source data which have been collected regularly throughout that period. As a result, a compromise is used to characterize  $G_i^D(t)$ . One particular laser run, run 4540 (taken on December 13, 2012), is used to fix  $G_i^D(t_{4540})$ , and equation 4.21 is used to extrapolated using thorium source data:

$$G_i^D(t) \approx G_i^D(t_{4540}) \cdot S_i(t)/S_i(t_{4540}). \quad (4.22)$$

This assumption makes use of the approximation that  $G_i^E(t)$  is roughly constant in time, which is probably only accurate to one significant figure; therefore when an electronics change is made to a channel, we can expect that the accuracy of  $G_i^D(t)$  is no better than one significant figure. These results mean that we can also estimate with the same level of accuracy:

$$f_i(\vec{x}) \approx \frac{S_i(t_{4540})}{G_i^D(t_{4540})} \cdot \frac{R_i(\vec{x})}{1.9 \cdot c G_i^E(t)}. \quad (4.23)$$

The set of inputs needed to use equations 4.18 are  $L_i(\vec{x}, t)$ ,  $G_i^D(t)$ ,  $G_i^E(t)$ ,  $\sigma_{NU}^2$ ,  $\sigma_{G_i}^2(t)$ , and  $c$ . The lightmap  $L_i(\vec{x}, t)$  is measured in chapter 6. Our approximations for  $G_i^D(t)$  and  $G_i^E(t)$  have been described in equations 4.22 and 4.20, respectively.  $c \approx 82,000$  was identified for equation 4.14. We have stated that  $\sigma_{NU}^2$  is set equal to zero for this analysis, and is retained in this work to facilitate future investigations. Equation 4.8 has estimated  $\sigma_{G_i}^2(t) \approx (G_i^D(t))^2$ .

Thus, we have specified fully the parameters needed as inputs to equations 4.18.

We now have at our disposal a full model for the Poissonian noise on APD channels. We are finally prepared with all tools necessary to derive an optimal energy estimator, and this is done in section 4.5.

## 4.5 Derivation of an Optimal Energy Estimator

It is now possible to specify the optimization criteria for generating an energy estimate from the APD waveforms. We wish to identify an energy estimator which is unbiased and has a minimal expected error. For the problem to remain tractable, we demand that the estimator be linear. Furthermore, although the Fourier-transformed waveforms  $\tilde{X}_i[f]$  are complex-valued, we require that the energy estimate be strictly real-valued. This section describes the optimization criteria and constraints for the energy estimator, and then proceeds to derive an optimal estimator satisfying those constraints.

We recall from equation 4.4 our model for the APD waveforms:

$$\tilde{X}_i[f] = \sum_a M_{ia} \tilde{Y}_{ia}[f] + \tilde{N}_i[f], \quad (4.24)$$

where  $M_{ia}$  and  $\tilde{N}_i[f]$  are random variables with known probability distributions, we choose to drop the zero-frequency component, and the probability distribution of  $M_{ia}$  reflects the energy parameter which we intend to estimate. We therefore take

the energy estimator  $\hat{E}_a$  for the energy of scintillation cluster  $a$  to be of the form:

$$\hat{E}_a = \sum_{if} A_{ia}[f] \tilde{X}_i^R[f] + B_{ia}[f] \tilde{X}_i^I[f], \quad (4.25)$$

where we recall from section 4.2 that  $*^R$  and  $*^I$  are the real and imaginary parts, respectively, of a complex-valued parameter. This expression is one form for the most general real-valued linear functional on  $X_i[f]$ . The goal of denoising is therefore reduced to identifying the optimal parameters  $A_{ia}[f]$  and  $B_{ia}[f]$  for this estimator.

The mean squared error  $\epsilon_a^2$  in the energy estimate  $\hat{E}_a$  of  $E_a$  is defined by:

$$\epsilon_a^2 = \left\langle \left( \hat{E}_a - E_a \right)^2 \right\rangle. \quad (4.26)$$

Our goal is to minimize  $\epsilon_a^2$  under the constraint of no bias, ie. that:

$$\left\langle \hat{E}_a - E_a \right\rangle = 0 \quad (4.27)$$

or, by substitution of equation 4.24 and applying our knowledge of the expectation value of  $M_{ia}$  from equation 4.18a and our knowledge that the noise terms have mean zero, the no-bias constraint is equivalent to:

$$\sum_{ifb} \left[ A_{ia}[f] \tilde{Y}_{ib}^R[f] + B_{ia}[f] \tilde{Y}_{ib}^I[f] \right] L_i(\vec{x}_b, t_b) E_b = E_a. \quad (4.28)$$

This constraint holds for all values of the scintillation cluster indices  $a$  and  $b$ , indicating that even in the presence of multiple scintillation clusters we still demand

that the energy estimators are unbiased.

However, we find that it is necessary to specify a slightly stronger constraint. In particular, it is desirable to ensure that the constraints are as independent of energy as possible to reduce the need to input an estimated energy into our energy estimator; therefore we freely employ the stronger constraint

$$\sum_{if} \left[ A_{ia}[f] \tilde{Y}_{ib}^R[f] + B_{ia}[f] \tilde{Y}_{ib}^I[f] \right] L_i(\vec{x}_b, t_b) = \delta_{ab} \text{ for all } b, \quad (4.29)$$

which implies the earlier forms and leads to advantageous cancellations of terms. Conceptually, this constraint is equivalent to saying that estimates of the energy  $E_a$  of a scintillation cluster  $a$  should be unbiased and independent of any other energies  $E_b$  which are present on the same waveform.

We now proceed with the optimization. We start by expanding  $\epsilon_a^2$ :

$$\epsilon_a^2 = \left\langle \left( \hat{E}_a - E_a \right)^2 \right\rangle \quad (4.30)$$

$$= \left\langle \hat{E}_a^2 \right\rangle - E_a \left\langle \hat{E}_a \right\rangle - \left\langle \hat{E}_a - E_a \right\rangle E_a \quad (4.31)$$

We employ the constraint of equation 4.27 to simplify the second term of this expansion, and eliminate the third altogether; we then proceed:

$$\epsilon_a^2 = \left\langle \hat{E}_a^2 \right\rangle - E_a^2 \quad (4.32)$$

$$= \left\langle \left( \sum_{if} \left[ A_{ia}[f] \tilde{X}_i^R[f] + B_{ia}[f] \tilde{X}_i^I[f] \right] \right)^2 \right\rangle - E_a^2 \quad (4.33)$$

$$\begin{aligned} &= \left\langle \left( \sum_{if} \left[ A_{ia}[f] \tilde{N}_i^R[f] + B_{ia}[f] \tilde{N}_i^I[f] \right] \right. \right. \\ &\quad \left. \left. + \sum_{ifb} \left[ A_{ia}[f] \tilde{Y}_{ib}^R[f] + B_{ia}[f] \tilde{Y}_{ib}^I[f] \right] M_{ib} \right) \right. \\ &\quad \left. \left. \right)^2 \right\rangle - E_a^2 \end{aligned} \quad (4.34)$$

The noise  $\tilde{N}$  and pulse magnitude  $M_{ia}$  are uncorrelated, so multiplicative cross-terms have an expectation value of zero:

$$\begin{aligned} \epsilon_a^2 &= \left\langle \left( \sum_{if} \left[ A_{ia}[f] \tilde{N}_i^R[f] + B_{ia}[f] \tilde{N}_i^I[f] \right] \right)^2 \right\rangle \\ &\quad + \left\langle \left( \sum_{ifb} \left[ A_{ia}[f] \tilde{Y}_{ib}^R[f] + B_{ia}[f] \tilde{Y}_{ib}^I[f] \right] M_{ib} \right) \right. \\ &\quad \left. \left. \right)^2 \right\rangle - E_a^2 \end{aligned} \quad (4.35)$$

Additionally, electronic noise cross-terms between different frequencies evaluate to zero:

$$\begin{aligned}
\epsilon_a^2 &= \left\langle \sum_{ijf} \left[ A_{ia}[f] \tilde{N}_i^R[f] + B_{ia}[f] \tilde{N}_i^I[f] \right] \left[ A_{ja}[f] \tilde{N}_j^R[f] + B_{ja}[f] \tilde{N}_j^I[f] \right] \right\rangle \\
&\quad + \left\langle \left( \sum_{ifb} \left[ A_{ia}[f] \tilde{Y}_{ib}^R[f] + B_{ia}[f] \tilde{Y}_{ib}^I[f] \right] M_{ib} \right)^2 \right\rangle - E_a^2 \quad (4.36) \\
&= \sum_{ijf} \left[ A_{ia}[f] A_{ja}[f] \left\langle \tilde{N}_i^R[f] \tilde{N}_j^R[f] \right\rangle + A_{ia}[f] B_{ja}[f] \left\langle \tilde{N}_i^R[f] \tilde{N}_j^I[f] \right\rangle \right. \\
&\quad \left. + B_{ia}[f] A_{ja}[f] \left\langle \tilde{N}_i^I[f] \tilde{N}_j^R[f] \right\rangle + B_{ia}[f] B_{ja}[f] \left\langle \tilde{N}_i^I[f] \tilde{N}_j^I[f] \right\rangle \right] \\
&\quad + \sum_{\substack{ifb \\ jgc}} \left[ A_{ia}[f] \tilde{Y}_{ib}^R[f] + B_{ia}[f] \tilde{Y}_{ib}^I[f] \right] \left[ A_{ja}[g] \tilde{Y}_{jc}^R[g] + B_{ja}[g] \tilde{Y}_{jc}^I[g] \right] \langle M_{ib} M_{jc} \rangle - E_a^2 \\
&\quad \quad \quad (4.37)
\end{aligned}$$

We now expand  $\langle M_{ib}M_{jc} \rangle$  using equation 4.18 and take advantage of the stronger form of our constraint 4.29 to simplify the expression:

$$\begin{aligned}
\epsilon_a^2 &= \sum_{ijf} \left[ A_{ia}[f]A_{ja}[f] \left\langle \tilde{N}_i^R[f]\tilde{N}_j^R[f] \right\rangle + A_{ia}[f]B_{ja}[f] \left\langle \tilde{N}_i^R[f]\tilde{N}_j^I[f] \right\rangle \right. \\
&\quad \left. + B_{ia}[f]A_{ja}[f] \left\langle \tilde{N}_i^I[f]\tilde{N}_j^R[f] \right\rangle + B_{ia}[f]B_{ja}[f] \left\langle \tilde{N}_i^I[f]\tilde{N}_j^I[f] \right\rangle \right] \\
&\quad + \left( \sum_{ifb} \left[ A_{ia}[f]\tilde{Y}_{ib}^R[f] + B_{ia}[f]\tilde{Y}_{ib}^I[f] \right] L_i(\vec{x}_b, t_b) E_b \right)^2 - E_a^2 \\
&\quad - \sum_b \left( \sum_{if} \left[ A_{ia}[f]\tilde{Y}_{ib}^R[f] + B_{ia}[f]\tilde{Y}_{ib}^I[f] \right] L_i(\vec{x}_b, t_b) \right)^2 \frac{E_b}{c} \\
&\quad + \sum_{ifgb} \left[ A_{ia}[f]\tilde{Y}_{ib}^R[f] + B_{ia}[f]\tilde{Y}_{ib}^I[f] \right] \left[ A_{ia}[g]\tilde{Y}_{ib}^R[g] + B_{ia}[g]\tilde{Y}_{ib}^I[g] \right] q(i, b) \quad (4.38) \\
&= \sum_{ijf} \left[ A_{ia}[f]A_{ja}[f] \left\langle \tilde{N}_i^R[f]\tilde{N}_j^R[f] \right\rangle + A_{ia}[f]B_{ja}[f] \left\langle \tilde{N}_i^R[f]\tilde{N}_j^I[f] \right\rangle \right. \\
&\quad \left. + B_{ia}[f]A_{ja}[f] \left\langle \tilde{N}_i^I[f]\tilde{N}_j^R[f] \right\rangle + B_{ia}[f]B_{ja}[f] \left\langle \tilde{N}_i^I[f]\tilde{N}_j^I[f] \right\rangle \right] \\
&\quad + \sum_{ib} \left( \sum_f \left[ A_{ia}[f]\tilde{Y}_{ib}^R[f] + B_{ia}[f]\tilde{Y}_{ib}^I[f] \right] \right)^2 q(i, b) \\
&\quad - \frac{E_a}{c} \quad (4.39)
\end{aligned}$$

We are now in a position to evaluate the partial derivatives of  $\epsilon_a^2$  with respect

to the parameters  $A_{ia}[f]$  and  $B_{ia}[f]$ . They are:

$$\begin{aligned} \frac{\partial \epsilon_a^2}{\partial A_{ia}[f]} &= 2 \sum_j \left[ A_{ja}[f] \left\langle \tilde{N}_i^R[f] \tilde{N}_j^R[f] \right\rangle + B_{ja}[f] \left\langle \tilde{N}_i^R[f] \tilde{N}_j^I[f] \right\rangle \right] \\ &\quad + 2 \sum_{gb} \left[ A_{ia}[g] \tilde{Y}_{ib}^R[g] + B_{ia}[g] \tilde{Y}_{ib}^I[g] \right] q(i, b) \tilde{Y}_{ib}^R[f] \end{aligned} \quad (4.40a)$$

$$\begin{aligned} \frac{\partial \epsilon_a^2}{\partial B_{ia}[f]} &= 2 \sum_j \left[ A_{ja}[f] \left\langle \tilde{N}_i^I[f] \tilde{N}_j^R[f] \right\rangle + B_{ja}[f] \left\langle \tilde{N}_i^I[f] \tilde{N}_j^I[f] \right\rangle \right] \\ &\quad + 2 \sum_{gb} \left[ A_{ia}[g] \tilde{Y}_{ib}^R[g] + B_{ia}[g] \tilde{Y}_{ib}^I[g] \right] q(i, b) \tilde{Y}_{ib}^I[f] \end{aligned} \quad (4.40b)$$

We use Lagrange's method to minimize  $\epsilon_a^2$  while satisfying our constraints; we define

$$C_{ab} = \sum_{if} \left[ A_{ia}[f] \tilde{Y}_{ib}^R[f] + B_{ia}[f] \tilde{Y}_{ib}^I[f] \right] L_i(\vec{x}_b, t_b), \quad (4.41)$$

where the indices of  $C_{ab}$  are ordered, and restate the constraints of equation 4.29 as

$$C_{ab} = \delta_{ab}. \quad (4.42)$$

Then, the partial derivatives of these constrained expressions are:

$$\frac{\partial C_{bc}}{\partial A_{ia}[f]} = \tilde{Y}_{ic}^R[f] L_i(\vec{x}_c, t_c) \delta_{ab} \quad (4.43a)$$

$$\frac{\partial C_{bc}}{\partial B_{ia}[f]} = \tilde{Y}_{ic}^I[f] L_i(\vec{x}_c, t_c) \delta_{ab} \quad (4.43b)$$

Denoting the set of Lagrange multipliers for  $\epsilon_a^2$  with  $\lambda_{ab}$ , where the indices are ordered, and allowing these parameters to absorb constant factors, we can at last

identify the full set of linear equations describing the optimal energy estimator  $\hat{E}_a$ :

$$\begin{aligned} & \sum_j \left[ A_{ja}[f] \left\langle \tilde{N}_i^R[f] \tilde{N}_j^R[f] \right\rangle + B_{ja}[f] \left\langle \tilde{N}_i^R[f] \tilde{N}_j^I[f] \right\rangle \right] \\ & + \sum_{gb} \left[ A_{ia}[g] \tilde{Y}_{ib}^R[g] + B_{ia}[g] \tilde{Y}_{ib}^I[g] \right] q(i, b) \tilde{Y}_{ib}^R[f] \\ & + \sum_b \lambda_{ab} \tilde{Y}_{ib}^R[f] L_i(\vec{x}_b, t_b) = 0 \quad \text{for each } i, f \end{aligned} \quad (4.44a)$$

$$\begin{aligned} & \sum_j \left[ A_{ja}[f] \left\langle \tilde{N}_i^I[f] \tilde{N}_j^R[f] \right\rangle + B_{ja}[f] \left\langle \tilde{N}_i^I[f] \tilde{N}_j^I[f] \right\rangle \right] \\ & + \sum_{gb} \left[ A_{ia}[g] \tilde{Y}_{ib}^R[g] + B_{ia}[g] \tilde{Y}_{ib}^I[g] \right] q(i, b) \tilde{Y}_{ib}^I[f] \\ & + \sum_b \lambda_{ab} \tilde{Y}_{ib}^I[f] L_i(\vec{x}_b, t_b) = 0 \quad \text{for each } i, f \end{aligned} \quad (4.44b)$$

$$\sum_{if} \left[ A_{ia}[f] \tilde{Y}_{ib}^R[f] + B_{ia}[f] \tilde{Y}_{ib}^I[f] \right] L_i(\vec{x}_b, t_b) = \delta_{ab} \quad \text{for each } b \quad (4.44c)$$

It is important to note here that energies  $E_b$ , which we are intending to measure, do in fact enter into this linear set of equations. At first this would seem to demonstrate that the equations here are impossible to apply, but in fact they remind us that our Poissonian noise is dependent on the energy. Statistical fluctuations in the number of photons observed on each APD, for instance, scale like the square root of the number of photons emitted. This is in contrast to the electronic noise, which is not correlated with the energies.

We can see, then, that some estimate of energy is necessary to know the relative importance of different forms of noise. But the constraint equation ensures that our estimate is unbiased regardless of what energy estimates are fed into the system of

equations, so we can be confident that it is only a rough estimate of the energy scale which is needed, and not worry that the optimization is biased to estimate energies similar to the estimates we feed in. For this purpose, it is sufficient to use the charge-only energy as an estimate of the scintillation-only energy.

The optimal energy estimator is now fully specified by the parameters  $A_{ia}[f]$  and  $B_{ia}[f]$  which solve equations 4.44, and the theory of denoising is fully specified. We can see that the optimal estimator varies from event to event, reflecting the facts that we should weight channels differently according to the event position and that the balance of electronic to Poissonian noise changes based on the estimated energy of an event, so we need to solve this system of equations separately for each event in the detector. Sections 4.6-4.9 consider the computational aspects of solving for this energy estimator.

## 4.6 Matrix Formulation of Denoising

We intend to solve the system of equations 4.44 numerically, and note that it is linear in the unknown parameters  $A_{ia}[f]$  and  $B_{ia}[f]$ . It is most convenient if we can restate the system of equations as a matrix equation before attempting to solve it. This section specifies a matrix formulation of the system of equations.

First, we must choose an ordering of the unknowns; the best ordering is the one which groups nonzero entries into blocks, since this allows us to make more

efficient use of matrix software libraries. We define:

$$\vec{A}_a = \begin{pmatrix} A_{1a}[1] & B_{1a}[1] & A_{2a}[1] & B_{2a}[1] & \cdots & B_{i_{max}a}[1] & A_{1a}[2] & \cdots \\ \cdots & A_{1a}[f_{max}] & A_{2a}[f_{max}] & \cdots & A_{i_{max}a}[f_{max}] \end{pmatrix} \quad (4.45)$$

so that the entries alternate between  $A$  and  $B$ , iterating quickly through channels and more slowly through frequencies. Note that only the  $A$  terms are included for the maximum frequency; this is because  $X_i[t]$  is real-valued, so  $\tilde{X}_i[0]$  and  $\tilde{X}_i[f_{max}]$  are real-valued as well. We also find it convenient to define the matrix:

$$\mathbf{A} = \begin{pmatrix} \vdots & & \vdots \\ \vec{A}_1 & \cdots & \vec{A}_{a_{max}} \\ \vdots & & \vdots \end{pmatrix} \quad (4.46)$$

which includes the parameters needed for each of the estimators  $\hat{E}_a$  corresponding to each of the scintillation clusters  $a$ .

We can then define the electronic noise blocks as:

$$\mathbf{N}_f = \begin{cases} \text{COV} \left( \tilde{N}_1^R[f], \tilde{N}_1^I[f], \tilde{N}_2^R[f], \dots, \tilde{N}_{i_{max}}^I[f] \right) & \text{for } f < f_{max} \\ \text{COV} \left( \tilde{N}_1^R[f], \tilde{N}_2^R[f], \dots, \tilde{N}_{i_{max}}^R[f] \right) & \text{for } f = f_{max} \end{cases} \quad (4.47)$$

where  $\mathbf{COV}$  specifies the covariance matrix of an ordered list of random variables,

$$\mathbf{COV}(x_1, x_2, \dots, x_n) = \begin{pmatrix} cov(x_1, x_1) & cov(x_1, x_2) & \cdots & cov(x_1, x_n) \\ cov(x_2, x_1) & cov(x_2, x_2) & \cdots & cov(x_2, x_n) \\ \vdots & \vdots & \ddots & \vdots \\ cov(x_n, x_1) & cov(x_n, x_2) & \cdots & cov(x_n, x_n) \end{pmatrix}. \quad (4.48)$$

Note that because our noise variables  $\tilde{N}_i^R[f]$  and  $\tilde{N}_i^I[f]$  have mean zero (for  $f \neq 0$ ), we can move smoothly between expectation values of products and covariances:

$$cov(\tilde{N}_i^R[f], \tilde{N}_j^R[f]) = \langle \tilde{N}_i^R[f] \tilde{N}_j^R[f] \rangle \quad (4.49a)$$

$$cov(\tilde{N}_i^R[f], \tilde{N}_j^I[f]) = \langle \tilde{N}_i^R[f] \tilde{N}_j^I[f] \rangle \quad (4.49b)$$

$$cov(\tilde{N}_i^I[f], \tilde{N}_j^R[f]) = \langle \tilde{N}_i^I[f] \tilde{N}_j^R[f] \rangle \quad (4.49c)$$

$$cov(\tilde{N}_i^I[f], \tilde{N}_j^I[f]) = \langle \tilde{N}_i^I[f] \tilde{N}_j^I[f] \rangle. \quad (4.49d)$$

We pack together the blocks of equation 4.47 into a sparse noise matrix:

$$\mathbf{N} = \begin{pmatrix} \mathbf{N}_1 & \mathbf{0} & \dots & \mathbf{0} \\ \mathbf{0} & \mathbf{N}_2 & \dots & \mathbf{0} \\ \vdots & \vdots & \ddots & \vdots \\ \mathbf{0} & \mathbf{0} & \dots & \mathbf{N}_{f_{\max}} \end{pmatrix}. \quad (4.50)$$

In a similar way, we can define the other noise terms in terms of matrix operations. We find that it is possible to describe the Poissonian noise terms as a product

of two matrices,  $\mathbf{P} = \mathbf{P}_1 \mathbf{P}_2$ . First we define the matrix  $\mathbf{P}_1$ , which steps horizontally through the APD channels and scintillation clusters. (It does not matter what ordering is used provided  $\mathbf{P}_2$  follows the same one.) For a particular choice of indices  $j$  and  $b$ , the corresponding column of  $\mathbf{P}_1$  is:

$$\mathbf{P}_1(\text{column } j, b) = \begin{pmatrix} \widetilde{Y}_{jb}^R[1]\delta_{1j} \\ \widetilde{Y}_{jb}^I[1]\delta_{1j} \\ \widetilde{Y}_{jb}^R[1]\delta_{2j} \\ \vdots \\ \widetilde{Y}_{jb}^I[1]\delta_{i_{max,j}} \\ \widetilde{Y}_{jb}^R[2]\delta_{1j} \\ \vdots \\ \widetilde{Y}_{jb}^R[f_{max}]\delta_{1j} \\ \widetilde{Y}_{jb}^R[f_{max}]\delta_{2j} \\ \vdots \\ \widetilde{Y}_{jb}^R[f_{max}]\delta_{i_{max,j}} \end{pmatrix} \sqrt{q(j, b)}. \quad (4.51)$$

Note that in each column, only a small subset of the entries are nonzero.

This means that  $\mathbf{P}_2$  should be a matrix with rows that step through the APD channels and scintillation clusters as well (and with the same ordering as  $\mathbf{P}_1$ ). For

a particular choice of indices  $j, b$ , the corresponding row of  $\mathbf{P}_2$  is:

$$\begin{aligned} \mathbf{P}_2(\text{row } j, b) = & \\ & \left( \begin{array}{cccccc} \tilde{Y}_{jb}^R[1]\delta_{1j} & \tilde{Y}_{jb}^I[1]\delta_{1j} & \tilde{Y}_{jb}^R[1]\delta_{2j} & \cdots & \tilde{Y}_{jb}^I[1]\delta_{i_{max}j} & \tilde{Y}_{jb}^R[2]\delta_{1j} & \cdots \\ \cdots & \tilde{Y}_{jb}^R[f_{max}]\delta_{1j} & \tilde{Y}_{jb}^R[f_{max}]\delta_{2j} & \cdots & \tilde{Y}_{jb}^R[f_{max}]\delta_{i_{max}j} \end{array} \right) \sqrt{q(j, b)}. \end{aligned} \quad (4.52)$$

Since we use the product  $\mathbf{P} = \mathbf{P}_1 \mathbf{P}_2$ , it clearly must be the case that the ordering of columns in  $\mathbf{P}_1$  is the same as the ordering of rows in  $\mathbf{P}_2$ . Because in practice there are always be more APD channels than scintillation clusters, it is generally advantageous to iterate through  $j$  fastest, and step through  $b$  more slowly. We can also see that  $\mathbf{P}_1 = \mathbf{P}_2^\top$ , so

$$\mathbf{P} = \mathbf{P}_2^\top \mathbf{P}_2. \quad (4.53)$$

The constraint equations are represented by a matrix  $\mathbf{C}$  with rows that step through the scintillation clusters; for a particular choice of  $b$  the corresponding row of  $\mathbf{C}$  is:

$$\begin{aligned} \mathbf{C}(\text{row } b) = & \\ & \left( \begin{array}{ccc} \tilde{Y}_{1b}^R[1]L_1(\vec{x}_b, t_b) & \tilde{Y}_{1b}^I[1]L_1(\vec{x}_b, t_b) & \tilde{Y}_{2b}^R[1]L_2(\vec{x}_b, t_b) \\ \cdots & \tilde{Y}_{i_{max}b}^I[1]L_{i_{max}}(\vec{x}_b, t_b) & \tilde{Y}_{1b}^R[2]L_1(\vec{x}_b, t_b) \\ \cdots & \tilde{Y}_{1b}^R[f_{max}]L_1(\vec{x}_b, t_b) & \tilde{Y}_{2b}^R[f_{max}]L_2(\vec{x}_b, t_b) \\ & \cdots & \tilde{Y}_{i_{max}b}^R[f_{max}]L_{i_{max}}(\vec{x}_b, t_b) \end{array} \right). \end{aligned} \quad (4.54)$$

Finally it is possible to restate the full linear equation specified above in matrix form, where we can simultaneously include the equations for all of the estimators

$\widehat{E}_a$ :

$$\begin{pmatrix} \mathbf{N} + \mathbf{P} & \mathbf{C}^\top \\ \mathbf{C} & \mathbf{0} \end{pmatrix} \mathbf{A} = \begin{pmatrix} \mathbf{0} \\ \mathbf{I} \end{pmatrix}. \quad (4.55)$$

The matrix  $\mathbf{N}$  is the same as the covariance matrix of the electronic noise, so it must be symmetric and positive-semidefinite. Similarly, we have seen that  $\mathbf{P} = \mathbf{P}_2^\top \mathbf{P}_2$ , implying that  $\mathbf{P}$  must be symmetric and positive-semidefinite. This means that there is a Cholesky decomposition  $\mathbf{N} + \mathbf{P} = \mathbf{L}\mathbf{L}^\top$ , where  $\mathbf{L}$  is a lower-triangular matrix, and that  $\mathbf{N} + \mathbf{P}$  is symmetric and positive semi-definite. This implies that the full matrix equation is symmetric; however, it is insufficient for showing that the full system is positive semi-definite, so we are not able to make use of specialized solver algorithms which exploit positive semi-definiteness.

We also note the important observation that this matrix is sparse. Given roughly 1000 frequency components in our Fourier-transformed waveforms, only 0.1% of the entries of  $\mathbf{N}$  are non-zero. And with 70 APD channels and only a small number of scintillation clusters we wish to denoise, the combined number of non-zero entries in  $\mathbf{P}_1$  and  $\mathbf{P}_2$  is easily an order of magnitude less than the number of non-zero entries in  $\mathbf{N}$ . As a result, we can conclude that this matrix is extremely sparse, and should ensure that whatever method we use to solve these equations takes advantage of this sparsity.

The resulting system of equations 4.55 fully specifies the optimal energy estimators for all scintillation clusters in an event. In sections 4.7-4.9 we discuss computational aspects of the efficient solution of that system of equations.

## 4.7 Preconditioning of the Matrix Formulation

We have specified scintillation energy estimators with matrix equation 4.55 which we now wish to solve. However, it is generally recommended that large matrix equations should not be solved directly. Instead, it is recommended that the matrix should be preconditioned. This means that if a matrix equation  $\mathbf{A}\vec{x} = \vec{b}$  should be solved, one should first find a matrix  $\mathbf{A}'$  which is approximately equal to  $\mathbf{A}$  and which is easily invertible. Finding the right balance between the quality of the approximation  $\mathbf{A}' \approx \mathbf{A}$  and the difficulty of computing the inverse  $(\mathbf{A}')^{-1}$  is more art than science, but this section presents a preconditioning matrix which seems to strike a good balance for this particular system.

The matrix equation we wish to solve takes the form:

$$\begin{pmatrix} \mathbf{N} + \mathbf{P} & \mathbf{C}^\top \\ \mathbf{C} & \mathbf{0} \end{pmatrix} \mathbf{A} = \begin{pmatrix} \mathbf{0} \\ \mathbf{I} \end{pmatrix} \quad (4.56)$$

Let us define  $\mathbf{D} = \text{diag}(\mathbf{N})$  and approximate

$$\begin{pmatrix} \mathbf{N} + \mathbf{P} & \mathbf{C}^\top \\ \mathbf{C} & \mathbf{0} \end{pmatrix} \approx \begin{pmatrix} \mathbf{D} & \mathbf{C}^\top \\ \mathbf{C} & \mathbf{0} \end{pmatrix} \quad (4.57)$$

This approximate form is easy to invert (assuming every frequency component of every channel has non-zero noise and every constraint is satisfiable, which is true in practice), and can be used to precondition our problem for better numerical

behavior.

We can further factor this approximate form of the matrix:

$$\begin{pmatrix} \mathbf{D} & \mathbf{C}^\top \\ \mathbf{C} & \mathbf{0} \end{pmatrix} = \begin{pmatrix} \mathbf{D}^{1/2} & \mathbf{0} \\ \mathbf{CD}^{-1/2} & \mathbf{H} \end{pmatrix} \begin{pmatrix} \mathbf{D}^{1/2} & \mathbf{D}^{-1/2}\mathbf{C}^\top \\ \mathbf{0} & -\mathbf{H}^\top \end{pmatrix} \quad (4.58)$$

$$= \begin{pmatrix} \mathbf{D}^{1/2} & \mathbf{0} \\ \mathbf{0} & \mathbf{I} \end{pmatrix} \begin{pmatrix} \mathbf{I} & \mathbf{0} \\ \mathbf{CD}^{-1/2} & \mathbf{H} \end{pmatrix} \begin{pmatrix} \mathbf{I} & \mathbf{D}^{-1/2}\mathbf{C}^\top \\ \mathbf{0} & -\mathbf{H}^\top \end{pmatrix} \begin{pmatrix} \mathbf{D}^{1/2} & \mathbf{0} \\ \mathbf{0} & \mathbf{I} \end{pmatrix} \quad (4.59)$$

where  $\mathbf{H}$  is a lower-diagonal square matrix defined uniquely as the Cholesky decomposition  $\mathbf{HH}^\top = \mathbf{CD}^{-1}\mathbf{C}^\top$ . (The solution is guaranteed to be real because  $\mathbf{D}$  is positive-semidefinite in all cases, and positive-definite in practice – it consists of noise variance terms, which are strictly positive in practice.) Note that  $\mathbf{CD}^{-1}\mathbf{C}^\top$  has dimensions equal to the number of scintillation clusters in an event, which in practice is small enough that we can compute its Cholesky decomposition  $\mathbf{HH}^\top$  directly.

The two diagonal factors are easily inverted; we further define

$$\mathbf{K}_1 = \begin{pmatrix} \mathbf{I} & \mathbf{0} \\ \mathbf{CD}^{-1/2} & \mathbf{H} \end{pmatrix} \quad \mathbf{K}_1^{-1} = \begin{pmatrix} \mathbf{I} & \mathbf{0} \\ -\mathbf{H}^{-1}\mathbf{CD}^{-1/2} & \mathbf{H}^{-1} \end{pmatrix} \quad (4.60a)$$

$$\mathbf{K}_2 = \begin{pmatrix} \mathbf{I} & \mathbf{D}^{-1/2}\mathbf{C}^\top \\ \mathbf{0} & -\mathbf{H}^\top \end{pmatrix} \quad \mathbf{K}_2^{-1} = \begin{pmatrix} \mathbf{I} & \mathbf{D}^{-1/2}\mathbf{C}^\top\mathbf{H}^{-\top} \\ \mathbf{0} & -\mathbf{H}^{-\top} \end{pmatrix}, \quad (4.60b)$$

where  $\mathbf{M}^{-\top}$  represents the inverse of the transpose of  $\mathbf{M}$ . We then follow the standard prescription for preconditioning a linear system by replacing our original

matrix equation with the new form:

$$\mathbf{K}_1^{-1} \begin{pmatrix} \mathbf{D}^{-1/2} & \mathbf{0} \\ \mathbf{0} & \mathbf{I} \end{pmatrix} \begin{pmatrix} \mathbf{N} + \mathbf{P} & \mathbf{C}^\top \\ \mathbf{C} & \mathbf{0} \end{pmatrix} \begin{pmatrix} \mathbf{D}^{-1/2} & \mathbf{0} \\ \mathbf{0} & \mathbf{I} \end{pmatrix} \mathbf{K}_2^{-1} \tilde{\mathbf{A}} = \mathbf{K}_1^{-1} \begin{pmatrix} \mathbf{D}^{-1/2} & \mathbf{0} \\ \mathbf{0} & \mathbf{I} \end{pmatrix} \begin{pmatrix} \mathbf{0} \\ \mathbf{I} \end{pmatrix} \quad (4.61a)$$

$$\tilde{\mathbf{A}} = \mathbf{K}_2 \begin{pmatrix} \mathbf{D}^{1/2} & \mathbf{0} \\ \mathbf{0} & \mathbf{I} \end{pmatrix} \mathbf{A} \quad (4.61b)$$

which reduces to

$$\mathbf{K}_1^{-1} \left[ \begin{pmatrix} \mathbf{D}^{-1/2} \mathbf{N} \mathbf{D}^{-1/2} & \mathbf{0} \\ \mathbf{0} & \mathbf{0} \end{pmatrix} + \begin{pmatrix} \mathbf{D}^{-1/2} \mathbf{P} \mathbf{D}^{-1/2} & \mathbf{D}^{-1/2} \mathbf{C}^\top \\ \mathbf{C} \mathbf{D}^{-1/2} & \mathbf{0} \end{pmatrix} \right] \mathbf{K}_2^{-1} \tilde{\mathbf{A}} = \begin{pmatrix} \mathbf{0} \\ \mathbf{H}^{-1} \end{pmatrix} \quad (4.62a)$$

$$\mathbf{A} = \begin{pmatrix} \mathbf{D}^{-1/2} & \mathbf{0} \\ \mathbf{0} & \mathbf{I} \end{pmatrix} \mathbf{K}_2^{-1} \tilde{\mathbf{A}} \quad (4.62b)$$

This preconditioned set of equations is numerically quite stable. It is also possible to provide an excellent initial guess  $\tilde{\mathbf{A}}_0$  by taking the approximate form of the matrix to be exact, yielding

$$\tilde{\mathbf{A}}_0 = \begin{pmatrix} \mathbf{0} \\ \mathbf{H}^{-1} \end{pmatrix} \quad (4.63)$$

Based on these various advantages, it is this system which we attempt to solve rather than the original form. Below we define matrices  $\mathbf{M}$  and  $\mathbf{B}$  for convenience, and

summarize the system to be solved:

$$\mathbf{M} = \mathbf{K}_1^{-1} \left[ \begin{pmatrix} \mathbf{D}^{-1/2} \mathbf{N} \mathbf{D}^{-1/2} & \mathbf{0} \\ \mathbf{0} & \mathbf{0} \end{pmatrix} + \begin{pmatrix} \mathbf{D}^{-1/2} \mathbf{P} \mathbf{D}^{-1/2} & \mathbf{D}^{-1/2} \mathbf{C}^\top \\ \mathbf{C} \mathbf{D}^{-1/2} & \mathbf{0} \end{pmatrix} \right] \mathbf{K}_2^{-1} \quad (4.64a)$$

$$\mathbf{B} = \tilde{\mathbf{A}}_0 = \begin{pmatrix} \mathbf{0} \\ \mathbf{H}^{-1} \end{pmatrix} \quad (4.64b)$$

$$\mathbf{M}\tilde{\mathbf{A}} = \mathbf{B} \quad (4.64c)$$

$$\mathbf{A} = \begin{pmatrix} \mathbf{D}^{-1/2} & \mathbf{0} \\ \mathbf{0} & \mathbf{I} \end{pmatrix} \mathbf{K}_2^{-1} \tilde{\mathbf{A}} \quad (4.64d)$$

## 4.8 Matrix Solver

The matrix equation we have derived is sparse: most of its entries are equal to zero.

The challenge to solving this system is therefore to find an algorithm which takes advantage of that sparsity to speed up computations. Although there are some direct methods to solving sparse matrix equations by finding a decomposition which preserves the sparsity structure, we find that these are not very effective for our particular sparsity structure. Instead, we choose to adopt an iterative solver which works by repeated multiplication of vectors by our matrix; then we can take advantage of the sparsity of our matrix simply by writing a matrix-vector multiplication routine which is efficient. Section 4.9 describes how we make our matrix-vector multiplication routine efficient; this section describes the iterative matrix solver algorithm we have chosen.

The matrix  $\tilde{\mathbf{A}}$  for which we attempt to solve has as many columns as there are scintillation clusters we wish to denoise within an event; often there is only one scintillation cluster and  $\tilde{\mathbf{A}}$  is simply a column vector. However, there certainly are many events with multiple scintillation clusters; we also discuss extended applications of denoising where we may treat events as having additional pulses in section 4.11.1. In these cases the number of columns may be larger. In such cases it would be possible to solve for each column of  $\tilde{\mathbf{A}}$  independently, but more efficient to solve the entire system simultaneously. In this way, information obtained from multiplying the matrix by one column may be exploited to solve the other columns as well, effectively multiplying the benefit from each matrix-multiplication by the number of columns of  $\tilde{\mathbf{A}}$ .

Matrix-solving algorithms which handle multiple vectors simultaneously are commonly referred to as block algorithms. We use the Block-BiCGSTAB algorithm [119], an iterative method based on the popular stabilized biconjugate-gradient (BiCGSTAB) method. BiCGSTAB and Block-BiCGSTAB are notable for being able to deal with arbitrary matrices rather than requiring that the matrix be positive-definite (which our matrix is not). The algorithm is reproduced in the form used by our code as Algorithm 1. This algorithm only requires that we are able to left-multiply vectors and matrices by  $\mathbf{M}$  quickly, which makes it possible to exploit the sparsity of  $\mathbf{M}$ .

Since each column of  $\tilde{\mathbf{A}}$  corresponds to one scintillation cluster, the norm of the corresponding column of  $\mathbf{R}$  tells us how well we have identified the optimal magnitude estimator for that scintillation cluster; thus, to test for termination we

---

**Algorithm 1** Block-BiCGSTAB Algorithm

---

```
1:  $\tilde{\mathbf{A}} \leftarrow \tilde{\mathbf{A}}_0$ 
2:  $\mathbf{R} \leftarrow \mathbf{B} - \mathbf{M}\tilde{\mathbf{A}}$ 
3:  $\mathbf{S} \leftarrow \mathbf{R}$ 
4:  $\tilde{\mathbf{R}}_0 \leftarrow \mathbf{R}$ 
5: loop
6:    $\mathbf{V} \leftarrow \mathbf{MS}$ 
7:   Solve  $(\tilde{\mathbf{R}}_0^\top \mathbf{V})\alpha = (\tilde{\mathbf{R}}_0^\top \mathbf{R})$  for  $\alpha$ .
8:    $\mathbf{R} \leftarrow \mathbf{R} - \mathbf{V}\alpha$ 
9:    $\mathbf{T} \leftarrow \mathbf{MR}$ 
10:   $\omega \leftarrow \langle \mathbf{T}, \mathbf{S} \rangle_F / \langle \mathbf{T}, \mathbf{T} \rangle_F$ , where  $\langle \cdot, \cdot \rangle_F$  is the Frobenius matrix norm.
11:   $\tilde{\mathbf{A}} \leftarrow \tilde{\mathbf{A}} + \mathbf{S}\alpha + \omega\mathbf{R}$ 
12:   $\mathbf{R} \leftarrow \mathbf{R} - \omega\mathbf{T}$ 
13:   $\mathbf{R}$  currently equals  $\mathbf{B} - \mathbf{M}\tilde{\mathbf{A}}$ 
14:  if all columns of  $\mathbf{R}$  have sufficiently small magnitudes then
15:    return  $\tilde{\mathbf{A}}$ 
16:  end if
17:  Solve  $(\tilde{\mathbf{R}}_0^\top \mathbf{V})\beta = -(\tilde{\mathbf{R}}_0^\top \mathbf{T})$  for  $\beta$ .
18:   $\mathbf{S} \leftarrow \mathbf{R} + (\mathbf{S} - \omega\mathbf{V})\beta$ 
19: end loop
```

---

should evaluate the norm of each column of  $\mathbf{R}$ , and while any of those norms are above some threshold, the solver must be permitted to continue. Because our resolution is only on the order of 1%, solutions generally need not be very accurate; in practice, we establish reasonable thresholds by plotting resolution against threshold for a small subset of data, and observing when the resolution stops improving.

## 4.9 Computational Considerations

Section 4.8 describes the matrix solver algorithm which we have chosen; as we describe there, the key to its efficiency is that we use an efficient matrix-vector multiplication routine. In this section we describe the tricks used to ensure our matrix-vector multiplication takes full advantage of any special structure in our

problem.

The majority of non-zero matrix entries comes from the electronic noise matrix  $\mathbf{N}$ , making it the computational bottleneck of the algorithm.  $\mathbf{N}$  is block-diagonal, as seen in equation 4.50; if we assume roughly 70 APD channels, then the last block of  $\mathbf{N}$  has  $70^2$  non-zero entries and all other blocks have  $4 \cdot 70^2$  non-zero entries. With waveforms having 2048 samples, and ignoring the baseline component, the problem of multiplying a vector by the electronic noise terms thus consists of 1024 matrix-matrix multiplications, with each of our 1024 left sub-matrices  $\mathbf{N}_f$  containing roughly 20,000 non-zero terms and each right matrix consisting of  $O(1)$  columns and roughly 150 rows. (The number of columns in the right matrix is equal to the number of scintillation clusters, which may be sometimes 3–5 or more; however, it is always much smaller than 150, and describing it as  $O(1)$  captures this fact.)

The key points here which create an opportunity for optimization are that:

- The electronic noise terms generally do not change event-by-event. They are treated as constant across many runs.
- It is possible to multiply two  $N \times N$  matrices together much faster than it is possible to perform  $N$  multiplications of an  $N \times N$  matrix with  $N$   $N \times 1$  matrices. This can be achieved with a combination of algorithms faster than naive  $O(N^3)$  speed and exploitation of low-level computer hardware features such as the CPU cache [120, 121].

What we wish to do, then, is reorganize the solver algorithm so that whenever multiplication by the electronic noise matrix is required, rather than performing

that multiplication on a “skinny”  $150 \times O(1)$  matrix, we pack together many such “skinny” matrices into a single matrix with many columns. Multiplication can then be performed in bulk; and individual columns from the result can be extracted and used as before.

Additionally, it is important that matrix multiplication be made as fast as possible. It has long been known that matrix multiplication provides significant opportunities for low-level optimizations [121]. For example, most of the time taken by naive matrix multiplication is spent fetching and writing data to and from RAM. Significant speedups can be achieved by minimizing the number of CPU cache misses, which can be accomplished by operating on matrices in blocks with size chosen so they fit entirely in the cache. Multiplication instructions can also often be packed into vector instructions such as SSE or AVX. For extremely large matrices, there are even algorithms which require fewer than  $O(N^3)$  multiplications, and these can sometimes be beneficial [121].

Optimization of matrix-matrix multiplication is a large field, but fortunately there are a number of well-tuned software libraries implementing matrix multiplication well-tuned to specific machines. These libraries generally provide the standard Basic Linear Algebra Subroutines (BLAS) interface, making them interchangeable with ease. In this instance, Intel’s MKL library has been used; benefits to this implementation are its availability on scientific computing platforms and its ability to adapt to heterogeneous compute clusters by detecting the architecture of the machine on which it is run [122].

Finally, implementation at the National Energy Research Scientific Computing

Center (NERSC) has the interesting feature that NERSC’s computing systems are designed for multi-core processing. The Hopper and Edison computing systems at NERSC allocate whole nodes, each of which contains 24 cores. Although it is possible to simply run 24 independent processes on each node, memory on NERSC machines is highly constrained; memory use can be reduced by sharing certain large data structures across multiple cores on a node. Additionally, as more events are packed together for electronic-noise multiplication, greater savings can be realized; so it is better to handle many events in coordination. To this purpose, a multi-threaded version of the program has been developed to exploit portions of the code which are conveniently distributed. Because NERSC nodes have a Non-Uniform Memory Access (NUMA) architecture, processes are constrained to only run on cores with a similar memory access pattern; on Hopper this results in four 6-threaded processes per node, while on Edison this results in two 12-threaded processes per node.

As a result, and because the bulk of our computational time is spent multiplying by  $\mathbf{N}$ , we pursue the following strategies to improve code performance:

1. One denoising process runs on each NUMA node of a NERSC machine. Processes should be run in “strict memory mode,” where a process only has access to memory resources on its own NUMA node.
2. Within a process, algorithm 1 should be performed in parallel on all available cores to maximize CPU utilization.
3. When a thread encounters the need for a matrix multiplication in lines 2, 6,

or 9, the thread should not multiply by  $\mathbf{N}$ . Instead, it should push the left hand side into new columns of a matrix  $\mathbf{RHS}$  of “thin” matrices needing to be multiplied by  $\mathbf{N}$ .

4. When enough columns have accumulated in  $\mathbf{RHS}$ , collect the running threads; these threads should each perform some fraction of the matrix multiplications between blocks of  $\mathbf{N}$  and the corresponding rows of  $\mathbf{RHS}$ . When this is complete, the threads should resume their processing of algorithm 1 in parallel on the available pool of events.
5. Every matrix multiplication should be performed by a direct call to the Intel MKL library. To facilitate this process,  $\mathbf{N}$  should be stored in a format that ensures its blocks are accessed in a contiguous segment of memory. Furthermore, because there is ample opportunity for higher-level parallelization, at no time should a multithreaded BLAS operation be invoked; this reduces computational overhead of parallelization.

These represent the most significant set of computational optimizations. However, there are also smaller optimizations which can still produce non-negligible speedups. The Block-BiCGSTAB algorithm (in the case of only one scintillation cluster in an event) requires two matrix-vector multiplications, but it also requires a number of vector-vector operations, and the cumulative cost of these vector-vector operations can become non-negligible. One obvious shortcut is to reuse our computation of  $\tilde{\mathbf{R}}_0^\top \mathbf{V}$  from line 7 of Algorithm 1 to save work in line 17.

Another speedup for our vector-vector operations consists of combining mul-

tiple operations into one step. We see on line 7 that both  $\tilde{\mathbf{R}}_0^\top \mathbf{V}$  and  $\tilde{\mathbf{R}}_0^\top \mathbf{R}$  are computed. As described earlier in the context of multiplication of vectors by electronic noise, it is possible to take advantage of caching and speed up vector operations by packing multiple vectors together into a more square-shaped matrix. In this case, rather than computing these two products separately, we can pack  $\mathbf{V}$  and  $\mathbf{R}$  together and compute

$$\tilde{\mathbf{R}}_0^\top \begin{pmatrix} V & R \end{pmatrix} \quad (4.65)$$

as one step. The rest of the algorithm is not affected by the fact that these two matrices are stored contiguously in memory.

This section has described the optimizations which are available to us to accelerate matrix-vector operations. However, even with the application of these tricks, the amount of computation required to denoise our full dataset is quite large. Each event in our dataset requires us to solve a matrix equation where the matrix has roughly twenty million non-zero entries, and our full dataset contains hundreds of millions of events. Denoising our full dataset currently takes a total of roughly fifty thousand core-hours on the NERSC computing system, making it manageable but not light on resources. Bottlenecks to the code remain, including latency in data access and some inefficient use of multiple cores; improving the speed of denoising remains a high priority and continues to be investigated.

## 4.10 Denoising in Practice

The preceding description of denoising has been intended to convey our fullest current understanding of denoising as it should be performed. However, due to the computational intensity of this algorithm it is not feasible to conduct routine data processing of the full EXO-200 dataset whenever updates to the code base are implemented. As a result, the most recent denoised data available from EXO-200 demonstrates certain deviations from the description above. It is known, and has been demonstrated, that correcting some of these flaws can lead to further improvements in resolution, but no physics analysis will be performed with those improvements until the computational cost of denoising is again deemed worthwhile.

In this section we outline the places where the denoising used for the current physics analysis differs from the description above. Differences in implementation also exist, but are not described here. The differences of denoising are:

- The Poisson noise coming from sources internal to the APDs was not fully understood when denoising was first implemented, and as a result its magnitude is significantly underestimated. Specifically, in place of equations 4.7b and 4.9b we take

$$\left\langle P_{ia}^{(3)} P_{jb}^{(3)} \right\rangle = (1.9)^2 \cdot G_i^D(t_a) G_j^D(t_b) \left\langle P_{ia}^{(1)} P_{jb}^{(1)} \right\rangle. \quad (4.66)$$

- We have described with equation 4.20 that the electronic gain is treated as having a constant value of  $1.1 \cdot 10^{-3}$  ADC counts per electron emitted from

the APDs. The wires use a similar set of electronics; however, their gain is nominally set to a different value of roughly  $6.3 \cdot 10^{-4}$  ADC counts per electron collected on the wires. In the EXO code the two numbers are mistakenly reversed. As a result,  $G_i^E(t)$  was underestimated by almost a factor of two; the effect of this is to overestimate by almost a factor of two the number of photons being deposited on APDs, which again causes us to underestimate the Poisson noise introduced within the APDs.

The effect of both of these issues is to underestimate the importance of Poisson noise, effectively fooling denoising into believing its photon statistics are greater than they truly are; this, in turn, leads it to attach too much weight to too few channels in its energy estimator. Thus, the resolution is negatively impacted by these mistakes; the effect of these two issues can be summarized in one scaling factor which controls the importance of Poisson noise. In figure 4.5 sample runs are denoised with different values of this scaling factor, including the value of 0.6 which was used for the present analysis and 1.6 which we would expect to be the optimal choice. It appears that an improvement in resolution of roughly 0.05 percentage points at 2615 keV will be gained when these issues are addressed.

However, neither of these mistakes have any impact on the correctness of the constraints. As a result, the denoised energy measurements should still be unbiased even though they are non-optimal. Results from the use of this data will be described in chapter 7.

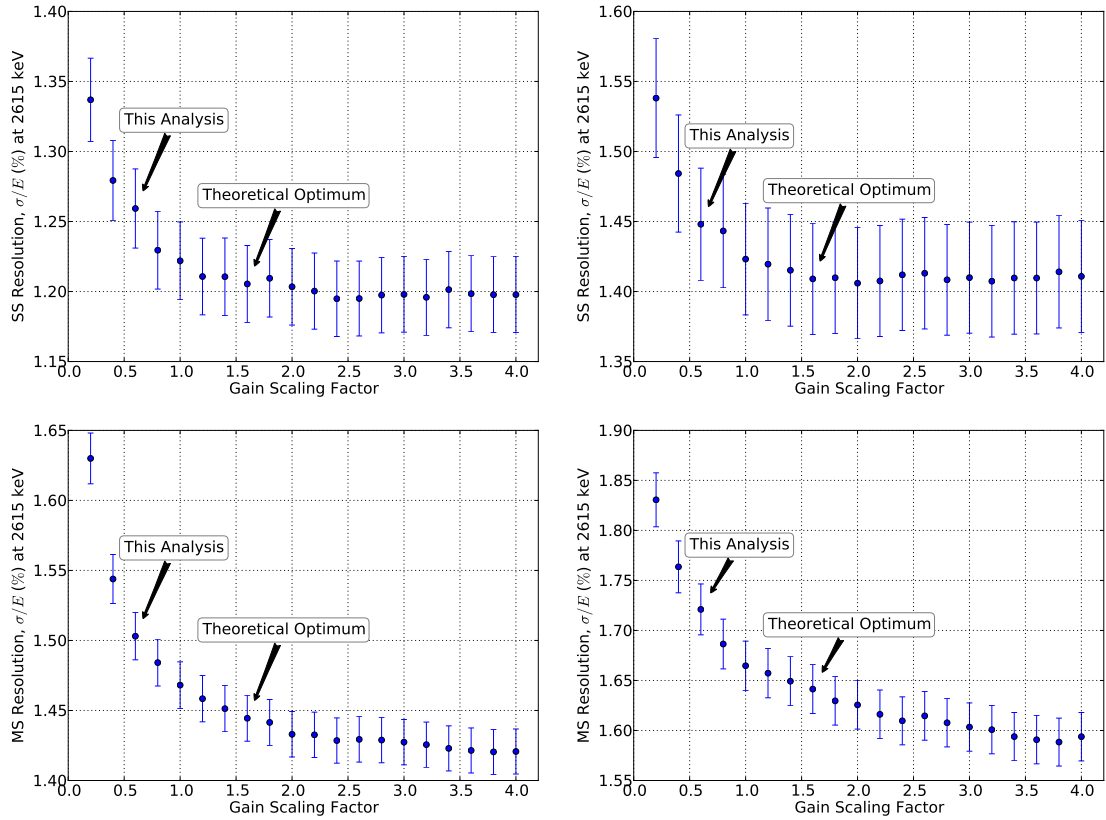


Figure 4.5: It is known that the parameters used for denoising in this analysis are not optimal. Here we use a scaling factor to adjust the parameter controlling the importance of Poisson noise. Data from run 3516 and 4544 are shown on the left and right, respectively; top plots show single-site resolution, bottom plots show multi-site resolution. We can see that an improvement of roughly 0.05 percentage points at 2615 keV could be achieved by moving from the expected optimum. It is not currently understood why scaling factors above the expected optimum yield further improvements to resolution.

## 4.11 Future Extensions to Denoising

We have shown that denoising is capable of producing optimal estimates of the total energy emitted in scintillation by a particular event. However, this algorithm can be applied to a more general range of problems in the EXO-200 detector with only minor modifications. Here we describe possible extensions of the denoising technique to produce anticorrelated energies of individual clusters and to produce denoised wire waveforms.

### 4.11.1 Anticorrelated Cluster Energies

One important generalization is in our definition of scintillation clusters. In the body of this chapter, we have defined a scintillation cluster to include all energy deposits which occur simultaneously in time. By requiring that different scintillation clusters occur at different times, we ensure that the pulse template  $\tilde{Y}_{ia}[f]$  has a different shape for each scintillation cluster  $a$ , so we can disentangle waveform contributions from each energy parameter  $E_a$  and estimate all of them separately.

Historically, time was the only observable available for this sort of discrimination. However, now that we use all APD channels independently, we can use the pattern of pulse magnitude for different channels as a clue to the position of the source of scintillation photons. Even if two scintillation deposits occur simultaneously in time it is possible to estimate their separate energies  $E_a$  based on their positions  $\vec{x}_a$  and our knowledge, from the APD lightmap, of which channels collect

the strongest pulse from those positions. Thus, it is possible for the energy estimators described in this chapter to assign scintillation energies to individual clusters, which would lead to anticorrelated energies of individual clusters with better energy resolution than charge alone can currently provide.

In principle, this is achievable – in the extreme case, when two clusters are at opposite ends of the detector we can expect them to produce light on an entirely different set of channels, and it should be quite easy to separate pulses produced by each. However, charge clusters may be quite close together. For denoising to measure the scintillation from two simultaneous charge clusters solely based on their relative position, they must be spatially separate enough that their respective light yields on nearby APD channels are significantly different. As a result, denoising can only measure scintillation for individual charge clusters if it first performs a re-clustering process in which clusters occurring near each other are artificially merged together for the purpose of scintillation measurement.

Anticorrelated cluster energies would not have a significant impact on single-site data, so it would have minimal impact on our primary goal of searching for neutrinoless double-beta decay. However, it could have a significant impact on a search for excited-state two-neutrino double-beta decay by improving the resolution of gamma lines associated with barium de-excitation. Barabash states in [123] that the dominant mode of excited-state  $2\nu\beta\beta$  decay is to the  $0_1^+$  state, which in  $^{136}Ba$  would lead to the emission of a 760 keV and 819 keV gamma in coincidence; if we could produce anticorrelated energy measurements for individual clusters, the sensitivity to these gamma lines could be significantly enhanced.

There are also potential benefits to our understanding of the detector itself. Currently the only mono-energetic beta calibration available for EXO is the double-escape peak, formed when a gamma particle enters the detector, pair-produces an electron and positron, and the positron interacts with an electron and emits gammas which travel sufficiently far from the initial interaction site so that the initial electron interactions and gamma interactions can be clearly separated. Currently we have the ability to separately measure charge yield from the gammas and the initial electron in some of these events, allowing us to understand the different charge yields from gammas and betas. However, we have no similar capabilities for light yield because the scintillation energy of the whole event is measured together. If we could separate the light yield from these spatially separated clusters, we could use these events to understand both the light and charge yield for different types of interactions.

Another type of detector study which might benefit from anticorrelated cluster energies is the Compton telescope. This is a technique that combines our knowledge of cluster energies and scattering angles, along with the Compton scattering formula [124], and allows us to produce estimates of the origin of the incident gamma. Such a technique permits us to study the sources of our backgrounds, informing future attempts to reduce them by indicating which materials had the most significant negative effect. The accuracy with which we locate the origin of the incident gammas is strongly related to the accuracy of our measurements of the energies of the individual clusters, so it is expected that improving the accuracy of our cluster energies would have a positive impact on our ability to locate the backgrounds of our experiment.

The last benefit to this approach is more technical: evaluating the lightmap for a multi-site event requires an energy-weighted combination of the values of the lightmap at individual cluster locations, as shown in equation 4.3. This process is complicated and error-prone, and can be avoided entirely when we treat each scintillation cluster as having a single well-defined position.

### 4.11.2 Wire Denoising

The current EXO-200 resolution is limited by the scintillation resolution of the APDs. As a result, little benefit is anticipated from denoising the wires. However, it is possible that a future detector could reduce the scintillation noise to a point where resolution of the wires is non-negligible; alternatively, a future detector could have noise which is correlated between wires and APDs, making it possible to use noise information from the wires to improve our scintillation resolution even though no direct benefit is expected to the wire resolution itself.

In any case, it is possible to apply equations 4.44 to a system with a combination of wires and APDs without significant adjustment. The template functions  $Y[t]$  will of course be significantly different, and must include a time offset to account for the different time of arrival of the electrons and photons. The “lightmap” of charge will be far less diffuse than for APDs because charge from any location generally drifts directly to only a small number of wires along externally imposed field lines. And finally, because electron statistics should be negligible and pulse amplification should not be a noisy process, for wire channels we would modify equation 4.17 to

state that  $q(i_{\text{wire}}, a) = 0$ . In this sense, denoising of wires consists of minimizing the variance in the energy estimator due to electronic noise, and using the wires to improve our denoising of APDs consists of making use of correlations between wire and APD noise without expecting any correlations between APD and wire pulses, all while ensuring that the energy estimates are unbiased by retaining the same constraints.

## 4.12 Summary

We have shown in this chapter that a technique exists to produce an optimal linear energy estimate for the scintillation clusters in EXO-200 and is fully described by equations 4.64. It requires detailed knowledge of the origins of noise in APD waveforms and a full lightmap describing the scintillation yield on each channel as a function of cluster position. Chapters 5 and 6 describe aspects of how we measure electronic noise and the APD lightmap, both of which have proven to be critical inputs to denoising. We will show in section 7.6 that the result is a significant improvement in the energy resolution of EXO-200 and a corresponding increase in its sensitivity to  $\beta\beta0\nu$  decay.

# Chapter 5: Electronic Noise Measurements

As described in chapter 4, a detailed noise model is required to perform our denoising algorithm. Equation 4.5 specifies that the correlations in electronic noise are taken as inputs to denoising; in this chapter we describe the measurement of those correlations in EXO-200. Section 5.1 specifies the desired measurement; section 5.2 identifies the time-dependent behavior of noise; and section 5.3 describes the algorithm to measure noise from data. We conclude in section 5.4 with some possible future work to improve the quality of the noise measurements and their use in other aspects of the EXO-200 analysis.

## 5.1 Mathematical Framework for Noise Correlations

A waveform on channel  $i$  with no pulse on it consists entirely of a noise function  $N_i[\tau]$ . The noise is a random function: its value at each time  $\tau$  is a random variable. Our goal is to describe the joint probability distribution of those random variables. Noise on different channels is correlated, so our joint probability distribution should

describe not only the noise for all time samples  $\tau$  on a particular channel  $i$ , but also the relation between noise on any distinct pair of channels  $i$  and  $j$ .

We can guarantee that the noise is stationary (meaning that the distribution does not change over time, ie. due to a drifting baseline) because the waveforms are all subject to shaping in the front-end electronics which removes low-frequency noise components, as described in section 3.5. It is conventional to study stationary noise in Fourier space. This may lead to sharper features because noise often originates from environmental factors that demonstrate periodic behavior. In EXO-200, examples of possible sources of periodic waveform noise include acoustic noise from the cleanroom, mechanical vibrations of the various wires and cables in the TPC, or switching noise from the digital power supplies. The Fourier transform can also lead to a simpler characterization (at lowest order) of noise correlations: in a steady-state environment the second-order correlations between noise components at different frequencies is always zero because the inner product of two sinusoidal functions with different frequencies is always zero.

We write the discrete Fourier transform of  $N_i[\tau]$  as  $\tilde{N}_i[f]$ , consistent with the notation described in section 4.2. Although the specific choice of convention will not matter for any of the analysis in this work, for completeness we specify explicitly the definition of the discrete Fourier transform and its inverse as

$$\tilde{N}_i[f] = \sum_{\tau=0}^{T-1} N_i[\tau] e^{-2\pi i \tau f / T} \quad (5.1)$$

$$N_i[\tau] = \frac{1}{T} \cdot \sum_{f=0}^{T-1} \tilde{N}_i[f] e^{2\pi i \tau f / T}, \quad (5.2)$$

where  $T$  is the (unitless) number of samples in the time domain waveform and the roman-font  $i$  is  $\sqrt{-1}$ . Both of these waveforms are assumed to be periodic, so we store  $N[\tau]$  with  $\tau \in [0, T)$  and  $\tilde{N}[f]$  with  $f \in [0, \lfloor \frac{T}{2} \rfloor]$ , where  $\lfloor \cdot \rfloor$  indicates that rounding is performed downward. This set of conventions matches the conventions of the real-to-complex discrete Fourier transform implemented by the popular FFTW library, which is available on all major computational platforms [125].

Our sampling frequency of 1 MHz means that we can associate  $\tilde{N}_i[f]$  with noise at a frequency of  $f/T$  MHz (where we again recall that  $T$  and  $f$  are unitless). The accuracy of this association is dependent on the accuracy of the nominal 1 MHz sampling. This is controlled by a nominal 80 MHz oscillator in the master TEM unit; preliminary investigations indicate that this frequency changes over time, and may deviate from a true 80 MHz period by as much as ten parts per million [113, 126]. Since we apply low-pass filters with a combined effective cutoff frequency around 167 kHz, as described in section 3.5, this is expected to have a negligible effect on our noise measurements.

To quantify the second moments of the noise, we have seen in equation 4.44 that it will be useful to measure expectation values of the real-valued quantities for each pair of channels  $i, j$  and each frequency index  $f$ :

$$\left\langle \tilde{N}_i^R[f] \tilde{N}_j^R[f] \right\rangle \quad (5.3a)$$

$$\left\langle \tilde{N}_i^R[f] \tilde{N}_j^I[f] \right\rangle \quad (5.3b)$$

$$\left\langle \tilde{N}_i^I[f] \tilde{N}_j^I[f] \right\rangle, \quad (5.3c)$$

where  $\tilde{N}^R$  and  $\tilde{N}^I$  denote the real and imaginary parts of the noise in Fourier space, respectively.

We can see that equations 5.3 possess some symmetries which may reduce the size of a file and permit the exploitation of faster matrix operations. First, equations 5.3a and 5.3c are symmetric under exchange of channel indices  $i$  and  $j$ , so we can store these values on disk more compactly by only storing the expectation values where  $i \leq j$ .

A second symmetry comes from the observation that for most frequencies the phase is random because a waveform trigger time is uncorrelated with the phase of any noise frequency. More specifically, we can decompose  $\tilde{N}[f]$  into a real-valued amplitude  $A[f]$  and phase  $\theta[f]$  by

$$\tilde{N}[f] = A[f]e^{\theta[f]\text{i}}. \quad (5.4)$$

The phase and amplitude cannot be correlated because the phase depends solely on where we choose to sample a waveform from the detector, whereas the amplitude at a particular frequency is constant in time. By the Nyquist-Shannon sampling theorem (see for example [127]) we can reconstruct this function unambiguously for all frequencies less than half of the sampling rate; in our case, we can reconstruct perfectly all parameters for  $f < T/2$ . This means that in a waveform with odd-valued  $T$  we can perfectly reconstruct all components, and in a waveform with even-valued  $T$  we can perfectly reconstruct all components except  $f = T/2$ .

For the frequency  $f = T/2$  in an even-length time-domain waveform, we cope

with the ambiguous reconstruction of  $A[T/2]$  and  $\theta[T/2]$  by asserting that  $\theta[T/2]$  is zero, so that the last Fourier coefficient is strictly real-valued; this comes automatically from equation 5.1. Additionally, for the zero-frequency component  $\theta[0] = 0$  is enforced by the fact that  $N[\tau]$  is real-valued. In all other frequency components, however, there is a unique choice of  $\theta[f] \in [0, 2\pi)$ , and it can have no directional preference because the time of the event trigger has no preference. Put another way, for some fixed time  $\tau_0$  it is equally likely that we sample a waveform starting at  $\tau_0$ ,  $\tau_0 + 1$ , ..., each of which would result in a different phase  $\theta[f]$ . This can also be viewed as a symmetry of the noise: if we translate the time of the waveform we sample, it has the effect of rotating the phase  $\theta[f]$ . All expectation values should be invariant under such an action.

We can then expand equation 5.3a, taking (as discussed earlier) only the phase to be random:

$$\langle \tilde{N}_i^R[f] \tilde{N}_j^R[f] \rangle = \langle A_i[f] A_j[f] \cos(\theta_i[f]) \cos(\theta_j[f]) \rangle \quad (5.5)$$

$$= \langle A_i[f] A_j[f] \rangle \cdot \frac{\langle \cos(\theta_i[f] + \theta_j[f]) + \cos(\theta_i[f] - \theta_j[f]) \rangle}{2}. \quad (5.6)$$

We can see that  $\theta_i[f] + \theta_j[f]$  is not invariant under time translation, because a small shift in time  $\delta t$  will decrease the value of a phase  $\theta_i[f]$  by  $-2\pi f \delta t / T$ ; as a result, we can assert that the left term must have an expectation value equal to zero. On the other hand,  $\theta_i[f] - \theta_j[f]$  is invariant under time translation, so that term can survive:

$$\langle \tilde{N}_i^R[f] \tilde{N}_j^R[f] \rangle = \frac{\langle A_i[f] A_j[f] \rangle}{2} \cdot \langle \cos(\theta_i[f] - \theta_j[f]) \rangle. \quad (5.7)$$

Similarly for the other expectation values:

$$\langle \tilde{N}_i^R[f] \tilde{N}_j^I[f] \rangle = \frac{\langle A_i[f] A_j[f] \rangle}{2} \cdot \langle \sin(\theta_j[f] - \theta_i[f]) \rangle \quad (5.8)$$

$$\langle \tilde{N}_i^I[f] \tilde{N}_j^I[f] \rangle = \frac{\langle A_i[f] A_j[f] \rangle}{2} \cdot \langle \cos(\theta_i[f] - \theta_j[f]) \rangle. \quad (5.9)$$

We can see from equations 5.7-5.9 that for frequencies other than 0 and  $T/2$ , the following identities hold:

$$\langle \tilde{N}_i^R[f] \tilde{N}_j^R[f] \rangle = \langle \tilde{N}_i^I[f] \tilde{N}_j^I[f] \rangle \quad (5.10)$$

$$\langle \tilde{N}_i^R[f] \tilde{N}_j^I[f] \rangle = -\langle \tilde{N}_j^R[f] \tilde{N}_i^I[f] \rangle. \quad (5.11)$$

Taking advantage of these symmetries, we can compute that for 71 channels and waveforms containing 2048 samples we need to store roughly five million independent values to characterize the noise correlations; this results in a file of size roughly 40 megabytes for each snapshot of the noise correlations. We show in sec-

tion 5.2 that only a small number of snapshots appear to be necessary, so this can be a manageable dataset.

## 5.2 Time Windows of Constant Noise

Section 5.1 has described the noise correlation information which denoising requires and demonstrated that a snapshot of the noise will require roughly 40 MB of data. Although EXO-200 has a significant amount of noise information available and is capable of producing a detailed history of the noise variations in time, taking such an approach would quickly produce an unmanageable quantity of data. This section explains how the noise behavior appears to be stable for long periods of time, permitting us to create a coarse-grained history of the noise without losing significant accuracy.

The approach to identifying these constant-noise time windows is two-fold. Firstly, we identify certain environmental changes which are likely to have a significant impact on the noise observed on the APDs. Since the times at which these changes occur are generally known precisely (and usually fall between runs), we can place time boundaries accurately when an environmental change is traced as the origin of a change.

Secondly, we develop a set of parameters which can easily be viewed in plots versus time. These trend plots are then reviewed qualitatively by collaboration members, and stepwise changes in any of these parameters can be interpreted as a change in detector noise at the time of the step. Although sometimes it is necessary

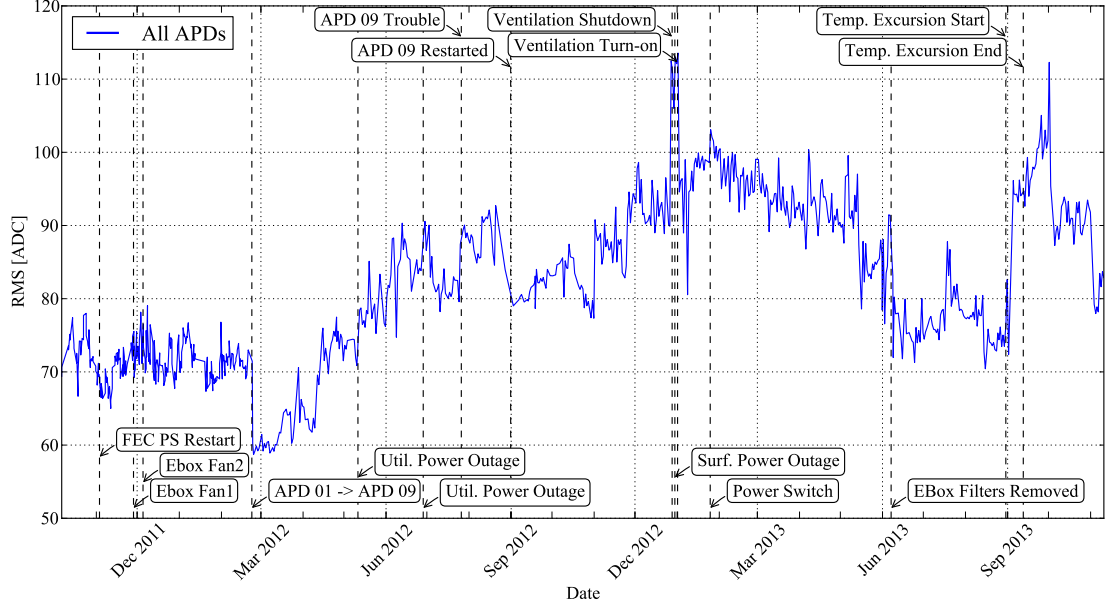


Figure 5.1: Sum noise for all APD channels measured from charge injection runs, with environmental changes indicated which may correlate with observed changes in noise. Data provided by Josiah Walton.

to guess the precise time when a change in noise occurred, when possible we review the environmental conditions of the detector in more detail and search for possible causes for the change in noise which would permit us to pinpoint the time of the change.

One source of noise information is provided from charge injection runs. These runs have been taken daily for the entire history of our dataset, and are designed to inject a known pulse half-way through the 2048-sample waveform. Since the pulse time is known, it is also generally true that the pretrace has no pulse on it and can be viewed as a pure noise sample. It is possible by coincidence for a low-background event to deposit energy which is observed as a pulse in the pretrace, but this is extremely rare.

Runs	Dates	Comments
2401-2423	9/28/2011-9/30/2011	APDs biased to special “9-28-11” settings.
2424-2690	9/30/2011-11/2/2011	FEC voltage adjustment on 11/2/2011.
2691-2852	11/2/2011-11/28/2011	Cooling fan installed on Ebox 1, 11/28/2011.
2853-2891	11/28/2011-12/4/2011	Cooling fan installed on Ebox 2, 12/4/2011.
2892-3117	12/4/2011-1/13/2012	Power outage, no data 1/13-1/19.
3118-3326	1/13/2012-2/23/2012	During runs 3314-3320 (2/22) APD channel 163 was disconnected. During runs 3324-3331 (2/23) front-end cards were swapped.
3327-3700	2/23/2012-5/11/2012	Brief power outage on 5/11.
3701-3933	5/11/2012-7/10/2012	Possibly associated with a TEM temperature spike on the morning of 7/10; cause not known.
3934-4003	7/10/2012-7/24/2012	Possibly associated with a new TEM module on 7/24.
4004-4126	7/24/2012-8/28/2012	Power outage, no data 8/28-8/30, messy recovery of APD01.
4127-4589	8/28/2012-12/27/2012	Pump reset on 12/27, but it is not clear this is the cause of the short spike in APD noise.
4590-4609	12/27/2012-1/1/2013	As mysteriously as the noise came on 12/27, it disappeared sometime between 1/1 and 1/2.
4609-4779	1/1/2013-2/20/2013	Not clear that anything happened on 2/20; we should review this boundary to ensure it is significant.
4780-5061	2/20/2013-5/14/2013	Noise on TPC2 changed sometime around 5/14-5/20. Thermal stores stopped cooling on the evening of 5/17, but it is unclear how this would impact the APDs.
5062-5197	5/14/2013-6/7/2013	Modifications to electronics boards on 6/7.
5198-5590	6/7/2013-8/31/2013	Temperature excursions in the cleanroom around 8/31 permanently impacted the APD behavior.
5591-5892	8/31/2013-11/11/2013	Differential-pressure excursion on 11/11.

Table 5.1: Recommended noise windows, based on the current understanding of changes in noise and their possible causes. This is not the same as the noise windows actually used in the present analysis; for those, please see table 5.2.

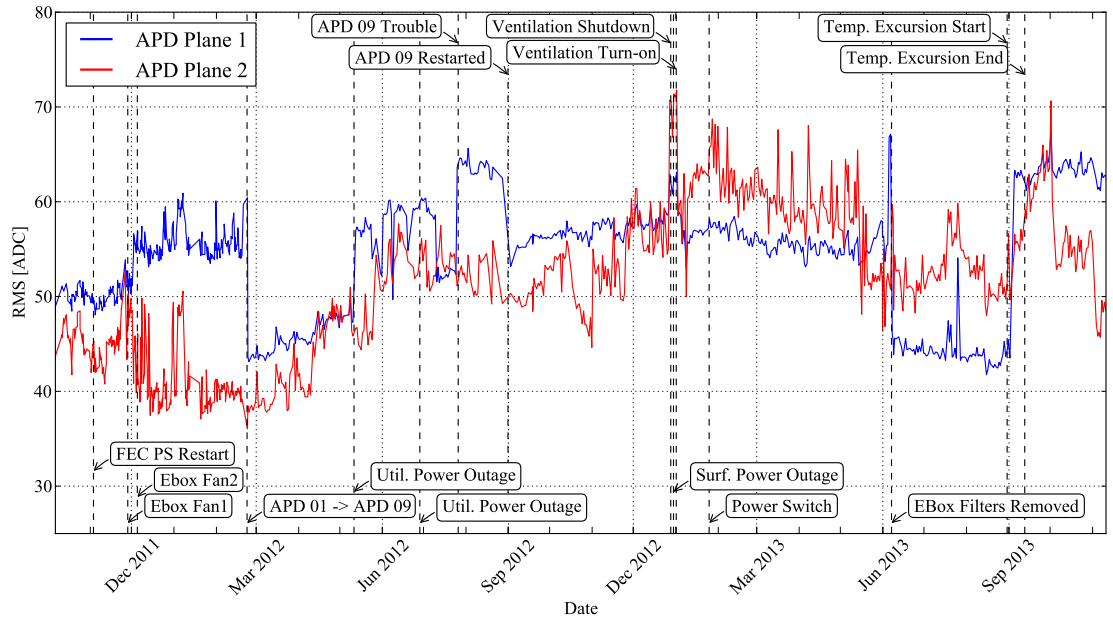


Figure 5.2: Sum noise for each APD plane measured from charge injection runs, with environmental changes indicated which may correlate with observed changes in noise. Data provided by Josiah Walton.

Runs	Dates
2401-2423	9/28/2011-9/30/2011
2424-2690	9/30/2011-11/2/2011
2691-2852	11/2/2011-11/28/2011
2853-2891	11/28/2011-12/4/2011
2892-3117	12/4/2011-1/13/2012
3118-3326	1/13/2012-2/23/2012
3327-3700	2/23/2012-5/11/2012
3701-3949	5/11/2012-7/12/2012
3950-4140	7/12/2012-9/2/2012
4141-4579	9/2/2012-12/24/2012
4580-4779	12/24/2012-2/20/2013
4780-5197	2/20/2013-6/7/2013
5198-5590	6/7/2013-8/31/2013
5591-5892	8/31/2013-11/11/2013

Table 5.2: Noise windows used for the current analysis. For the noise windows recommended for future analyses and a more detailed explanation of the causes of changes in noise behavior, see table 5.1.

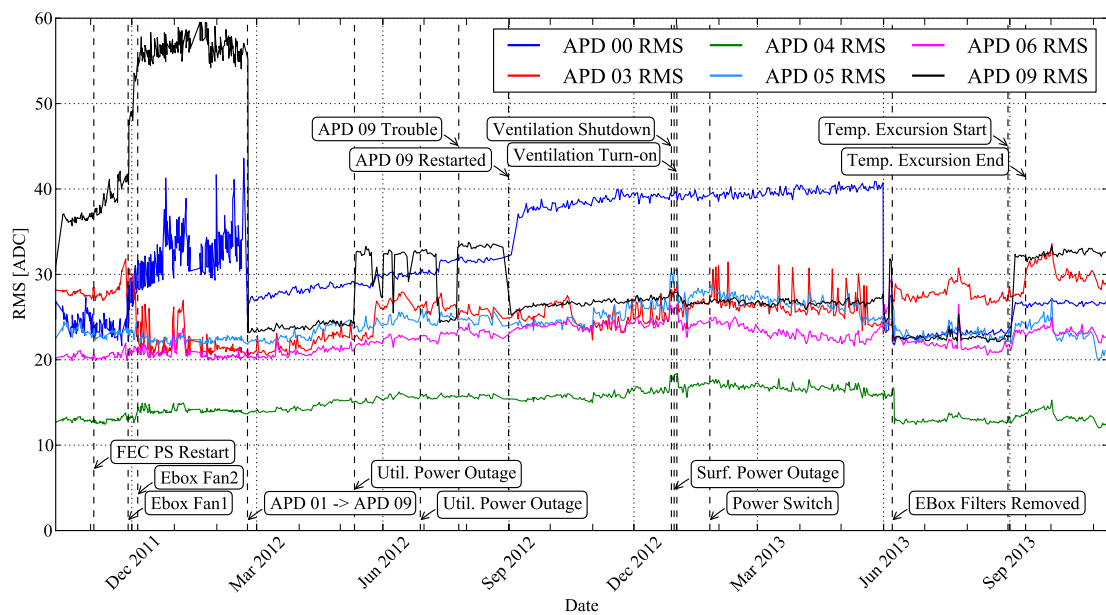


Figure 5.3: Sum noise for each APD electronics board measured from charge injection runs, with environmental changes indicated which may correlate with observed changes in noise. Data provided by Josiah Walton.

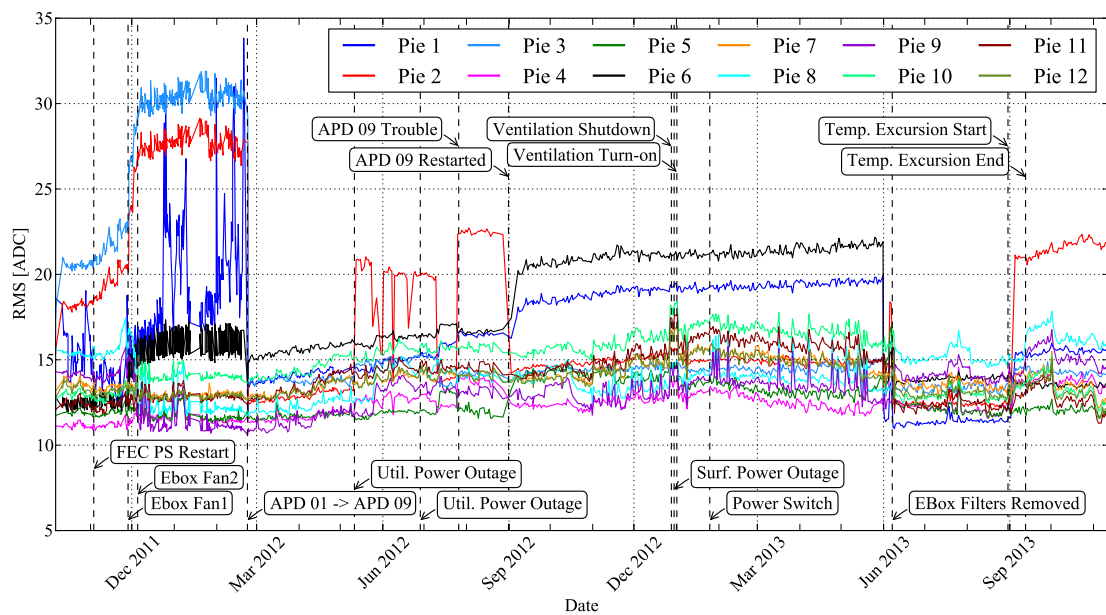


Figure 5.4: Sum noise for each APD pie (6-7 channels) measured from charge injection runs, with environmental changes indicated which may correlate with observed changes in noise. Data provided by Josiah Walton.

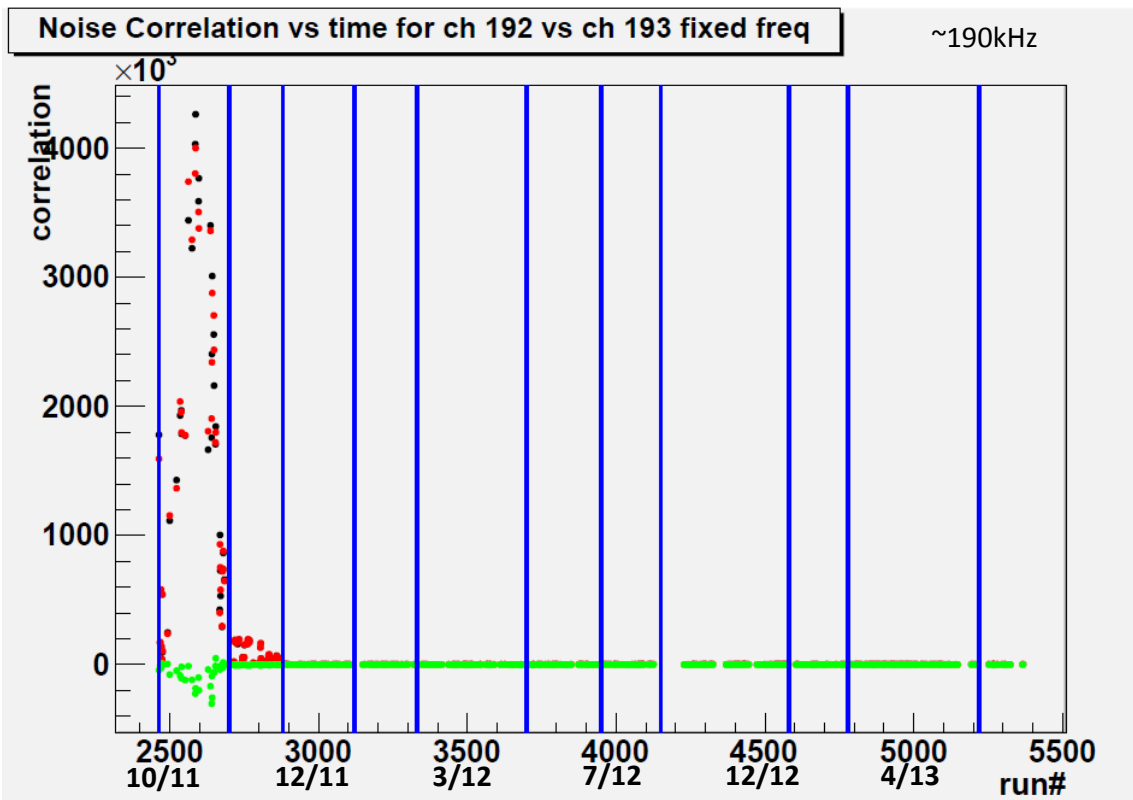


Figure 5.5: Time trend of  $\langle \tilde{N}_{192}^R[385] \tilde{N}_{193}^R[385] \rangle$  (black),  $\langle \tilde{N}_{192}^R[385] \tilde{N}_{193}^I[385] \rangle$  (green), and  $\langle \tilde{N}_{192}^I[385] \tilde{N}_{193}^I[385] \rangle$  (red) corresponding to the correlations between channels 192 and 193 at 188 kHz. Blue lines indicate tentative noise windows. This frequency is chosen because it is associated with a peak in the noise power spectrum, and the pair of channels is selected as a representative example for seeking changes in noise behavior. A restart of the front-end power supply at run 2700 is coincident with the reduction in correlated noise shown here, but the reason for this effect is not understood [128].

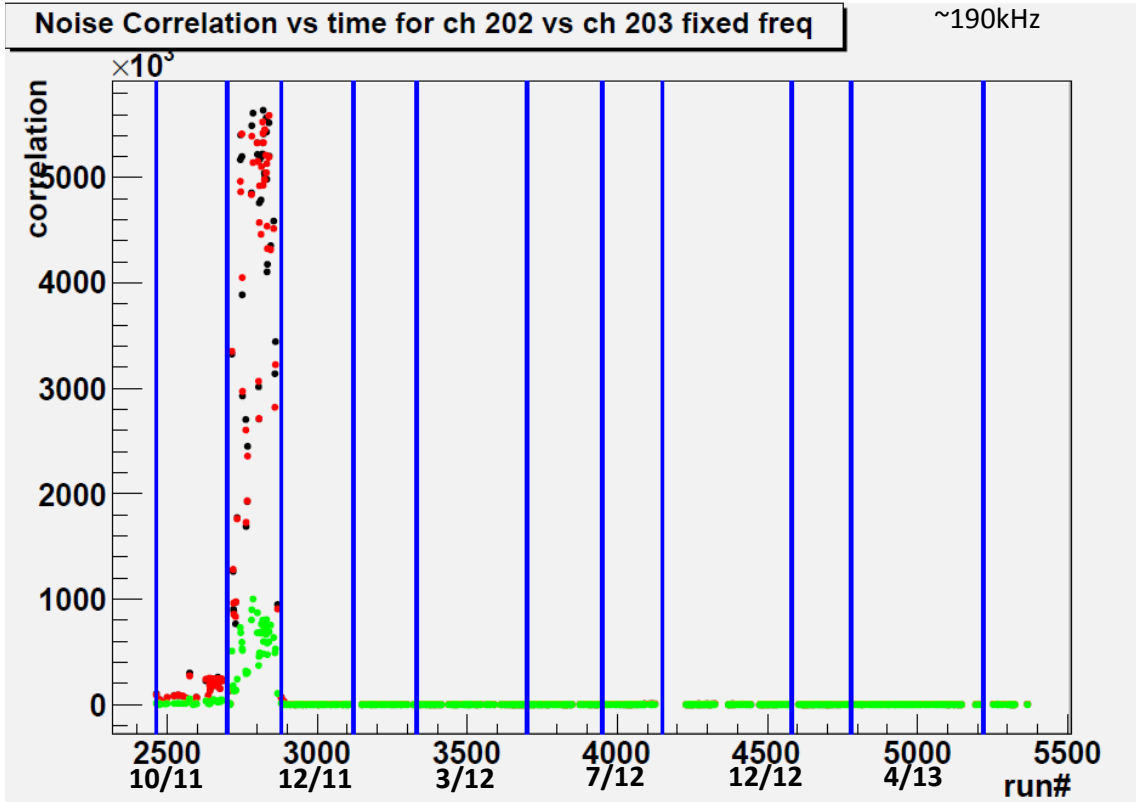


Figure 5.6: Time trend of  $\langle \tilde{N}_{202}^R[383]\tilde{N}_{203}^R[383] \rangle$  (black),  $\langle \tilde{N}_{202}^R[383]\tilde{N}_{203}^I[383] \rangle$  (green), and  $\langle \tilde{N}_{202}^I[383]\tilde{N}_{203}^I[383] \rangle$  (red) corresponding to the correlations between channels 202 and 203 at 187 kHz. Blue lines indicate tentative noise windows. This frequency is chosen because it is associated with a peak in the noise power spectrum, and the pair of channels is selected as a representative example for seeking changes in noise behavior. Installation of electronics board cooling fans is coincident with the reduction of noise around run 2900, with different installation times for different channels, but the reason this particular noise frequency is so strongly affected is not understood [128].

The approach described in [129] is to use the pretrace samples between 200 and 800  $\mu\text{s}$  from charge injection runs as noise samples. In that reference, subset of waveforms – APD pies, electronics boards, planes, or all APD channels together – are summed together for each event, and the root-mean-square variation in the summed waveform is averaged over the samples between 200 and 800  $\mu\text{s}$  and over all events in the charge injection run. Each charge injection run contains 13,200 events, all of which can be used to improve the quality of this average root-mean-square measurement of noise on that subset of channels.

Figures 5.1, 5.2, 5.3, and 5.4 show the noise for all APDs, APD planes, APD electronics boards, and APD pies respectively, with notable environmental changes overlaid to demonstrate their correlation with changes in noise. These trending plots demonstrate that although the noise undergoes day-to-day fluctuations (possibly due to insufficient sample statistics in the charge injection runs) and some gradual changes over time, the dominant effects are from stepwise changes which are generally correlated with a change in the detector environment.

Another approach to understanding the behavior of noise with respect to time is to compute noise correlations  $\langle \tilde{N}_i^R[f] \tilde{N}_j^R[f] \rangle$ ,  $\langle \tilde{N}_i^R[f] \tilde{N}_j^I[f] \rangle$ , and  $\langle \tilde{N}_i^I[f] \tilde{N}_j^I[f] \rangle$  for some particular choice of channels  $i$  and  $j$  and frequency  $f$ , and identify changes in those particular values over time. The algorithm for computing these noise correlations will be described fully in section 5.3; the philosophy is simply that it is difficult to visualize changes in a dataset of five million values, but easy to visualize changes in some very small subset of those values. Changes in the small subset are expected to indicate changes in overall noise behavior; by sampling enough choices

of  $i$ ,  $j$ , and  $f$  we can hope to identify all times when the noise behavior changed.

To guide this search, we focus our attention on known peaks in the noise power spectrum; furthermore, we focus on frequencies which have been observed to produce noise that is highly correlated across channels. One example of such a noise peak is around 190 kHz, and examples of the trending of noise correlation values are shown in figures 5.5 and 5.6. There we can see that the changes in noise correlations for a particular frequency and channel pair can be dramatic. This method of understanding our noise seems to be a powerful and sensitive approach to complement studies based on root-mean-square noise measurements described earlier.

The currently recommended noise run windows are listed in table 5.1. An attempt has also been made to identify the reasons for changes in noise behavior, but in some cases there is no clear change to the detector that is correlated with the change in noise. Future work may include combining all sources of noise trending information to obtain a more precise understanding of exactly when the behavior change occurred.

The run windows recommended in table 5.1 are recommended for future work; however, they differ in some instances from the run windows used for the present analysis. These are listed in table 5.2. In some instances the change in run range is minor and comes from a closer examination of exactly when the noise behavior changed; in others, more careful analysis revealed additional stepwise changes to the noise which had not previously been observed. The energy resolution achieved will be shown in section 7.3.4 to be fairly stable in time, so it is not believed that

the present analysis was significantly impacted by these slight variations in choice of noise run windows, but this assertion has not been quantified.

Future work can continue to improve the choice of noise run windows. One detail which is neglected in the present analysis is the selection of runs to be used within a run range. In the present analysis, all low-background runs which were used in the final dataset are also used for noise measurements. However, this may not always be ideal.

A specific example comes from runs 3321-3323, which occur after channel 163 was disconnected but before electronics boards were replaced. It is not advisable in this case for so few runs to form their own noise window because the quantity of statistics would be insufficient, but retaining them in the noise window formed by runs 3118-3326 could bias our estimates of noise on channel 163. Instead, those runs should not have been used to measure noise at all; this will be corrected in future work.

Additional studies may be necessary if denoising is extended to include the wire channels. The wire noise is generally more stable than the APD noise [129]. However, there are exceptions to this observation; one known exception comes from the Spring of 2012, when u-wire channel 16 was mistakenly dropped from data acquisition. If data prior to run 2464 is used in a future analysis, the change in u-wire electronics in early Fall 2011 would also need to be accounted for.

The most significant future work, though, simply consists of more careful study to characterize exactly when the noise behavior changed and whether slow changes in noise behavior may warrant the creation of additional time windows. These

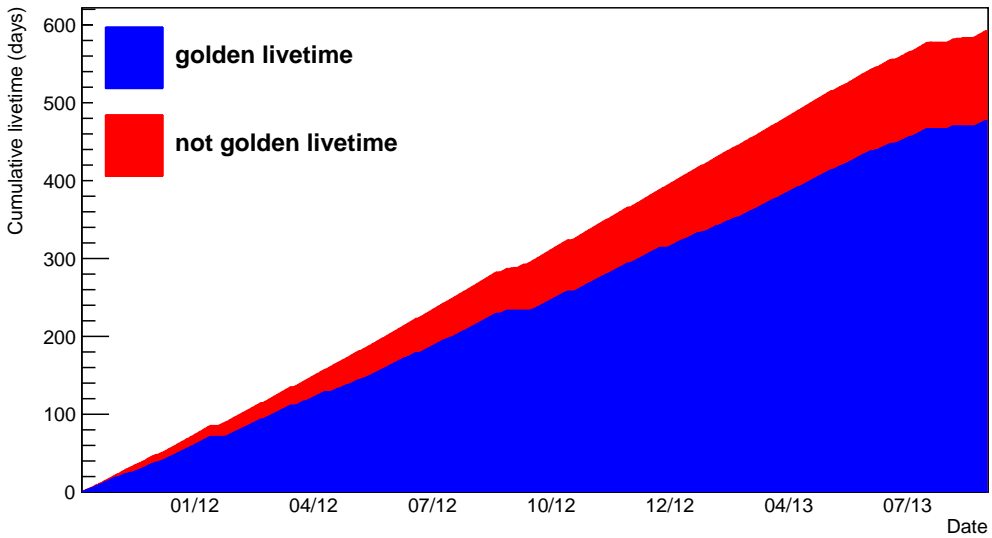


Figure 5.7: Cumulative low-background livetime collected in EXO-200.  
Figure provided by David Auty.

investigations will feed into further improvements to denoising, but they may also inform a better understanding of the noise in our detector. The current body of work already constitutes a rich set of studies performed by many collaboration members, and has enabled the use of a manageable set of noise files to characterize the whole history of our detector.

### 5.3 Algorithm for Measuring Noise

For each of the noise windows specified in table 5.2, it is necessary to locate a pool of “clean” events when no pulse occurred; these will be interpreted as samples of pure noise. This section will describe the selection cuts for clean events, followed by the data format currently used to store noise correlation information.

Although EXO-200 does occasionally take noise data, which consists of rapid requests for waveforms without any corresponding physics trigger, these runs have not been taken consistently throughout the EXO-200 dataset and will not be usable for measuring noise that changes over time. However, during all low-background data-taking it has been standard practice to force one trigger every ten seconds. These solicited triggers, though infrequent, have cumulatively amounted to an enormous quantity of data which is expected to be purely noise. Figure 5.7 shows the cumulative low-background livetime which has been collected, and we can see that it is approximately evenly distributed across the dataset and, at a rate of 0.1 Hz, millions of solicited triggers have been taken during the livetime of the detector.

The cuts we will make to select clean events are:

- Only golden-quality low-background runs (those deemed usable for final fits) will be used for noise measurements, to reduce the inclusion of anomalously noisy runs.
- Events which occur during a “bad” time (times identified as anomalous within a run, eg. due to loud noises) are excluded. Also, events occurring during the clean room siren are explicitly excluded, even though these times should generally also be marked as bad.
- Only solicited-trigger events are used; events where a physics trigger fired may contain a pulse, regardless of what is found by reconstruction.
- Truncated waveforms are not used, because they cannot provide the same set of noise frequencies as a full 2048-sample waveform.

- Waveforms which saturate in any channel are not used.
- Waveforms which are flagged as a known type of sporadic noise are excluded.
- Events on which any u-wire or APD pulse was found by reconstruction are excluded.

From the set of acceptable events produced in this way, calculation of the noise correlation values is done in exactly the way implied by the definition of our noise correlation terms. The expectation values are computed as averages over the set of events, so for example  $\langle \tilde{N}_i^R[f] \tilde{N}_j^R[f] \rangle$  is evaluated for a particular pair of channels  $i, j$  and frequency index  $f$  by computing  $\tilde{N}_i^R[f] \tilde{N}_j^R[f]$  for all acceptable events, and then using the average of these values. The symmetries of equations 5.10 and 5.11 are not currently used, but future versions of the code will exploit these symmetries to effectively double the number of independent measurements of each noise correlation.

The data are currently stored in a binary file as a sequence of eight-byte floating point numbers. Binary portability has not been a serious concern because all machines on which the files are used have a similar architecture (little-endian, IEEE floating point format). To allow studies of u-wire denoising, correlations are computed between all u-wire and APD channels, so the ordered list of channels in the file is

$$[0, 1, 2, \dots, 36, 37, 76, 77, \dots, 112, 113, 152, 153, \dots, 225]. \quad (5.12)$$

No channel mapping is included in the file, so the set of included channels must be

fixed regardless of the addition or subtraction of channels in the data (specifically, channel 163 and channel 16, both of which are only present in some of our data, and channels 178, 191, and 205, which were never active channels); these channels are included in the noise file, with noise fixed to zero where appropriate, and it is assumed that downstream software will be intelligent enough to use only those noise values which are meaningful.

The file stores noise correlations as a sequence of matrices, with one matrix for each frequency component except the baseline component  $f = 0$ . We recall from equation 4.48 that the covariance matrix of a list of random variables is defined as:

$$\text{COV}(x_1, x_2, \dots, x_n) = \begin{pmatrix} \text{cov}(x_1, x_1) & \text{cov}(x_1, x_2) & \cdots & \text{cov}(x_1, x_n) \\ \text{cov}(x_2, x_1) & \text{cov}(x_2, x_2) & \cdots & \text{cov}(x_2, x_n) \\ \vdots & \vdots & \ddots & \vdots \\ \text{cov}(x_n, x_1) & \text{cov}(x_n, x_2) & \cdots & \text{cov}(x_n, x_n) \end{pmatrix}. \quad (5.13)$$

We recall that when  $\langle x \rangle = \langle y \rangle = 0$ , the covariance of random variables  $x$  and  $y$  will be simply  $\langle xy \rangle$ ; for us, all noise coefficients with  $f > 0$  have mean zero. For frequencies  $0 < f < 1025$ , we define an ordering for the electronic noise coefficients

$$\vec{\tilde{N}}[f] = (\tilde{N}_0^R[f], \tilde{N}_1^R[f], \dots, \tilde{N}_{225}^R[f], \tilde{N}_0^I[f], \dots, \tilde{N}_{225}^I[f]) \quad (5.14)$$

where the channel index ranges over the channels listed in equation 5.12. For  $f =$

1025 the imaginary components are all identically zero, so we define

$$\vec{\tilde{N}}[1025] = \left( \tilde{N}_0^R[1025], \tilde{N}_1^R[1025], \dots, \tilde{N}_{225}^R[1025], \tilde{N}_0^I[1025], \dots, \tilde{N}_{225}^I[1025] \right). \quad (5.15)$$

Note that this is not the same as the index ordering used for computations in denoising and identified in equation 4.47; since the on-disk format outlined here will need to be read into memory anyway, and since the list of channels on disk is different from the list of channels used for denoising, this is not a technical challenge but only a point which requires careful programming.

The binary-format noise file is then the sequence  $\text{COV}\left(\vec{\tilde{N}}[1]\right)$ ,  $\text{COV}\left(\vec{\tilde{N}}[2]\right)$ , ...,  $\text{COV}\left(\vec{\tilde{N}}[1025]\right)$ , where each covariance matrix in turn is serialized to disk. No current analysis requires baseline information, so the  $f = 0$  covariance matrix is omitted. Covariance matrices are symmetric, so the matrix serialization can be viewed equally well as column-major or row-major. The matrices are all currently stored in unpacked format, meaning that no symmetries are currently exploited; future work should include specifying a more efficient packing of the noise coefficients which takes advantage of the symmetries described in section 5.1.

Besides the anticipation of a change in file format in future versions of the code, there are other improvements to this algorithm which should be pursued in the future. Some applications have been considered which would require knowledge of the noise on all channels, so the noise on v-wire channels should be recorded as well. As another means of improving the usability of these files for other applications, an independent interface to the file format should be designed. This

could perhaps be written as a wrapper around some matrix serialization library, which could simplify the conversion between packed (for storage) and unpacked (for computation) symmetric matrix formats.

The highest priority, of course, will continue to be improving the quality of the noise correlations which are calculated. Future topics for improvement are detailed in the next section.

## 5.4 Future Directions with Noise Measurement

Although the noise correlations described in this chapter have been sufficient for the present analysis, and there are no current indications that they are the limiting factor on denoising, still there are a number of possible improvements and extensions which could be investigated in future work. Here we describe possible improvements to the quality of the noise correlations, followed by possible applications outside of denoising which may benefit from the use of noise correlations described in this chapter.

The general algorithm for creating noise correlations is fairly straightforward: identify time windows of constant noise behavior, select events within a noise window which appear to be clean representations of noise, and measure the average noise correlations (pairwise products) within those clean events. However, there are potential improvements in all of these steps which may be subjects for future study.

For identifying the time windows, the current analysis is quite detailed in its attempt to correlate dramatic changes in noise behavior to known changes to the

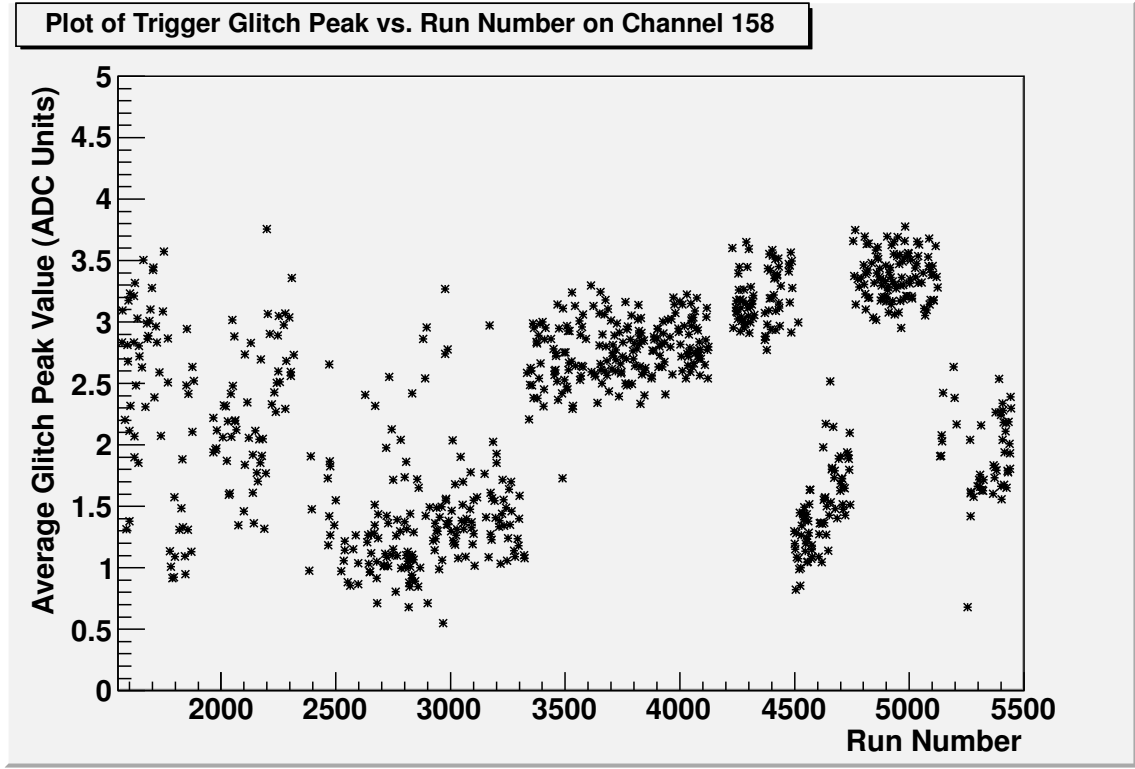


Figure 5.8: The amplitude of the TEM injected pulses (“glitch” pulses) over time for channel 158. Figure provided by Sam Homiller.

detector. However, we have only begun to understand the more gradual changes to noise; one can imagine slow changes to noise on the order of weeks or months, or daily variations due to varying temperature, and neither would be well-captured by the current methods of identifying noise windows. Combining charge injection noise and low-background noise studies should allow us to form a high-resolution map of the noise behavior over time, and it should be possible for us to understand exactly how stable the detector noise is over all time scales. This is perhaps the most pressing need for future noise analysis.

The selection of clean events is also a topic requiring further study. Although solicited triggers are treated as clean events, it has long been known that the TEM

can inject pulses into events during solicited triggers; the mechanism by which it does so is unknown. This injected pulse is correlated with the trigger time, meaning that it has a non-random phase; Sam Homiller has made a preliminary study to separate the injected pulses from noise by exploiting this property of non-random phase, and the amplitudes of these pulses over time for a particular channel are shown in figure 5.8. In the present analysis these injected pulses are assumed to be small and ignored. However, the tools to subtract the mean injected pulses have already been developed, and we should investigate:

- Do injected pulses occur with all trigger types, or only solicited triggers?
- Does subtraction of injected pulses improve the quality of the noise correlations or the results from denoising?

Finally, section 5.1 described how we neglect the possible aliasing of extremely low-frequency noise. To a first approximation this would simply be observed as a drift in the baseline of waveforms, which has no significant effect on the offline analysis (though it may have an impact on the online triggering threshold). However, a more accurate treatment may observe that low-frequency noise is aliased into the low Fourier components with  $f = 0, 1, 2, \dots$  in a way which does not accurately reflect the true noise in the detector. Such aliasing would perhaps lead to an event-by-event bias in reconstructed peak magnitudes, both from standard reconstruction and denoising. It may be possible to estimate the contribution from aliasing by looking for periodicity in the low frequency Fourier components event-by-event; noise runs (such as run 4796, a ten-minute 50-Hz solicited trigger run taken under

normal running conditions) would be a particularly good place to look for such an effect because of the higher rate of usable noise events in that data. One approach to combining many events into a single estimate of noise frequency components that extends to lower frequency could be to use a non-equispaced Fourier transform [130].

Another extension of the current work with noise correlations, related to the question of whether aliasing is a significant effect, is to study whether we can interpolate from the noise correlations of a 2048-sample waveform what the expected noise correlations for a shorter (truncated) waveform would be. Generally, it is expected that the longer a waveform is, the more information it will provide; so it should be true that a 2048-sample noise waveform provides more information than a truncated waveform provides. We would like to be able to downsample the noise correlations from a 2048-sample waveform to the expected noise correlations for a truncated waveform on this premise. However, if aliasing is a significant factor then it may be that the low-frequency aliasing observed in a 2048-sample waveform is different from the aliasing observed in a truncated waveform, and it may be that a simple interpolation of the 2048-sample noise correlations is not an accurate reflection of the noise observed on truncated waveforms. (Conversely, it may be that truncated waveforms are more vulnerable to low-frequency aliasing than 2048-sample waveforms; in this case it may be that the downsampled noise from a 2048-sample waveform is an accurate reflection of noise on the truncated waveform, but that the Fourier transform of the shorter waveform still exhibits too much aliasing to be usable.) Understanding the degree to which we can understand noise on truncated waveforms and evade low-frequency aliasing issues for truncated waveforms would

be a key step to understanding whether denoising can be extended to operate on such events.

It may also be hoped that these noise correlations will find uses beyond denoising and other signal processing applications. One example which is currently under consideration is for simulated noise. It is a general observation within EXO-200 that the noise model employed in our simulations is simple, ignoring all correlations and all noise frequency peaks which have been observed in data. For many purposes this is sufficient, but to fully model our energy threshold a more accurate model is needed. Preliminary investigations have focused on sampling noise directly from the observed waveforms and using these noise samples, as described in section 7.1.2. However, it would also be possible to use the noise correlations described in this chapter to represent our most complete understanding of the noise in the detector, and simulate noise which matches those noise correlations. This can be accomplished by computing the Cholesky decomposition of the noise correlations, viewed as a covariance matrix, as described in [131].

This chapter has described the measurement of electronic noise correlations from low-background data, with significant input from charge injection runs as well. Noise is one of the central features of the EXO-200 analysis, and understanding it in detail is a critical component to an effective denoising strategy. Thus, the result of this chapter can be understood as one of the two key inputs to denoising. The other, the APD lightmap, is described in chapter 6.

# Chapter 6: The Lightmap

EXO-200 uses a lightmap to characterize the expected scintillation pulse magnitudes from scintillation clusters with a known position and energy. Chapter 7 has shown that the lightmap is a critical input to the denoising algorithm. In this chapter, we develop from a simpler type of lightmap used in prior analysis to a fully detailed individual-APD lightmap which characterizes scintillation pulse magnitudes on every channel as they depend on scintillation cluster position. All of this is done in a time-dependent fashion, so the main result of this chapter will be, for each APD channel, a four-dimensional function of scintillation cluster position and time that yields the expected pulse magnitudes. In section 6.1 we describe the lightmap which existed prior to this work, its accomplishments, and its issues which made an upgrade necessary. Section 6.2 will present details of the production of the lightmap from empirical data; deviations from that algorithm for the present analysis are presented in section 6.4. Visualizations of the result are provided in section 6.5.

## 6.1 A History of EXO-200 Lightmaps

The EXO-200 detector has roughly 450 APDs ganged into 74 data channels of five to seven APDs each. Three of the APD ganged channels were disabled due to noisy components before physics data collection began; a fourth channel was disabled in February 2012 due to increasing noise. The APDs are set into the two endcaps of the cylindrical EXO-200 detector. To improve light collection, teflon sheets cover the inside of the detector and reflect light back into the liquid xenon rather than allowing it to be absorbed by the vessel walls.

Scintillation is not collected uniformly by all APDs. Given the same amount of energy deposited into the detector, APDs channels nearest to the deposited energy show significantly larger pulses than APD channels far from the deposit. To accurately measure the true scintillation energy, it is critical to map out the response of the APDs as a function of deposit position  $\vec{x}$ .

Furthermore, the APDs and their front-end electronics show time-dependent changes. Gains drift in each APD channel at a variety rates, and stepwise changes occur when the electronics are changed or channels are disabled. This has happened on multiple occasions during the course of the experiment. This means that, in addition to mapping the response of the APDs as a function of deposit position  $\vec{x}$ , we must also map it as a function of time. We call this the lightmap.

Earlier lightmaps were derived from periodic source calibration campaigns collected over one or more days. The “strong” thorium-228 source (34.04 kBq, or

$0.9201 \mu\text{Ci}$ , on September 1, 2009 [132]) was used, and an on-site expert would position the source in a wide range of locations around the detector. The 2615-keV single-site gamma line of the thallium-208 (a daughter product of thorium-228, see figure 7.4) allows the pulse magnitude from a single-position mono-energetic deposit in the detector to be determined in offline analysis.

Even with such a significant quantity of source data, statistics are generally insufficient to fully characterize the lightmap with this method. The source guide tube shown in figure 3.14 does not approach near to every region of the detector; as a result, some regions are difficult to illuminate with the 2615 keV gamma line. Additionally, APD pulses on individual channels may be quite small for cluster positions which are not quite near to the APDs, compounding the problem of low statistics. To simplify the problem, pulses on the waveforms of each endcap can be summed together (without gain corrections) such that the 70 or 71 active APD channels can be treated as merely two APD sum channels. This effectively increases the size of the pulses and the signal-to-noise ratio of these waveforms. It also makes the spatial dependence of the response smoother, so that a coarser binning of the position coordinates is sufficient to characterize the response. The resulting lightmap was characterized in [98] and used in [14, 74] to perform a precision measurement of the rate of  $\beta\beta2\nu$  decay and a search for  $\beta\beta0\nu$  decay in  $^{136}\text{Xe}$ .

Although this lightmap permitted an energy resolution of 1.67% at our  $Q$ -value to be achieved in [14], it is an incomplete characterization of the APD response. For example, for  $\beta\beta0\nu$  studies we place a fiducial volume cut as close to the edges of the detector as possible, and in certain regions of the detector the scintillation pulse

Nominal Source Position	Deployment Position	Triggers
P2_nz	S2	6207613
P4_px	S5	85931937
P2_pz	S8	5395820
P4_py	S11	6775279
P4_ny	S17	5482649
Other	Other	1773128

Table 6.1: The total number of thorium triggers taken at each source position; data include only runs which were used to generate the lightmap. Nominal source position follows a code where the number is 2 for anode runs and 4 for cathode runs; the second part of the code indicates the non-zero coordinate, eg. ‘px’ means positive-x direction, ‘nz’ means negative-z direction. A diagram of the source tube is shown in figure 3.14.

is highly concentrated on a small number of channels. Summing together multiple channels is, in this case, a lossy form of compression of the data, and it is possible to extract a better energy measurement if it is avoided.

The present chapter addresses the challenges inherent with the formulation of an individual-APD lightmap. We do this primarily by a significant increase in available statistics: whereas the older lightmap used thorium data from a specific calibration campaign lasting for only a few days, we combine all thorium data that has ever been collected by the EXO-200 detector between October 5, 2011 and June 24, 2013. The total number of triggers included in this dataset are listed in table 6.1. This vast extension of the available data raises the challenge that APD behavior is time-dependent, so pulse magnitudes may not be constant throughout the dataset; we account for this with a parametrization of the lightmap which permits us to simultaneously extract this time-dependent behavior and the position-dependent light yield that is independent of time. The result is a complete characterization of light yield in EXO-200.

The denoising algorithm described in chapter 4 describes one analysis by which we can exploit knowledge of the behavior of individual APD channels; other analyses include reducing our scintillation thresholds by allowing us to search for pulses in subsets of the APDs rather than only in sums across entire endcaps. Thus, characterizing the APD yield on individual APD-gang channels is a key component of denoising and may enable additional future studies which would benefit from individual APD channel information. Section 6.2 describes the method used to extract an individual-APD lightmap.

## 6.2 Four-Dimensional Lightmap

As described above, in constructing a channel-by-channel lightmap we face two conflicting needs: we must use as much data as possible to handle the rapid spatial variation and smaller pulses which are expected, but if too much data is included then we run the risk of combining data taken when an APD or the electronics had a different gain. If we truly wish to use all available data, then we must simultaneously understand the full time-dependence of the gain. In other words, rather than forming a small number of independently-measured three-dimensional lightmaps, we instead measure a four-dimensional lightmap  $L(\vec{x}, t)$ . Since we use thorium-228 source data to generate the lightmap, we require that our lightmap should predict the magnitude of the pulses on each APD gang induced by a single-site deposit of energy 2615 keV. Figure 4.4 shows our definition of a unit-magnitude pulse.

This may at first seem infeasible. After all, adding an extra time dimension

to the arguments of the lightmap is equivalent to generating a new lightmap for every time bin, which is exactly the situation we wish to avoid. But we can make a simplifying assumption that the lightmap is separable. In a physical sense, we assume that:

1. From a given position  $\vec{x}$ , photons deposit on each APD channel at a constant rate.
2. Each APD channel amplifies and shapes its pulse with a gain which may vary in time, but does not depend on the point of origin of the photons.

So, we demand that the lightmap have the much simpler form

$$L(\vec{x}, t) = R(\vec{x})S(t) \quad (6.1)$$

Although this is a reasonable approximation, there are details which are omitted by this model. Since the electric field and the reflectivity of detector surfaces are constant in time, assumption 1 is likely to be valid.

However, assumption 2 may not hold in certain cases. For example, each channel draws its pulse from multiple APDs, each of which has an independent time-varying gain. Photons from a deposit may preferentially sample the gain from the closest APD within a channel, so deposits in different locations may track more closely the gain of the closest APD within a channel. A study of the impact of this effect is a topic for future study. The analysis presented here will treat it as a small effect.

One simple scheme to find  $R$  and  $S$  iteratively is described in algorithm 2. Step 1 of that algorithm is to select 2615-keV single-site events; it is understood that some compton-scattered events will inevitably leak into our selection window, but we use the best available energy measurements to minimize that likelihood. As analysis improvements continue to improve the energy resolution, the number of selected compton-scattered events will become smaller and the quality of the lightmap will improve. The rest of the algorithm describes how we can efficiently converge on estimates of  $R(\vec{x})$  and  $S(t)$  through an iterative approach. We do not prove that the algorithm is guaranteed to converge; however, in practice  $S(t)$  is almost constant, resulting in fairly rapid convergence.

---

**Algorithm 2** Generating a Lightmap

---

- 1: Tabulate, using the best energy measurement available, a list of single-site 2615-keV events from thorium-228 source data.
  - 2: Set  $S(t) = 1$  for all APD channels.
  - 3: **repeat**
  - 4:     For each APD channel, estimate  $R(\vec{x}) = L(\vec{x}, t)/S(t)$  from the set of events tabulated in line 1.
  - 5:     For each APD channel, estimate  $S(t) = L(\vec{x}, t)/R(\vec{x})$  from the set of events tabulated in line 1.
  - 6: **until** convergence is reached.
- 

### 6.3 Algorithm Details

The previous section outlines a general algorithm for computing a four-dimensional channel-by-channel lightmap from source data. In this section we specify the implementation choices which are made in the code currently in use by EXO-200. In attempt to encourage future experimentation, alternative options will also be listed

in some detail, along with some motivations for these alternatives. Time has not permitted testing of all of these options, but it is hoped that they will be explored in the future.

### 6.3.1 Event Selection

The single-site thorium-228 spectrum is well-peaked at 2615 keV, making it an excellent monoenergetic calibration line. Our challenge is to select truly 2615-keV events as efficiently as possible, while simultaneously avoiding near-2615-keV events which may leak into the dataset. Any events which are not truly 2615-keV events will reduce the accuracy of our lightmap, so by ensuring that we have a clean sample of truly 2615-keV events we reduce the impact of input energy resolution on the accuracy of the lightmap.

This is inherently an iterative process. The first lightmap is constructed from events selected based on an ionization-only spectrum because no useful position-corrected scintillation measurement yet exists. The resolution of the ionization-only spectrum is relatively poor, roughly  $3.5\%$  (sigma) of the energy, as described in [98], and compromises are made to keep the Compton-shoulder leakage to acceptable levels. [98] required events to have ionization between  $+0.33\sigma$  and  $+3\sigma$  of the ionization peak.

Such a strongly asymmetric cut is chosen to avoid leakage from compton shoulder events. However, because of the anticorrelation between scintillation and ionization, events whose ionization fluctuates high preferentially selects events whose

scintillation fluctuates low, introducing a bias in the pulse magnitude. Additionally, the cut accepts less than 37% of good events, which is a substantial loss of event statistics. This has a significant impact in certain low-statistics regions of the detector.

The current work benefits from this existing position-corrected scintillation measurement of [98], leading to a rotated energy spectrum with resolution of roughly 1.8%. As a result, it is possible to accept more events while still keeping Compton shoulder leakage small. We currently accept events within  $2\sigma$  of the peak, with better than 95% acceptance and only small leakage. An additional benefit is that the improved energy resolution allows us to use a symmetric acceptance region, avoiding the implicit bias introduced from the earlier asymmetric cut window.

Preliminary investigations have been conducted to see the impact of using the denoised scintillation measurements which are the subject of this work in the event selection itself. Presently the improvement in resolution (to 1.53%) has not demonstrated any significant improvement in the quality of the next iteration of the lightmap beyond what we can achieve with 1.8% resolution, suggesting that energy resolution is no longer an important factor in event selection. This is a topic of continuing study.

Beyond the cuts described above (single-site within an appropriate energy window), other basic cuts are applied to ensure only well-behaved scintillation pulses are selected (where we emphasize that all scintillation cuts are with reference to the old reconstruction scale, which was not normalized):

- Charge and light must individually lie within a reasonable range: charge must lie between 1 and 5000 uncalibrated keV, and light must lie between 1 and 15000 counts in the old scintillation reconstruction scale.
- The charge-to-light ratio must not identify an event as an alpha decay: the light counts  $L$  and charge counts  $C$  must obey the relation  $L < 3.405 \cdot C + 2600.67$ .
- The scintillation time must be well-separated from any other scintillation clusters in same event frame: a scintillation cluster is only acceptable if no other scintillation clusters occur within  $220 \mu\text{s}$  before or  $180 \mu\text{s}$  after it.
- All charge clusters which are assigned to this scintillation cluster must be assigned unambiguously: for each charge cluster assigned to this scintillation cluster, there can be no other scintillation cluster occurring within  $140 \mu\text{s}$  before or  $5 \mu\text{s}$  after it.
- All three position coordinates of the charge deposit must be reconstructed. (No fiducial cut is placed, since that would restrict the volume where the lightmap is specified.)

Many of these cuts are probably unnecessary. As the energy resolution has improved, the chances of Compton-shoulder contamination have decreased. Note that our  $\beta\beta0\nu$  decay search analysis only accepts events with a single scintillation cluster, a requirement which would carry a high cost in lost statistics for determination of the lightmap. (Strong thorium runs (34.04 kBq, or 0.9201  $\mu\text{Ci}$ , on September 1,

2009 [132]) produce a significant rate of events with multiple scintillation clusters in a single 2 ms event frame. These statistics are quite valuable, particularly because they are the primary source of events in some poorly illuminated regions of the detector.)

### 6.3.2 Function Parametrization

Because we are attempting to empirically measure the functions  $R(\vec{x})$  and  $S(t)$  from a finite dataset, we must specify some more limited form for them to take. All current approaches to describing  $R(\vec{x})$  first bin the detector volume into three-dimensional voxels, and then define  $R(\vec{x})$  to interpolate linearly between known values at the center of the voxels. The size of these voxels must be chosen with some care; if they are too small, then low per-voxel statistics cause the statistical errors on the pulse magnitude to dominate, whereas if the voxels are too large then the spatial variation of the lightmap is not fully captured.

In the current lightmap, the detector is binned into  $1 \text{ cm}^3$  voxels; the detector is easily contained within a box with sides 40 cm long, leading to 64,000 voxels (of which roughly 20% lie outside of the detector and will be empty). The choice of voxel size was made based on the size of an individual APD, which is roughly 2.5 cm in diameter. Near the anode we would like for the size of a voxel to be much smaller than 2.5 cm. When  $1 \text{ cm}^3$  voxels are used, much of the detector has sufficient statistics per voxel; however, there are some regions of the detector with fewer than ten hits per voxel, indicating that  $R(\vec{x})$  may have quite significant statistical error

in these regions.

It is possible to justify a choice of larger voxels. The APDs lie at  $\pm 204$  mm from the cathode, which means that there is more than 2 cm between our fiducial volume and the APDs. At this distance, the dependence of the lightmap on  $x$  and  $y$  is expected to be much slower than at the APD plane, indicating that perhaps 2 cm binning in  $x$  and  $y$  may be sufficient. Additionally,  $z$ -dependence of the lightmap is expected to be fairly smooth throughout the detector. Since we interpolate linearly between voxels, it may be possible to use a  $z$ -binning much coarser than 1 cm. This is a topic for future investigation.

It is also worth mentioning that alternative voxel geometries have been tried in the past. The older APD-plane lightmap [98] used a cylindrical-coordinate binning. Binning in  $r$  was selected to make the bin volumes roughly constant along the  $r$  axis, binning in the angular coordinate was uniform, and binning in  $z$  was chosen to be coarser near the anodes and finer near the cathode to reflect faster variation there. In all cases the binning was coarser than with the current cubic voxels being used. Our finer binning is made possible by the larger quantity of available statistics from combining the full set of thorium source data, and is justified by the potential for the yield on a single APD gang to vary more rapidly than the yield averaged across an entire APD plane.

It is well-known [133] that when it is necessary to estimate a multivariate function from limited statistics, a choice of binning can have a significant impact on the result. It is preferable to use an unbinned technique such as kernel regression. In particular, our data density is highly non-uniform, and it should be possible to

measure the lightmap with high fidelity in regions of high statistics, while smoothly transitioning to a coarser interpolation in regions of low statistics to minimize the impact of uncertainty from individual hits. State-of-the-art solutions to this problem would rely on locally adaptive kernel regression; see [133] for a detailed explanation of the related issues in non-parametric multivariate regression. Attempting to use a locally adaptive kernel regression for  $R(\vec{x})$  should be considered a highly appealing extension to the algorithm described here for generating a lightmap.

The parametrization of  $S(t)$  presents a very different set of choices. Thorium data is taken in bursts, with the time between mostly filled by low-background runtime. When we choose to treat  $S(t)$  as a smoothly varying function, it becomes critical to interpolate properly – after all, the low-background runtime is the critical part of the experiment. (If we only produce a lightmap accurate during source calibration runtime, we will measure an energy resolution from source data which is not borne out in the low-background data, so we should in fact be able to give some guarantee that  $S(t)$  is almost as accurate during the low-background runtime as during the source runtime.) Fortunately, it is generally true that the time variation of the APD response is quite slow; exceptions are generally due to changes in the electronics which occur at well-specified times.

Currently each source run is treated as a burst of data taken at the midpoint of the run, and  $S(t)$  is measured at that point only from the data of that run; then  $S(t)$  is linearly interpolated between those points. In principle it is possible that between two source runs an electronics change may have been performed, which would mean that a better interpolation would be to assume  $S(t)$  is flat except for a step at the

time of the electronics change; in practice, though, EXO-200 has generally taken a source run immediately before and after an electronics change, so no high-value data is taken during that interval and this detail can be ignored.

Another concern with this method is the treatment of short source runs. If a run is too short, then the measurement of  $S(t)$  coming from that run may have significant errors. We currently mitigate this issue by entirely throwing out all data from runs with fewer than 100 usable events. We justify this approach by claiming that even though those events might in principle have contributed some useful information on  $R(\vec{x})$ , without a good measurement of the relevant  $S(t)$  it is impossible to use that data.

In the future, it would be useful if instead we performed smoothed interpolations between electronics changes. This could be done in the same style as EXO's lifetime corrections, using polynomial fits, where the degree of the polynomial could be determined by eye. A candidate set of time intervals when  $S(t)$  might be treated as constant could be the same as the set of constant noise windows described in chapter 5. It would be possible to check whether this time binning is fine enough by looking at the thorium scintillation peak position versus time in denoised data – if it appears to drift in time within a window where  $S(t)$  is treated as constant, then it is likely that  $S(t)$  needs to be binned more finely.

Alternatively, often there is a long string of consecutive source runs which should be combined into one higher-statistics dataset. This process must be done by hand, and has not been performed for the current analysis, but it could benefit the accuracy of the  $S(t)$  function and also recover some statistics in cases where the

individual runs might be too short for inclusion in the lightmap dataset.

The choice of binning or parametrization for  $R(\vec{x})$  and  $S(t)$  can have a profound impact on the accuracy of the lightmap, and the current analysis has only skimmed the surface of the various options. It is hoped that further work on the lightmap will include significant investigation in these topics.

### 6.3.3 Convergence and Error Estimation

Our treatment of the convergence of algorithm 2 and the resulting statistical errors in  $L(\vec{x}, t)$  is rudimentary. Cronvergence is checked not by analysis of the lightmap itself, but by verifying that the energy resolution from denoising is not improved by further iterations through algorithm 2. Lightmap errors do not directly enter into the calculations of denoising (which treats the lightmap as perfectly known), so they are not estimated at all in the current analysis.

As a proxy for estimation of the statistical errors in the lightmap, we instead study the number of hits observed in each position voxel of the detector (see section 6.5), and presume that the most significant source of error comes from low-statistics regions of the detector. This information can motivate future data-taking campaigns to probe the light response in those regions of the detector and reduce these uncertainties. However, no explicit estimation of the lightmap uncertainty has been attempted.

One difficulty with estimating the errors in the lightmap function  $L(\vec{x}, t)$  comes from the correlation between errors in  $R(\vec{x})$  and  $S(t)$ . If one of those two compo-

nents were known perfectly, then we could treat the fit uncertainties of each hit as independent errors, and propagate those errors into an uncertainty for each voxel of  $R(\vec{x})$  (if  $S(t)$  is assumed to be perfectly known) or  $S(t)$  (if  $R(\vec{x})$  is assumed to be perfectly known). But on the contrary, all of the measurements of  $R(\vec{x})$  are correlated with all of the measurements of  $S(t)$ , meaning that even the errors of different voxels of  $R(\vec{x})$  or different times in  $S(t)$  are correlated with each other. Fully characterizing these errors would require a significant effort and computation.

Although a full estimate of lightmap errors with correlations would probably be computationally quite intensive to produce, it might be possible to estimate the independent errors of each voxel of the position lightmap  $R(\vec{x})$  or each independent run making up  $S(t)$  by treating the other function as perfectly known, as described above. This would generally produce an underestimate of the uncertainty in each, but the estimate might still give some benefit.

To produce a more accurate estimate of errors, it would probably be necessary to do a simultaneous fit by varying both  $R(\vec{x})$  and  $S(t)$  together. In the current scheme,  $R(\vec{x})$  contains far more complexity than  $S(t)$  with roughly 50,000 non-empty voxels, so for each APD gang we would need to simultaneously vary roughly 50,000 parameters to obtain the optimal lightmap. It is exactly this time-intensive process which was avoided by choosing the iterative approach for measuring the lightmap; however, it would only need to be performed occasionally when deriving a new lightmap, so it is not infeasible to imagine attempting this project. The prospect of feeding in a high-quality guess obtained from the iterative method presents an additional significant time-saver. This method would not fully account for the cor-

relations between errors of the different voxels of  $R(\vec{x})$  or runs in  $S(t)$ , but it would come closer than the naive method described earlier.

However, it is also possible that identifying the error of each voxel or run is heading down the wrong path. As described earlier, it is likely that the optimal (lowest-error) method for estimating the lightmap will be an unbinned method such as a locally-adaptive kernel regression method. Error estimation in kernel regression presents significant additional challenges compared to errors from binned parametrizations. At present, I am not aware of any simple scheme to manage this difficulty, meaning that there may be a paradoxical tradeoff that using the best method for minimizing lightmap errors simultaneously makes those errors infeasible to estimate.

Note that under the iterative method, the most naive method for estimating errors is not valid. It might appear that when  $S(t)$  is initialized to a constant value of 1, we could also assign to it some constant error. Then when we compute  $R(\vec{x})$ , we could propagate independent errors from the fit uncertainties of pulses and from  $S(t)$ ; and when we compute  $S(t)$  we could propagate independent errors from the fit uncertainties and from  $R(\vec{x})$ ; and so forth. However, such a scheme provides no compensating feedback mechanism to force the iterated errors to a reasonable or accurate value, so there is no reason to believe the errors from such a system (if, that is, they converge at all). This difficulty may underscore the fundamental challenge associated with measuring the lightmap errors within our scheme – iterative methods are well-suited to solving a system, but when correlated errors are mistreated as uncorrelated an iterative method can easily magnify the

impact of that mistreatment.

On the topic of convergence, it has been mentioned already that by starting with a generally accurate initial guess for  $S(t)$  as constant, the iterative solution method tends to converge rapidly. As a result, and because iterations take only a few hours to perform on a single machine, we currently perform three iterations and claim that convergence is approximately reached. Ideally, we would require that none of the position voxels or runs change value within an iteration by more than some fraction of their estimated errors; but in the absence of estimated errors, this is of course impossible.

It would be possible, in a conservative approach, to require each value to converge to some small fraction of an ADC unit, ensuring that the convergence is better than our ability to measure pulses. Such a requirement might force us to compute more iterations than are truly warranted by our lightmap errors, but given the reasonable speed of each iteration, such a method still might not be unreasonable.

## 6.4 Implementation for this Analysis

The physics analysis which will be described in this paper includes data from EXO runs 2464 to 5597, which were taken between October 5, 2011 and September 1, 2013. However, at the time when the initial denoising processing was begun, the tentative range of runs to be used only extended up to 5367 on June 24, 2013. As a result, calibrated data at that point was only available up to June 24, 2013, and the lightmap had only been generated using the same set of thorium source data.

When the run range for the present analysis was extended, a significant portion of the dataset had already been denoised with the lightmap based only on data extending to June 24, 2013. Although the possibility of creating a new lightmap was considered, this would have required a re-analysis and re-verification of the existing denoised dataset. As a result, the existing lightmap continued to be used. The functions  $S(t)$ , which had only been directly measured up to June 24, 2013, were assumed to remain constant between June 24 and September 1, 2013; no known changes to the APDs occurred during this time, nor did any known environmental factors change, so this assumption was considered acceptable. Future lightmaps of course will make use of a more complete dataset rather than relying on extrapolation.

Furthermore, one bug was discovered in the lightmap which was used for denoising. A set of radium-226 source data was taken before the corresponding identifier could be set in data files, and as a result they were provisionally labeled as thorium runs. These runs were mistakenly incorporated into the generated lightmap, and events from the 2204-keV gamma line of the bismuth-214 daughter product of radium-226 were selected and handled as though they were legitimate 2615-keV events.

It was possible to partially remedy this after the fact: since currently there is a one-to-one relationship between individual source runs and their corresponding points in the functions  $S(t)$ , it was possible to artificially erase the data points of  $S(t)$  originating from radium runs. It is not so easy to remove the impact they may have had on  $R(\vec{x})$ . However, the radium runs were taken at a location which is extremely well-populated by thorium data throughout the life of the detector; since

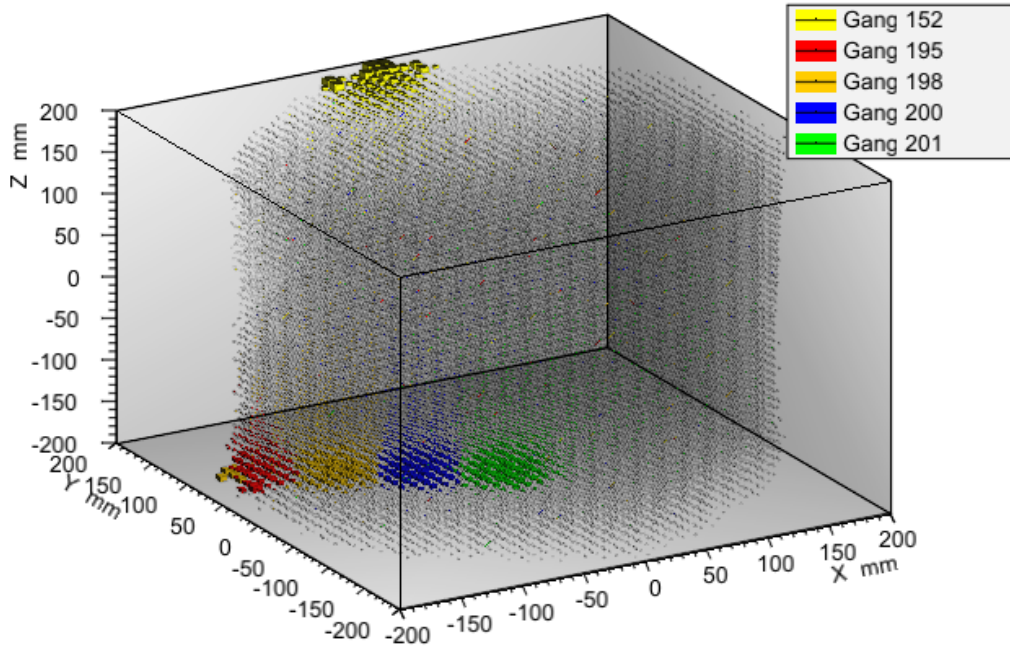


Figure 6.1: Lightmap position-dependence  $R(\vec{x})$  for selected APD gangs.

the quantity of radium data is small by comparison, the effect on  $R(\vec{x})$  is presumed to be quite small. Subsequent studies using a correctly-generated lightmap on small subsets of data indicate that the effect is indeed negligible, as expected.

## 6.5 Visualization

Although it is not strictly necessary to be able to visually inspect the lightmap for it to be useful, nevertheless it is reassuring to see that the lightmap is qualitatively similar to intuitive expectations of how light should propagate through the detector. We have chosen to store the position-dependent  $R(\vec{x})$  for each APD gang as a set of ROOT TH3D objects, and fortunately ROOT provides a number of excellent

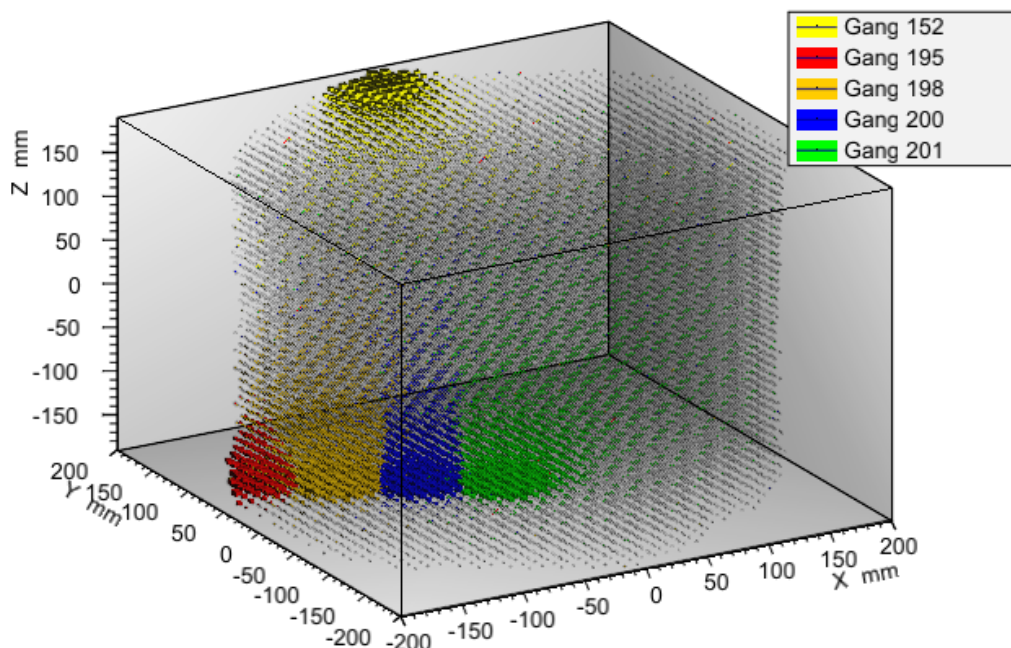
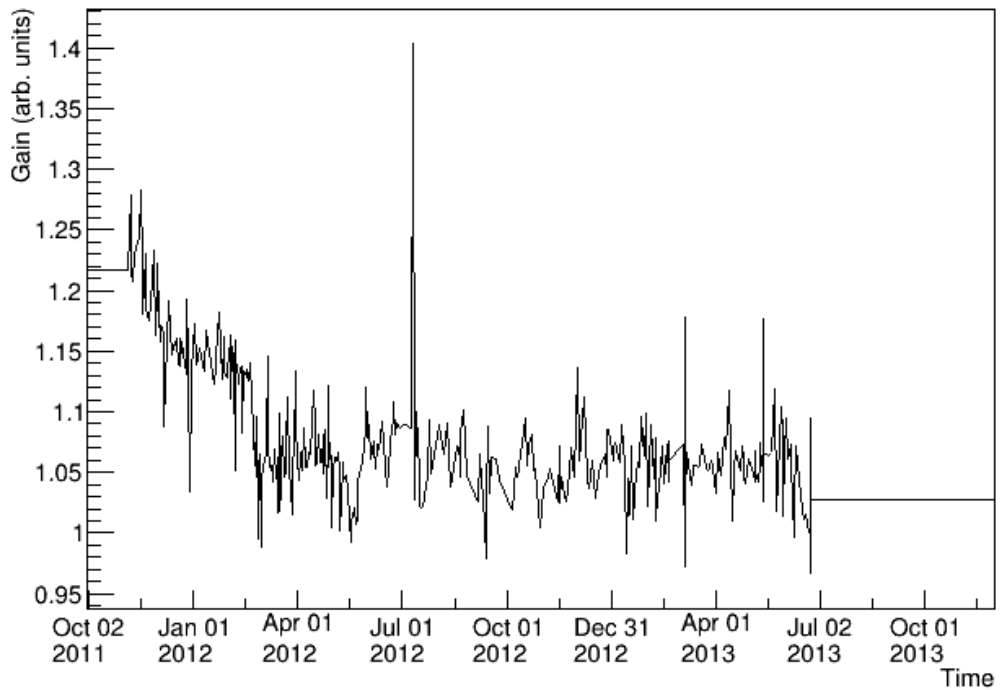


Figure 6.2: Lightmap position-dependence  $R(\vec{x})$  for selected APD gangs. Here extreme anode positions are omitted to permit better contrast for the lightmap in the fiducial volume.

Gain on Channel 152



Gain on Channel 195

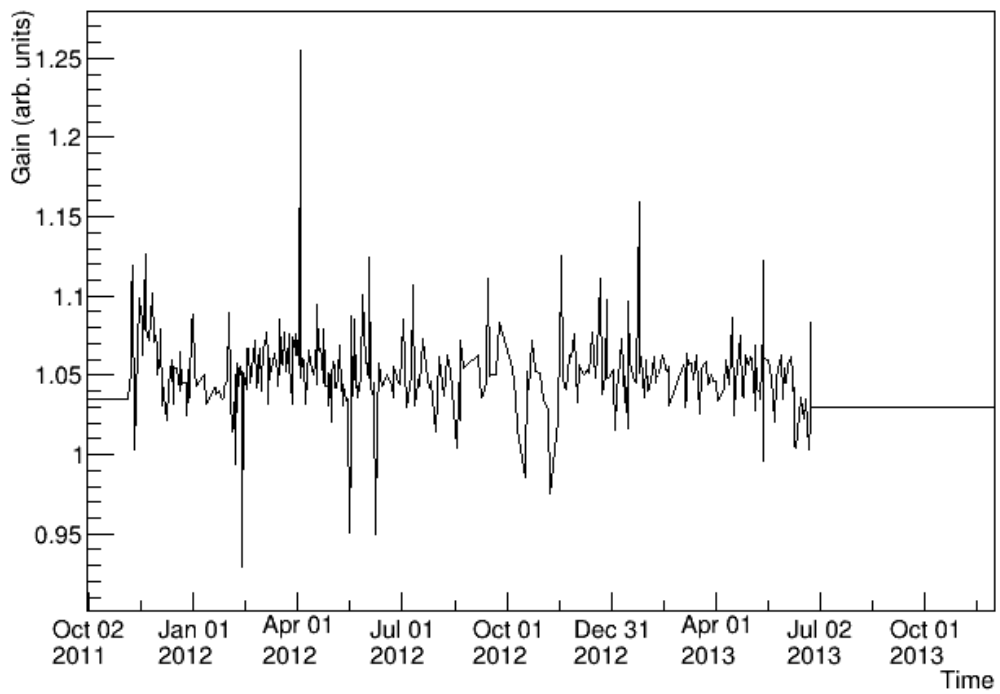
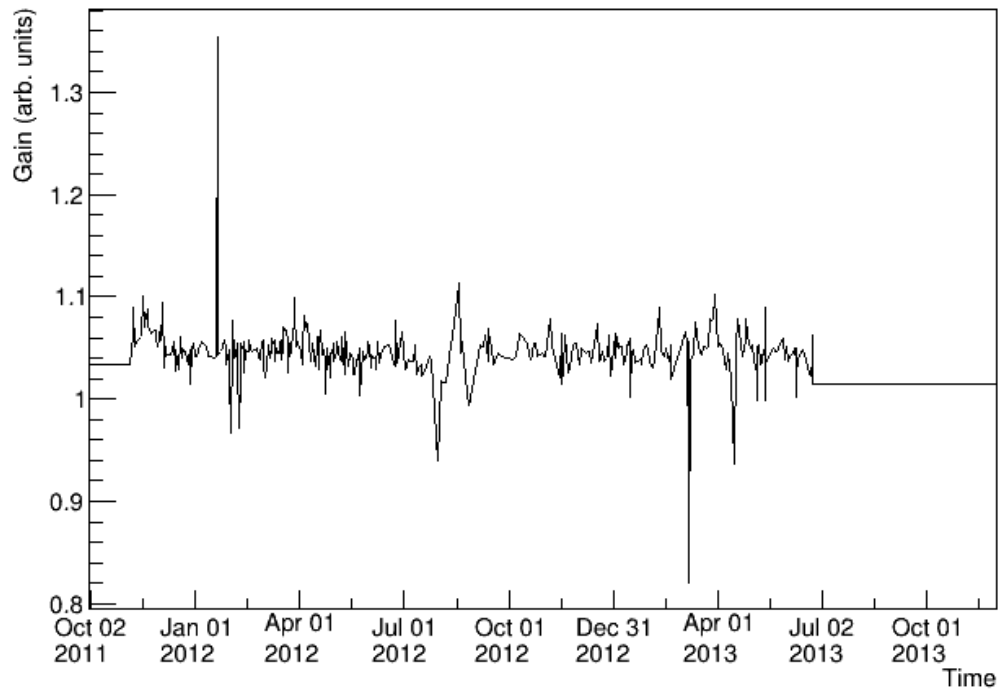


Figure 6.3: Functions  $S(t)$  for selected channels.

Gain on Channel 198



Gain on Channel 200

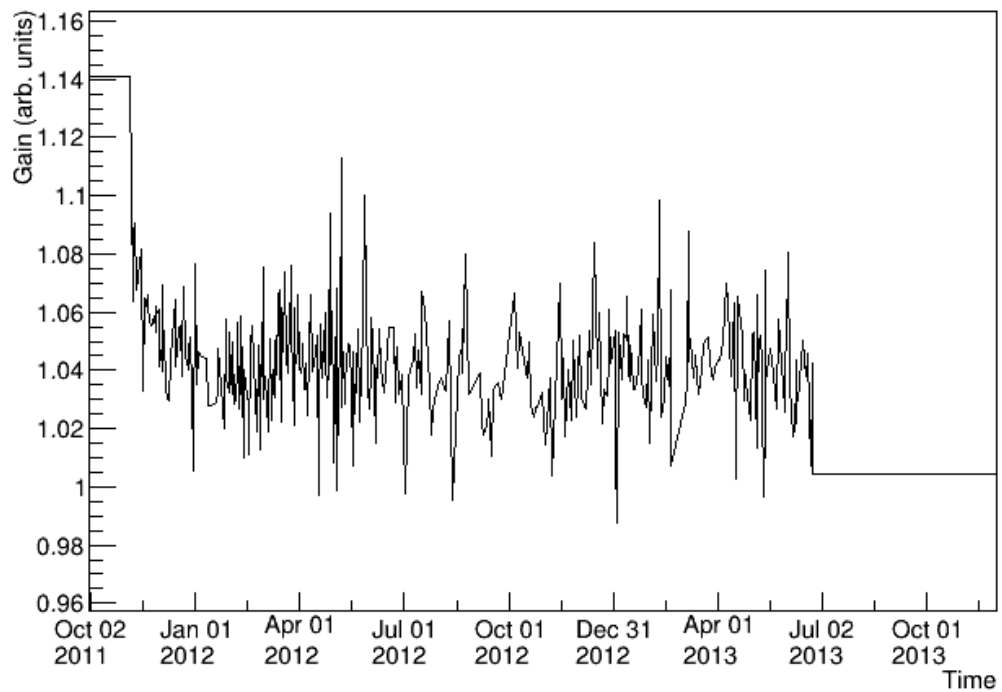


Figure 6.4: Functions  $S(t)$  for selected channels.

### Gain on Channel 201

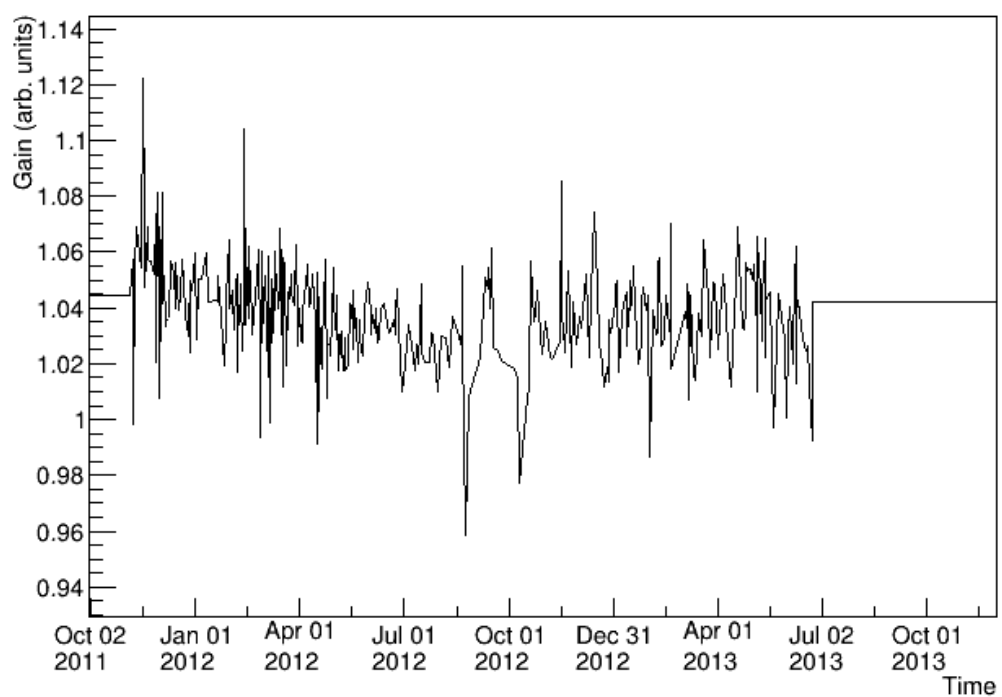


Figure 6.5: Functions  $S(t)$  for selected channels.

plotting features suitable for a three-dimensional dataset. In figure 6.1, it is possible to view the values of  $R(\vec{x})$  for a sample of gangs on top of each other. Larger boxes and denser color indicates a higher yield on the APD gang in question, and it is immediately apparent that events near the anodes produce light which is highly concentrated on a single APD gang.

Figure 6.1 shows the highest yield on the very boundary of the detector, well outside of our fiducial volume; to permit us to more easily view contrast inside of the detector, figure 6.2 shows the same map while omitting the most extreme bin near either anode. Viewing this map, we can see more interesting characteristics of the lightmap:

- Events near the anodes show a high pulse concentration on the one gang nearest to their position; however, even deep into the detector near the cathode it is still possible to see the higher concentration of pulse magnitude on the gang directly aligned with the event.
- We can also see, from gang 201 (green) in this visualization, that events can produce significant pulse magnitudes on APD gangs which are not directly aligned (in the Z direction); yield on gang 201 can be seen to decrease smoothly in all directions.
- APD gangs in the corners of the detector, such as gang 195 (red), are not effective at measuring light from events which are far away; even directly above gang 195, it is clear that gang 198 is more effective at collecting light farther away than about five to ten centimeters. This can be attributed to the

reflection of photons by teflon, which may enhance the light yield on gangs which are not hidden in corners.

Figures 6.3, 6.4, and 6.5 show the functions  $S(t)$  for the same sample of gangs.

The vertical scale can be treated as having arbitrary units; we note that all of these functions lie roughly around 1, which is attributed to the initial placement of  $S(t) = 1$  in algorithm 2. We draw the following primary observations from these plots:

- Many of the gangs show their values of  $S(t)$  decreasing rapidly up to around February 2012; some of the gangs also show a sharp decrease in value at that point. The decrease in gain corresponds with observations which were made at the time, leading to a decision to replace electronics on some APD channels on February 23, 2012. Thus, we do see “real” features from these plots.
- The functions  $S(t)$  are otherwise dominated by jitter between points, indicating that we do not collect enough statistics from each run to sufficiently constrain  $S(t)$ . This is taken as the strongest evidence that we should use a coarser time binning for  $S(t)$ , as described in section 6.3.2. Preliminary work has been performed to do this with more recent lightmaps, but no studies have evaluated the impact on energy resolution.
- Individual points on these functions may spike by as much as 40%. These points have been investigated, and their cause is not understood. These jumps, along with the overall jitter, will certainly be reduced by the use of a coarser time binning.

## 6.6 Summary

In this chapter we have described the generation of an individual-APD lightmap which characterizes the expected pulse magnitude on each APD channel as a function of scintillation origin, calendar time, and the quantity of energy. The two key steps to this process are the use of the full dataset for extra statistics and the assumption that the lightmap is separable between position and time coordinates, as shown in equation 6.1. Previous lightmaps could only characterize the light yield on large sums of waveforms; by providing a full lightmap for every channel, we enable the denoising algorithm of chapter 4 to make use of channel-by-channel pulse and noise information, so this lightmap is a key component of denoising and the improvement in resolution presented in section 7.6.

# Chapter 7: EXO-200 Analysis and Results from Denoising

The dataset used for the present work extends from October 5, 2011 to September 1, 2013 with a cumulative livetime of  $477.60 \pm 0.01$  days [89]. This chapter describes the analysis which has been applied to this livetime. Sections 7.1-7.4 describe the basic elements of the EXO-200 analysis. Section 7.5 presents the results from this set of data. In section 7.6 we compare the results obtained using the denoising scheme of chapter 4 to the results which would have been obtained without that algorithm applied and demonstrate that denoising has contributed to the strength of our physics reach.

## 7.1 Simulation

Here we describe the simulation of ionizing events in the EXO-200 detector. We begin by describing the framework for simulating the deposition of energy from primary decay particles into the liquid xenon and surrounding materials. From there, we continue to describe the simplified electric field model which permits us

to model the trajectory of ionization drifting towards the anode wires.

### 7.1.1 Simulation of Particles using GEANT

To simulate the deposition of energy from primary decay particles, version 4.9.3p02 of the GEANT software package is used [134,135]. This package includes a database containing attenuation properties of many common materials as well as detailed decay modes for most radioactive isotopes.

A model of the EXO-200 detector is simulated in GEANT with a collection of simple geometric volumes which can be composed to form more complicated structures. Simulation speed decreases as more volumes are generated, and we expect that it is unimportant to simulate fine geometrical details far away from the liquid xenon. We attempt to find a balance between accurate modeling of detailed features and simplification of distant features [111]. In figure 7.1 we see the full geometry described in GEANT, where distant objects are constructed from a small number of geometric pieces. Figure 7.2 shows how the TPC is described in GEANT, and we can see the level of detail is much greater.

To simulate particles, GEANT uses a Monte Carlo method. This means that it models decay processes as a sequence of samples from a probability distribution which are chosen using a pseudorandom number generator. The energy and direction of the emitted particle, its interaction locations and quantity of deposited energy, and the formation of secondary particles are all generated randomly as choices from a set of options with known probabilities. It is possible to override these probability

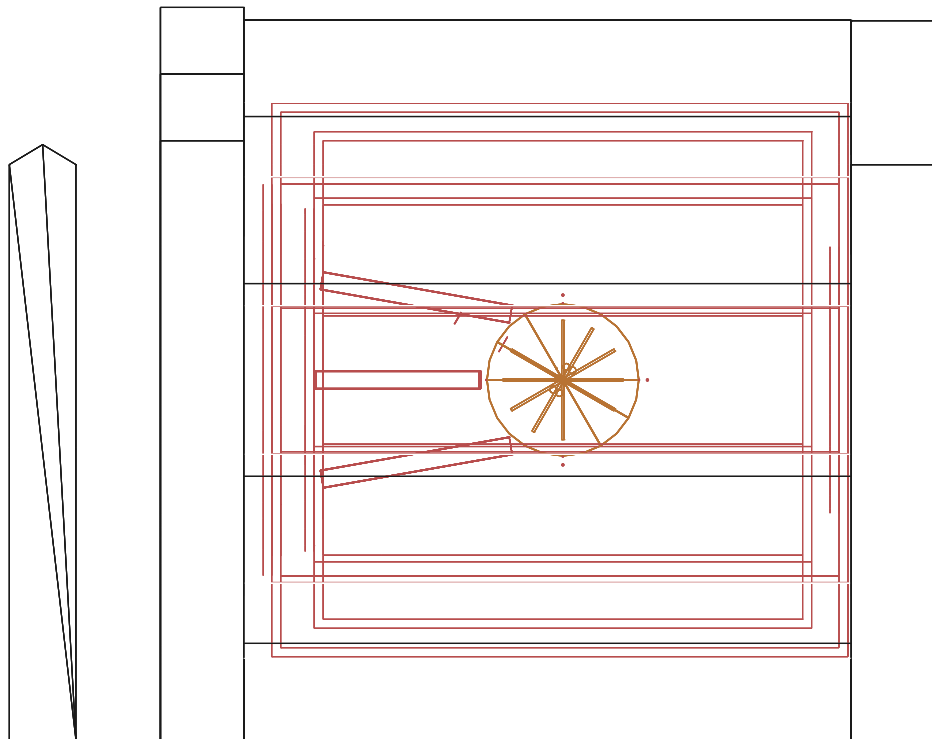


Figure 7.1: The GEANT simulation includes large-scale features of the EXO-200 detector, including the outer and inner lead wall (black), outer and inner cryostat and TPC legs (red), and the TPC itself (brown). Components are assembled from simple geometrical shapes, and distant objects are only described coarsely [111].

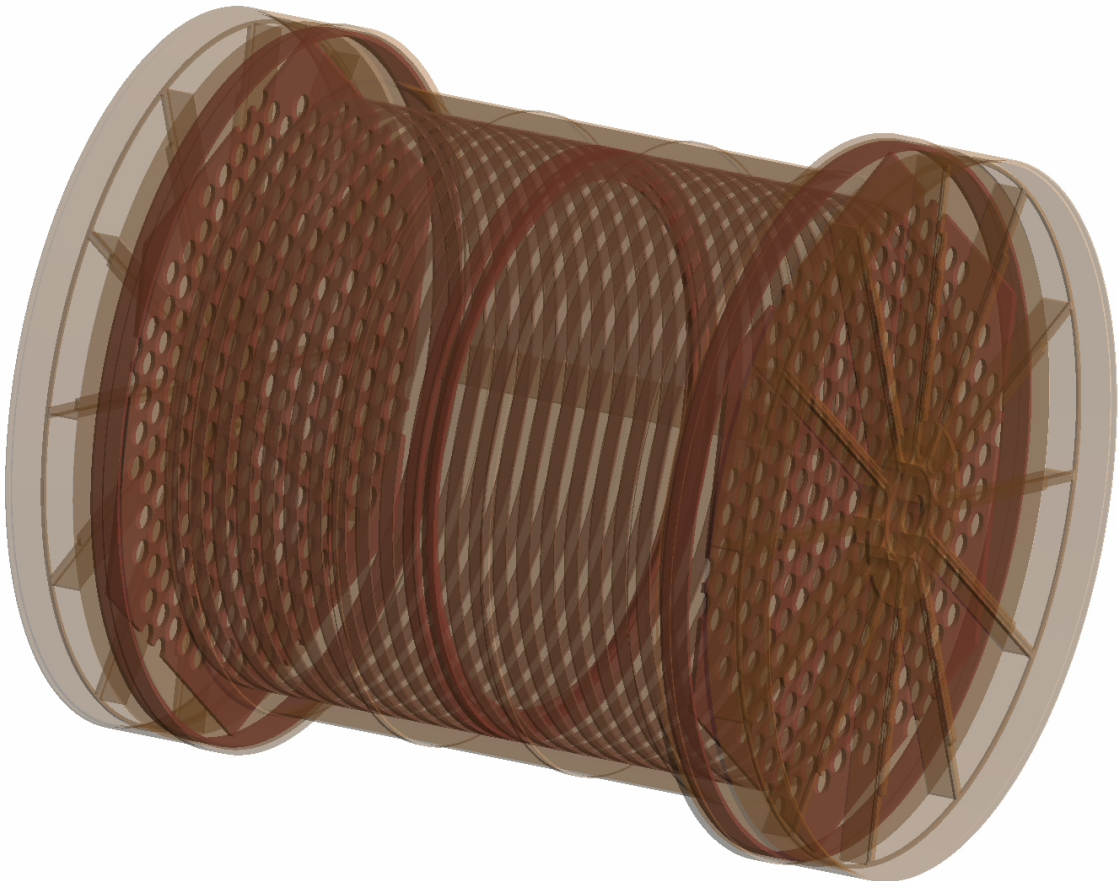


Figure 7.2: To ensure computational time is only spent on important details, detector components which are close to the liquid xenon are simulated in GEANT with greater accuracy than distant objects. The TPC contains the xenon, so it is simulated in detail [111].

distributions when necessary; for example, EXO-200 uses its own double-beta and forbidden beta decay spectra rather than the defaults provided by GEANT. Generally, though, the existing options in GEANT are suitable for simulating nuclear and electromagnetic processes [111].

Only energy which is deposited in the liquid xenon is observable. When primary decays are simulated far from the detector, it may be that most of those simulated events deposit no energy in the liquid xenon and are not observable; the simulation continues running until a sufficient number of simulated events deposit energy in the liquid xenon. This means that sources which are farther from the liquid xenon require significantly more computational time to accumulate a usable number of statistics. We find that sources outside of the HFE-7000 are subject to 4.5 attenuation lengths before reaching the liquid xenon, and events reaching the liquid xenon from the inner cryostat can only be simulated at 0.01 Hz/core by this approach [111].

To improve this rate, importance sampling is employed for distant sources. This approach consists of the following techniques to maximize the impact of limited computational time: [111, 136]

- Low-energy beta and alpha particles outside of the TPC may be “killed”, or prematurely eliminated from the simulation based on our knowledge that their attenuation length is quite short.
- The detector is surrounded by importance sampling “boundaries”: when a particle passes into a boundary it may be cloned (with a user-selected prob-

ability), where the rate of cloning is tracked by a corresponding decrease in particle “weight.”

- To avoid biasing the spectrum, it is also necessary to kill particles which pass out of a boundary with the same probability, and increase their weight accordingly.

Implicitly, importance sampling simulates the properties of particles reaching the outermost boundary; then draws samples from that distribution and simulates the properties of particles reaching the next boundary; and so forth, amplifying the impact of statistics at each stage. This also means that statistical errors in the simulated particle distributions at outer boundaries are magnified by this amplification process. For far backgrounds, though, an approach such as this is essential: simulation speeds from the inner cryostat are increased from 0.01 Hz/core to a few Hz/core, and simulations from outside the lead wall which would be wholly infeasible are made possible [111].

The result of these GEANT simulations is a measurement of the efficiency with which events from various sources reach the liquid xenon, and also of the energy and position spectra of energy deposits from these sources. Representative spectra of our primary backgrounds,  $^{238}\text{U}$  and  $^{232}\text{Th}$ , are shown in figures 7.3 and 7.4 respectively.

### 7.1.2 Digitization of Waveforms

After energy deposits are simulated using GEANT, it is necessary to model the conversion of those energy deposits into collected photons and electrons, and then

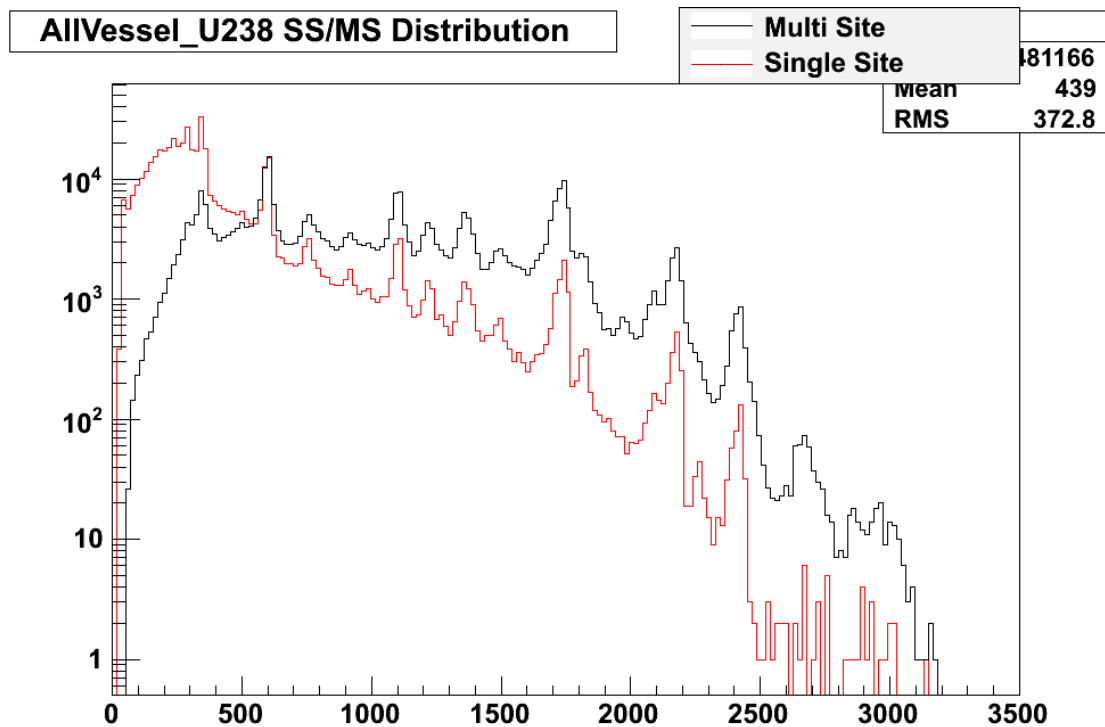


Figure 7.3: Energy spectra from  $^{238}\text{U}$  in the TPC vessel for single-site (red) and multi-site (black) events. No energy smearing is performed; peak widths are due to energy loss outside of the liquid xenon [111].

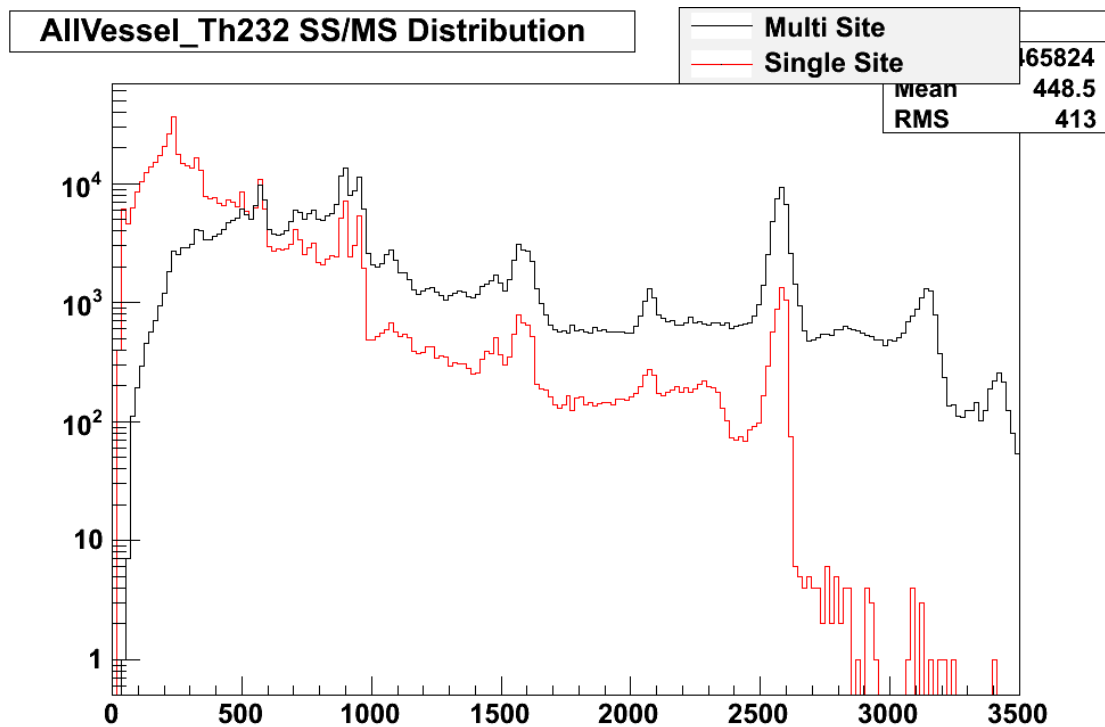


Figure 7.4: Energy spectra from  $^{232}\text{Th}$  in the TPC vessel for single-site (red) and multi-site (black) events. No energy smearing is performed; peak widths are due to energy loss outside of the liquid xenon [111].

the generation of digitized waveforms resembling the waveforms which are collected in real data.

To generate a scintillation pulse, a purely empirical model is used to estimate the relative pulse magnitudes on the north and south APD planes. This model only takes into account Z-dependence of the light collection, and does not incorporate the different light yields expected on each individual APD channel. This model is therefore rather crude, and can only be used as a rough check on the pulse-finding efficiency for scintillation as a function of energy. Attempts to track optical photons in the TPC have met with only partial success which is insufficient to justify their significant computational cost. Thus, the EXO simulations are unable to model most aspects of scintillation pulses. Section 7.4 will describe the methods used to cope with this aspect of simulation.

Simulation of charge pulses is better-understood. The detector's electric field is modeled in a two-dimensional geometry illustrated in figure 7.5 where, rather than one-dimensional wires arranged in two-dimensional planes, we have wire "points" at fixed voltage which are grouped in a one-dimensional pattern. The v-wires are treated as stacked directly on top of the u-wires; it is impossible in two dimensions to model the true orientation of the v-wires which is rotated relative to the u-wires, but this has generally proven to be a minor detail for us. Only one TPC half is modeled because of the approximate mirror symmetry of the detector across the cathode. We assume that the two-dimensional geometry is periodic along the direction of the wire "plane", which permits us to always locate drifting charge above the central wire. Only a few wires to either side of the center are simulated because each wire

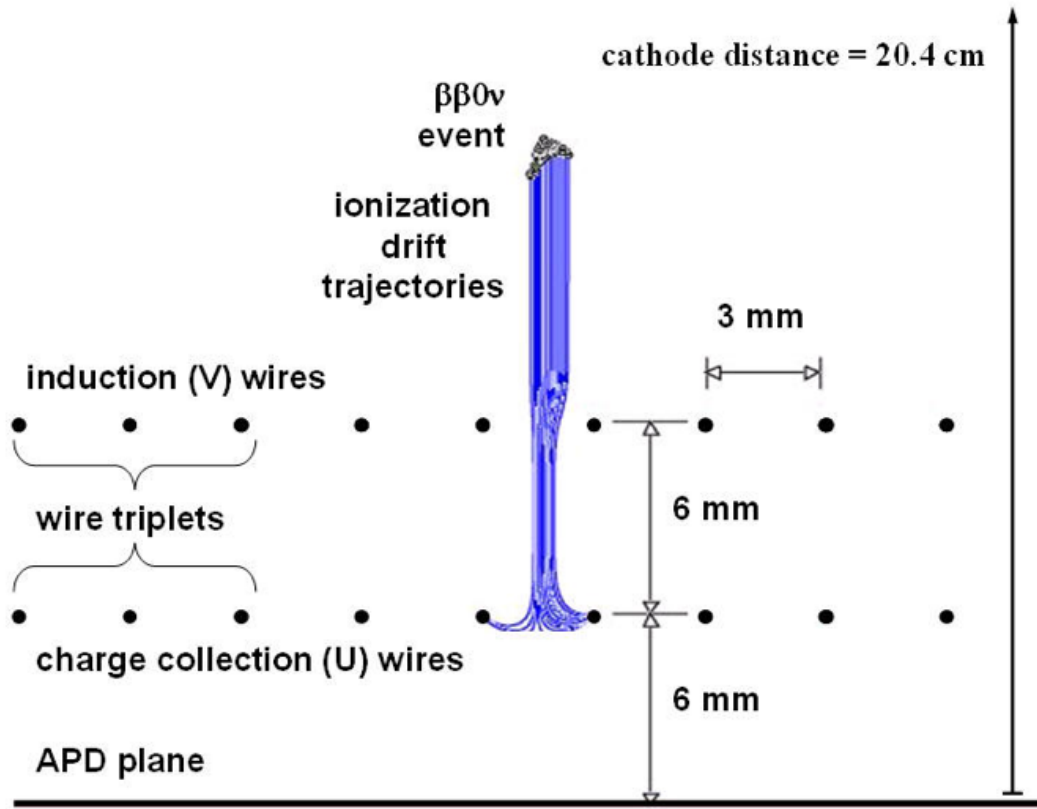


Figure 7.5: The wire planes are modeled in only two dimensions; charge drifts along the field lines, which are arranged to terminate only on the u-wires [111].

acts as a shield between wires to its left and right, so the electrostatic effect of any one wire will not extend beyond a few wire spacings [111].

Electrostatic effects are simulated using the ANSYS Maxwell field simulator. To simulate the electric fields in the detector, wires are treated as circles with a radius matching the approximate radii of the physical wires, with a constant voltage on their surfaces. The APD plane and cathode plane are treated as constant-voltage boundaries, and a periodic boundary condition is established on the two remaining boundaries of the model geometry.

These electric fields can be used to trace the paths followed by charge deposits in the detector. Charge deposits are drifted in small steps based on the direction of the electric field. The speed of drift is taken from external measurements rather than from the magnitude of the electric field; in most of the bulk of xenon, the electric field and drift velocity are treated as constant, but near the u-wire plane the drift velocity is increased slightly to account for higher electric fields experienced in that region of the detector. Charge attenuation due to finite purity can be modeled at this step, but generally is treated as infinite here; charge diffusion effects are ignored.

We have discussed in section 3.5 that charge is induced on the u-wires and v-wires; this means that we must record the amount of charge induced at each step along the drift path of the charge deposit. This is done based on the Shockley-Ramo Theorem, which states that the change in induced charge  $\delta q_i$  on an electrode  $i$  is equal to:

$$\delta q_i = Q\delta W_i, \quad (7.1)$$

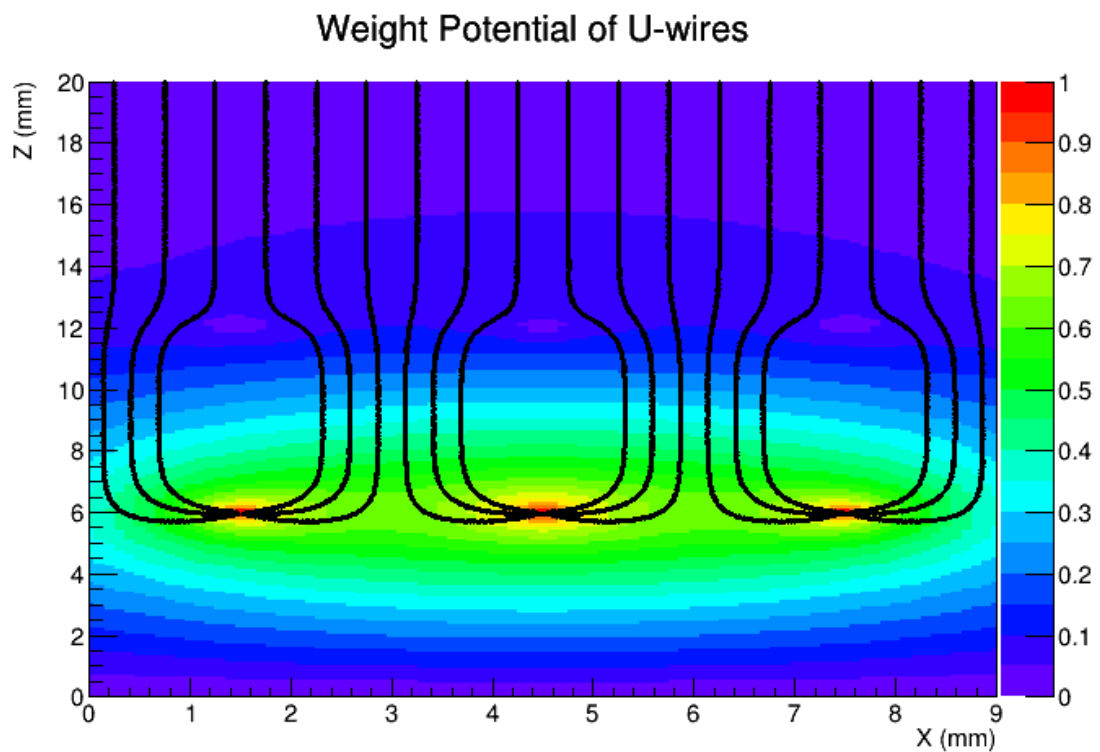


Figure 7.6: Weight potential of a u-wire channel consisting of three ganged wires. Electric field lines are superimposed [111].

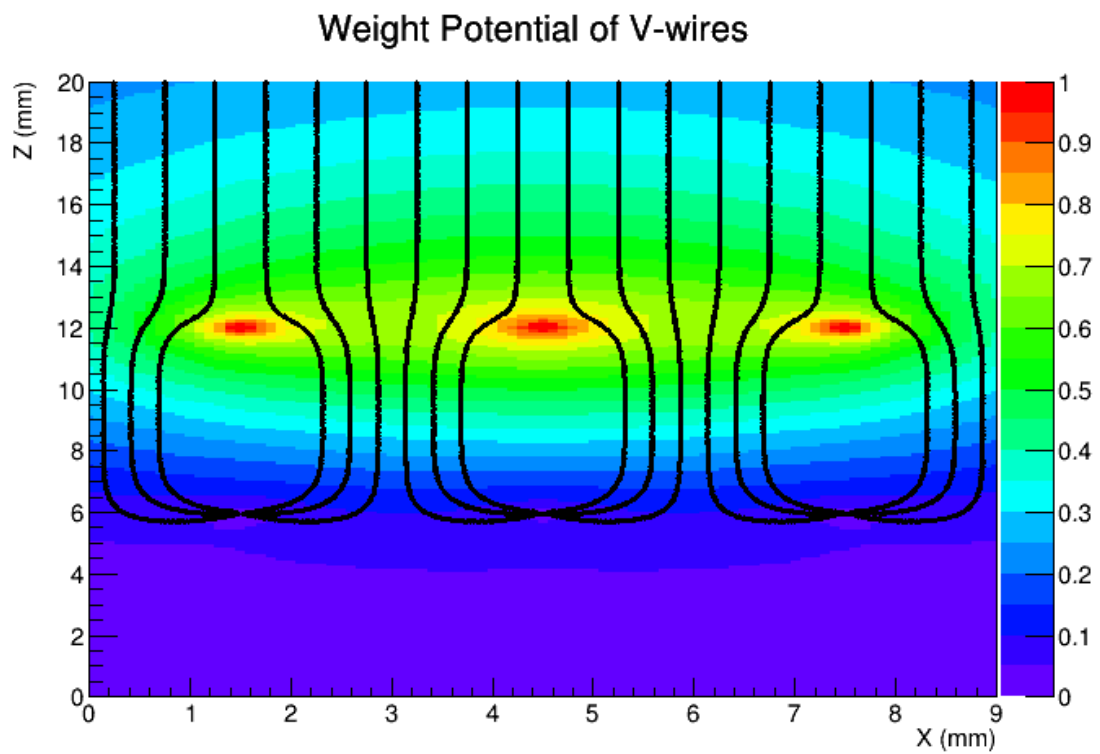


Figure 7.7: Weight potential of a v-wire channel consisting of three ganged wires. Electric field lines are superimposed [111].

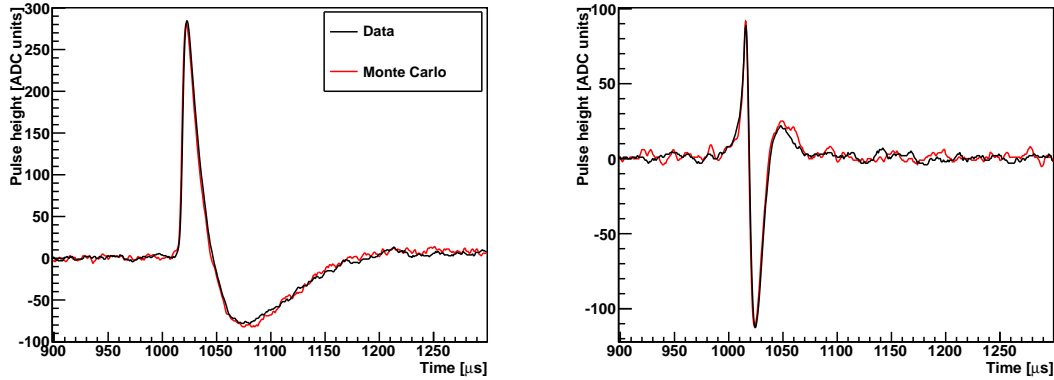


Figure 7.8: Comparison between simulated and observed waveforms on a u-wire (left) and v-wire (right) from  $^{228}\text{Th}$  sources. The events are chosen to have similar energies so that the magnitudes match [111].

where  $Q$  is the total drifting charge and  $W_i$  is the weighting potential of electrode  $i$ , defined as the potential which would be induced in our geometry if the potential on electrode  $i$  were set to one and the potential on all other boundaries were set to zero [137, 138]. Figures 7.6 and 7.7 illustrate the weighting potentials of a u-wire and v-wire channel, respectively.

Finally, the functions of integrated charge versus time must be converted to shaped digitized waveforms, and noise must be added. The shaping and gain amplification is performed to match the electronics described in section 3.5. To ensure accurate time shaping, the functions are all sampled at a bandwidth of 10 MHz, and then downsampled after shaping to the nominal 1 MHz. Digitization is performed by converting voltages into units of ADC counts, then truncating to an integer value. To model saturation effects, this number is pulled into the integer range  $[0, 4096)$ .

We have the ability to add electronic noise to the pulses by extracting a set of representative noise waveforms from real data. These are taken from a large number

of solicited triggers which have been checked for the absence of a coincident event.

To increase the number of noise waveforms available, the noise waveforms sampled from the detector are spliced together, and simulated events may draw their noise from any subrange of the spliced-together noise waveform. This method provides our most accurate noise model because it can include all noise frequency peaks and channel correlations without requiring a full understanding of those features.

However, current analyses do not employ this method; instead, we simulate noise which is white (has a flat Fourier spectrum) before shaping, and then shaped to have a spectrum which roughly resembles the one observed in the detector. Figure 7.8 compares waveforms observed from a sample event in data and simulation, and demonstrates that at high energies excellent agreement is achieved [111].

In this way, we are able to generate simulated data which in most respects resembles real data collected from the detector. The EXO-200 simulation has shown remarkable agreement with the detector in the properties of energy and cluster location, as illustrated in figure 7.9. A significant effort has been made to achieve excellent agreement between simulation and data, and the result is that we can claim a strong understanding of the behavior of the EXO-200 detector.

## 7.2 Cluster Reconstruction

The first stage of data processing involves locating candidate pulses in the waveforms and fitting for the magnitude and time of any candidate pulses which are found. The methods of accomplishing this are described in sections 7.2.1 and 7.2.2. We

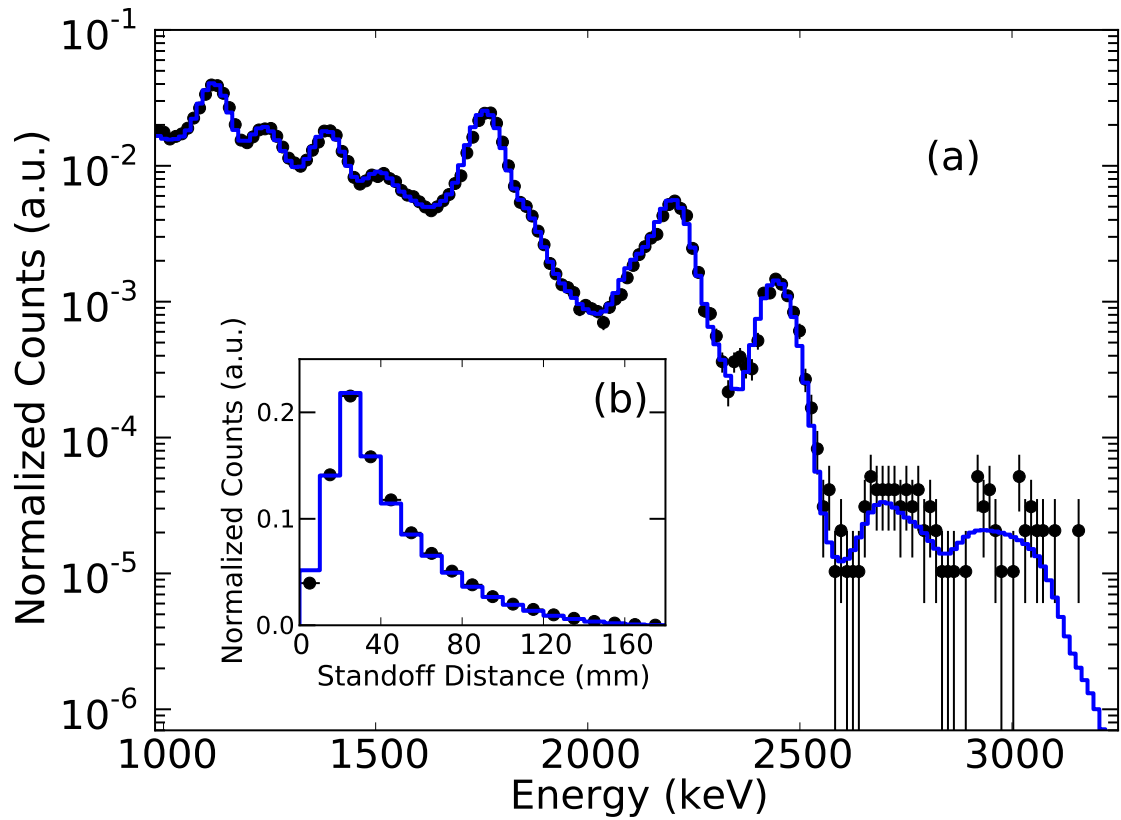


Figure 7.9: Comparison between simulated and observed energy spectra (a) and standoff distance (b) in single-site  $^{226}\text{Ra}$  events from a source located at position S5 [89].

will complete our description of cluster reconstruction with a brief explanation of the approach to the clustering of waveform pulses into three-dimensional clusters in section 7.2.3.

### 7.2.1 Pulse Finding

Pulse-finding proceeds in two steps. First, on u-wire, v-wire, and summed APD waveforms a matched filter is applied to do a preliminary search on all channels. Then, a secondary search is performed on the u-wire waveforms to improve sensitivity to multiple pulses near in time.

The matched filter algorithm was first described by D.O. North in 1943 [139]. It attempts to decide between the null hypothesis that a waveform  $X[\tau]$  consists of only noise and an alternative hypotheses that the waveform contains a pulse and noise:

$$\begin{cases} H_0 : & X[\tau] = n[\tau] \\ H_1 : & X[\tau] = s[\tau] + n[\tau]. \end{cases} \quad (7.2)$$

To discriminate between these hypotheses optimally, we search for a linear functional  $L_0$  which will act on  $X[\tau]$  and maximize the expected signal-to-noise ratio,

$$SNR = \frac{(L_0 \{s[\tau]\})^2}{\langle (L_0 \{n[\tau]\})^2 \rangle}. \quad (7.3)$$

In other words, if a waveform is composed of only noise, the functional should result in a small value; however, if the waveform contains a pulse then the functional should result in a large value.

We omit the derivation, which is a standard result, and simply state that the linear functional which maximizes the expected signal-to-noise ratio can be expressed as: [139]

$$L_0 \{X[\tau]\} = \mathcal{F}^{-1} \left\{ \frac{\mathcal{F}\{X\}[f] \mathcal{F}\{s\}^*[f]}{\langle \mathcal{F}\{n\}[f] \mathcal{F}\{n\}^*[f] \rangle} \right\} [0], \quad (7.4)$$

where  $\mathcal{F}$  represents the Fourier transform and  $\mathcal{F}^{-1}$  represents the inverse Fourier transform. (The  $\tau = 0$  index in this test statistic indicates that here we are testing for a pulse at only one instant in time.) This expression has an added benefit that if instead we'd like to test the hypothesis that the translated pulse  $s[\tau - \Delta]$  is contained in the waveform, substitution lets us show that we can do so with the related test statistic:

$$L_\Delta \{X[\tau]\} = \mathcal{F}^{-1} \left\{ \frac{\mathcal{F}\{X\}[f] \mathcal{F}\{s\}^*[f]}{\langle \mathcal{F}\{n\}[f] \mathcal{F}\{n\}^*[f] \rangle} \right\} [\Delta]. \quad (7.5)$$

Finally, we can define a test statistic  $T$  for the waveform  $X[\tau]$  to have a pulse anywhere with:

$$T = \max_{\Delta} L_\Delta \{X[\tau]\}. \quad (7.6)$$

The values  $L_\Delta$  for all  $\Delta$  can be computed efficiently using the fast Fourier transform. The time of the pulse is guessed as the value of  $\Delta$  which led to the maximum of  $L_\Delta \{X[\tau]\}$ .

The first phase of pulse-finding performs a search using the matched filter on:

- All u-wire channels.
- All v-wire channels.

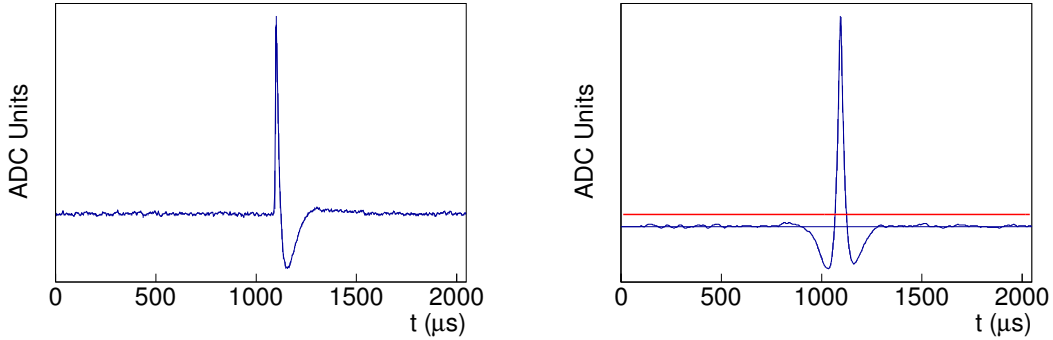


Figure 7.10: A u-wire waveform (left) and the output from operation of the matched filter (right). The red line on the right indicates our filtered pulse threshold; the matched filter output exceeds the threshold, so this waveform is determined to contain a pulse [112].

- The sum of all APD channels in the North plane.
- The sum of all APD channels in the South plane.

An example application of the matched filter to a u-wire waveform is shown in figure 7.10.

The matched filter has proven to be an excellent metric for deciding whether a waveform has a pulse on it or not. However, it is not as effective at distinguishing between the cases where one or multiple pulses occur on a waveform. We would particularly like to be able to classify u-wire waveforms by the number of distinct pulses they contain because this can help us distinguish between single-site and multi-site events, which can reduce our background as described in section 3.4. The matched filter output function is designed to have a tall peak in the presence of a pulse, but it may also be a broad peak which is difficult to resolve as the sum of two distinct pulse contributions.

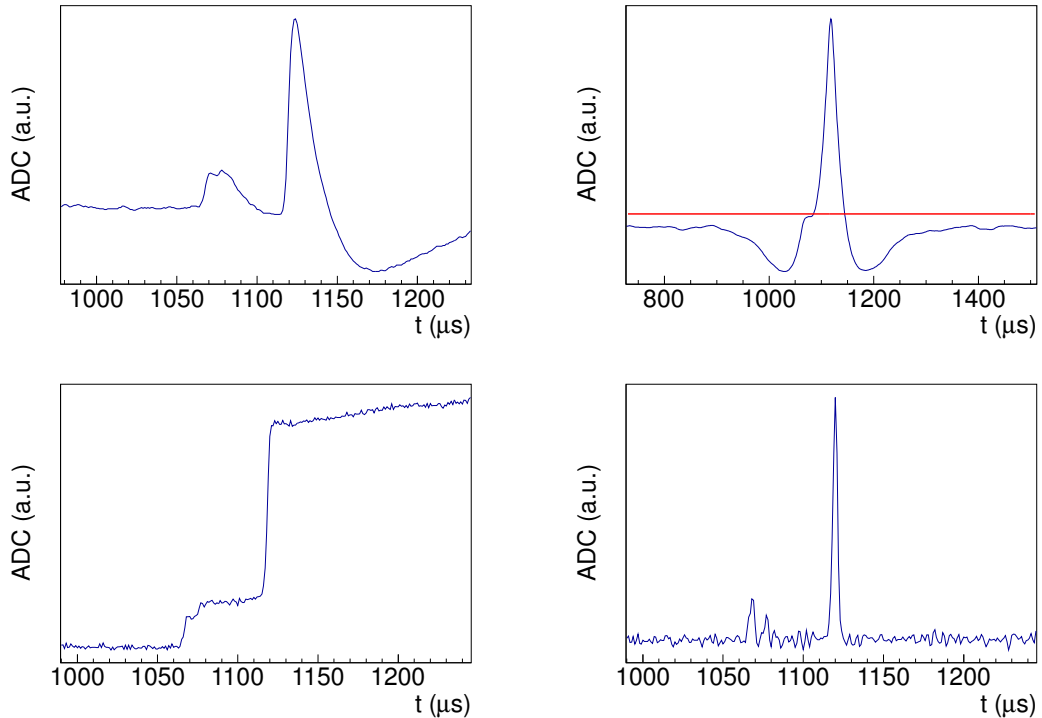


Figure 7.11: A u-wire waveform composed of two pulses near in time is shown (top left); the matched filter (top right) correctly detects the presence of a pulse, but does not detect the presence of two distinct pulses. At bottom left, the waveform is unshaped; at bottom right the waveform is reshaped with shorter differentiation times, leading to easier detection [112].

To improve sensitivity to multiple pulses in u-wire waveforms, a second pass is performed on u-wire channels using a multiple-signal finder. This scheme consists of first unshaping the waveform offline to remove the effect of the shapers, and then reshaping the waveform using shorter differentiation times than the hardware shapers apply. This is a type of high-pass filter; in a multiple-pulse waveform, it can have the effect of damping the first pulse faster to reduce its overlap in time with the second pulse. It is then possible to search for pulses using a simple threshold which is not as sensitive to small pulses as the matched filter, but is capable of detecting additional pulses to complement the matched filter. This process is illustrated in figure 7.11, and is the last procedure for finding pulses [112].

### 7.2.2 Pulse Fitting

After finding pulses, it is necessary to perform a fit to the expected pulse shape. Fits are performed allowing both the pulse magnitude and time to float freely, where only the initial guesses for these parameters come from the finding step. The metric for fits is a simple chi-square between waveform data and the expected pulse shape, where error on each point is estimated by the root-mean-square noise of the channel.

To minimize the impact of pulse templates whose shape may not perfectly reflect the shaping times in hardware, and also to reduce the effect which waveform noise may have on our fit, we do not fit the entire waveform to our pulse model. Instead, we use only an  $80\mu\text{s}$  fit window in the case of v-wires and APDs, and a  $180\mu\text{s}$  fit window in the case of u-wires. The fit windows are illustrated with example

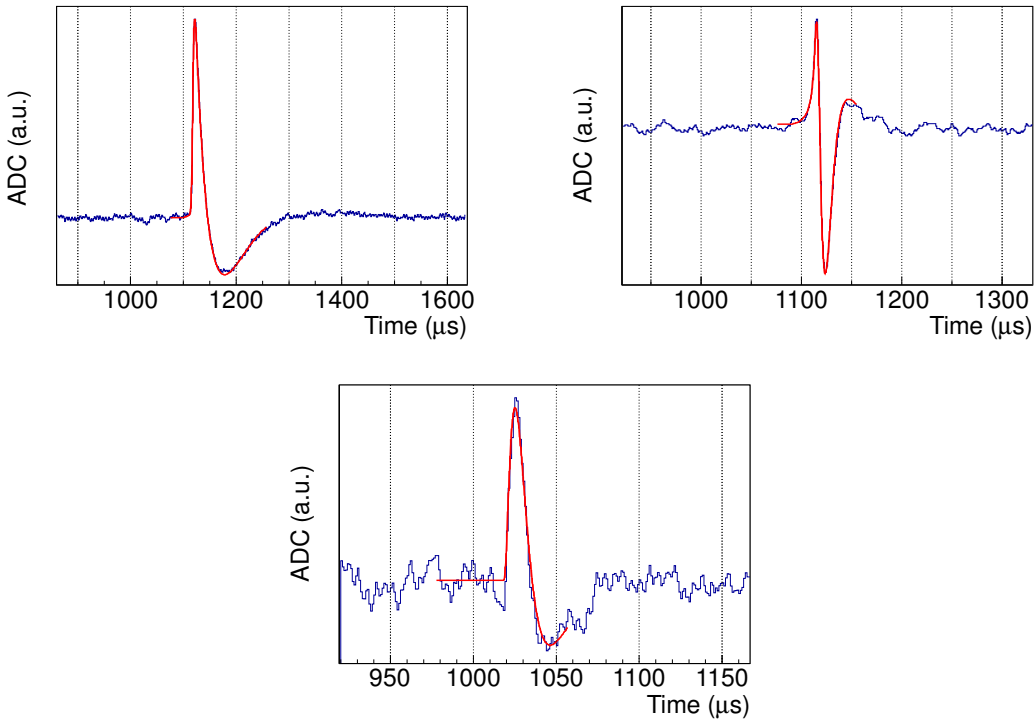


Figure 7.12: Fits to data for a u-wire (top left), v-wire (top right), and summed-APD waveform (bottom). The red model line indicates the time extent of the fit window [112].

events in figure 7.12.

As pulse times and magnitudes are extracted, it may be discovered at this phase of processing that two pulses on the same waveform which were separately reported by the finding phase are extremely close together in time. In this case, we can generally conclude that the finding phase inadvertently reported the same pulse multiple times; the multiple candidate pulses should then be merged together, and the waveform refit. The specific criteria for merging or removing candidate pulses are: [112]

- If two pulses occur within  $10 \mu\text{s}$  of each other and one pulse has a fit magnitude error of at least 15 ADC counts, the two pulses are merged.
- If any pulse has a magnitude to magnitude-error ratio of less than 6.0 for u-wires, 5.0 for summed APD waveforms, or 3.0 for v-wires, then the smallest such pulse is removed.
- If any pulse has a magnitude of less than 5 ADC counts, then the smallest such pulse is removed.

Each time a single pulse is removed or a pair of pulses is merged, the fit is re-run and we search again for any pulses warranting removal. In this way, we attempt to ensure at the pulse-fitting stage that only appropriate fit results are retained.

### 7.2.3 Clustering Pulses into Deposit Sites

The result of pulse finding and fitting is a list of pulse magnitudes and times for each channel. It remains for reconstruction to combine this information into three-

dimensional clusters, where each cluster should have a three-dimensional position, time, and estimates for charge and light pulse magnitudes.

We begin by bundling groups of similar u-wire, v-wire, and APD pulses. Multiple u-wire pulses may be bundled together when they occur on neighboring channels close together in time. This may represent a cluster which occurred halfway between two u-wire channels and was split, with some charge being collected by each u-wire channel; it may also represent a combination of charge being collected on one channel and an induced charge pulse on a nearby u-wire channel due to the proximity of the charge drift path to that neighboring channel. V-wire pulses are bundled together based on a combination of pulse magnitude and time to account for the observation that the passage of a single charge cloud will induce pulses on many nearby v-wires. APD pulses are bundled based on time only, particularly to ensure that when a pulse is observed on both the North and South APD planes, the pulses are interpreted as originating from the same event in the detector.

We then attempt to join u-wire pulse bundles and APD pulse bundles into two-dimensional charge clusters, identified by their U-Z positions and the time of the energy deposit. The algorithm to do this is simple: for each u-wire pulse bundle, we join it with the most recent APD pulse bundle in the event. The maximum difference in time is the maximum drift time of charge clusters in the detector,  $116\mu\text{s}$ . To allow for fit errors in the time parameters of the APD and u-wire pulses, an additional  $3\mu\text{s}$  allowance is added on either end of the permitted time difference; thus, an APD and u-wire pulse bundle may be joined if the APD occurred between  $119\mu\text{s}$  before and  $3\mu\text{s}$  after the u-wire collection time, and from these candidates the latest APD

pulse bundle is selected for each u-wire pulse bundle. The cluster's charge energy is the sum of the energies attributed to all of the u-wire pulses in the u-wire pulse bundle; no attempt is made to measure the cluster's scintillation energy.

Finally, we cluster v-wire pulse bundles with two-dimensional charge clusters to form three-dimensional clusters possessing X-Y-Z positions, deposit time, and charge energy. The only information taken from the v-wire pulse bundle is the third position coordinate; it is not used to adjust our estimates of energy. The challenge to this portion of clustering is that charge clusters may arrive at the same u-wire or v-wire at the same time, yet from two different locations. For example, it may be that what appeared to be one u-wire pulse bundle in fact comes from two charge clusters with common U-Z positions and different V-positions. So, in addition to searching for the most likely associations between u-wire/APD clusters and v-wire pulse bundles, we must consider the possibility of splitting a two-dimensional cluster or v-wire pulse bundle into pieces before performing this association.

To do this, every possible combination of u-wire/APD cluster and v-wire pulse bundle is considered, along with every possible choice of split for clusters or pulse bundles. A likelihood is assigned to each possible combination; this likelihood takes into account:

- The ratio of v-wire and u-wire pulse magnitudes. These pulse magnitudes are expected to be linearly related because they both are observations of the same charge drift cloud, and deviations from that linear relation are penalized by a decreased likelihood.

- The time difference between the v-wire and u-wire pulses. There is an expected drift time between the v-wires and u-wires which is measured from data; if the observed time difference deviates from this expectation, the likelihood is decreased to reflect a preference for a more realistic pairing.
- The two-dimensional position which the pairing implies. Due to the geometry of the detector, not all pairs of u-wire and v-wire can be hit by the same charge cluster. When a u-wire and v-wire lie in different halves of the TPC, it is of course impossible for the same charge cloud to induce pulses on both. In some cases a u-wire and v-wire may almost overlap, and it may be considered possible yet unlikely that the same charge cloud could induce pulses on both; these instances are penalized as well.

Further details of the clustering criteria may be found in [112].

This section has described the situation where the pulses of an event may be reconstructed as a set of three-dimensional clusters with well-defined position, time, and charge energy. Although every effort is made to accomplish this whenever possible, in practice there are events for which some clusters may not be fully reconstructible. Primarily this occurs when charge deposits on a u-wire near the edge of the detector where no v-wires exist; because a cluster falls below the threshold for v-wire pulse-finding, or the event falls below the scintillation threshold; because the pulse finder reports a false positive, yielding a non-physical pulse; or because an event has extremely high multiplicity and it is not possible to select a preferred clustering. Such events are difficult to use in higher-level analyses and will generally

be removed, with an associated energy-dependent efficiency loss of 9.1% [89].

## 7.3 Energy Corrections

Each cluster which is found can be assigned a preliminary energy estimate based on the fit magnitudes of its pulses. However, to achieve the best possible energy resolution it is necessary to make an assortment of energy corrections. These corrections are identified in this section. We first describe the corrections which are made to charge energies on a cluster-by-cluster basis, and then the corrections made to the denoised scintillation energy. Section 7.3.3 describes the calibration of a rotated energy measurement using charge and light together, and section 7.3.4 describes the measurement of the energy resolution of this rotated energy measurement.

### 7.3.1 Charge Corrections

The preliminary charge cluster energy measurements come from the sum of the u-wire pulse magnitudes described in section 7.2.2. These magnitudes reflect the quantity of charge which is collected by the u-wire.

However, each u-wire channel has its own set of electronics, so pulse magnitudes must be adjusted by a gain correction which depends on the channel. These gains are extracted from source data by selecting pair production events from the thorium source, in which a 2615-keV gamma pair-produces an electron and positron, and the positron subsequently annihilates with another electron to emit two 511-keV gammas. The high multiplicity of these events makes it possible to select them

accurately, and the process guarantees that a single 1593-keV cluster at the site of the pair production must be truly single-site because it originates from a single electron-positron pair. These properties make it ideal for producing an accurate u-wire gain measurement. Using the resulting gain corrections, individual u-wire pulse magnitudes are corrected based on their gain, and the charge cluster energy measurements are corrected according to the corrections on their bundled u-wire pulses [110].

There are also two Z-dependent energy corrections which must be applied to clusters. The first accounts for charge attenuation due to the imperfect purity of the xenon, as discussed in section 3.1. As electrons drift, some will attach to electronegative impurities such as oxygen or nitrogen; the exact nature of the electronegative impurities in EXO-200 are not known. The level of impurities in the xenon are time-dependent due to the strong effects which the xenon pump speed and periodic injections of additional xenon may have.

To extract the purity correction, the dataset is divided into time windows when the pump speed was constant and no feeds occurred; the purity is assumed to be constant during these time intervals. It is then possible to combine all thorium source data during these time windows and fit for the 2615-keV single-site  $^{208}\text{Tl}$  gamma line in Z-bins ranging from the North to the South anode. An illustration of the ionization peak position versus Z is shown in figure 7.13. Charge attenuation is exponential with a typical  $e$ -fold attenuation occurring in 4 – 5 ms drift time; the purity correction to charge energy is typically 2 – 3% for charge deposits at the cathode [140].

### Electron Lifetime measurement, total

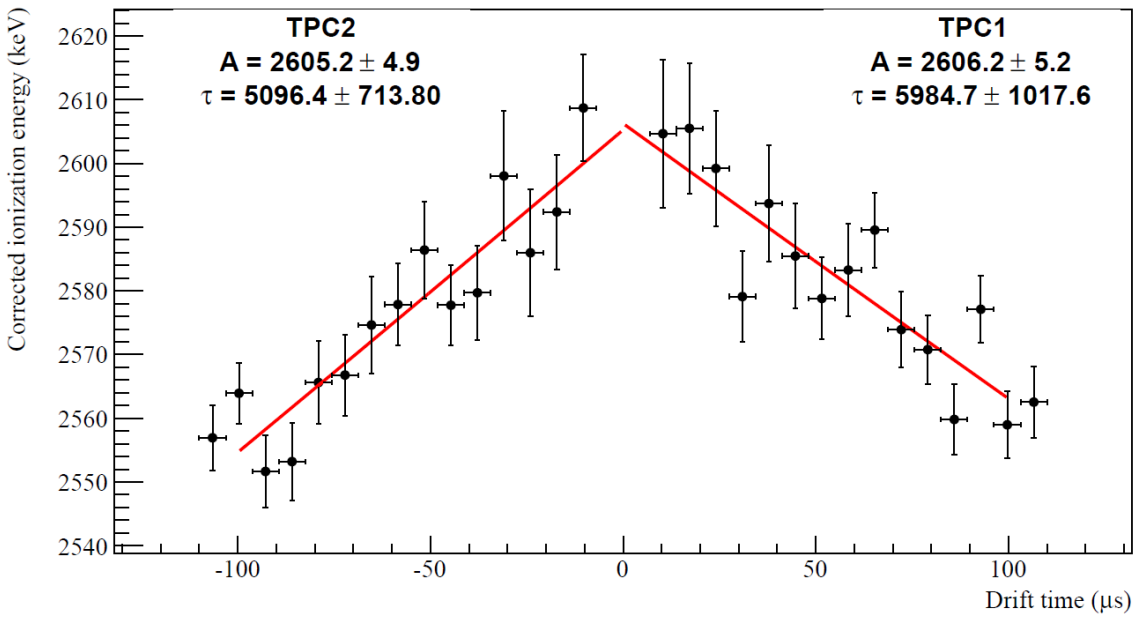


Figure 7.13: The purity charge correction is measured by fitting the 2615-keV  $^{208}\text{Tl}$  gamma line as a function of Z-position [140].

### Projection of Weight Potential

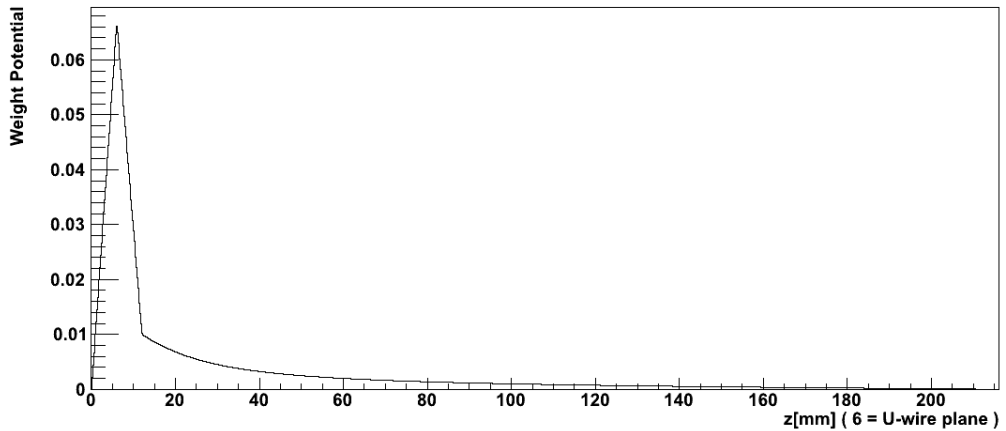


Figure 7.14: The expected grid correction of a u-wire as a function of Z-position. In this plot,  $Z = 6$  mm represents the position of the u-wire plane and  $Z = 12$  mm is the position of the v-wire plane [110].

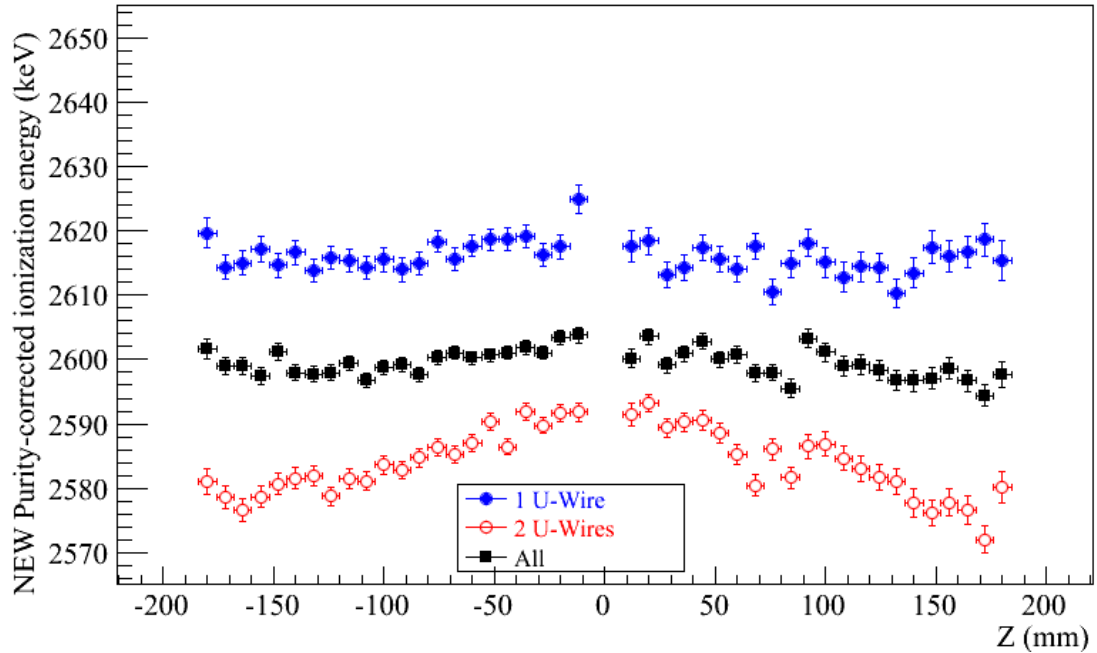


Figure 7.15: After applying all charge corrections, we find that the 2615-keV  $^{208}\text{Tl}$  ionization peak is observed at the expected location for single-wire events; however, for two-wire events a residual bias is observed which also exhibits Z-dependence [140].

The other Z-dependent charge correction is from the shielding grid. Section 3.5 described the process by which both electron clouds and ionized xenon will induce pulses on the wires. The electron cloud drifts rapidly, and its pulse is observable; the ionized xenon will drift quite slowly, and will not produce an observable pulse in our electronics. However, the ionized xenon will counteract the induced current pulse from the drifting electrons by holding some electrons on the wire; the degree to which they are able to influence the observed current pulse depends on the weight potential of the wire evaluated at the position of the xenon ions. The simulated weight potential of a u-wire is shown as a function of Z in figure 7.14, and we can see that inside the v-wire plane this correction is expected to remain below 1% [110].

These are all of the known corrections to the charge energy. However, we find that after applying them, there remains a residual z-dependence in the charge calibration. Figure 7.15 shows that although the 2615-keV  $^{208}\text{Tl}$  ionization peak has been properly corrected for clusters which deposit on only one u-wire, for clusters which are split between two u-wires there is a residual offset in peak position of roughly 1% and an additional z-dependent effect of up to roughly 0.3%. These effects are not presently understood; however, they are believed to induce a Z-dependent bias effect in the lightmap which is used for scintillation denoising, which in turn is believed to cause the scintillation z-bias described in section 7.3.2 [140]. Active work is underway to understand this z-bias in charge and develop an appropriate correction.

### 7.3.2 Light Corrections

Although scintillation measurements are made from fitting the magnitudes of the scintillation pulses found on the summed North and South APD planes in reconstruction, as described in section 7.2.2, these scintillation measurements are superseded by the denoised scintillation energies estimated using the denoising method of chapter 4. This subsection will describe evaluations of the success of that denoising effort and subsequent corrections made to the denoised scintillation energy.

When the denoising algorithm operates properly, it should be constrained to produce scintillation energy measurements calibrated in keV. This calibration is accomplished by the lightmap, which retains information about the magnitude of

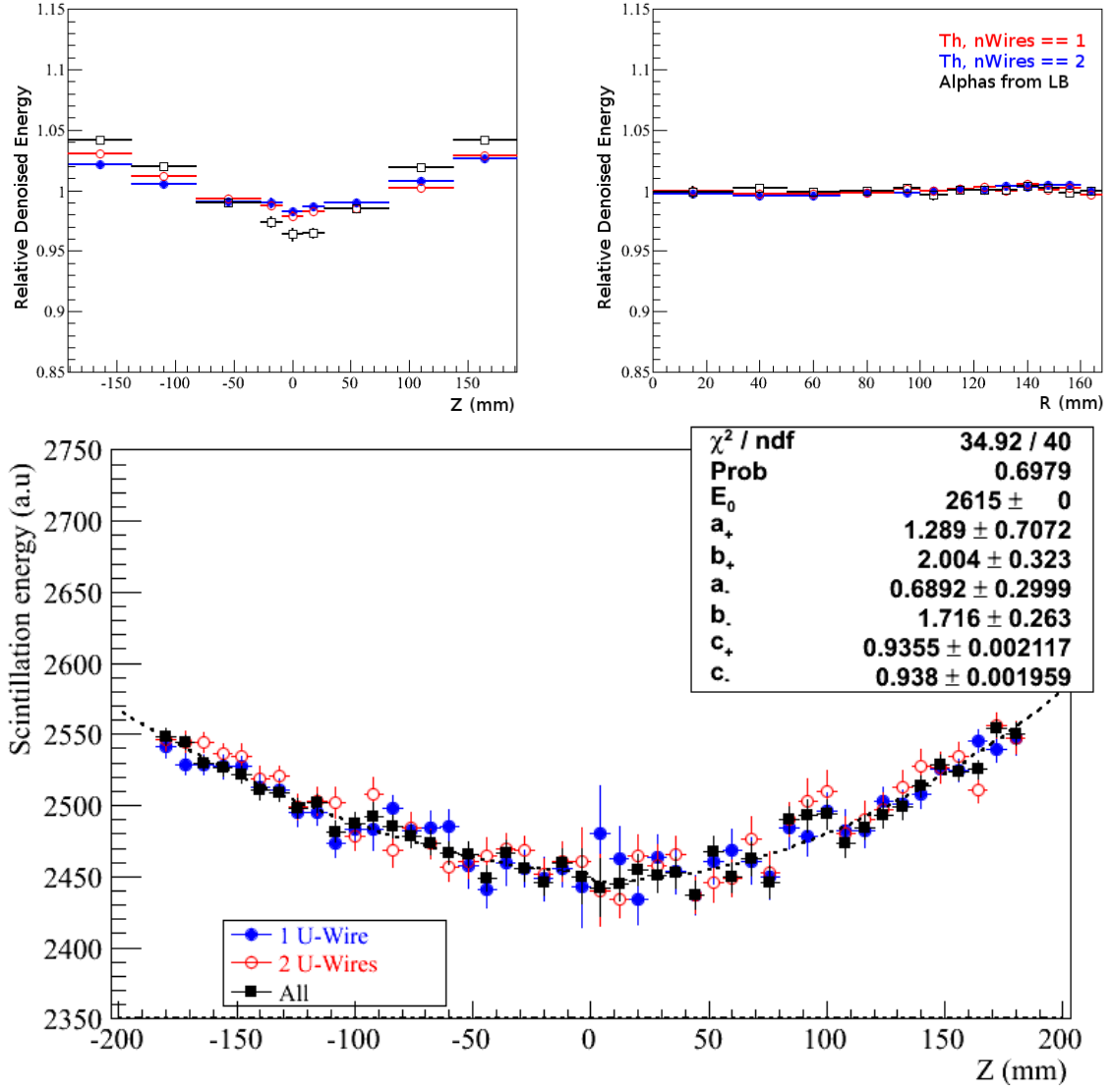


Figure 7.16: A residual calibration offset and Z-dependent behavior is observed in the denoised scintillation measurements. The top plots show the relative peak position of the scintillation-only 2615-keV  $^{208}\text{Tl}$  peak (one-wire and two-wire) and average alpha energy from  $^{222}\text{Rn}$  versus Z (top left) and R (top right). The bottom plot shows the absolute denoised scintillation energy from the 2615-keV  $^{208}\text{Tl}$  peak for one and two wires, with the measured correction function (equation 7.7) overlaid [140].

pulses produced by 2615-keV energy deposits. However, in practice it is seen that the denoised scintillation measurements are not properly calibrated; this can be seen in figure 7.16, where it is clear that events of all types (alpha decays in low-background data and both one-wire and two-wire single-site gamma decays from an external source) measure a scintillation energy which is systematically too low and displays significant Z-dependence. The thorium data, which provides the best measurement statistics, shows a mis-calibration which ranges from 2.5% near the anodes to 6.5% at the cathode [140].

The cause for the discrepancy in scintillation energy measurements is not currently known. One hypothesis is that the discrepancy in two-wire charge cluster measurements described in section 7.3.1 may lead to inaccurate event selection in the generation of the lightmap described in section 6.3.1; poor event selection would lead to a systematic error in the lightmap which could depend on Z, and would be capable of creating the observed bias. Attempts to address this Z-bias within the generation of the lightmap or investigate alternative explanations for its origin have so far been unsuccessful, but these investigations continue, and it is hoped that this issue can be fixed for the next analysis.

For the present analysis an empirical correction of the discrepancy is applied. The scintillation correction function takes the form:

$$E_{corr} = E_{meas} \cdot \begin{cases} [(c_-) + (a_-) \cdot |Z|^{b_-}]^{-1} & \text{if } Z < 0 \\ [(c_+) + (a_+) \cdot |Z|^{b_+}]^{-1} & \text{if } Z > 0, \end{cases} \quad (7.7)$$

where we measure from data  $c_- = 0.9380$ ,  $c_+ = 0.9355$ ,  $b_- = 1.71$ ,  $b_+ = 2.00$ ,  $a_- = 0.69$ ,  $a_+ = 1.3$ , and  $Z$  is in units of meters. The bottom plot of figure 7.16 shows this empirical correction overlaid on one-wire and two-wire thorium source data, demonstrating that the function agrees well with the observed  $Z$ -dependent offset [140].

### 7.3.3 Rotated Energy Calibration

From the corrected scintillation and charge energy measurements, it is necessary to form a calibrated rotated energy measurement which combines them. This combination takes advantage of anticorrelation between charge and light to achieve an optimal energy resolution. To accomplish these measurements, it is necessary to use multiple calibration points; we use the 2615-keV gamma line from regularly-taken thorium source runs to measure time-dependent calibration parameters and the 662-keV cesium and 1173-keV and 1332-keV cobalt gamma lines from source runs to characterize the energy dependence of calibrations. The linear combination of scintillation and charge is selected to optimize the energy resolution of the thorium line; the precise measurement of energy resolution is described in section 7.3.4, but for this purpose we simply seek to make energy peaks as narrow as possible.

The calibrated rotated energy  $E$  is computed by a calibration function of the

form:

$$E_{rot} = E_S \cdot \sin(\theta(t)) + E_C \cdot \cos(\theta(t)) \quad (7.8a)$$

$$E_{ratio} = \frac{E_{rot}}{E_{rot}^{th}(t)} \quad (7.8b)$$

$$E = (E_{thorium} - E_{bias}) \cdot (p_0 + p_1 E_{ratio} + p_2 E_{ratio}^2), \quad (7.8c)$$

where  $E_C$  and  $E_S$  are the measured charge and scintillation energies (with corrections applied as described in sections 7.3.1 and 7.3.2),  $\theta(t)$  is a time-dependent rotation angle measured to optimize the fractional energy resolution of the thorium gamma line,  $E_{rot}^{th}(t)$  is the time-dependent location of the thorium peak in the spectrum of  $E_{rot}$ ,  $E_{thorium}$  is the true thorium peak position equal to 2615 keV, and  $E_{bias}$ ,  $p_0$ ,  $p_1$ , and  $p_2$  are time-independent calibration parameters. Entirely separate calibration parameters are obtained for single-site and multi-site events.

The result of this calibration for a particular thorium source calibration run is shown in figure 7.17. We can see here that a projection is performed from the two-dimensional charge-light spectrum along an axis that minimizes the width of the thorium gamma line. Figure 7.18 demonstrates the spectra we obtain from projections only in scintillation, only in ionization, and using the optimal linear combination we have described; the improvement in resolution from using an appropriate linear combination of scintillation and ionization is apparent, as the peak at 2615 keV becomes sharper and additional low-energy features of the spectrum become apparent which were washed out with worse resolution. The next section will describe the process of measuring the energy resolution.

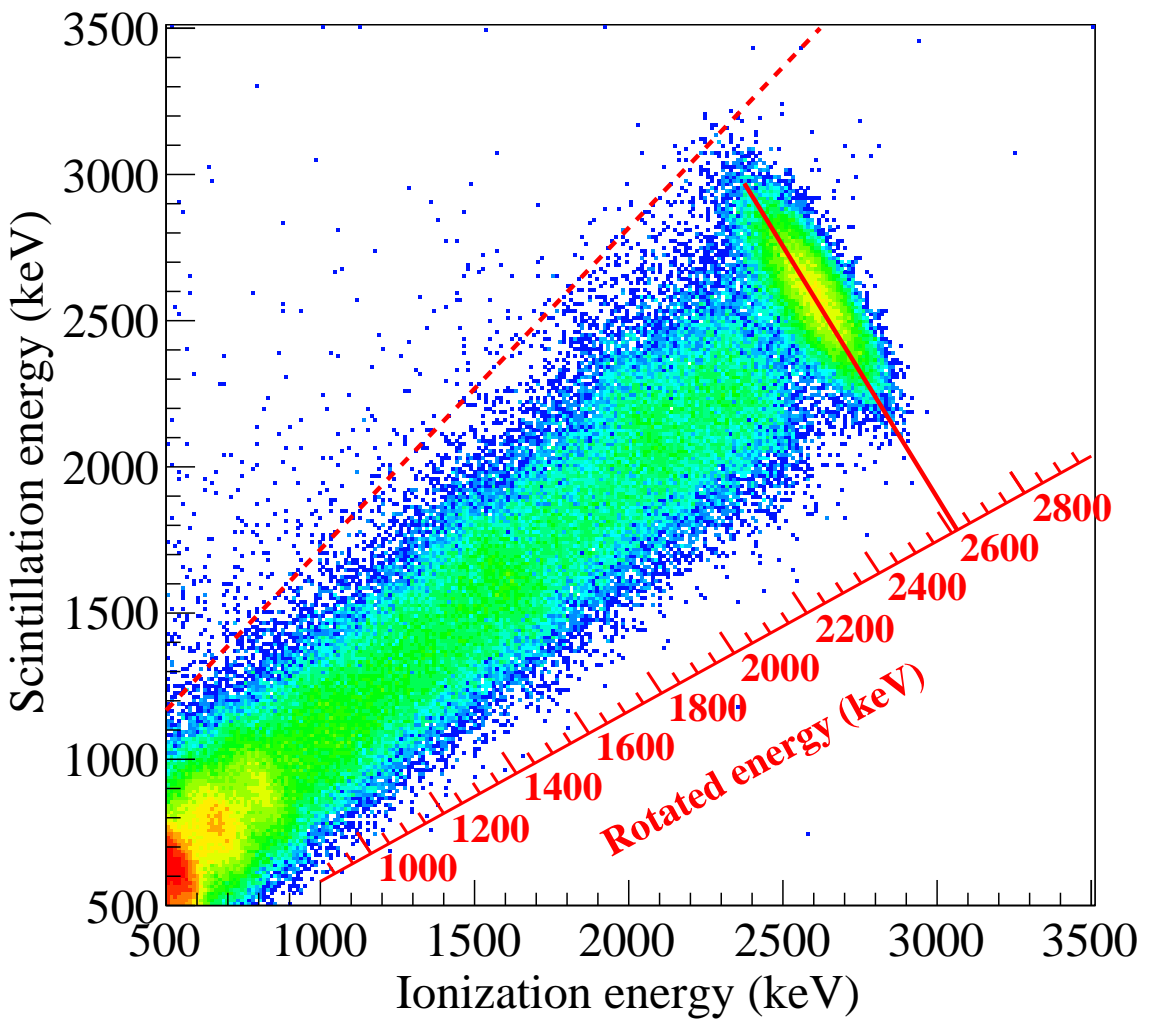


Figure 7.17: Corrected scintillation versus charge energy are shown for a thorium run. The projection angle for the rotated energy measurement is illustrated at the 2615-keV peak; the projection onto a calibrated axis is shown. The dotted red line indicates the diagonal cut described in section 7.4. Figure provided by Liangjian Wen.

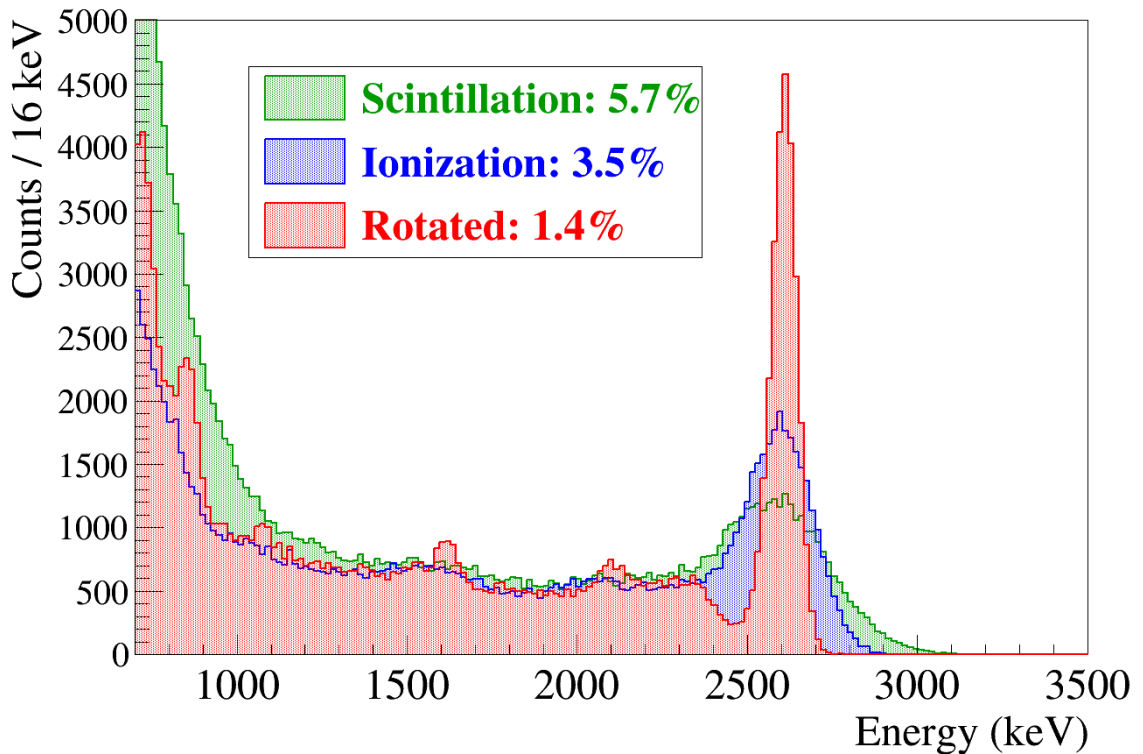


Figure 7.18: Charge-only, scintillation-only, and rotated energy spectra are shown from a thorium source run; the significant improvement in energy resolution with the rotated energy measurement is apparent, as are low-energy features which are washed out in the lower-resolution spectra. Figure provided by Liangjian Wen.

### 7.3.4 Measurement of Rotated Energy Resolution

The previous section has described the calibration of the rotated energy spectrum.

In this section, we describe the measurement of energy resolution with this rotated energy measurement.

The resolution is assumed to be energy-dependent; if a monoenergetic deposit is made in the liquid xenon, we hypothesize that the observed spectrum should be Gaussian and define the energy resolution at that energy to be the value of  $\sigma$ . We can parametrize the dependence of  $\sigma$  on energy as:

$$\sigma(E) = \sqrt{p_0^2 E + p_1^2 + p_2^2 E^2}, \quad (7.9)$$

where typically we interpret the parameters  $p_1$  to come from electronic noise (which contributes a smearing independent of energy),  $p_0$  to come from statistical fluctuations in the number of photons or electrons observed (which follows a Poisson distribution in the number of photons), and  $p_2$  to come from mis-calibration of components of the detector (whose effect increases linearly with the size of the pulse) [141]. We also often find it useful to refer to the relative or fractional energy resolution, defined as:

$$\sigma(E)/E = \sqrt{p_0^2/E + p_1^2/E^2 + p_2^2}. \quad (7.10)$$

The resolutions of single-site and multi-site events differ, so there are separate res-

Parameter	SS	MS	Units
$p_0$	0.628	0.602	$\sqrt{\text{keV}}$
$p_1$	20.8	25.8	keV
$p_2$	0.0011	0.0040	1

Table 7.1: Time-averaged resolution parameters for the single-site and multi-site denoised dataset [142].

olution functions measured for both classes of events.

The resolution functions are measured using only the cobalt and thorium calibration gamma lines (at 1173, 1332, and 2615 keV). The resolution parameters are time-dependent; average resolution parameters are computed by weighting the resolutions observed in different time windows by the fraction of EXO-200 low-background data taken within that window. The resulting resolution parameters are listed in table 7.1. Figure 7.19 shows the resulting resolution functions. We can see that at our typical energies of  $\approx 2500$  keV the  $p_0$  and  $p_1$  terms dominate the resolution function of equation 7.9, and this manifests itself as a concave-downward shape in the absolute resolution function. The shape of these resolution curves can be interpreted as meaning that the electronic noise and Poisson fluctuations dominate our resolution; this may not be surprising, since we recall from section 4.10 that Poisson fluctuations were underweighted in the version of denoising implemented for this analysis. Our interpretation is only suggestive because the curvature is slight and the energy-dependent calibration effects cannot be ruled out, but it will be interesting to see how these terms change when future work addresses the underweighting of Poisson fluctuations.

It may be tempting, given that the topic of this work is a system for denois-

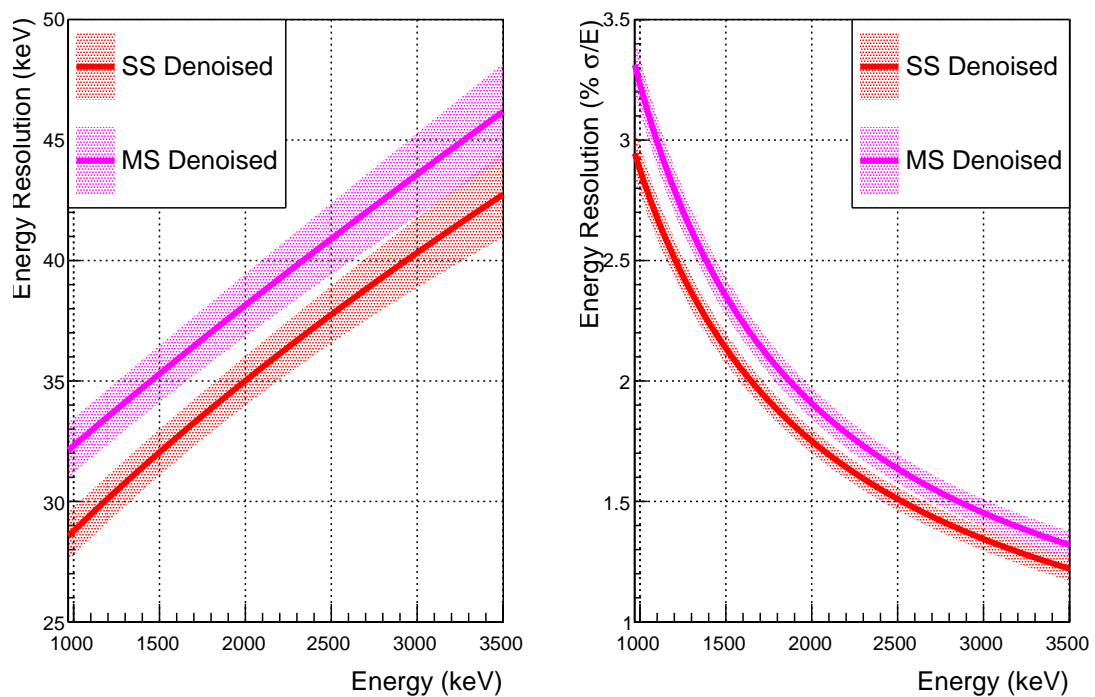


Figure 7.19: The time-averaged resolution functions (left) and relative resolution functions (right) for single-site (red) and multi-site (purple) denoised data. Shaded bands indicate uncertainties. Data provided by Caio Licciardi.

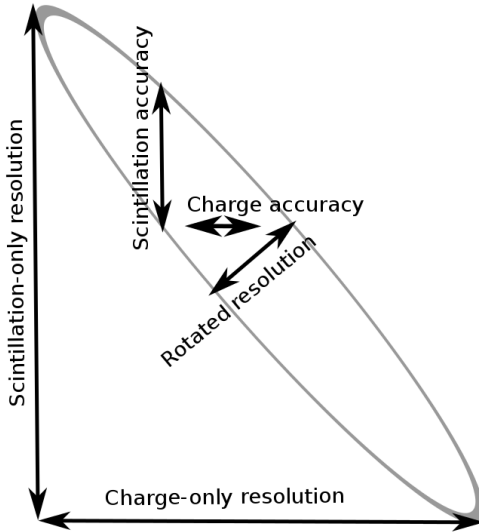


Figure 7.20: A typical monoenergetic gamma line, where the horizontal axis indicates ionization energy and the vertical axis indicates scintillation energy. We note that the ionization-only and scintillation-only resolutions are dominated by the length and angle of the island, which are dominated by xenon physics and the choice of electric field rather than the accuracy of the readouts in those channels.

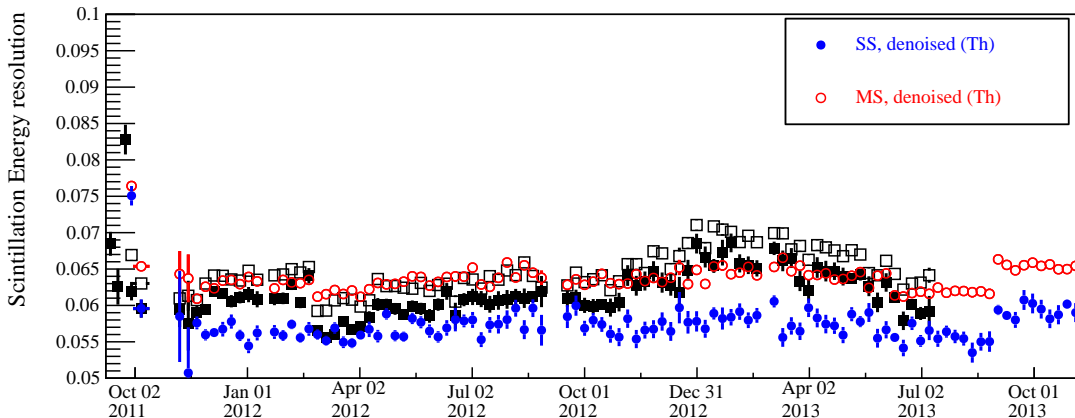


Figure 7.21: Scintillation-only resolution over time, including: single-site denoised (blue), multi-site denoised (red), single-site undenoised (black solid), multi-site undenoised (hollow square). Although denoising does show some improvement in the scintillation-only resolution, it is quite modest; this is because the scintillation-only resolution is dominated by fluctuations in light yield. [140].

ing scintillation waveforms, to prefer to focus on the scintillation-only resolution. However, the scintillation-only resolution is in fact dominated not by the accuracy of the readout system but by fluctuations in the fraction of deposited energy which is released in the scintillation channel. Figure 7.20 shows a schematic of a typical monoenergetic gamma line; the length and angle of the island represents the anti-correlation between light and charge. We can see that although the charge and light yield are highly correlated, individually they are also subject to significant fluctuations. A scintillation-only energy measurement is fundamentally limited by these fluctuations in light yield, and only to second order is it affected by the accuracy of our event-by-event measurements of light yield. A comparison between the denoised and undenoised scintillation-only resolution can be seen in figure 7.21, and as expected the improvement from denoising is quite modest. Considering that the scintillation-only energy measurement is not used in the final analysis and does not provide a window onto the performance of denoising, we will not consider it further in this work.

### 7.3.5 Cross-Checks on the Energy Calibration

The energy calibration is extracted from source data; the large quantity of source data leads to small statistical errors on the calibration constants. However, the calibration constants are time-dependent and it is valuable to have cross-checks verifying that the time-dependent nature of the calibration is accounted for properly.

To cross-check the time-dependence of the calibrations derived from sources,

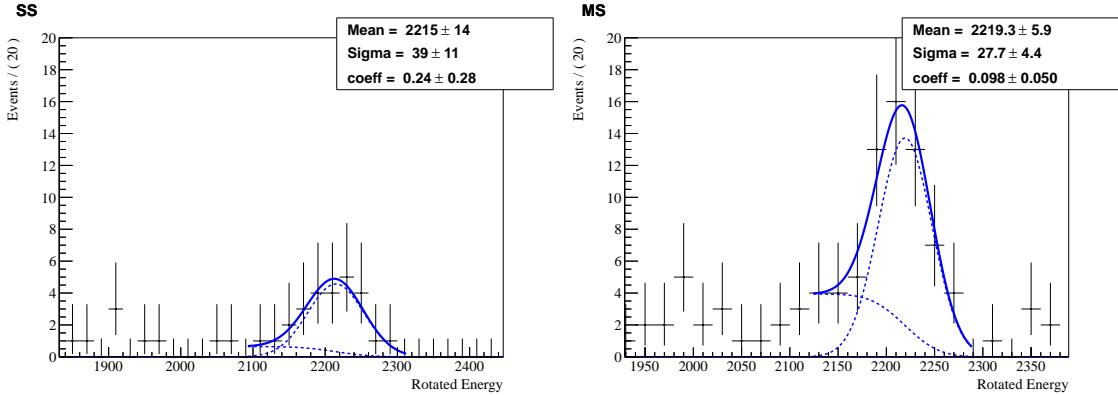


Figure 7.22: The single-site (left) and multi-site (right) gamma line at 2.2 MeV from neutron capture on hydrogen can be used as a low-background cross-check on the resolution calibration. Here, data which is coincident with a muon veto is shown to include the expected neutron capture peak [140].

we use gamma lines in the low-background data. These can verify that gamma lines from a wide range of times are combined to produce coherent peaks in our cumulative energy spectrum; they can also verify that the time-averaged resolutions extracted from source data are accurate because the resolution extracted from low-background peaks is inherently averaged over the duration of the data run. Two energy lines from the low-background spectrum have been identified as particularly useful.

One gamma line in the low-background data comes from neutron capture on hydrogen in the HFE-7000 refrigerant. Such events are generally vetoed by the coincidence cuts, primarily the veto panels, so their impact on the low-background data is suppressed; conversely, it is possible to study only events which occur in coincidence with muon detection by the veto panels, thereby enriching our dataset in neutron capture spectra. Neutron capture on hydrogen emits a 2.2 MeV gamma;

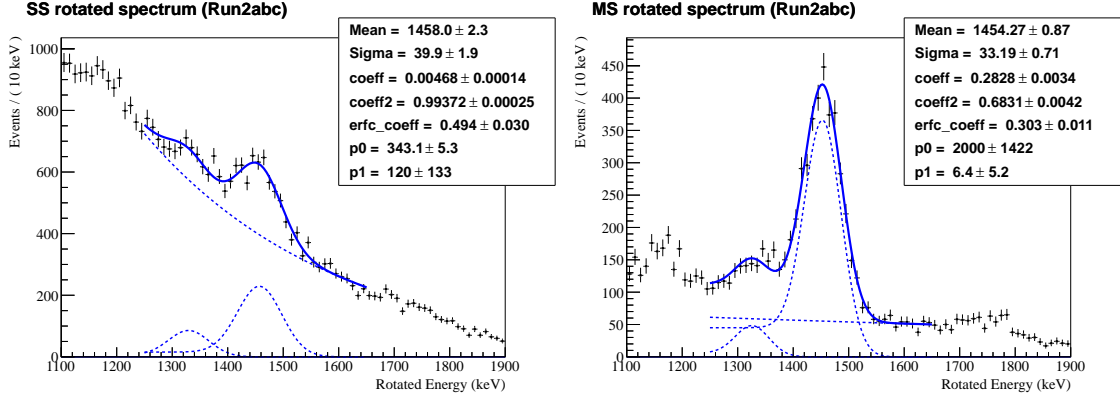


Figure 7.23: The low-background potassium peak at 1461 keV is used as a cross-check on the single-site (left) and multi-site (right) energy calibrations. Fits also include the nearby 1332-keV cobalt peak [140].

figure 7.22 shows the data which is produced by this source with a fit to a Gaussian function and simple background model. [99, 140].

The other gamma line which has been used as a cross-check is the 1461-keV  $^{40}\text{K}$  gamma line.  $^{40}\text{K}$  is expected to occur in the copper of the TPC at some low level, and this gamma line is readily visible in the multi-site spectrum of low-background data. The improved energy resolution of denoised data allows us to also identify the  $^{40}\text{K}$  single-site peak over the  $\beta\beta2\nu$  background, which was not previously possible. These peaks are shown in figure 7.23.

The result from combining all of these calibration points is shown in figure 7.24. We can see that all sources agree well with the calibration, indicating that the calibration derived from thorium and cobalt extends well to the other calibration sources and captures time-dependent calibration information well. (With 14 independent measurements under consideration, the  $2\sigma$  discrepancy of the 662 keV cesium multi-site peak position should not be considered significant.)

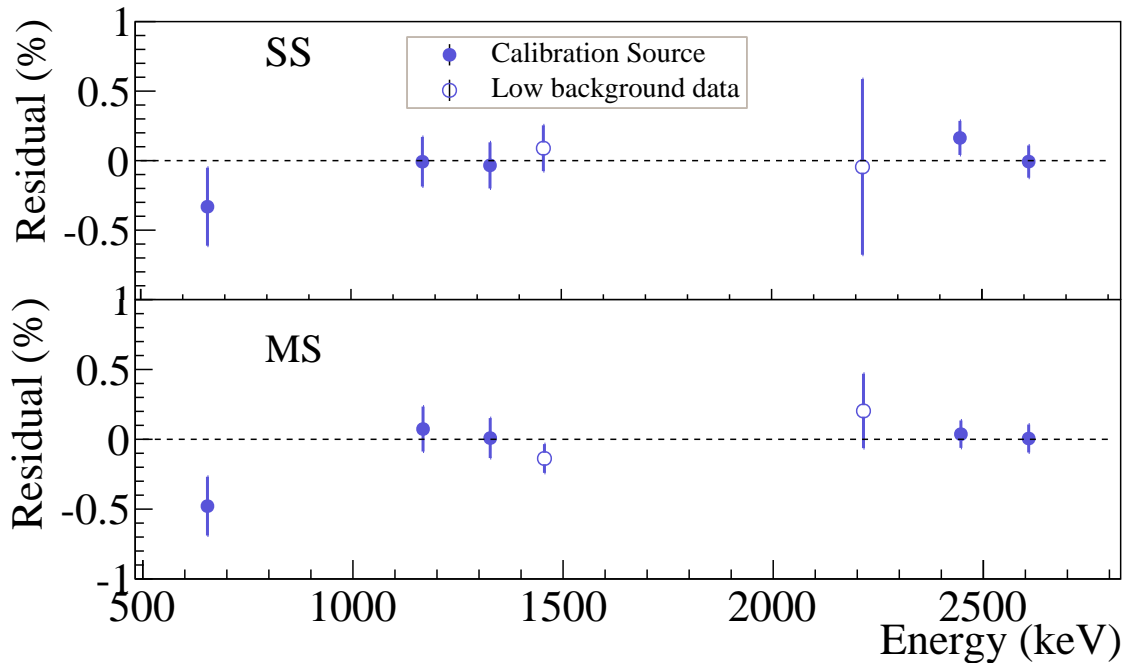


Figure 7.24: The residuals between calibrated and true peak positions for all sources is compared. Calibrations were obtained from the  $^{137}\text{Cs}$ ,  $^{60}\text{Co}$ , and  $^{232}\text{Th}$  peaks at 662, 1173, 1332, and 2615 keV. The peak from  $^{226}\text{Ra}$  at 2448 keV is also shown, but was not used for calibration. Low-background calibration lines are neutron capture on hydrogen (2200 keV) and  $^{40}\text{K}$  (1461 keV). Figure from [140].

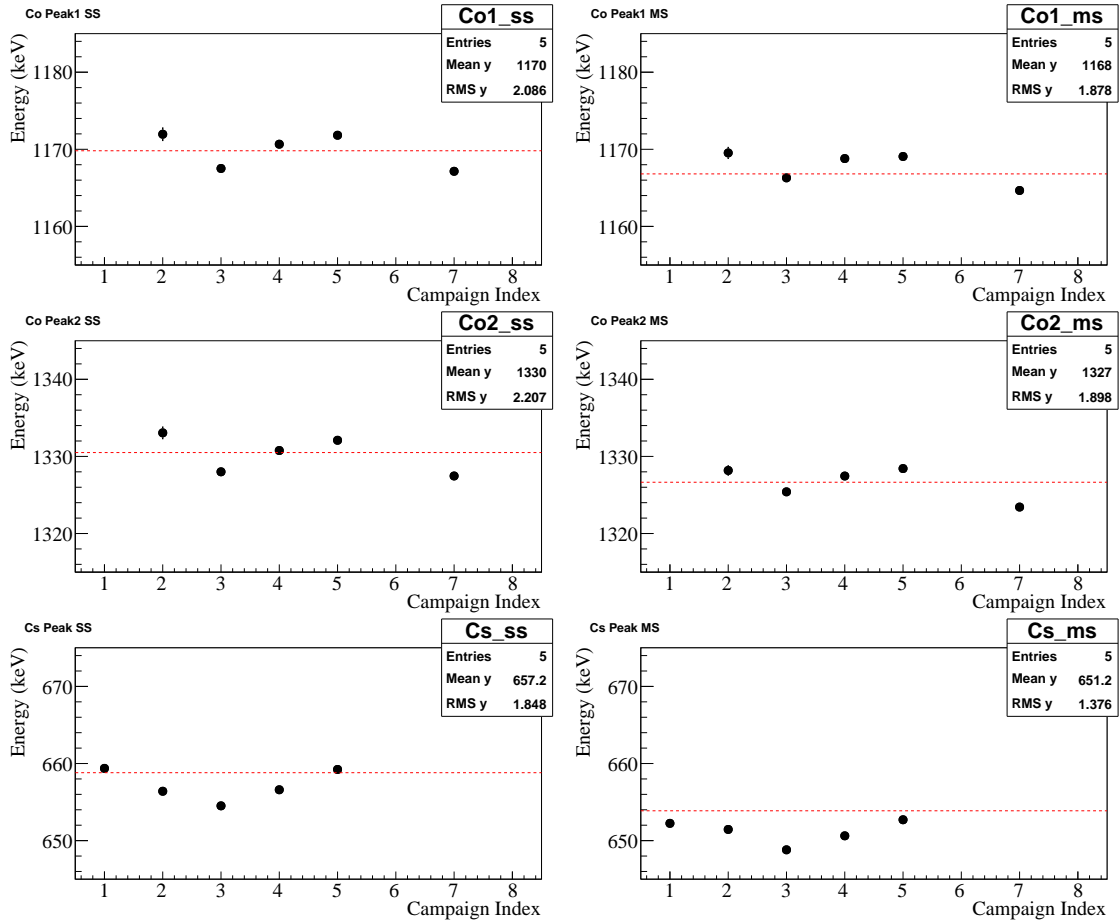


Figure 7.25: Time-dependence of the peak positions from all calibration campaigns. Error bars, when not visible, are smaller than the circle. Top row is the  $^{60}\text{Co}$  peak at 1173 keV; middle row is the  $^{60}\text{Co}$  peak at 1332 keV; bottom row is the  $^{137}\text{Cs}$  peak at 662 keV. Thorium is not included because it is used to measure the time-dependence of the peak positions, so it is necessarily calibrated to a time-independent value. Figure from [140].

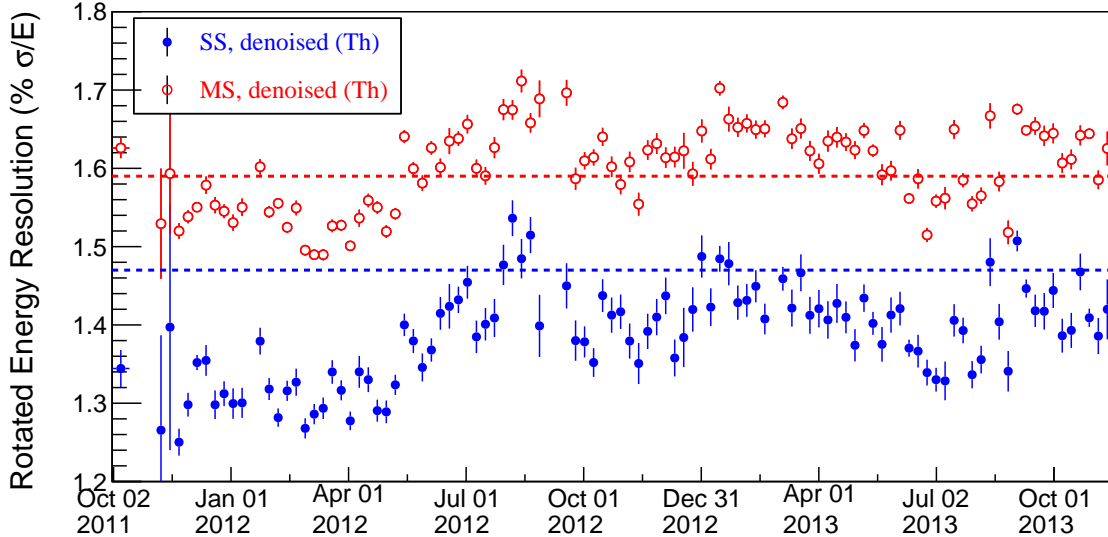


Figure 7.26: Time-dependence of the energy resolution at the  $^{208}\text{Tl}$  2615 keV gamma line. Single-site (blue) and multi-site (red) energy resolutions are shown. The time-averaged energy resolutions (1.47%  $\sigma/E$  for single-site, 1.59%  $\sigma/E$  for multi-site, both at 2615 keV) are shown in blue and red dashed lines, respectively. Data provided by Liangjian Wen.

We also use the calibration source peak positions to check that the calibrated peak positions remains constant over time. This is automatic for the thorium peak position at 2615 keV because that peak is used to measure the time-dependence of the calibration. However, if we see that the cesium calibrated peak position changes over time, for example, then this would indicate that the time-dependent calibration parameters  $\theta(t)$  and  $E_{rot}^{th}(t)$  of equation 7.8 are inadequate to describe the time-dependent behavior of the detector. The peak positions of cesium and cobalt are shown in figure 7.25. There we can see that indeed the peak positions of these sources do vary by more than their statistical error bars. In this analysis, the variations in peak position are treated as variations in the spectral shapes of sources and incorporated as a systematic effect [140, 143].

Lastly, it is necessary to study the energy resolution as a time-dependent quantity. This is only done with the thorium source because of the regularity of thorium runs that have been taken. The time-dependent resolution observed from thorium calibration runs is shown in figure 7.26. We can see that there are statistically significant variations in resolution over time; these, combined with the time-varying peak positions shown in figure 7.25, lead to a weakened time-averaged energy resolution which accounts for the smearing of low-background peaks over the span of our dataset [142].

The cross-checks described here identify features of the energy response which are not fully calibrated; these are treated as smearing effects over time and lead to a weakening of our time-averaged energy resolution. Future work will be targeted toward understanding the peak position variations with event position shown in figure 7.16 and with time shown in figures 7.25 and 7.26. Resolving these issues should lead to further improvements in the time-averaged resolution of EXO-200 in later analyses.

## 7.4 Fitting

After the energy calibrations have been performed, it is possible to produce a set of data with calibrated energy measurements. This section describes the selection of usable events from this dataset, the creation of corresponding background probability distribution functions (PDFs), the fitting of data to extract the best-fit number of  $\beta\beta0\nu$  events in the dataset, and the association of errors with that number. Re-

sults from the current analysis are demonstrated along the way, leading to a limit for  $\beta\beta0\nu$  decay.

It is necessary to perform a number of cuts on the dataset before it is usable. These cuts are intended to reject events which may not agree with the model used to generate background PDFs. These cuts are: [143]

- A fiducial volume cut to remove events with any energy deposits outside of a pre-defined volume. We choose to define a fiducial volume defined in Z by  $10\text{mm} < |Z| < 182\text{mm}$  and in the X-Y plane as the area within a hexagon with an apothem of 162 mm, as illustrated in figure 7.27. These cuts allow us to ignore regions near the detector walls or v-wire plane where the electric fields may not behave as expected. They also ensure that beta or alpha backgrounds from the walls of the detector do not penetrate into our fiducial volume, allowing us to simplify the set of backgrounds modeled and included in fits.
- A “diagonal” cut to remove events with excessive scintillation relative to ionization. Alpha decays produce a light-to-charge ratio much higher than beta and gamma decays, as described in section 3.4, so excluding events with excessive light permits us to neglect alpha-decay backgrounds dissolved in the xenon. Events with excessive light can also be caused by decays outside of our active xenon, where charge is not collected efficiently; these events will be difficult to calibrate, and should not be included. Both are excluded by a cut on the light-to-charge ratio, as shown in figure 7.17.

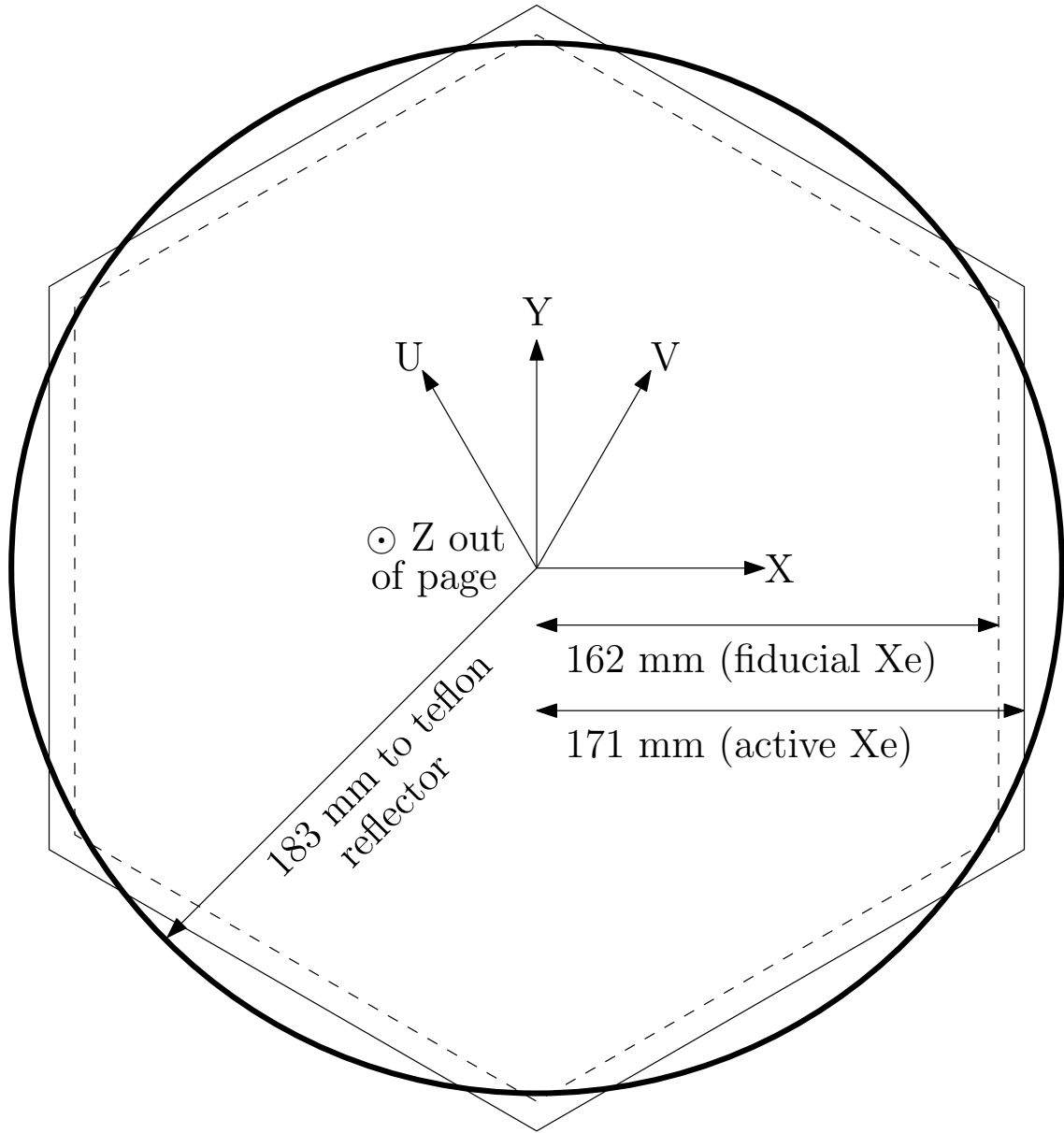


Figure 7.27: Here the X-Y orthogonal coordinates are shown along with the U-V coordinates that run orthogonal to the wire planes. The X-Y fiducial cuts applied to the data (dashed hexagon) do not include the entire active volume (solid hexagon); for the  $\beta\beta0\nu$  search we find that aggressive fiducial cuts optimize our sensitivity, so very little active xenon is left unused.

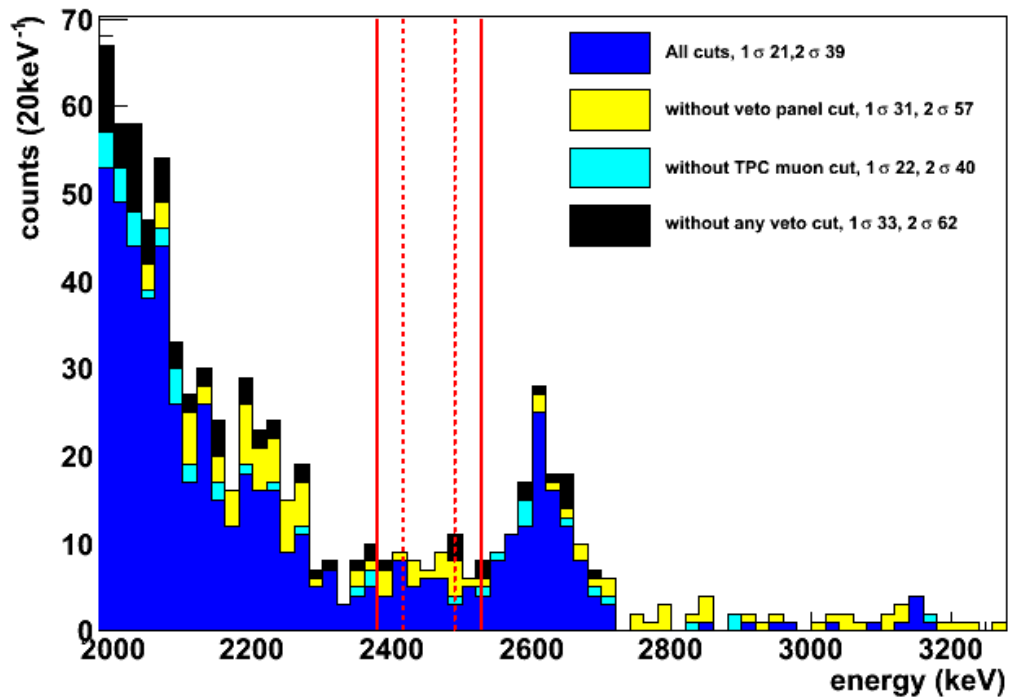


Figure 7.28: Vetoing events coincident with muons can reduce our  $1\sigma$  and  $2\sigma$  event counts. Figure provided by David Auty.

- A coincidence cut to remove events occurring near in time to a passing muon.

Muons and their spallation products can produce a wide range of backgrounds which is difficult to model; most of these backgrounds are quite short-lived, so a coincidence cut can provide an effective means of reducing them. Currently we cut all events occurring within one minute of a muon observed passing directly through the TPC and within 25 ms after a muon observed passing through the veto panels. Furthermore, events which occur within one second of each other are both cut based on the expectation that the events were probably correlated and therefore more likely to be some form of background. Figure 7.28 demonstrates the significant reduction in data rate which is achieved by applying this coincidence cut.

The fiducial volume identified above corresponds to a fiducial  $^{136}\text{Xe}$  mass of 76.3 kg; for our livetime of  $477.60 \pm 0.01$  days identified at the beginning of the chapter, the dataset has a combined  $^{136}\text{Xe}$  exposure of 99.8 kg-years [89].

Probability distribution functions (PDFs) must also be formed from Monte Carlo data which reflects the spectrum expected from different sources. We have discussed the simulation of these datasets in section 7.1, and noted that the simulations are sufficiently realistic that they are reconstructed in exactly the same way as data. However, we cannot hope to measure energy in simulation and data the same way because the scintillation pulse amplitudes are not simulated realistically.

Instead, energy is taken directly from simulation and smeared by the energy resolution function which has been measured from data. Smearing is performed by

first producing a binned perfect-resolution PDF which models perfect energy resolution, and then looping over the bins of the perfect-resolution PDF and smearing each bin by a Gaussian function with width equal to the absolute resolution at that energy [143].

Fits are then performed using the profile-likelihood method, as described in [144]. An energy window of 980-9800 keV is used; this window is chosen to avoid lower-energy parts of the spectrum where pdf shape agreement is poor [89]. Each data point is assigned a likelihood  $\text{PDF}(x)$  equal to the evaluation of the normalized PDF at that point; the test statistic of interest is the negative log-likelihood (NLL), defined by:

$$\text{NLL} = - \sum_i \ln [\text{PDF}(x_i)] + \text{constraints}. \quad (7.11)$$

Constraints are Gaussian penalty terms applied to parameters whose value is constrained by independent studies external to the fit. The best fit is the one which minimizes the NLL. Fit errors on parameters are extracted by observing how the NLL changes when those parameters are forced away from their best-fit values;  $1\sigma$  limits are placed where the NLL changes by 0.5 units from its best-fit value, and 90% limits are placed where the NLL changes by 1.35 units from its best-fit value. In cases where the best-fit value of a parameter is near its boundary, these errors may not provide a good estimate of the true confidence interval or limits, so when this situation occurs for a parameter of significant interest (specifically, the rate of  $\beta\beta\nu$ , which fits near to zero) we can verify that the confidence limit is not overstated using

toy Monte Carlo studies [143].

The fits make use of three observables. The first, event energy, has been discussed at length in section 7.3.3. The second is the event classification as single-site or multi-site; we define an event as single-site if reconstruction located only one cluster, and that cluster deposited charge on no more than two u-wire channels [143]. This choice of definition ensures that a dense cloud of charge which approaches the anode at a midpoint between two u-wire channels and gets split apart will still be counted as single-site.

The third observable is called standoff distance, and it attempts to capture the nearness of an event to the TPC walls. Most backgrounds are external, and can be expected to deposit energy preferentially near the walls of the TPC; by contrast,  $\beta\beta0\nu$  and  $\beta\beta2\nu$  decay come from the xenon, and should be distributed uniformly through the detector. We define the standoff distance to be the shortest distance between some deposit cluster and either the v-wire planes or the teflon walls. Ideally, it would be possible to capture finer position information by using all three position coordinates as observables; however, in practice it is difficult to construct a PDF with sufficient statistics in so many dimensions, so the standoff observable has been constructed to capture the most interesting distances in a single observable. The exact definition is not too important provided it is modeled properly by the simulation; figure 7.9 demonstrates that standoff distance is simulated well for all but the smallest values (closest to the TPC walls or anode), and this is accounted for as a shape systematic [143].

Fit parameters include the number of counts observed from each PDF and the

fraction of counts from each PDF which populate the single-site spectrum; the latter is constrained based on the agreement between simulated and observed single-site fraction from source runs, but is allowed to float within those uncertainties. The PDFs which are included are:

- $^{136}\text{Xe}$   $\beta\beta2\nu$  decay.
- $^{136}\text{Xe}$   $\beta\beta0\nu$  decay.
- $^{232}\text{Th}$  from the TPC vessel.
- $^{232}\text{Th}$  from distant sources (HFE-7000 refrigerant or cryostat).
- $^{238}\text{U}$  from the TPC vessel.
- $^{214}\text{Bi}$  from the TPC cathode ( $^{238}\text{U}$  chain).
- $^{214}\text{Bi}$  from the air gap inside the lead wall ( $^{238}\text{U}$  chain).
- $^{214}\text{Pb}$  dissolved in active xenon ( $^{238}\text{U}$  chain).
- $^{222}\text{Rn}$  dissolved in inactive xenon ( $^{238}\text{U}$  chain).
- $^{60}\text{Co}$  from the TPC vessel.
- $^{40}\text{K}$  from the TPC vessel.
- $^{65}\text{Zn}$  from the TPC vessel.
- $^{54}\text{Mn}$  from the TPC vessel.
- $^{137}\text{Xe}$  from neutron capture on  $^{136}\text{Xe}$ .

- $^{135}\text{Xe}$  from neutron capture on  $^{134}\text{Xe}$ .
- Various neutron captures on xenon, copper, and hydrogen.

Similar PDFs from different locations are included because the sharpness and relative intensity of peaks can be affected by intervening material. The rate of  $^{214}\text{Bi}$  from the air gap is constrained by measurements of radon levels in air, and the rates of  $^{214}\text{Bi}$  from the TPC cathode,  $^{214}\text{Pb}$  dissolved in active xenon, and  $^{222}\text{Rn}$  dissolved in inactive xenon are jointly constrained by independent searches for  $^{214}\text{Bi}$ - $^{214}\text{Po}$  rates. The overall rate of neutron captures is allowed to float, but the relative intensities of the captures on xenon, copper, and hydrogen are constrained by simulation, and the single-site fraction is fixed because there are not expected to be sufficient statistics in the single-site spectrum to constrain it [143].

In addition to the magnitude and single-site fraction parameters of the fit, there are a few global parameters which are also allowed to float. There is a normalization constant which is allowed to float within constraints and accounts for uncertainty in the fiducial volume or detection efficiency. Constraints on this term come from comparisons between the predicted and observed event rate from sources. Denoising does not currently operate on events whose waveforms are shorter than the standard length of  $2048\mu\text{s}$ ; since these occur more in source data than low-background data, an additional correction to the simulated event rate must be generated, and denoising may in this way worsen the event rate agreement in source data even though it is not expected to show a significant effect in low-background data. Additionally, the normalization constants for gamma and beta particles are

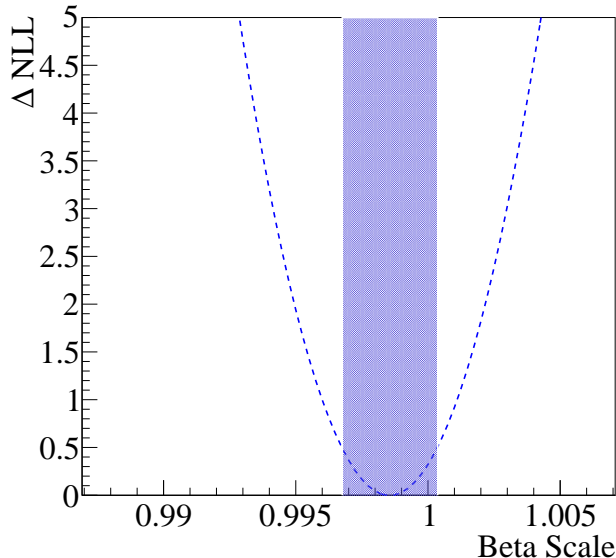


Figure 7.29: The fit provides constraints on the beta-scale. Figure provided by Liangjian Wen.

allowed to float separately because their reconstruction efficiency may be different.

Furthermore, it is expected that betas and gammas may need to be calibrated separately. To a first approximation, gammas deposit energy in the detector by exciting electrons, so these processes should be quite similar. However, to account for possible differences, we define a beta-scale  $\beta$  which quantifies a linear calibration offset between beta and gamma deposits:

$$E_\beta = \beta E_\gamma. \quad (7.12)$$

The beta scale is permitted to float, and is constrained by the fit; figure 7.29 shows the NLL profile with various choices of beta scale, and demonstrates that it is possible to constrain the beta scale to a value close to 1 using only the spectral

information in the fit. Uncertainty on the beta scale is incorporated by permitting it to float freely. We note that currently the beta scale is implemented by shifting beta-like PDF components ( $\beta\beta0\nu$ ,  $\beta\beta2\nu$ ,  $^{135}\text{Xe}$ ,  $^{137}\text{Xe}$ ) relative to the other components which are gamma-like; this ignores the detail that some events may contain clusters generated through both beta and gamma interactions, such as pair production from energetic gammas. These issues will be addressed in a future analysis, but for now the beta scale is assigned only to decays whose primary particle is a beta [143].

When all of this is done, it is possible to obtain a fit to the low-background spectrum; the maximum-likelihood fit is shown in figure 7.30. The best-fit expected background in the  $2\sigma$  single-site energy window around our  $Q$ -value is  $31.1 \pm 1.8(\text{stat}) \pm 3.3(\text{sys})$  counts, corresponding to a background rate of  $(1.7 \pm 0.2) \cdot 10^{-3}\text{keV}^{-1}\text{kg}^1\text{yr}^1$ . The backgrounds in this  $2\sigma$  energy window come from the thorium decay chain (51%), uranium decay chain (26%), and  $^{137}\text{Xe}$  (23%), with other contributions negligible. The observed event count in the  $2\sigma$  single-site energy window is 39 counts [89].

(We remind the reader at this point that the quoted limit on  $\beta\beta0\nu$  is not simply based on this comparison of counts, but based on the full set of energy and standoff-distance spectral information. Representative position information can be seen in figure 7.31. However, the simple comparison of counts can be instructive as an easier-to-understand approximation to the following limits.)

The likelihood profile for the total number of  $\beta\beta0\nu$  counts occurring in our detector during the lifetime of the experiment is shown in figure 7.32. Based on the profile, we can see that a  $1\sigma$  confidence interval for this parameter would exclude

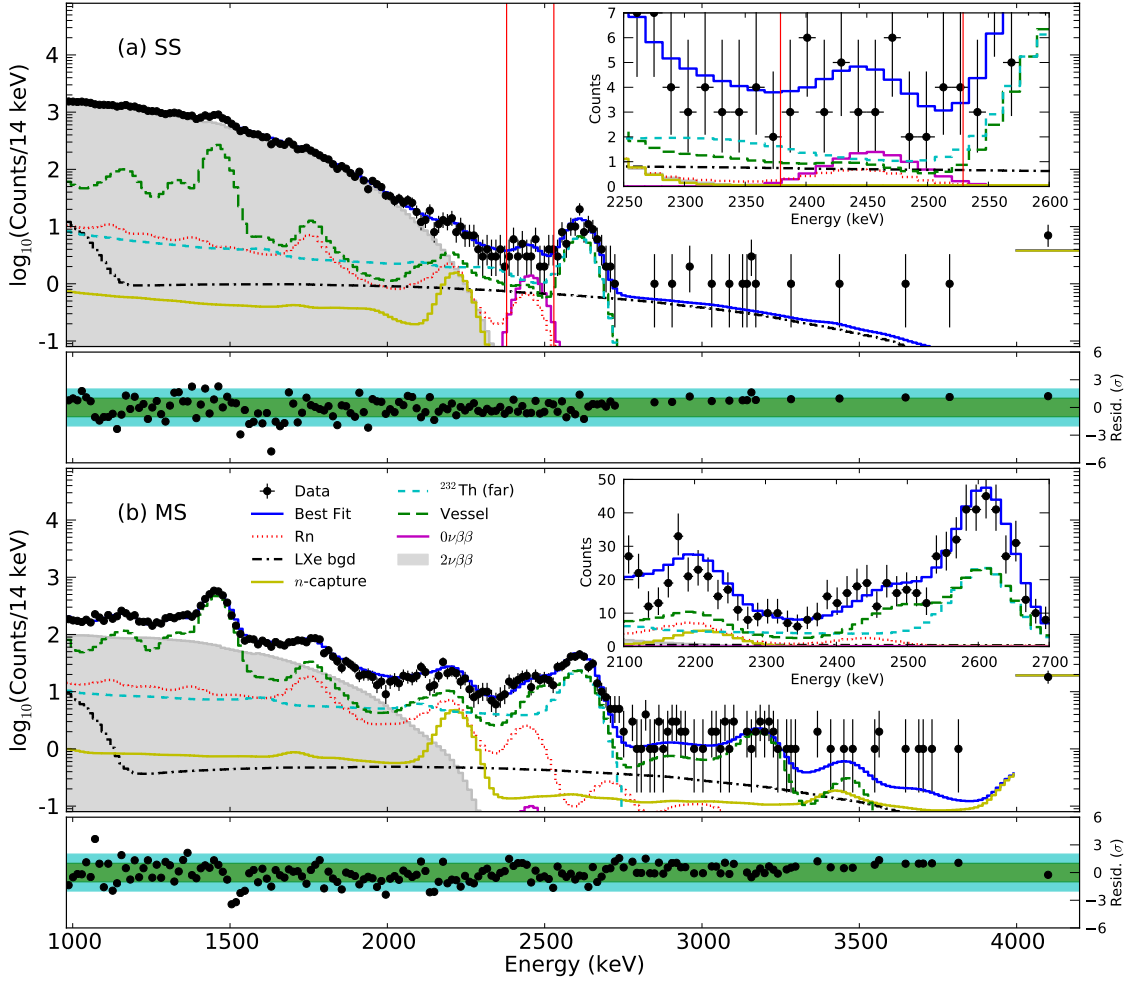


Figure 7.30: Energy spectra with best-fit PDFs for single-site (top) and multi-site (bottom). Residuals between data and the combined PDFs are shown below the spectra. The last bin of the spectra is an overflow bin. The  $2\sigma$  region of interest around the  $Q$ -value is shown on the single-site spectrum. Insets for single-site and multi-site zoom around the  $Q$ -value. The simultaneous standoff-distance fit is not shown [89].

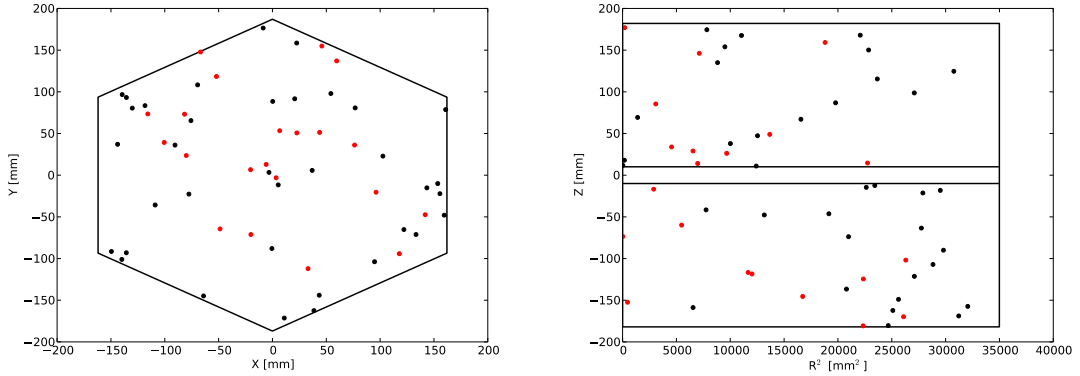


Figure 7.31: The positions of events in the  $1\sigma$  region of interest (red) and wider energy range 2325 – 2550 keV (black) are shown projected onto their X-Y (left) and  $R^2$ -Z (right) coordinates. Lines indicate the fiducial volume. Figure provided by Dave Moore.

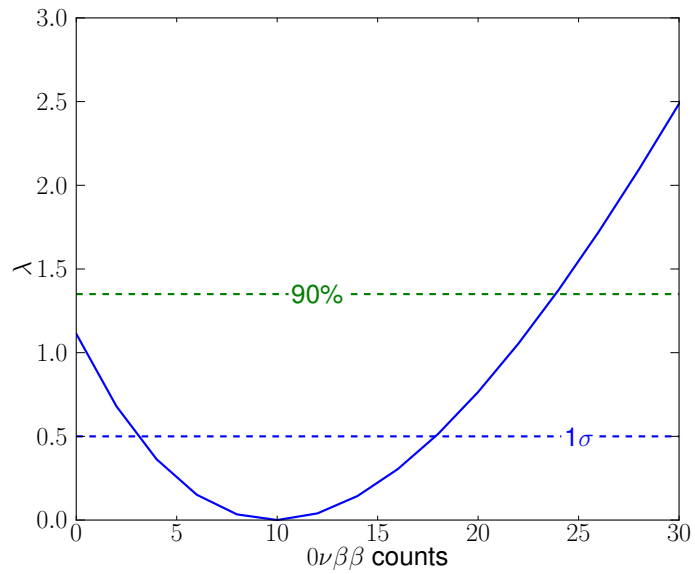


Figure 7.32: Profile scan of negative log-likelihood as a function of the number of fit  $\beta\beta 0\nu$  counts [89].

the null hypothesis of zero  $\beta\beta0\nu$  counts; however, only  $1\sigma$  exclusion of the null hypothesis is far too weak to make an inference of a non-zero signal. Instead, we follow the conventions of the field and quote a 90%-confidence upper limit of 24 total counts from  $\beta\beta0\nu$ . This corresponds to a 90%-confidence lower limit on the half-life of  $^{136}\text{Xe}$  decay by the  $\beta\beta0\nu$  mode of  $1.1 \cdot 10^{25}$  years [89].

## 7.5 Results and Physics Reach

We have stated the half-life limit on  $\beta\beta0\nu$  decay of  $^{136}\text{Xe}$ , which is the main result of the present analysis. We shall now continue to put this result in context with the expected sensitivity of the experiment and compare it to the limits and sensitivities achieved by other leading  $\beta\beta0\nu$  experiments.

To place the limit derived with the current dataset in context with the overall strength of the experiment, we generate a number of toy Monte Carlo datasets. We assume that our best-fit backgrounds are fully accurate and that the null hypothesis (no  $\beta\beta0\nu$ ) is true; we then use this best-fit background as our PDF and generate toy datasets. These can be used to study the “typical” results our detector would have produced if the same experiment could be repeated many times.

The resulting distributions are shown in figure 7.33. The top plot shows the distribution of 90%-confidence upper limits on the number of  $\beta\beta0\nu$  counts; we can see that typical datasets from the EXO-200 experiment result in limits ranging from 8 to 22 counts. The median limit, is 14 counts; this value is called the median sensitivity, and it illustrates the overall strength of an experiment. We contrast this

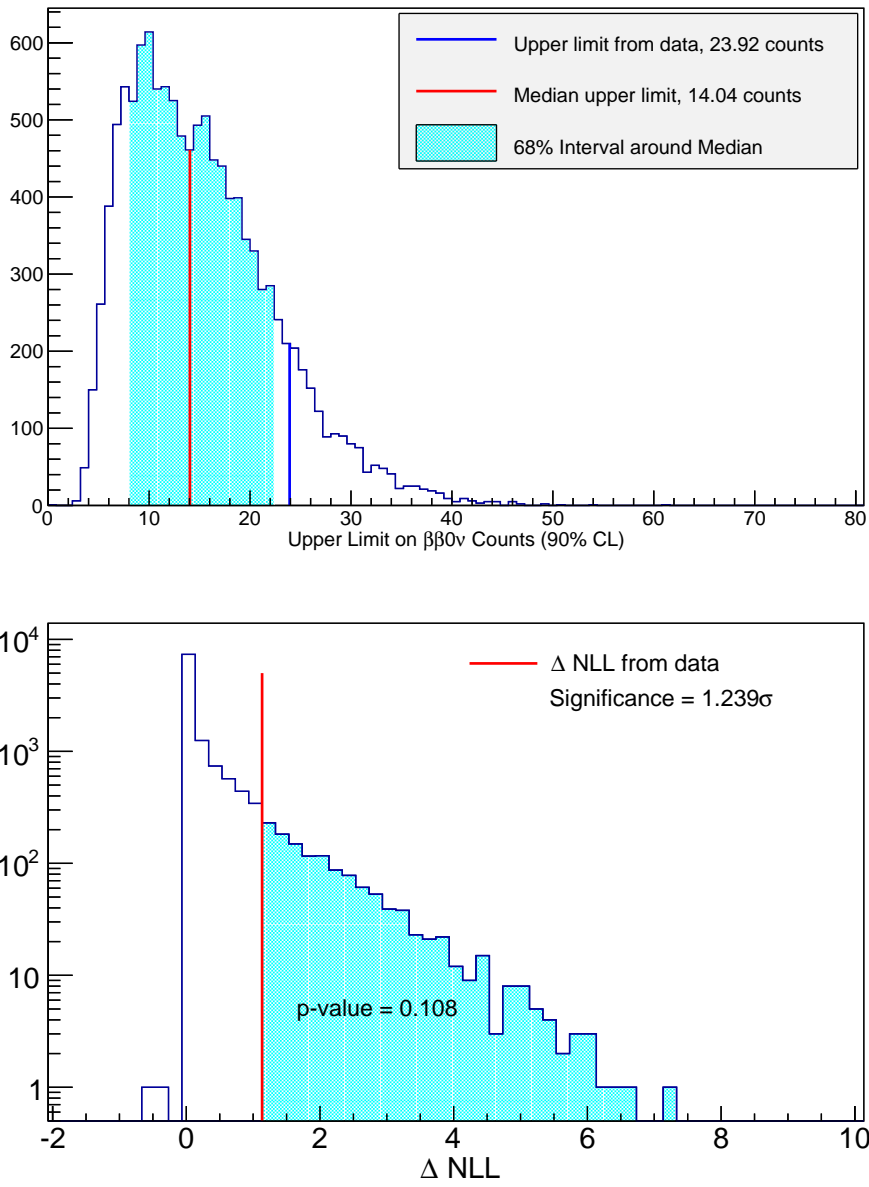


Figure 7.33: Assuming that the background measurements of EXO-200 from this analysis are accurate, toy datasets are simulated. The top plot shows the probability distribution of our 90% confidence limit; we find that our median upper limit is 14.04 counts attributed to  $\beta\beta0\nu$ , compared to our observed upper limit of 23.92 counts. The bottom plot shows the probability distribution of our ability to reject the null hypothesis (no  $\beta\beta0\nu$ ) based on the negative log-likelihood; we find that the present dataset rejects the null hypothesis with probability less than 90%. Figures provided by Ryan Killick.

with the observed limit of 24 counts; as is apparent from the distribution, this limit is consistent with an unlucky upward fluctuation in the backgrounds observed by EXO-200.

We saw in the NLL profile on the total number of  $\beta\beta0\nu$  counts in figure 7.32 that the NLL for the hypothesis of no  $\beta\beta0\nu$  counts is about 1.1 higher than for the best fit; this quantity reflects how well we can reject the null hypothesis in favor of the best fit. To put this in context, we also observe the distribution of this value from toy Monte Carlo datasets in the bottom plot of figure 7.33. Here, we see that 10.8% of identical experiments will yield an NLL profile which is at least 1.1 worse for no  $\beta\beta0\nu$  than for the best fits even though no  $\beta\beta0\nu$  is simulated. We can conclude that this difference in NLL is not strong enough to reject the null hypothesis with high confidence.

The wide spread of limits produced in toy Monte Carlo studies illustrates the significant role that luck plays in the limits set by low-statistics experiments such as EXO-200. To compare EXO-200 to other experiments, it is useful to compare both the limits and the median sensitivities (median 90% confidence limits). This is done in figure 7.34. Vertical lines correspond to the reported median sensitivities of the two leading  $^{136}\text{Xe}$  experiments, KamLAND-Zen and EXO-200; right-pointing arrows indicate the actual limits set by each. For both experiments we can see that statistical fluctuations in the background account for factor-of-two differences between median sensitivity and observed limits; EXO-200 claims to be the most sensitive  $^{136}\text{Xe}$  experiment, but KamLAND-Zen currently reports the strongest limit. Both experiments intend to continue running, and EXO-200 hopes that their next

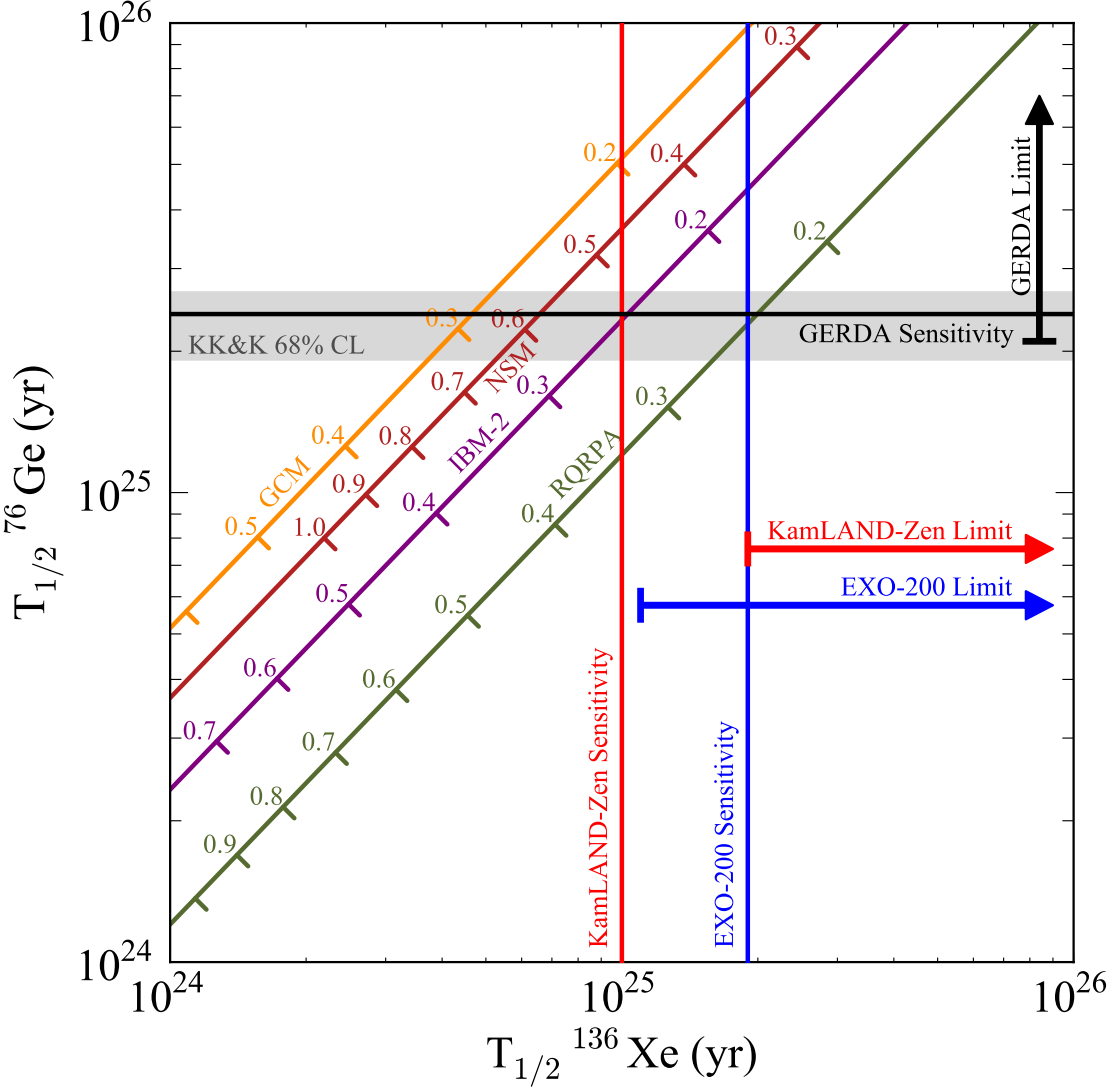


Figure 7.34:  $\beta\beta0\nu$  constraints are shown from  $^{136}\text{Xe}$  (horizontal) and  $^{76}\text{Ge}$  (vertical). The four diagonal lines represent four recent matrix element computations [71, 145–147] and one recent phase-space factor [94] relating the two half-lives; tick marks along the diagonal represent the corresponding mass  $\langle m_{\beta\beta} \rangle$ . 90% confidence limits and median 90% sensitivities are shown for the KamLand-Zen [13], GERDA [15], and EXO-200 experiments [89]; the claimed 2006 discovery by Klapdor-Kleingrothaus and Krivosheina is shown as a  $1\sigma$  confidence interval [148].

dataset is atypical in the other way.

Nuclear matrix elements have large uncertainties, as described in 2.3. Figure 7.34 illustrates four diagonal lines corresponding to four different modern nuclear matrix calculations, and uses these values to relate the half-lives of  $^{136}\text{Xe}$  and  $^{76}\text{Ge}$ . The current median sensitivity and limit on the  $\beta\beta0\nu$  half-life of  $^{76}\text{Ge}$  from GERDA are shown as a horizontal line and vertical arrow, respectively. This is contrasted with the 2006 claimed discovery by Klapdor-Kleingrothaus and Krivosheina of  $\beta\beta0\nu$  decay, which is not excluded by the more recent GERDA limit.

Furthermore, the nuclear matrix elements permit us to translate half-life lower limits into upper limits on the effective Majorana neutrino mass  $\langle m_{\beta\beta} \rangle$ . The relation is indicated, for each choice of nuclear matrix elements, by tick marks on the corresponding diagonal line. We can see that the GERDA and EXO-200 experiments are of similar strengths, depending most on the choice nuclear matrix elements; KamLAND-Zen is comparable in strength to GERDA for the RQRPA nuclear matrix elements, and stronger for all other choices in this plot. The 90%-confidence mass limit quoted by EXO-200 is  $\langle m_{\beta\beta} \rangle < 190 - 450$  meV, depending on the choice of matrix elements. Recalling figure 2.8, this corresponds to a 90%-confidence limit on the mass of the lightest neutrino eigenstate of  $m_{min} < 0.691.63$  eV under the most conservative choice of Majorana phases [89].

Parameter	Undenoised		Denoised	
	SS	MS	SS	MS
$p_0$	0	0	0.628	0.602
$p_1$	39.8	43.0	20.8	25.8
$p_2$	0.0107	0.0096	0.0011	0.0040
% $\sigma/E$ at $Q$ -value	1.94	2.00	1.53	1.65

Table 7.2: Time-averaged resolution parameters for denoised and undenoised data. For undenoised data, measurements were consistent with  $p_0 = 0$ , so this parameter was not used in the analysis of undenoised data. The resulting time-averaged resolutions at our  $Q$ -value are also shown [142].

## 7.6 Comparison to Results without Denoising

The results presented in section 7.5 are obtained using the most up-to-date analysis techniques adopted by the EXO-200 collaboration. These include the denoising technique described in chapter 4. In this section we compare physics results with and without denoising and demonstrate the degree to which resolution gains from denoising strengthen the EXO-200 result. We begin with a comparison of the energy measurements in section 7.6.1, and then proceed to a comparison of the physics results in section 7.6.2.

### 7.6.1 Comparison of Energy Resolution and Calibration

The process of denoising visibly sharpens source spectra, leading to easier extraction of peak positions and widths. Single-site source spectra for representative runs are shown in figures 7.35, 7.36, 7.37, all of which show significantly sharper peaks after denoising. The rest of this section will contrast the calibrations of energy and resolution for the two datasets.

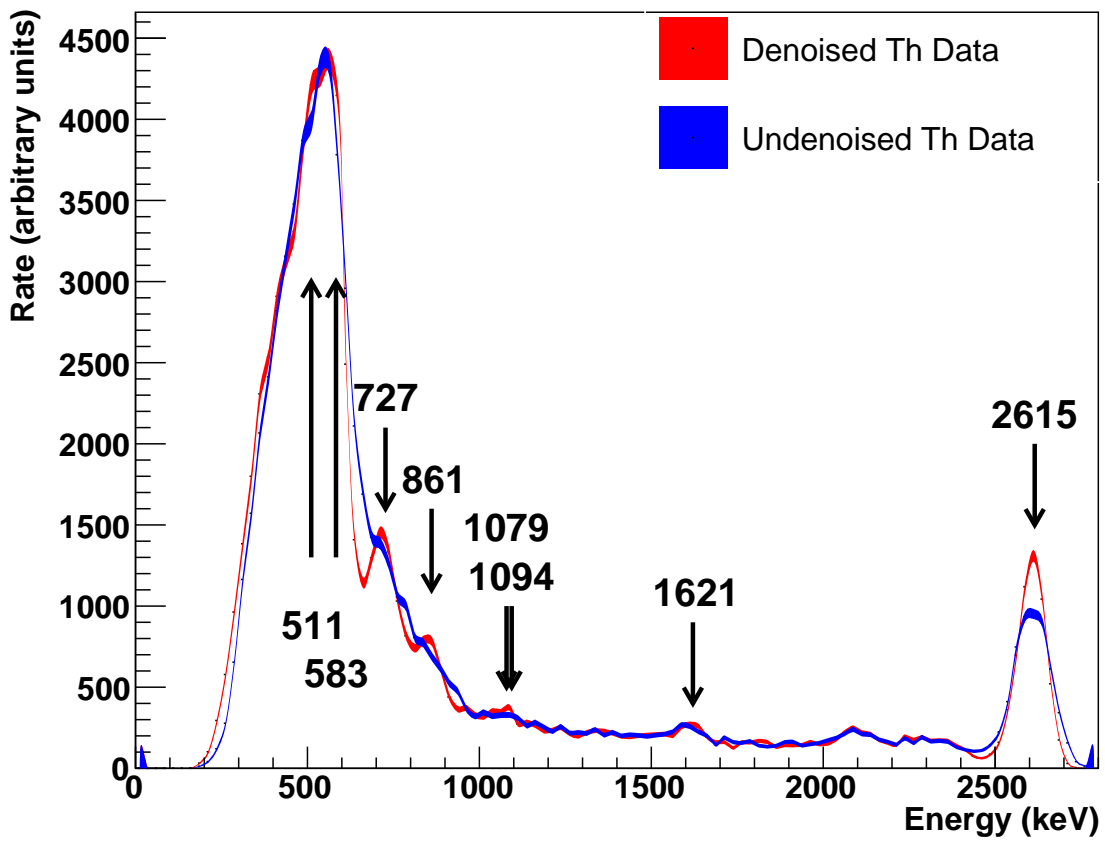


Figure 7.35: A comparison of the spectra before and after denoising for a set of representative thorium source runs (4758 and 4766). The thickness of the lines indicate Poisson error bars on the number of counts in a bin; smoothing is applied to the spectra to permit easier comparison of peaks. Important gamma lines are indicated. Around 500-600 keV threshold effects become significant, making comparison difficult.

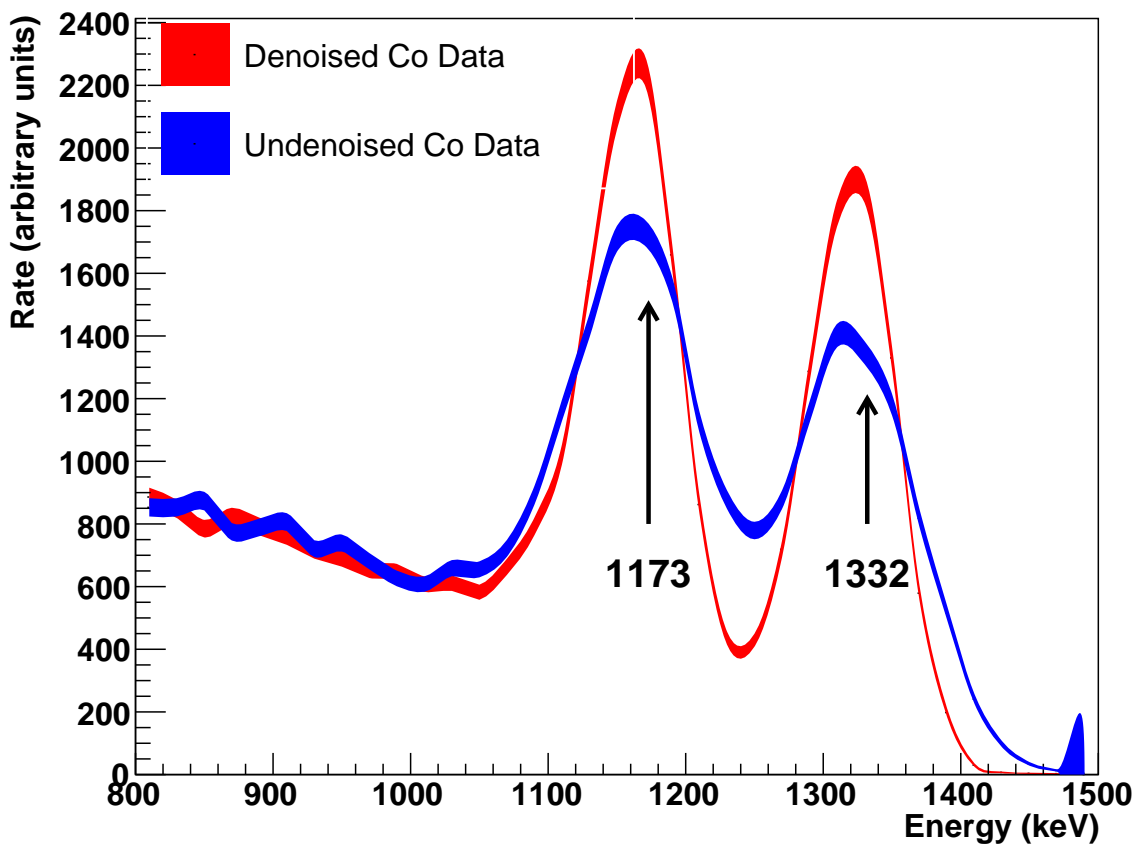


Figure 7.36: A comparison of the spectra before and after denoising for a representative cobalt source run (4787 and 4788). The thickness of the lines indicate Poisson error bars on the number of counts in a bin; smoothing is applied to the spectra to permit easier comparison of peaks. The two gamma lines of  $^{60}\text{Co}$  are indicated.

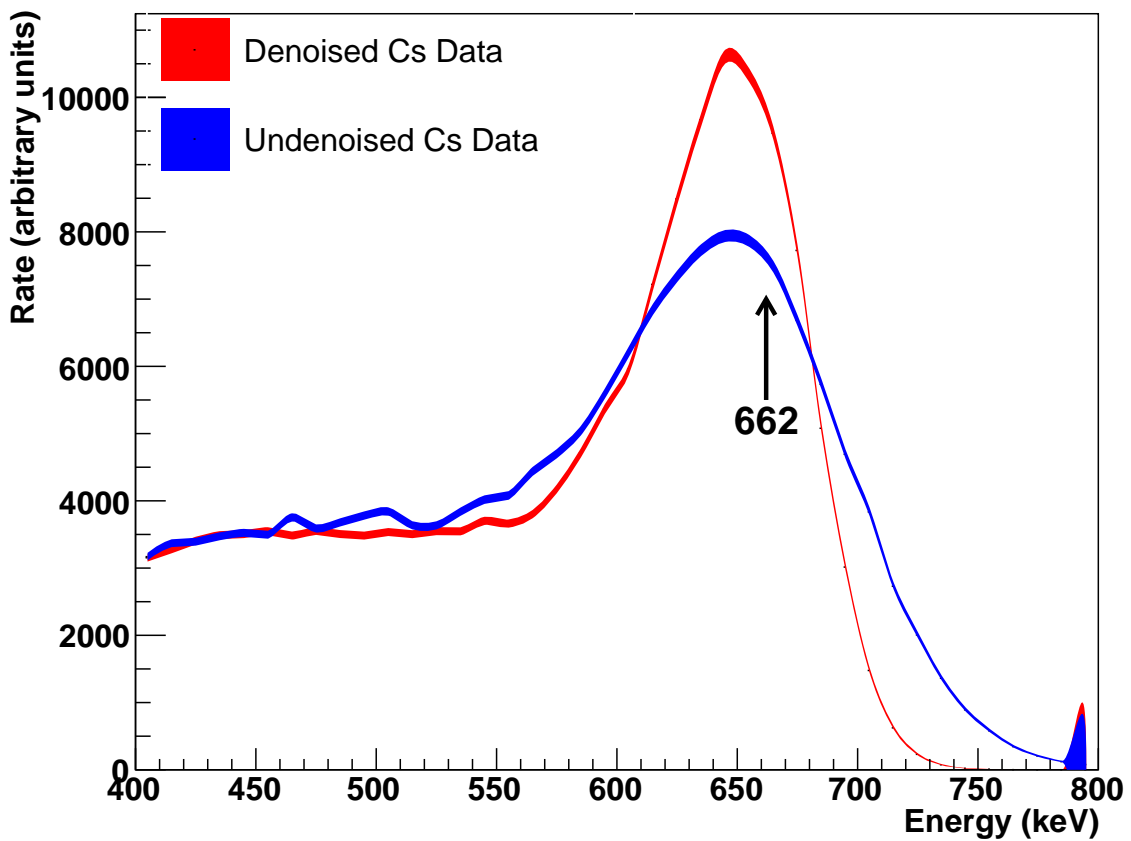


Figure 7.37: A comparison of the spectra before and after denoising for a representative cesium source run (4777-4781). The thickness of the lines indicate Poisson error bars on the number of counts in a bin; smoothing is applied to the spectra to permit easier comparison of peaks. The gamma line of  $^{137}\text{Cs}$  is indicated. Threshold effects are significant at this energy and the calibration is extrapolated from higher-energy sources, but the spectra illustrate the fact that resolution improves dramatically at low energy.

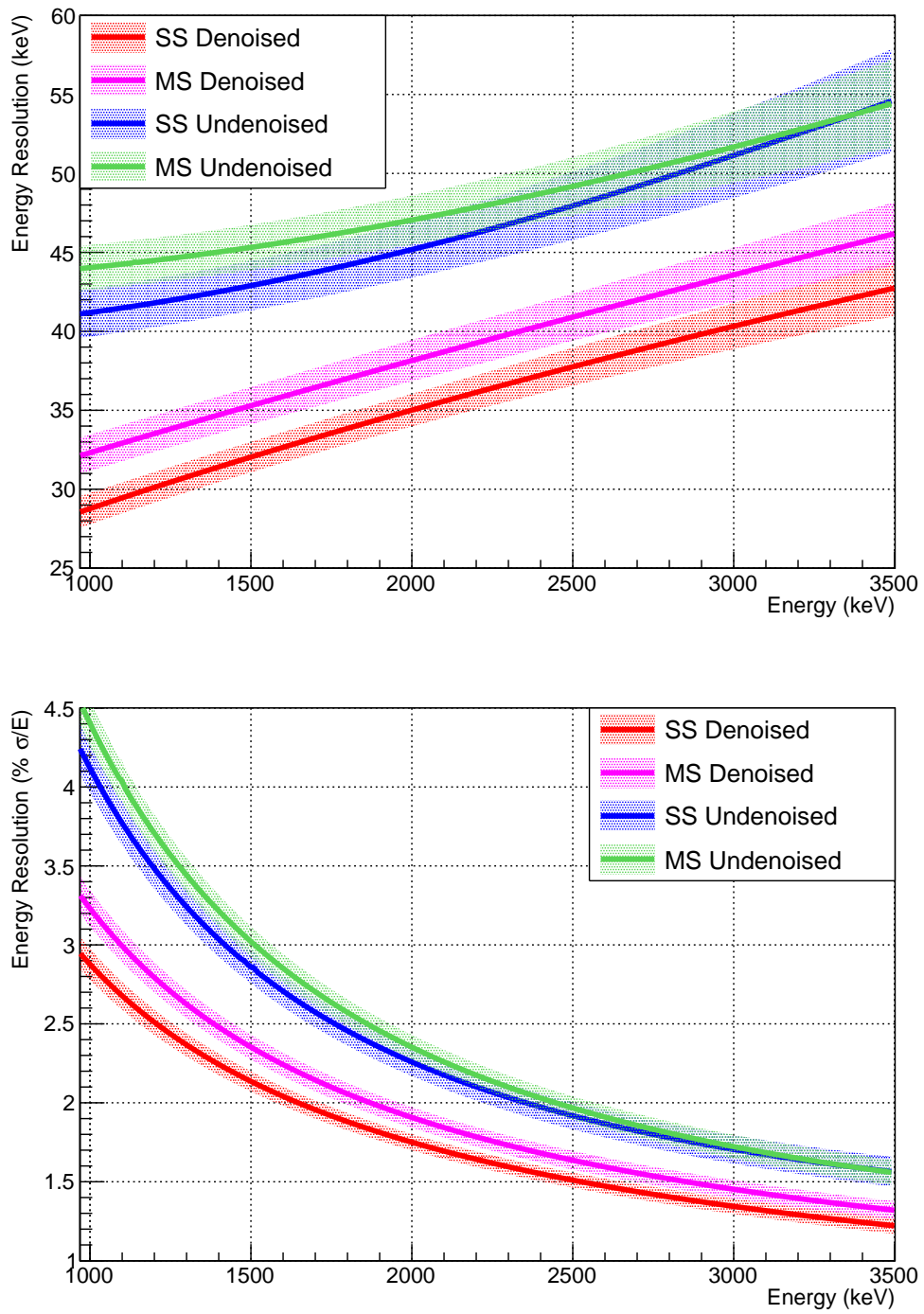


Figure 7.38: The time-averaged resolution functions (top) and relative resolution functions (bottom) are compared for denoised and undenoised data. Bands indicate uncertainties. Data provided by Caio Licciardi.

The energy resolution parameters with and without denoising, using the parametrization defined in equation 7.9, are listed in table 7.2. The undenoised resolution functions have fixed  $p_0 = 0$  because fits with undenoised data led to resolution functions consistent with zero. The resolution functions are compared in figure 7.38. The resolution at our  $Q$ -value is also indicated in table 7.2; in single-site data we can see that implementing denoising improves our energy resolution at the  $Q$ -value from 1.94% to 1.53%.

Recalling the interpretation of the resolution parameters which was described in section 7.3.4 leads to a number of suggestive observations. First,  $p_1$  has decreased by a factor of 1.9 in single-site data and 1.7 in multi-site data when we move from undenoised to denoised resolutions. The parameter  $p_1$  is associated with electronic noise, so we can interpret this to mean that we have indeed reduced the impact of electronic noise after denoising.

Secondly,  $p_2$  has decreased by a factor of 2.4 in the multi-site data and a factor of 9.7 for single-site data. The parameter  $p_2$  is associated with improper gain calibrations; the old method of APD reconstruction handled only a simple sum of APD waveforms with no APD channel gain corrections, whereas the lightmap used with denoising has detailed time-dependent gain information for every channel built into it. Thus, the reduction in  $p_2$  may be a reflection of the impact of improved APD gain information on our energy resolution.

And finally,  $p_0$  is observed to increase from a value consistent with zero to the dominant component of the denoised resolution at our  $Q$ -value. The parameter  $p_0$  is associated with Poisson fluctuations in the number of photons detected. In the

old method of APD reconstruction we always used a sum of all APD waveforms for scintillation measurements; implicitly, we were always using the full light collecting efficiency of the EXO-200 detector. By contrast, denoising is designed with the flexibility to weight fewer APD channels more heavily, effectively sacrificing light collection for the benefit of a reduction in electronic noise. It is likely that  $p_0$  is zero with undenoised data because Poisson fluctuations in the total light collection of EXO-200 are small, whereas denoising uses a sufficiently small number of APD channels that Poisson fluctuations become important. Moreover, we recall in section 4.10 that the current analysis mistakenly underestimates Poissonian noise produced inside the APDs, and this would manifest itself by subjecting the scintillation estimate to even more statistical fluctuations than would be ideal. We can imagine that when this error is corrected in future analyses the  $p_0$  parameter may respond by decreasing, possibly at the expense of a larger  $p_0$  value as more channels are used.

It should be noted that although these interpretations of  $p_0$ ,  $p_1$ , and  $p_2$  are highly suggestive, they depend on the assumption that scintillation energy resolution continues to be the dominant factor in our rotated energy resolution at all energy scales. As an alternative, it has been suggested that the rotation angle may have an energy dependence which is not described by our calibrations [110]; failure to include this dependence may be reflected by an energy dependence in the resolution function which does not agree with the interpretation we provide here. Also, the error bands in figure 7.38 are still somewhat broad, and more accurate resolution measurements from a wider range of energies would be useful to constrain the values

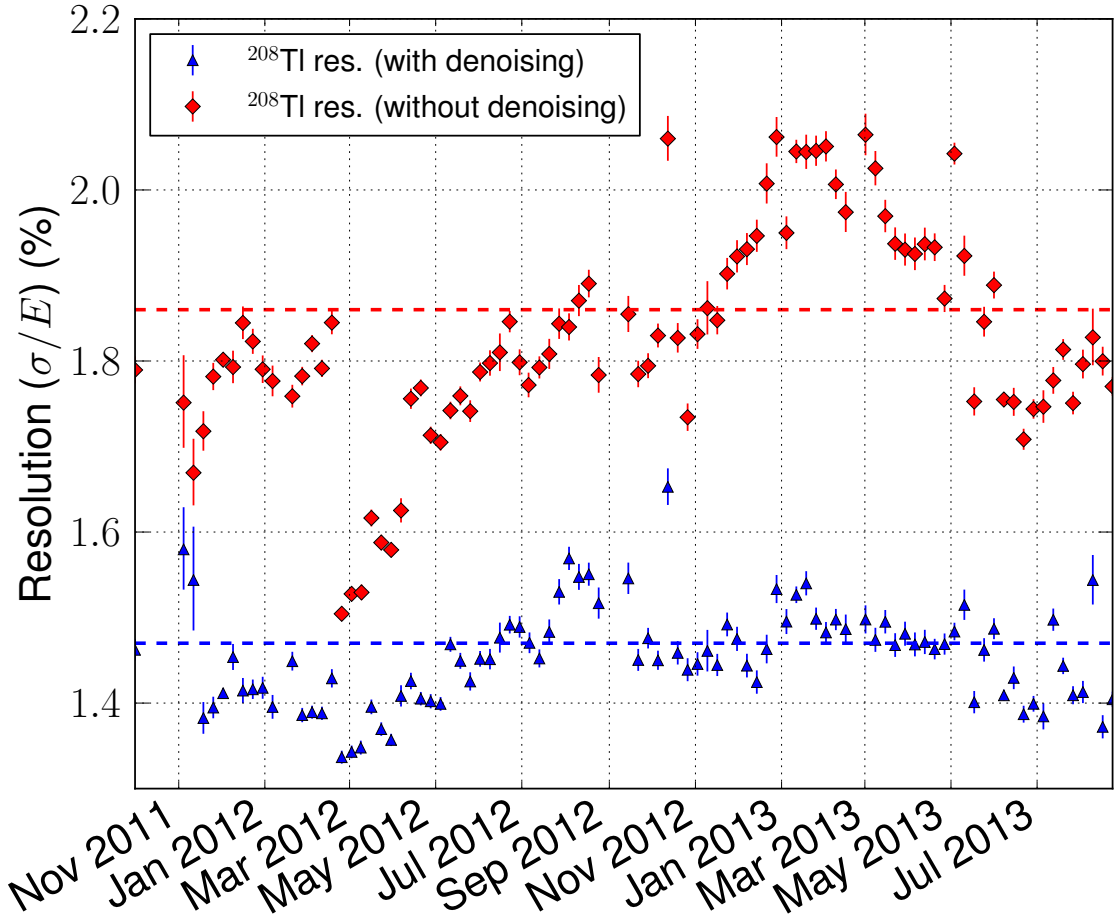


Figure 7.39: Time dependence of the single-site energy resolution at 2615 keV with denoised (blue) and undenoised (red) scintillation. Time-averaged energy resolutions at this energy (1.47% denoised, 1.86% undenoised) are overlaid as dashed lines. Data provided by Mike Marino.

of these parameters better. Further investigation will be required to verify that the scintillation energy measurement accuracy is still the dominant contributor to energy resolution at all energy scales.

We also find that the time-dependence of the energy resolution has been dramatically affected by denoising. Figure 7.39 compares the single-site energy resolutions at the  $^{208}\text{Tl}$  2615 keV gamma line with denoised and undenoised data, as

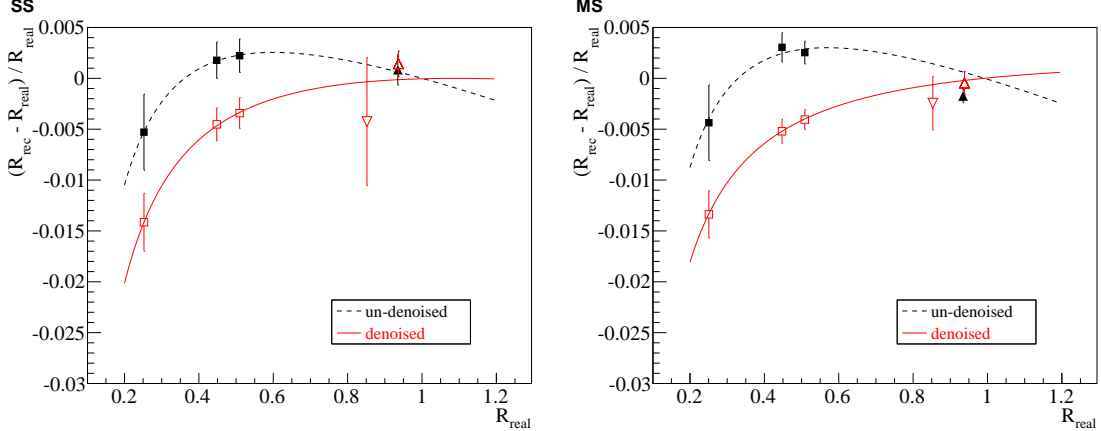


Figure 7.40: The non-linearity of the calibration is shown here for denoised (red) and undenoised (black) data in single-site (left) and multi-site (right).  $R_{rec}$  is defined as the ratio between the observed peak position and the observed peak position of the 2615 keV  $^{232}\text{Th}$  peak, and  $R_{real}$  is defined as the true ratio between the peak position and 2615 keV; the vertical axis shows the relative difference between  $R_{rec}$  and  $R_{real}$ , which reflects how much non-linear correction the calibration must perform. The cesium, cobalt, and thorium peaks (662, 1173, 1332, and 2615 keV) are used to obtain a calibration; the radium line at 2448 keV and the neutron capture line from hydrogen at 2200 keV are shown as cross-checks [140].

measured from  $^{232}\text{Th}$  source calibration data. The denoised energy resolution varies by as much as 0.3 percentage points, but the undenoised energy resolution varies by as much as 0.6 percentage points. We saw in figure 4.1 that the energy resolution of the detector was strongly correlated with APD noise, but after denoising this effect is significantly reduced. In particular, the period of particularly poor energy resolution November 2012 and May 2013 is no longer exceptional, indicating that this poor energy resolution came from noise which denoising can reduce to negligible levels [89].

One concern with the denoised energy calibration comes from the observed

non-linearity of the observation, shown in figure 7.40. The ratio of reconstructed peak positions become farther from what we expect with denoised energy, indicating more significant contributions from the  $E_{bias}$ ,  $p_0$ , and  $p_2$  parameters of the calibration defined in equation 7.8. This is not in itself a problem – it is the job of calibration to correct for such things – but as the calibration changes more rapidly with energy it becomes important for us to constrain it with more calibration points at a wide range of energies. Starting in June 2013 we have a  $^{226}\text{Ra}$  source which contains many gamma lines, including its primary line at 2448 keV which serves as an excellent constraint for the energy of our  $Q$ -value. For existing data, there is some hope of using the lower-energy gamma lines of the  $^{228}\text{Th}$  source, visible in figure 7.18, as a new set of calibration points which is accessible due to the improved resolution of the denoised dataset.

### 7.6.2 Comparison of Physics Results

We now proceed to compare the physics results obtained with denoising to those which would have been obtained without denoising. We recall from figure 3.6 that improvement of the energy resolution will have the strongest effect on our  $^{232}\text{Th}$  backgrounds, and will have a smaller (but not negligible) effect on our  $^{137}\text{Xe}$  backgrounds. Here we will show changes as they impact our  $2\sigma$  region of interest, and will conclude with a comparison of the profile likelihood scans obtained from full fits to the spectrum.

We begin by listing the events which occur in the denoised single-site spectrum

in the energy window from 2325 to 2550 keV. These are provided in table 7.3, which also includes the corresponding undenoised energy and the change in energy due to denoising. The table indicates whether the event would fall within the  $2\sigma$  region of interest in both the denoised and undenoised analysis.

Table 7.3: All single-site events which fall into the denoised energy window between 2325 and 2550 keV. This fully includes the  $2\sigma$  window around the  $Q$ -value; we indicate whether the event falls into that  $2\sigma$  window. The correponding undenoised energy is also indicated, along with whether that undenoised energy falls into the undenoised  $2\sigma$  region of interest.

Run#	Event#	Denoised		Undenoised		$\Delta E$ (keV)
		Energy (keV)	In ROI?	Energy (keV)	In ROI?	
2669	3889	2327.4	No	2322.6	No	4.8
2782	2237	2464.2	Yes	2560.3	No	-96.0
2831	4864	2488.5	Yes	2245.3	No	243.2
3155	2053	2524.6	Yes	2541.6	Yes	-17.0
3155	6861	2448.5	Yes	2403.4	Yes	45.1
3255	8687	2360.4	No	2353.4	No	7.0
3321	8688	2332.4	No	2315.2	No	17.2
3461	845	2357.7	No	2336.6	No	21.1
3573	1958	2406.1	Yes	2421.4	Yes	-15.2
3657	3515	2417.0	Yes	2399.1	Yes	17.8
3740	11325	2405.7	Yes	2324.8	No	80.9
3912	10712	2391.3	Yes	2399.8	Yes	-8.5
Continued on next page						

**Table 7.3 – continued from previous page**

Run#	Event#	Denoised		Undenoised		$\Delta E$ (keV)
		Energy (keV)	In ROI?	Energy (keV)	In ROI?	
3933	3459	2441.4	Yes	2507.3	Yes	-65.9
3964	9703	2459.2	Yes	2464.8	Yes	-5.6
3972	754	2509.6	Yes	2470.9	Yes	38.8
3994	12296	2412.7	Yes	2367.1	Yes	45.5
4030	5037	2502.1	Yes	2482.8	Yes	19.3
4032	2727	2426.4	Yes	2349.3	No	77.1
4065	2350	2428.8	Yes	2442.8	Yes	-14.0
4068	8841	2543.4	No	2640.4	No	-97.0
4068	9897	2423.9	Yes	2453.5	Yes	-29.7
4078	2595	2370.3	No	2372.4	Yes	-2.0
4229	9176	2541.3	No	2519.5	Yes	21.9
4258	13386	2340.7	No	2338.8	No	2.0
4288	1334	2333.9	No	2340.6	No	-6.7
4288	11179	2466.0	Yes	2494.1	Yes	-28.1
4288	13040	2418.6	Yes	2486.3	Yes	-67.7
4306	10543	2544.3	No	2574.1	No	-29.7
4373	3036	2349.4	No	2395.3	Yes	-45.8
4378	11150	2492.3	Yes	2494.2	Yes	-1.9

Continued on next page

**Table 7.3 – continued from previous page**

Run#	Event#	Denoised		Undenoised		$\Delta E$ (keV)
		Energy (keV)	In ROI?	Energy (keV)	In ROI?	
4402	10759	2393.0	Yes	2398.0	Yes	-5.1
4433	16390	2529.9	No	2494.1	Yes	35.8
4459	29435	2529.3	No	2472.2	Yes	57.1
4475	11191	2454.5	Yes	2521.3	Yes	-66.8
4490	4613	2441.5	Yes	2481.4	Yes	-40.0
4507	6129	2435.6	Yes	2412.4	Yes	23.2
4672	1891	2383.5	Yes	2418.5	Yes	-35.0
4705	5799	2404.6	Yes	2465.7	Yes	-61.1
4712	5996	2466.0	Yes	2439.5	Yes	26.5
4733	3595	2364.9	No	2381.2	Yes	-16.2
4809	3937	2427.7	Yes	2429.1	Yes	-1.4
4860	5170	2513.8	Yes	2596.3	No	-82.5
4882	310	2474.2	Yes	2450.2	Yes	24.1
4899	9833	2342.4	No	2323.7	No	18.7
4903	7366	2472.6	Yes	2456.7	Yes	15.9
4918	4313	2377.1	No	2458.2	Yes	-81.1
4957	8387	2398.6	Yes	2384.9	Yes	13.7
4978	6796	2521.1	Yes	2518.8	Yes	2.3

Continued on next page

**Table 7.3 – continued from previous page**

Run#	Event#	Denoised		Undenoised		$\Delta E$ (keV)
		Energy (keV)	In ROI?	Energy (keV)	In ROI?	
5010	2201	2365.3	No	2349.5	No	15.7
5082	9766	2517.7	Yes	2477.1	Yes	40.6
5097	7670	2472.1	Yes	2441.0	Yes	31.1
5105	15012	2548.5	No	2559.8	No	-11.3
5124	7626	2480.4	Yes	2411.8	Yes	68.6
5305	3256	2406.0	Yes	2393.2	Yes	12.8
5372	11466	2513.7	Yes	2557.9	No	-44.2
5380	4415	2458.2	Yes	2478.9	Yes	-20.7
5409	38	2405.1	Yes	2456.9	Yes	-51.8

To compare the limits set with denoised and undenoised data, figure 7.41 includes the profile likelihood curves derived from both datasets. The beta scale is included as a systematic here, broadening both curves. The 90% confidence limit is the value of  $\beta\beta0\nu$  at which the curve has a value of 1.35; for the denoised data we can set a 90% confidence limit of 24 counts, whereas with the undenoised data we set a 90% confidence limit of 27 counts. This means denoising has given us an 11% stronger half-life limit than the undenoised dataset could have provided; or, since the neutrino mass  $\langle m_{\beta\beta} \rangle$  is proportional to the square root of half-life, denoising

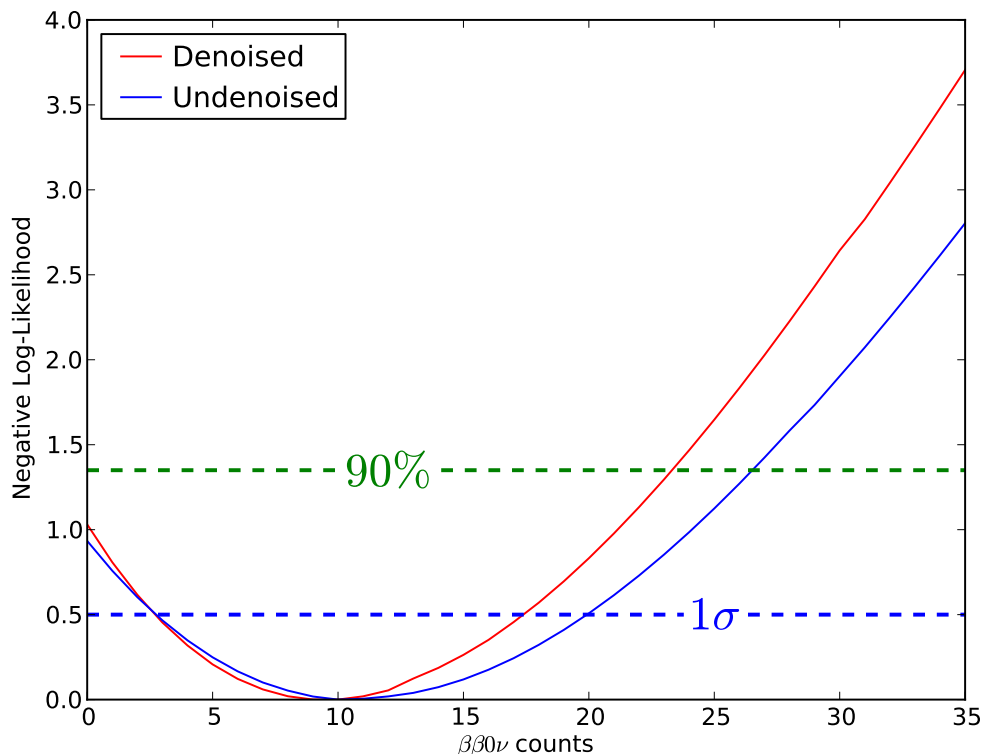


Figure 7.41: Denoised (red) and undenoised (blue) profile likelihood curves for  $\beta\beta0\nu$ .

gives us a 6% stronger limit on the neutrino mass.

Another way to compare the denoised and undenoised datasets is by studying their expected number of background counts. We choose to present the best fits where  $\beta\beta0\nu$  is fixed at zero, rather than the best fits overall. We do this because we are claiming in section 7.4 that the result is a limit on  $\beta\beta0\nu$  decay, not an observation; any differences in the best-fit number of  $\beta\beta0\nu$  counts should therefore be viewed as statistical fluctuations rather than meaningful results, and we do not wish to allow them to skew our comparison.

Figure 7.42 shows the denoised and undenoised data and total best-fit PDFs with the  $\beta\beta0\nu$  contribution fixed to zero. We can see that a significant portion of the expected background reduction in undenoised data comes from pulling the region of interest away from the  $^{208}\text{Tl}$  peak. The total expected background in the  $2\sigma$  region of interest is 37.4 counts in the denoised fit, as opposed to 54.8 counts in the undenoised fit.

We also show a number of features in the single-site and multi-site low-background spectra and contrast the data, total pdfs, and pdf contributions from individual components. Figures 7.43 and 7.44 illustrate the  $^{40}\text{K}$  gamma line at 1461 keV. Figure 7.45 shows the multi-site contribution from  $^{60}\text{Co}$  with gamma lines at 1173 and 1332 keV. Figures 7.46 and 7.47 show contributions from daughter products of  $^{238}\text{U}$ . Figures 7.48 and 7.49 show contributions from daughter products of  $^{232}\text{Th}$ . The change in contribution from  $^{137}\text{Xe}$  is shown in figure 7.50.

The observation that all of these features become sharper gives us confidence that the resolution improvements observed in source data are also seen in the low-

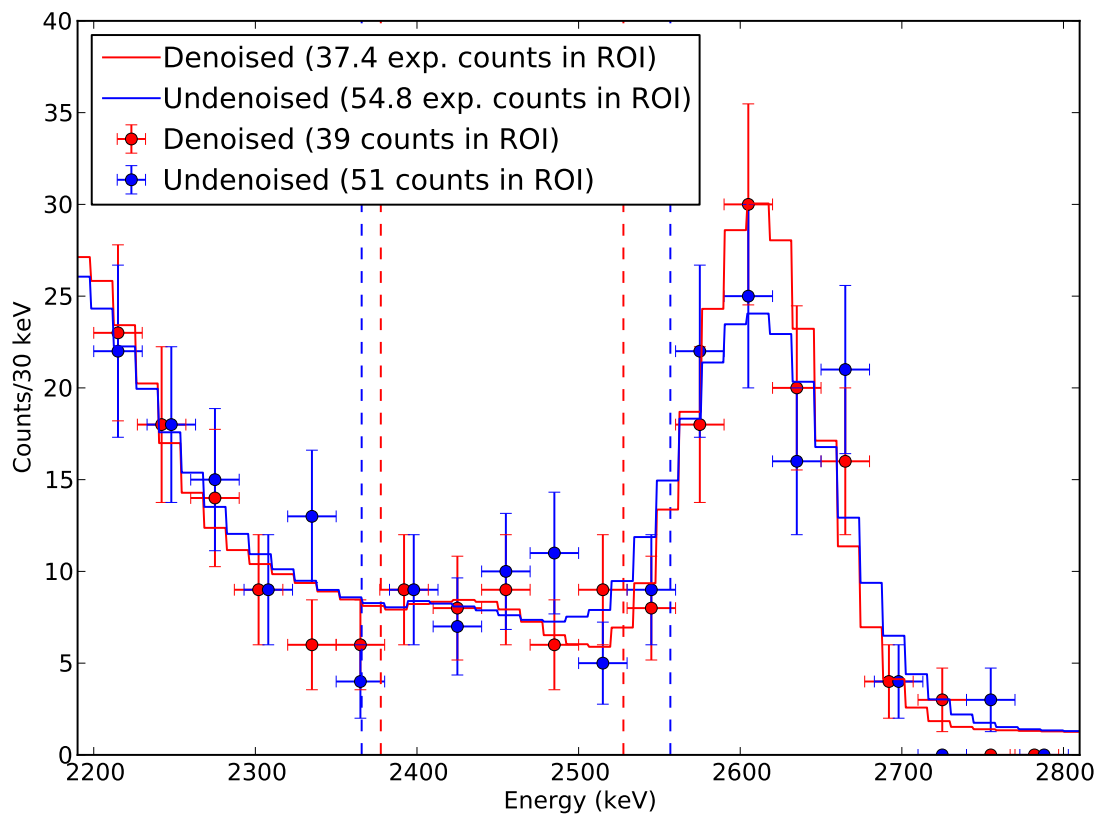


Figure 7.42: Denoised (red) and undenoised (blue) data counts are shown in 30 keV bins. The total best-fit PDF, where the  $\beta\beta0\nu$  contribution is fixed to zero, is overlaid for denoised and undenoised data. Dashed lines indicate the  $2\sigma$  region of interest.

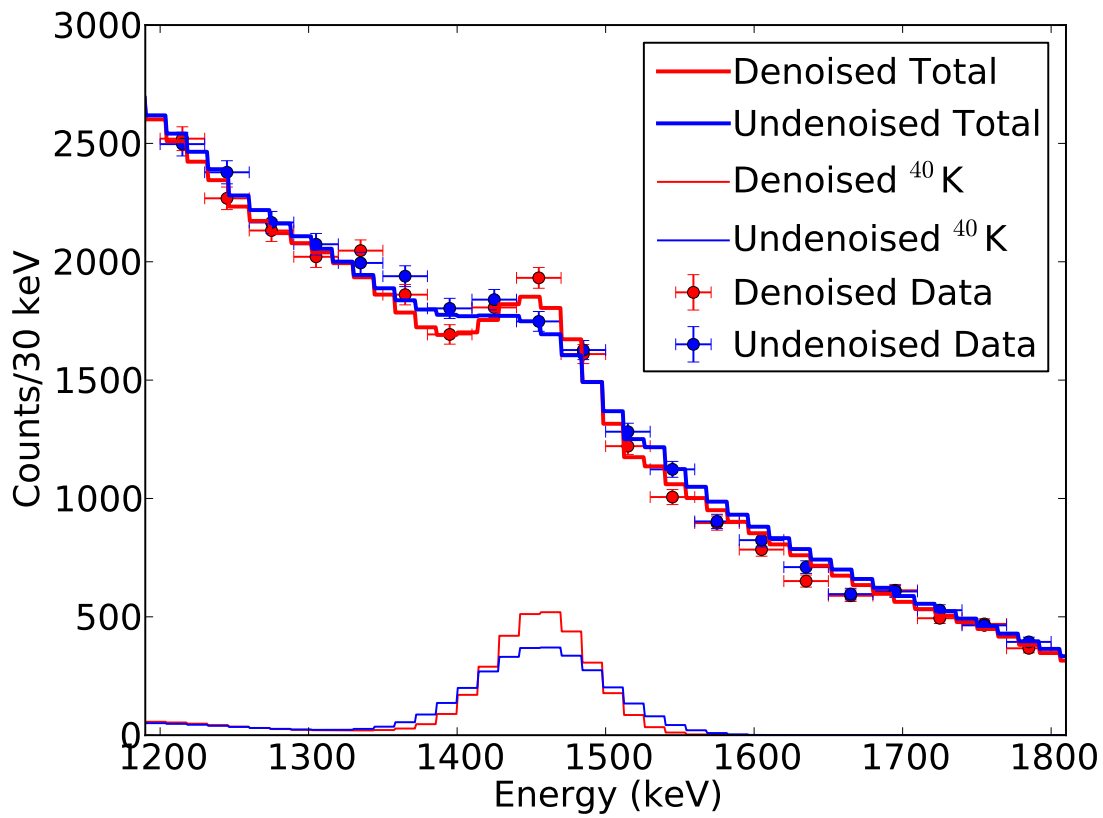


Figure 7.43: Denoised (red) and undenoised (blue) single-site low-background data and pdfs in the energy window from 1200 to 1800 keV. The thick lines indicate the total single-site pdfs; thin lines indicate contributions from  ${}^{40}\text{K}$ . Both fits are constrained to have no contribution from  $\beta\beta0\nu$ .

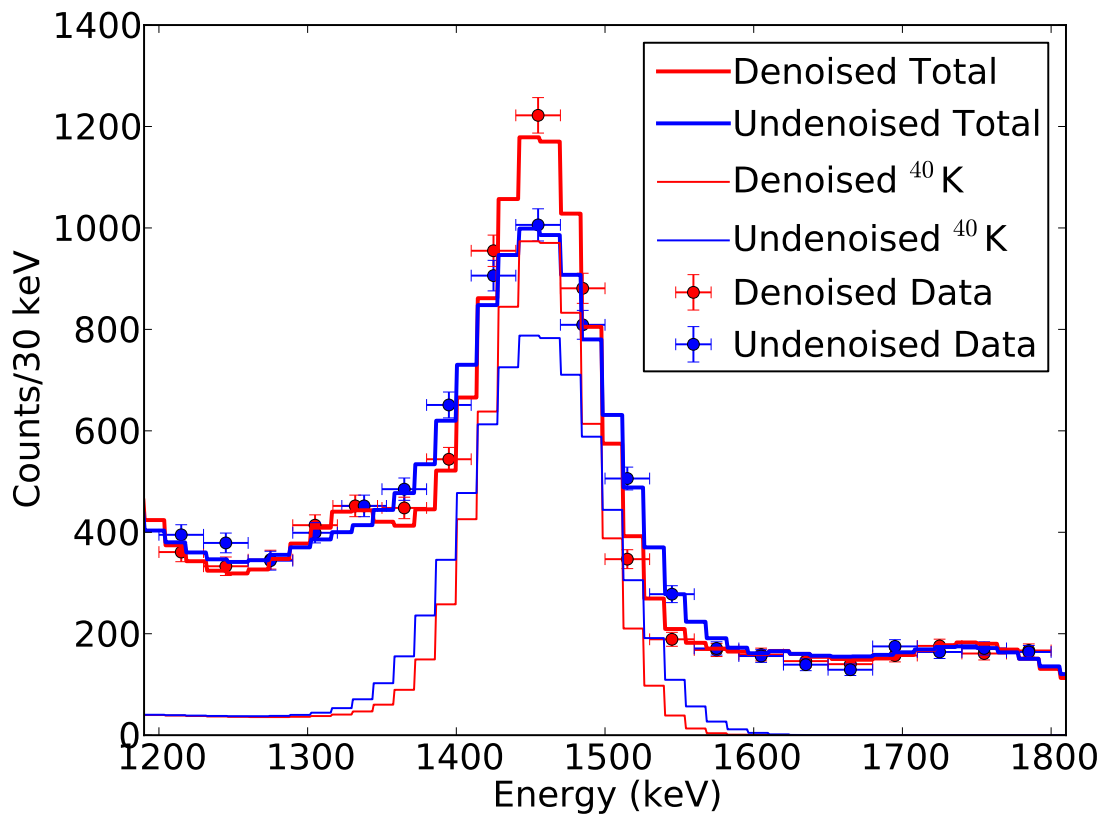


Figure 7.44: Denoised (red) and undenoised (blue) multi-site low-background data and pdfs in the energy window from 1200 to 1800 keV. The thick lines indicate the total multi-site pdfs; thin lines indicate contributions from  $^{40}\text{K}$ . Both fits are constrained to have no contribution from  $\beta\beta0\nu$ .

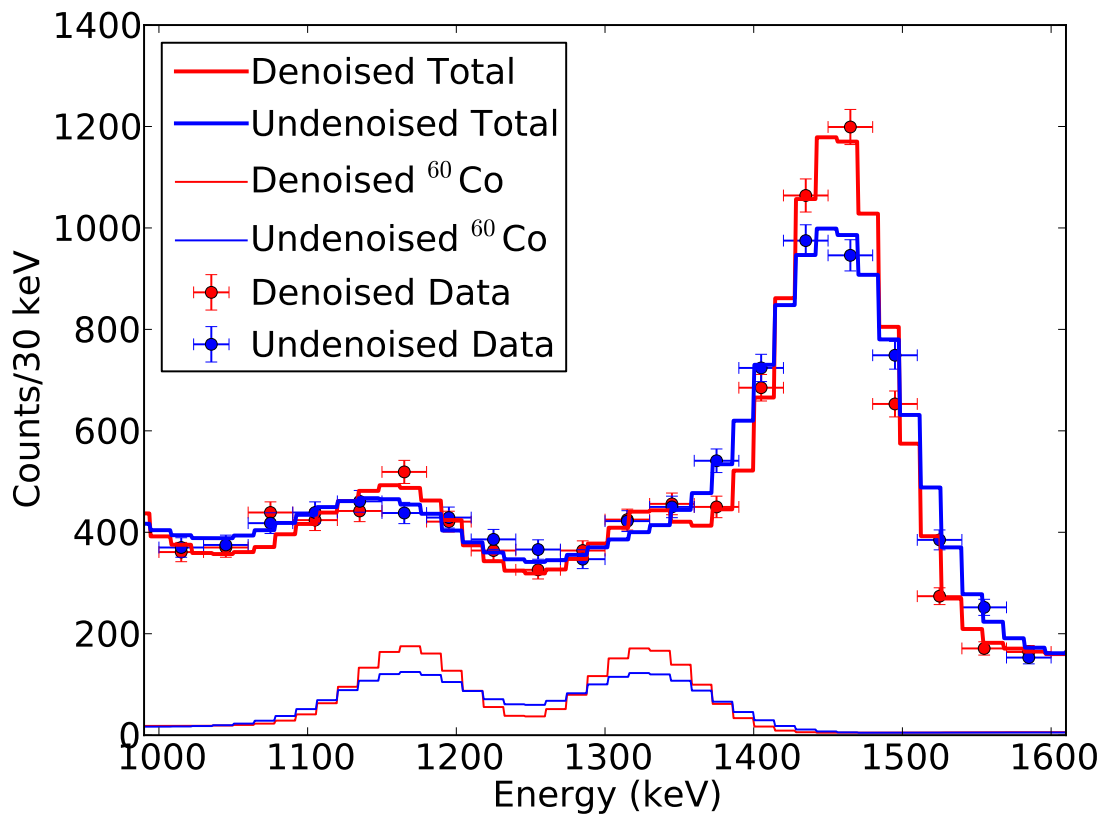


Figure 7.45: Denoised (red) and undenoised (blue) multi-site low-background data and pdfs in the energy window from 1000 to 1600 keV. The thick lines indicate the total multi-site pdfs; thin lines indicate contributions from  $^{60}\text{Co}$ . Both fits are constrained to have no contribution from  $\beta\beta0\nu$ .

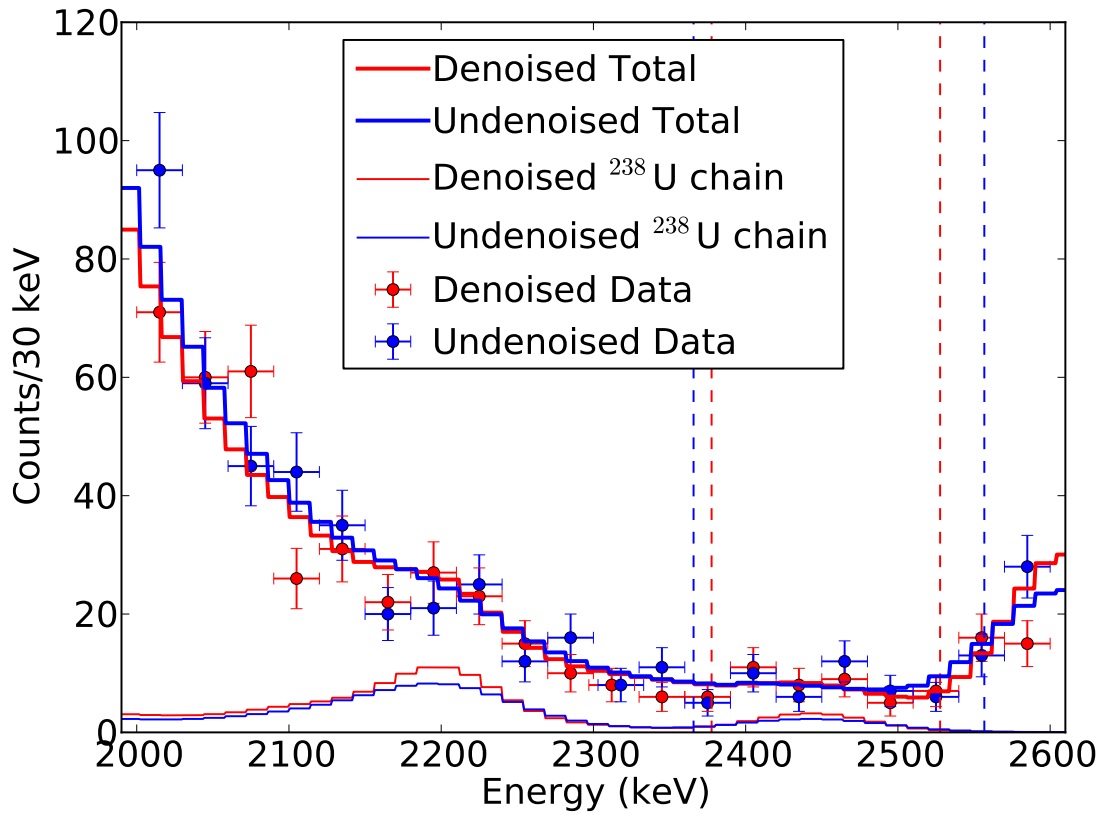


Figure 7.46: Denoised (red) and undenoised (blue) single-site low-background data and pdfs in the energy window from 2000 to 2600 keV. The thick lines indicate the total single-site pdfs; thin lines indicate contributions from isotopes in the  $^{238}\text{U}$  decay chain. Dashed vertical lines indicate the  $2\sigma$  region of interest around the  $Q$ -value. Both fits are constrained to have no contribution from  $\beta\beta0\nu$ . The uranium decay chain contributes 10.0 (8.9) mean expected counts in the  $2\sigma$  region of interest for denoised (undenoised) data.

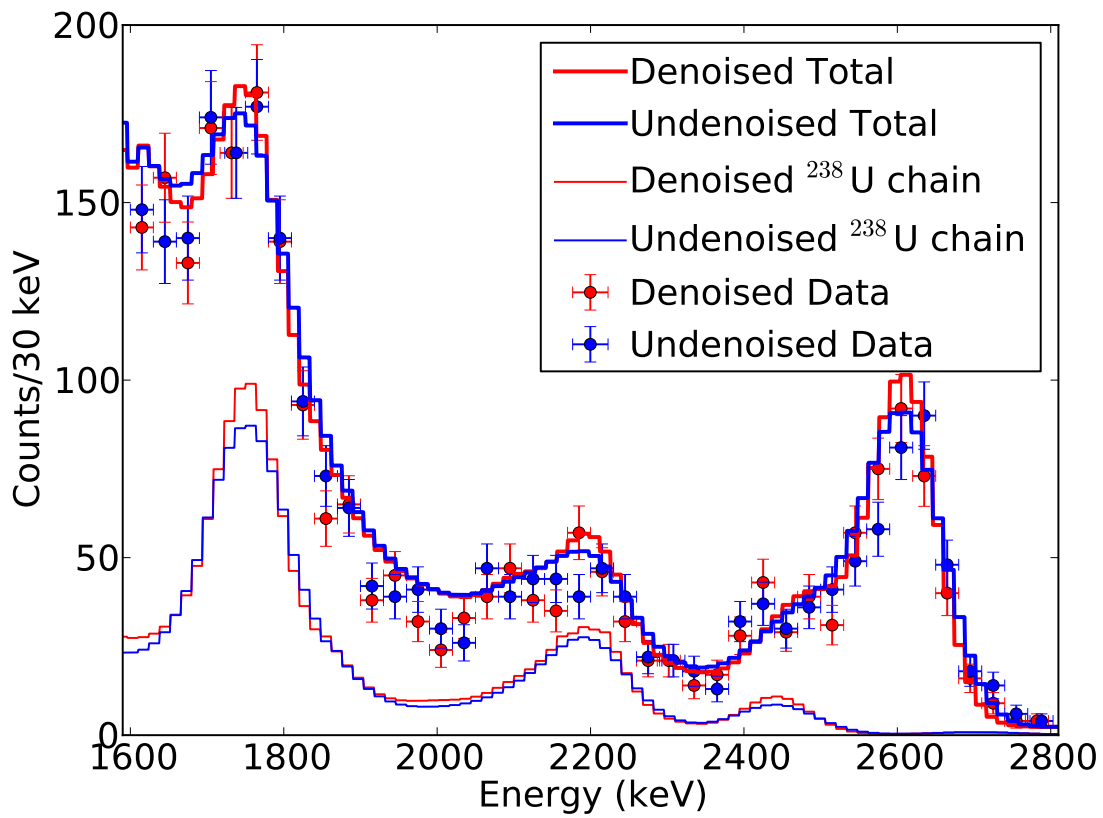


Figure 7.47: Denoised (red) and undenoised (blue) multi-site low-background data and pdfs in the energy window from 1600 to 2800 keV. The thick lines indicate the total multi-site pdfs; thin lines indicate contributions from isotopes in the  $^{238}\text{U}$  decay chain. Both fits are constrained to have no contribution from  $\beta\beta0\nu$ .

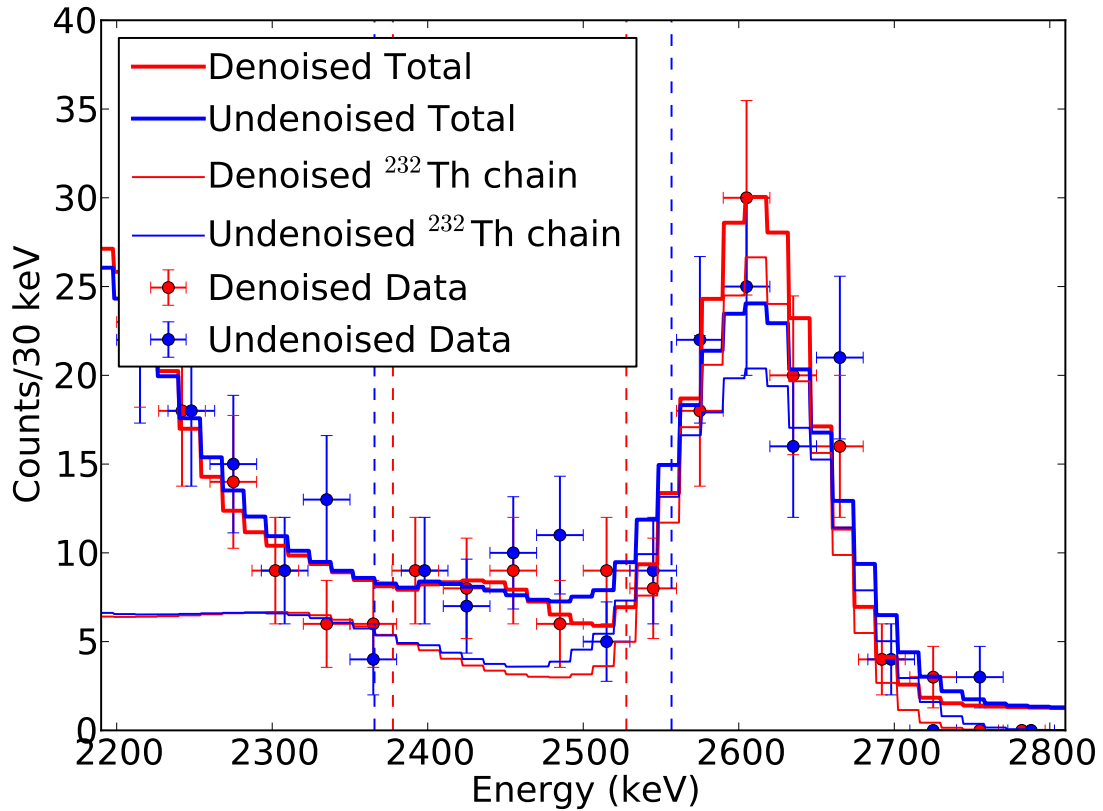


Figure 7.48: Denoised (red) and undenoised (blue) single-site low-background data and pdfs in the energy window from 2200 to 2800 keV. The thick lines indicate the total single-site pdfs; thin lines indicate contributions from isotopes in the  $^{232}\text{Th}$  decay chain. Dashed vertical lines indicate the  $2\sigma$  region of interest around the  $Q$ -value. Both fits are constrained to have no contribution from  $\beta\beta0\nu$ . The thorium decay chain contributes 18.7 (34.5) mean expected counts in the  $2\sigma$  region of interest for denoised (undenoised) data.

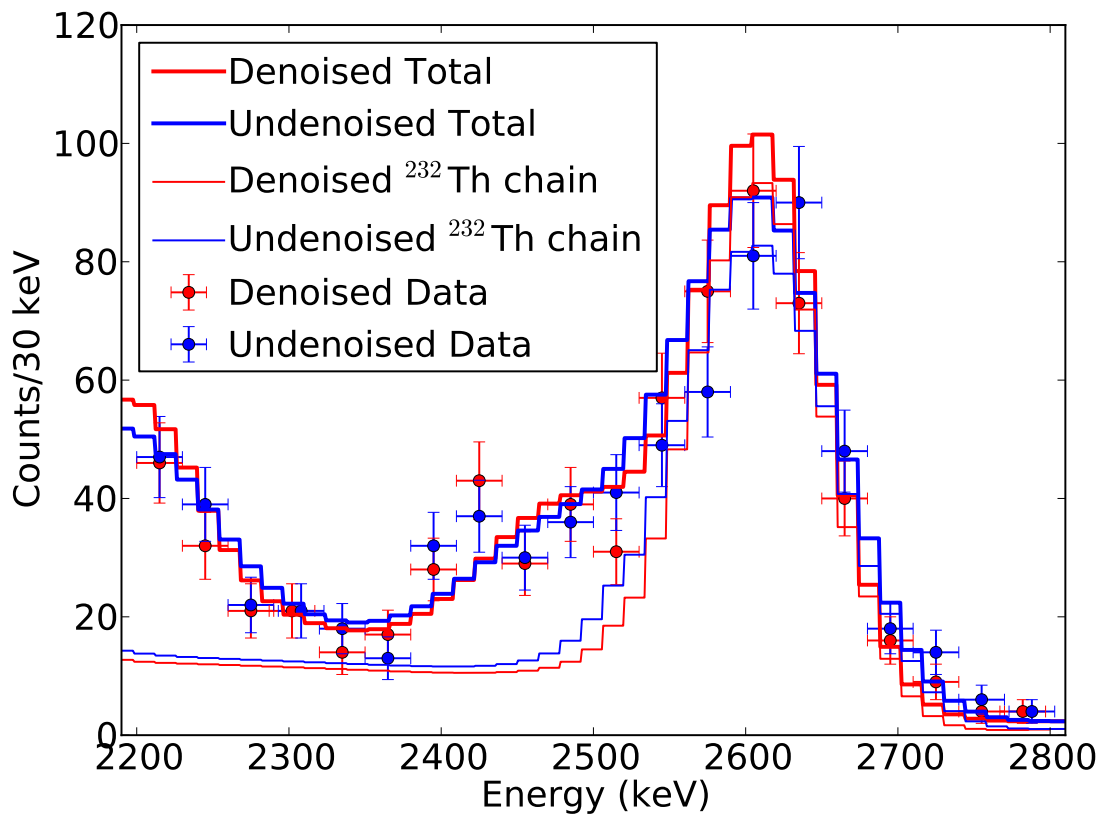


Figure 7.49: Denoised (red) and undenoised (blue) multi-site low-background data and pdfs in the energy window from 2200 to 2800 keV. The thick lines indicate the total multi-site pdfs; thin lines indicate contributions from isotopes in the  $^{232}\text{Th}$  decay chain. Both fits are constrained to have no contribution from  $\beta\beta0\nu$ .

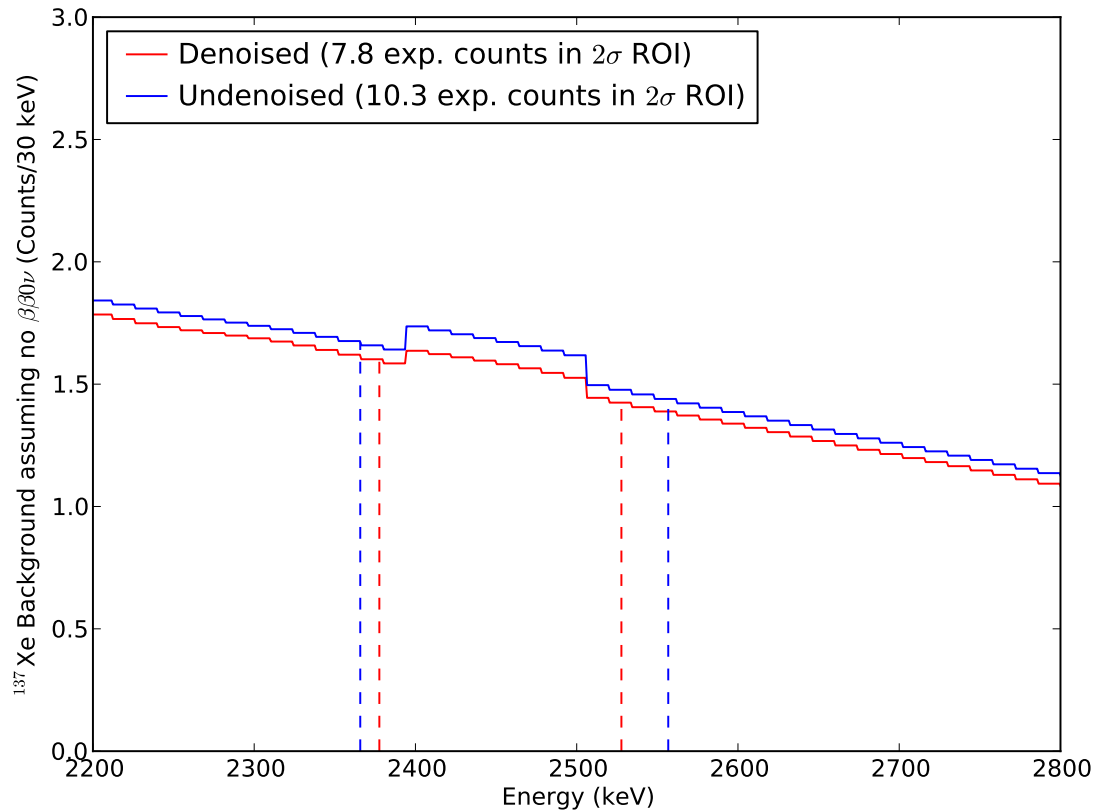


Figure 7.50: Denoised (red) and undenoised (blue) single-site PDF contributions from  $^{137}\text{Xe}$ , where we constrain  $\beta\beta0\nu$  to have no decays in both fits.

background spectrum; they also improve the ability of the fit to reduce correlations between different background components. These fits also permit us to gauge the change in expected background due to each background component. In particular, we see that background in the  $2\sigma$  region of interest due to thorium decreases dramatically after denoising, as expected. Background due to  $^{137}\text{Xe}$  decreases moderately. We expect no change in the expected background due to the uranium chain; in fact the expected number of background counts due to uranium increases slightly, but this is due to a shift in the best-fit rate of uranium components to 864 expected counts over the entire fit window, compared to only 724 in the undenoised dataset. The uranium decay chain, thorium decay chain, and  $^{137}\text{Xe}$  are our dominant backgrounds in both the denoised and undenoised data.

The mean expected number of background counts drawn from these fit results give some indication of how easily we could discover  $\beta\beta0\nu$  decay with the denoised and undenoised analysis because we expect background fluctuations to be similar to the square root of the number of expected counts, and to discover  $\beta\beta0\nu$  decay it must produce more counts than can be attributed to a typical background fluctuation. The number of expected background counts in denoised data is 32% lower than in undenoised data, so the number of  $\beta\beta0\nu$  counts required for a discovery of similar strength is  $\sqrt{32\%} = 17\%$  lower for denoised data than undenoised data. Since the neutrino mass  $\langle m_{\beta\beta} \rangle$  is proportional to the square root of the half-life  $T_{1/2}^{0\nu}$ , we can expect that denoising typically permits us to discover neutrino masses 9% lower than without denoising.

## 7.7 Summary

We have seen that denoising now occupies a central place in the EXO-200 analysis, providing one of the two energy quantities (charge and light) which together determine the size of the region of interest we must use. Denoising has been shown to produce a 21% improvements in single-site energy resolution at our  $Q$ -value and a 32% reduction in the mean expected backgrounds in our  $2\sigma$  region of interest. Even with denoising, the  $\beta\beta0\nu$  half-life limit we obtain is less than our mean sensitivity would lead us to hope; however, this fluctuation is not unreasonable and is a natural part of low-background physics research. The upgrade of the present analysis using denoising has led to exciting new investigations, and we can already see that our improved resolution has exposed new avenues for improvements in our calibration techniques. In chapter 8 we conclude with a reminder of the accomplishments of the present work and a look ahead to more anticipated upgrades to the EXO-200 system.

## Chapter 8: Conclusions and Future Plans

This work has presented a wide-ranging upgrade to the scintillation waveform analysis of EXO-200. The result has been a 21% improvement in the single-site energy resolution at the  $Q$ -value, from 1.94% to 1.53%  $\sigma/E$ . We strengthen the half-life limit of  $\beta\beta0\nu$  decay for this analysis by 11%, corresponding to a 6% stronger limit on the Majorana neutrino mass. Separate background fits to the denoised and undenoised data indicate that the  $2\sigma$  region of interest background is reduced 32% by denoising, corresponding to a mean sensitivity which is strengthened by 17% and a mean sensitivity for the Majorana mass which is 9% lower than could be achieved without denoising.

One question which must be asked is whether there is any room for further improvement in the energy resolution. Figure 8.1 shows simulations of the relationship between scintillation-only resolution and rotated energy resolution. Points indicate the resolutions measured from denoised and non-denoised data; we can see that the model agrees well with both sets of data. Based on these simulations, it is clear that further improvements to the scintillation resolution will indeed have a significant impact on the overall resolution of EXO-200; projections from figure 3.6

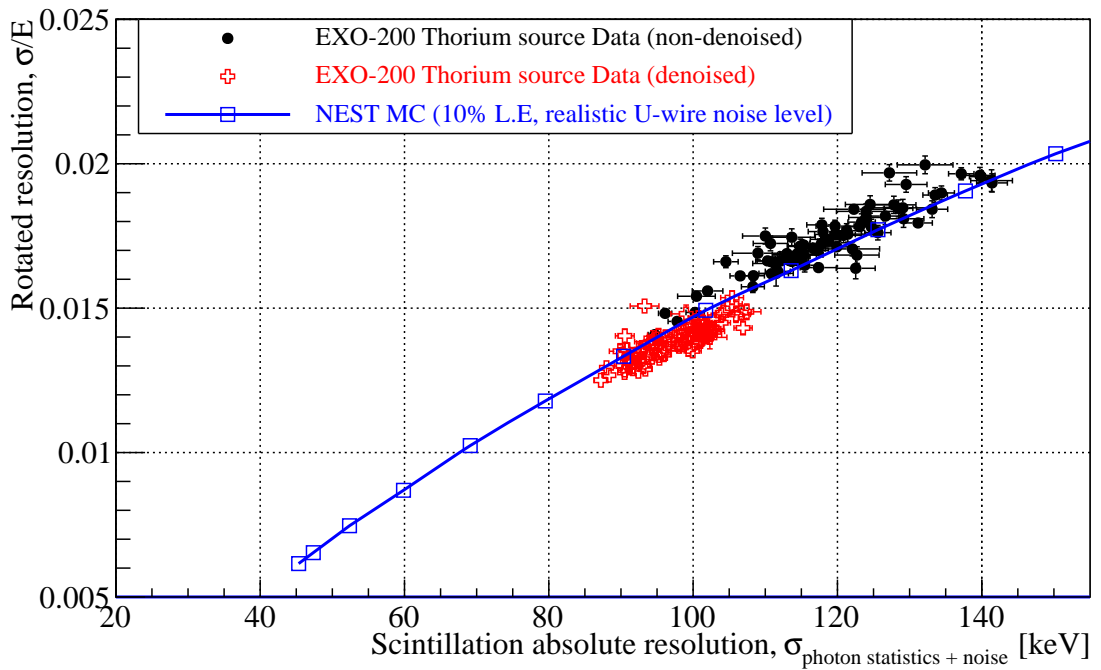


Figure 8.1: NEST simulation software has been used to estimate how the rotated energy resolution at 2615 keV (vertical axis) depends on the scintillation-only resolution at 2615 keV (horizontal axis); this theoretical estimate is shown in blue, as applicable to the EXO-200 detector with fixed electric field. Black points indicate measurements from thorium source runs without denoising; red points indicate measurements from thorium runs with denoising. Figure provided by Liangjian Wen using NEST software [118].

indicate that  $^{232}\text{Th}$  and  $^{137}\text{Xe}$  backgrounds can continue to be significantly reduced by resolution improvements, so these attempts are indeed worthwhile.

We have noted in section 4.10 that the parameters used for this denoising are not optimal, and that preliminary studies indicate roughly 0.05 percentage points can be gained in overall energy resolution at 2615 keV with an up-to-date set of denoising parameters. This issue is straightforward to address, and the next processing of our dataset will incorporate it.

Beyond this improvement, we have described in section 7.3.2 that the denoised scintillation peak position displays a large position dependence which cannot be fully calibrated in downstream analysis. The effect of this feature is to dilute our resolution improvements. Although the cause of this position dependence is not fully understood, we believe that it originates in the lightmap because the lightmap is the input to denoising which encodes position-dependent yield information; one preliminary theory is that the discrepancy between 1-wire and 2-wire charge peak positions described in section 7.3.1 leads to a bias in event selection for the lightmap. We believe that this issue can be addressed with further investigation and will lead to additional significant improvements in resolution.

The most exciting improvement in resolution may come not from offline analysis but from planned electronics upgrades. There are indications that the source of electronic noise in the APDs is now understood and can be fixed in hardware in the near future, with an expectation of energy resolutions below 1% after all upgrades [116]. Energy resolution improvements on this scale would have a significant impact on backgrounds and the sensitivity of EXO-200 to  $\beta\beta0\nu$  decay.

One may wonder, after a hardware upgrade which reduces electronic noise on the APDs, whether denoising will still be a necessary component of the analysis. It may indeed be the case that the full denoising scheme is not needed for lower-noise waveforms. However, certain components of this analysis will still be critical to good resolution. In particular, the techniques developed in this work to measure an APD-by-APD lightmap will still be needed to relate pulse magnitudes to deposit energies; we have seen hints in section 7.6.1 that application of channel-dependent gain corrections reduces their impact on energy resolution by a factor of 9.7 in single-site data, and if true then this will be a critical component of any scintillation measurements regardless of changes in electronic noise.

Beyond energy resolution upgrades to EXO-200, the techniques described in this work have led to the most complete understanding to date of what limits the energy resolution of EXO-200. This understanding is timely because the successor experiment to EXO-200, called nEXO, is currently in design stages of development. Options for nEXO which are currently being considered include the types of light sensors to use and how much to gang sensors together; studies are currently underway to understand exactly how design decisions have impacted EXO-200 scintillation energy resolution, and the results will provide useful feedback to the nEXO design process.

Additionally, other aspects of the EXO-200 analysis besides energy resolution may benefit from the progress discussed here. It may be possible that our improved understanding of scintillation enables us to enlarge the EXO-200 dataset. Currently, data taken between May 2011 and October 2011 is not used in the  $\beta\beta0\nu$  search

because it was prior to a u-wire electronics upgrade and an increase in the APD bias voltages. Studies which used that data were primarily charge-driven and only used scintillation to measure Z-positions of deposits. However, it is possible that denoising will permit us to make use of the weaker scintillation pulses from that dataset and achieve an acceptable energy resolution; the result could be months of added livetime for future studies.

Our deeper understanding of the scintillation pulses from an individual-APD lightmap also has the potential to improve our pulse-finding threshold. The EXO-200 energy threshold of 980 keV is limited by scintillation-finding. A lower energy threshold would not directly impact a  $\beta\beta0\nu$  search, but would allow backgrounds to be better-constrained by fits. Furthermore, there are low-energy physics searches like  $^{134}\text{Xe}$   $\beta\beta2\nu$  decay and  $^{136}\text{Xe}$   $\beta\beta0\nu\chi$  Majoron decay searches which have not been described in this work but which would benefit strongly from a lower energy threshold [98]. Currently all scintillation pulses are found on summed APD waveforms; our detailed APD lightmap should permit us to make use of individual-APD information, which may permit better noise rejection and lead to a lower pulse-finding threshold.

Another set of alternative physics searches which could be improved using techniques from this work are excited-state decay searches. We expect  $^{136}\text{Xe}$  to have a  $\beta\beta2\nu$  decay mode to the second excited state of  $^{136}\text{Ba}$ , followed by the prompt emission of two de-excitation gammas. Currently the EXO-200 analysis only produces scintillation measurements for all simultaneous charge deposits together, making it impossible to generate anticorrelated energy estimates for single energy deposits.

However, a natural extension of denoising would permit us to extract separately the scintillation energies of each deposit site, using knowledge of which channels collected photons to assign energy appropriately. By enabling anticorrelated individual-site energy measurements, we could improve our ability to identify the clusters produced by each of the de-excitation gammas from an excited-state decay.

Finally, there is a possibility, remote but tantalizing, that a variation of these methods could lead to improved discriminating power between beta and gamma deposits. The leading edge of u-wire pulses includes information about the size of the charge cloud: a diffuse charge cloud penetrates the v-wire shielding grid slowly, leading to a slowly-rising leading edge to the u-wire pulse, whereas a more pointlike charge cloud penetrates the v-wire shielding grid in a shorter span of time and leads to a sharply-rising leading edge to the u-wire pulse, so the risetime of a pulse may provide information about the size of its charge cloud. The leading edge of the u-wire pulse is quite short, contained in only a few samples, and current studies have shown no significant improvement in discriminating power when it is used; however, simulations hint that it should be possible to use this information. One plan for improving the quality of this discriminator is to denoise the u-wire waveforms so that the samples from the leading edge of the pulse are less noisy and provide a better measure of the risetime of the pulse. Improved ability to discriminate betas from gammas would lead to fewer backgrounds for  $\beta\beta0\nu$  decay, improving our sensitivity further.

These are some of the many ways in which the denoising techniques of this work may be applied. In all of these applications, the broader message we take away

from denoising is that having a complete model of a detector’s signals is a powerful thing. We have constructed a full description of the APD noise correlation behavior and a complete characterization of how photons generate pulses on waveforms and with what fluctuations. Neither tool was available previously, and using them we have been able to transform the challenge of improving energy resolution into a purely mathematical optimization. We have confidence that these same tools will yield benefits in many EXO-200 analyses to come.

# Bibliography

- [1] F. T. Avignone, III, S. R. Elliott, and J. Engel. Double beta decay, Majorana neutrinos, and neutrino mass. *Reviews in Modern Physics*, 80:481, 2008.
- [2] P.E. Hodgson, E. Gadioli, and E. Gadioli Erba. *Introductory Nuclear Physics*. Oxford Science Publications, 2003.
- [3] G. Audi, et al. The AME2012 atomic mass evaluation. *Chinese Physics C*, 36(12):1287–2014, 2012.
- [4] E. Majorana. Teoria simmetrica dell'elettrone e del positrone. *Nuovo Cimento*, 14:171, 1937.
- [5] H. Nishino, et al. Search for proton decay via  $p- > e^+\pi^0$  and  $p- > \mu^+\pi^0$  in a large water cherenkov detector. *Phys. Rev. Lett.*, 102:141801, Apr 2009. doi:10.1103/PhysRevLett.102.141801.
- [6] SINDRUM II Collaboration. Improved limit on the branching ratio of  $\mu \rightarrow e^+$  conversion on titanium. *Physics Letters B*, 422:334–338, 1998.
- [7] G. Feinberg, P. Kabir, and S. Weinberg. Transformation of muons into electrons. *Phys. Rev. Lett.*, 3:527, 1959.
- [8] J. Schechter and J.W.F. Valle. Neutrinoless double- $\beta$  decay in  $su(2) \times u(1)$  theories. *Phys. Rev. D*, 25:2951, 1982.
- [9] Rabindra N. Mohapatra and Goran Senjanović. Neutrino mass and spontaneous parity nonconservation. *Phys. Rev. Lett.*, 44:912–915, Apr 1980. doi:10.1103/PhysRevLett.44.912.
- [10] Murray Gell-Mann, Pierre Ramond, and Richard Slansky. Complex Spinors and Unified Theories. *Conf.Proc.*, C790927:315–321, 1979.
- [11] R.R.N. Mohapatra and P.P.B. Pal. *Massive Neutrinos in Physics and Astrophysics*. Lecture Notes in Physics Series. World Scientific Publishing Company, Incorporated, 1998. ISBN 9789810233730.
- [12] A. Gando, et al. Measurement of the double- $\beta$  decay half-life of  $^{136}\text{Xe}$  with the KamLAND-Zen experiment. *Phys. Rev. C*, 85:045504, Apr 2012. doi:10.1103/PhysRevC.85.045504.

- [13] A. Gando, et al. Limit on neutrinoless  $\beta\beta$  decay of  $^{136}\text{Xe}$  from the first phase of KamLAND-Zen and comparison with the positive claim in  $^{76}\text{Ge}$ . *Phys. Rev. Lett.*, 110:062502, Feb 2013. doi:10.1103/PhysRevLett.110.062502.
- [14] M. Auger, et al. Search for neutrinoless double-beta decay in  $^{136}\text{Xe}$  with EXO-200. *Phys. Rev. Lett.*, 109:032505, Jul 2012. doi:10.1103/PhysRevLett.109.032505.
- [15] M. Agostini, et al. Results on neutrinoless double- $\beta$  decay of  $^{76}\text{Ge}$  from phase I of the GERDA experiment. *Phys. Rev. Lett.*, 111:122503, Sep 2013. doi:10.1103/PhysRevLett.111.122503.
- [16] H.V. Klapdor-Kleingrothaus, et al. Latest results from the Heidelberg-Moscow double beta decay experiment. *The European Physical Journal A - Hadrons and Nuclei*, 12(2):147–154, 2001. ISSN 1434-6001. doi:10.1007/s100500170022.
- [17] L. Baudis, et al. Limits on the Majorana neutrino mass in the 0.1 ev range. *Phys. Rev. Lett.*, 83:41–44, Jul 1999. doi:10.1103/PhysRevLett.83.41.
- [18] C. E. Aalseth, et al. Neutrinoless double- $\beta$  decay of  $^{76}\text{Ge}$ : First results from the international germanium experiment (IGEX) with six isotopically enriched detectors. *Phys. Rev. C*, 59:2108–2113, Apr 1999. doi:10.1103/PhysRevC.59.2108.
- [19] C. E. Aalseth, et al. IGEX  $^{76}\text{Ge}$  neutrinoless double-beta decay experiment: Prospects for next generation experiments. *Phys. Rev. D*, 65:092007, May 2002. doi:10.1103/PhysRevD.65.092007.
- [20] E. Andreotti, et al.  $^{130}\text{Te}$  neutrinoless double-beta decay with CUORICINO. *Astroparticle Physics*, 34(11):822 – 831, 2011. ISSN 0927-6505. doi:<http://dx.doi.org/10.1016/j.astropartphys.2011.02.002>.
- [21] C. Arnaboldi, et al. Results from a search for the  $0\nu\beta\beta$ -decay of  $^{130}\text{Te}$ . *Phys. Rev. C*, 78:035502, Sep 2008. doi:10.1103/PhysRevC.78.035502.
- [22] C. Arnaboldi, et al. New limit on the neutrinoless  $\beta\beta$  decay of  $^{130}\text{Te}$ . *Phys. Rev. Lett.*, 95:142501, Sep 2005. doi:10.1103/PhysRevLett.95.142501.
- [23] C. Arnaboldi, et al. First results on neutrinoless double beta decay of  $^{130}\text{Te}$  with the calorimetric CUORICINO experiment. *Physics Letters B*, 584(34):260 – 268, 2004. ISSN 0370-2693. doi:<http://dx.doi.org/10.1016/j.physletb.2004.01.040>.
- [24] L Baudis, et al. The Heidelberg-Moscow experiment: improved sensitivity for  $^{76}\text{Ge}$  neutrinoless double beta decay. *Physics Letters B*, 407(34):219 – 224, 1997. ISSN 0370-2693. doi:[http://dx.doi.org/10.1016/S0370-2693\(97\)00756-9](http://dx.doi.org/10.1016/S0370-2693(97)00756-9).

- [25] R. Arnold, et al. First results of the search for neutrinoless double-beta decay with the NEMO 3 detector. *Phys. Rev. Lett.*, 95:182302, Oct 2005. doi: 10.1103/PhysRevLett.95.182302.
- [26] R. Arnold, et al. Study of  $2\beta$ -decay of  $^{100}\text{Mo}$  and  $^{82}\text{Se}$  using the NEMO3 detector. *Journal of Experimental and Theoretical Physics Letters*, 80(6):377–381, 2004. ISSN 0021-3640. doi:10.1134/1.1830651.
- [27] R. Arnold et al. Search for neutrinoless double-beta decay of  $^{100}\text{Mo}$  with the NEMO-3 detector. Preprint available at <http://arxiv.org/abs/1311.5695>.
- [28] A.A. Vasenko, et al. New results in the ITEP/YePI double beta-decay experiment with enriched germanium detectors. *Modern Physics Letters A*, 05(17):1299–1306, 1990. doi:10.1142/S0217732390001475.
- [29] R Bernabei, et al. Investigation of  $\beta\beta$  decay modes in  $^{134}\text{Xe}$  and  $^{136}\text{Xe}$ . *Physics Letters B*, 546(12):23 – 28, 2002. ISSN 0370-2693. doi:[http://dx.doi.org/10.1016/S0370-2693\(02\)02671-0](http://dx.doi.org/10.1016/S0370-2693(02)02671-0).
- [30] A. Balysh, et al. Measurement of the  $\beta\beta 2\nu$  decay of  $^{76}\text{Ge}$ . *Physics Letters B*, 322(3):176 – 181, 1994. ISSN 0370-2693. doi:[http://dx.doi.org/10.1016/0370-2693\(94\)91103-7](http://dx.doi.org/10.1016/0370-2693(94)91103-7).
- [31] D O Caldwell. Double beta decay-present and future. *Journal of Physics G: Nuclear and Particle Physics*, 17(S):S137, 1991.
- [32] C. Arnaboldi, et al. A calorimetric search on double beta decay of  $^{130}\text{Te}$ . *Physics Letters B*, 557(34):167 – 175, 2003. ISSN 0370-2693. doi:[http://dx.doi.org/10.1016/S0370-2693\(03\)00212-0](http://dx.doi.org/10.1016/S0370-2693(03)00212-0).
- [33] Ju. M. Gavriljuk, et al. Results of a search for  $2\beta$ -decay of Xe-136 with high pressure copper proportional counters in Baksan neutrino observatory INR RAS, 2011.
- [34] Ju.M. Gavriljuk, A.M. Gangapshev, V.V. Kuzminov, S.I. Panasenko, and S.S. Ratkevich. Results of a search for  $2\beta$  decay of  $^{136}\text{Xe}$  with high-pressure copper proportional counters in baksan neutrino observatory. *Physics of Atomic Nuclei*, 69(12):2129–2133, 2006. ISSN 1063-7788. doi:10.1134/S1063778806120180.
- [35] R. Luescher, et al. Search for  $\beta\beta$  decay in  $^{136}\text{Xe}$ : new results from the Gotthard experiment. *Physics Letters B*, 434(34):407 – 414, 1998. ISSN 0370-2693. doi: [http://dx.doi.org/10.1016/S0370-2693\(98\)00906-X](http://dx.doi.org/10.1016/S0370-2693(98)00906-X).
- [36] A. Alessandrello, et al. A search for neutrinoless double beta decay of  $^{130}\text{Te}$  with a thermal detector. *Physics Letters B*, 285(12):176 – 182, 1992. ISSN 0370-2693. doi:[http://dx.doi.org/10.1016/0370-2693\(92\)91319-5](http://dx.doi.org/10.1016/0370-2693(92)91319-5).

- [37] A. Alessandrello, et al. A new search for neutrinoless  $\beta\beta$  decay with a thermal detector. *Physics Letters B*, 335(34):519 – 525, 1994. ISSN 0370-2693. doi:[http://dx.doi.org/10.1016/0370-2693\(94\)90388-3](http://dx.doi.org/10.1016/0370-2693(94)90388-3).
- [38] A. Alessandrello, et al. Preliminary results on double beta decay of  $^{130}\text{Te}$  with an array of twenty cryogenic detectors. *Physics Letters B*, 433(12):156 – 162, 1998. ISSN 0370-2693. doi:[http://dx.doi.org/10.1016/S0370-2693\(98\)00645-5](http://dx.doi.org/10.1016/S0370-2693(98)00645-5).
- [39] A. Alessandrello, et al. New experimental results on double beta decay of  $^{130}\text{Te}$ . *Physics Letters B*, 486(12):13 – 21, 2000. ISSN 0370-2693. doi:[http://dx.doi.org/10.1016/S0370-2693\(00\)00747-4](http://dx.doi.org/10.1016/S0370-2693(00)00747-4).
- [40] J. C. Vuilleumier, et al. Search for neutrinoless double- $\beta$  decay in  $^{136}\text{Xe}$  with a time projection chamber. *Phys. Rev. D*, 48:1009–1020, Aug 1993. doi:[10.1103/PhysRevD.48.1009](https://doi.org/10.1103/PhysRevD.48.1009).
- [41] D. O. Caldwell, et al. Limits on neutrinoless  $\beta\beta$  decay, including that with majoron emission. *Phys. Rev. Lett.*, 59:419–422, Jul 1987. doi:[10.1103/PhysRevLett.59.419](https://doi.org/10.1103/PhysRevLett.59.419).
- [42] E. Bellotti, et al. A search for two neutrino and neutrinoless double beta decay of  $^{136}\text{Xe}$  in the Gran Sasso underground laboratory. *Physics Letters B*, 266(12):193 – 200, 1991. ISSN 0370-2693. doi:[http://dx.doi.org/10.1016/0370-2693\(91\)90767-K](http://dx.doi.org/10.1016/0370-2693(91)90767-K).
- [43] E. Bellotti, et al. A search for lepton number non-conservation in double beta decay of  $^{136}\text{Xe}$ . *Physics Letters B*, 221(2):209 – 215, 1989. ISSN 0370-2693. doi:[http://dx.doi.org/10.1016/0370-2693\(89\)91500-1](http://dx.doi.org/10.1016/0370-2693(89)91500-1).
- [44] E. Bellotti, et al. The milano experiment on lepton number nonconservation in double beta-decay of  $^{76}\text{Ge}$ . *Il Nuovo Cimento A*, 95(1):1–46, 1986. ISSN 0369-3546. doi:[10.1007/BF02768738](https://doi.org/10.1007/BF02768738).
- [45] E. Bellotti, et al. New limits on double beta decay of  $^{76}\text{Ge}$ . *Physics Letters B*, 146(6):450 – 456, 1984. ISSN 0370-2693. doi:[http://dx.doi.org/10.1016/0370-2693\(84\)90158-8](http://dx.doi.org/10.1016/0370-2693(84)90158-8).
- [46] E. Bellotti, et al. A new experimental limit on lepton non-conservation in double beta decay. *Physics Letters B*, 121(1):72 – 76, 1983. ISSN 0370-2693. doi:[http://dx.doi.org/10.1016/0370-2693\(83\)90205-8](http://dx.doi.org/10.1016/0370-2693(83)90205-8).
- [47] E. Bellotti, et al. An experimental investigation on lepton number conservation in double-beta processes. *Lettore al Nuovo Cimento*, 33(10):273–283, 1982. ISSN 0375-930X. doi:[10.1007/BF02725993](https://doi.org/10.1007/BF02725993).
- [48] D. Reusser, et al. Final report on the search for neutrinoless double- $\beta$  decay of  $^{76}\text{Ge}$  from the Gotthard underground experiment. *Phys. Rev. D*, 45:2548–2551, Apr 1992. doi:[10.1103/PhysRevD.45.2548](https://doi.org/10.1103/PhysRevD.45.2548).

- [49] H. Ejiri, et al. Limits on the Majorana neutrino mass and right-handed weak currents by neutrinoless double  $\beta$  decay of  $^{100}\text{Mo}$ . *Phys. Rev. C*, 63:065501, Apr 2001. doi:10.1103/PhysRevC.63.065501.
- [50] H. Ejiri, et al. Double beta decay of  $^{76}\text{Ge}(0^+)$  to  $0^+$  and  $2^+$  states in  $^{76}\text{Se}$  studied by the  $\beta - \gamma$  coincidence method. *Journal of Physics G: Nuclear Physics*, 13(6):839, 1987.
- [51] H. Ejiri, et al. Limits on neutrino-less double beta decay of  $^{100}\text{Mo}$ . *Nuclear Physics A*, 611(1):85 – 95, 1996. ISSN 0375-9474. doi:[http://dx.doi.org/10.1016/S0375-9474\(96\)00332-6](http://dx.doi.org/10.1016/S0375-9474(96)00332-6).
- [52] H. Ejiri, et al. Double beta decays of  $^{100}\text{Mo}$ . *Physics Letters B*, 258(12):17 – 23, 1991. ISSN 0370-2693. doi:[http://dx.doi.org/10.1016/0370-2693\(91\)91201-6](http://dx.doi.org/10.1016/0370-2693(91)91201-6).
- [53] M. Alston-Garnjost, et al. Experimental search for double- $\beta$  decay of  $^{100}\text{Mo}$ . *Phys. Rev. C*, 55:474–493, Jan 1997. doi:10.1103/PhysRevC.55.474.
- [54] M. Alston-Garnjost, et al. Experimental search for neutrinoless double- $\beta$  decay of  $^{100}\text{Mo}$ . *Phys. Rev. Lett.*, 71:831–834, Aug 1993. doi:10.1103/PhysRevLett.71.831.
- [55] M. Alston-Garnjost, et al. Search for neutrinoless double- $\beta$  decay of  $^{100}\text{Mo}$ . *Phys. Rev. Lett.*, 63:1671–1673, Oct 1989. doi:10.1103/PhysRevLett.63.1671.
- [56] P. Fisher, et al. A search for double beta decay in  $^{76}\text{Ge}$ . *Physics Letters B*, 218(2):257 – 262, 1989. ISSN 0370-2693. doi:[http://dx.doi.org/10.1016/0370-2693\(89\)91429-9](http://dx.doi.org/10.1016/0370-2693(89)91429-9).
- [57] F. T. Avignone, et al. New limits on the neutrino mass, lepton conservation, and no-neutrino double beta decay of  $^{76}\text{Ge}$ . *Phys. Rev. Lett.*, 50:721–724, Mar 1983. doi:10.1103/PhysRevLett.50.721.
- [58] F. T. Avignone, et al. Search for the double- $\beta$  decay of  $^{76}\text{Ge}$ . *Phys. Rev. C*, 34:666–677, Aug 1986. doi:10.1103/PhysRevC.34.666.
- [59] J. J. Simpson, P. Jagam, J. L. Campbell, H. L. Malm, and B. C. Robertson. New limit for neutrinoless double  $\beta$  decay of  $^{76}\text{Ge}$ . *Phys. Rev. Lett.*, 53:141–143, Jul 1984. doi:10.1103/PhysRevLett.53.141.
- [60] D. Dassié, et al. Two-neutrino double- $\beta$  decay measurement of  $^{100}\text{Mo}$ . *Phys. Rev. D*, 51:2090–2100, Mar 1995. doi:10.1103/PhysRevD.51.2090.
- [61] A. Forster, H. Kwon, J.K. Markey, F. Boehm, and H.E. Henrikson. Low background study of the neutrinoless double beta decay of  $^{76}\text{Ge}$  and upper limit for neutrino mass. *Physics Letters B*, 138(4):301 – 303, 1984. ISSN 0370-2693. doi:[http://dx.doi.org/10.1016/0370-2693\(84\)91665-4](http://dx.doi.org/10.1016/0370-2693(84)91665-4).

- [62] A. De Silva, M. K. Moe, M. A. Nelson, and M. A. Vient. Double  $\beta$  decays of  $^{100}\text{Mo}$  and  $^{150}\text{Nd}$ . *Phys. Rev. C*, 56:2451–2467, Nov 1997. doi:10.1103/PhysRevC.56.2451.
- [63] A.S. Barabash, et al. Results of the experiment on the search for double beta decay of  $^{136}\text{Xe}$ ,  $^{134}\text{Xe}$  and  $^{124}\text{Xe}$ . *Physics Letters B*, 223(2):273 – 276, 1989. ISSN 0370-2693. doi:[http://dx.doi.org/10.1016/0370-2693\(89\)90252-9](http://dx.doi.org/10.1016/0370-2693(89)90252-9).
- [64] E. Fiorini, A. Pullia, G. Bertolini, F. Cappellani, and G. Restelli. A search for lepton non-conservation in double beta decay with a germanium detector. *Physics Letters B*, 25(10):602 – 603, 1967. ISSN 0370-2693. doi:[http://dx.doi.org/10.1016/0370-2693\(67\)90127-X](http://dx.doi.org/10.1016/0370-2693(67)90127-X).
- [65] E. Fiorini, A. Pullia, G. Bertolini, F. Cappellani, and G. Restelli. Neutrinoless double-beta decay of  $^{76}\text{Ge}$ . *Il Nuovo Cimento A*, 13(3):747–763, 1973. ISSN 0369-3546. doi:10.1007/BF02784100.
- [66] I.R. Barabanov, V.N. Gavrin, S.V. Girin, V.N. Kornoukhov, and A.M. Pshukov. Double beta decay of Xe-136. *JETP Lett.*, 43:210–211, 1986.
- [67] S.I. Vasilev, A.A. Klimentko, S.B. Osetrov, A.A. Pomansky, and A.A. Smolnikov. Observation of the excess of events in the experiment on the search for a two neutrino double beta decay of Mo-100. *JETP Lett.*, 51:622–626, 1990.
- [68] L. W. Mitchell and P. H. Fisher. Rare decays of cadmium and tellurium. *Phys. Rev. C*, 38:895–899, Aug 1988. doi:10.1103/PhysRevC.38.895.
- [69] Y. Fukuda, et al. Evidence for oscillation of atmospheric neutrinos. *Phys. Rev. Lett.*, 81:1562–1567, Aug 1998. doi:10.1103/PhysRevLett.81.1562.
- [70] S. Cowell. Scaling factor inconsistencies in neutrinoless double beta decay. *Phys. Rev. C*, 73:028501, Feb 2006. doi:10.1103/PhysRevC.73.028501.
- [71] J. Barea, J. Kotila, and F. Iachello. Nuclear matrix elements for double- $\beta$  decay. *Phys. Rev. C*, 87:014315, Jan 2013. doi:10.1103/PhysRevC.87.014315.
- [72] J.J. Gmez-Cadenas, et al. Sense and sensitivity of double beta decay experiments. *Journal of Cosmology and Astroparticle Physics*, 2011(06):007, 2011.
- [73] Petr Vogel. The relation (or lack of it) between the  $0\nu$  and  $2\nu$  nuclear matrix elements, 2011. Presentation at August EXO Week.
- [74] J. B. Albert, et al. Improved measurement of the  $2\nu\beta\beta$  half-life of  $^{136}\text{Xe}$  with the EXO-200 detector. *Phys. Rev. C*, 89:015502, Jan 2014. doi:10.1103/PhysRevC.89.015502.
- [75] Kai Zuber. Summary of the workshop on: Nuclear matrix elements for neutrinoless double beta decay. Available at <http://arxiv.org/abs/nucl-ex/0511009>.

- [76] M. C. Gonzalez-Garcia and Yosef Nir. Neutrino masses and mixing: evidence and implications. *Rev. Mod. Phys.*, 75:345–402, Mar 2003. doi: 10.1103/RevModPhys.75.345.
- [77] A. Gando, et al. Constraints on  $\theta_{13}$  from a three-flavor oscillation analysis of reactor antineutrinos at KamLAND. *Phys. Rev. D*, 83:052002, Mar 2011. doi:10.1103/PhysRevD.83.052002.
- [78] P. Adamson, et al. Measurement of the neutrino mass splitting and flavor mixing by MINOS. *Phys. Rev. Lett.*, 106:181801, May 2011. doi:10.1103/PhysRevLett.106.181801.
- [79] F. P. An, et al. Improved measurement of electron antineutrino disappearance at Daya Bay. *Chinese Physics C*, 37(1):011001, 2013.
- [80] K. Abe, et al. Search for differences in oscillation parameters for atmospheric neutrinos and antineutrinos at Super-Kamiokande. *Phys. Rev. Lett.*, 107:241801, Dec 2011. doi:10.1103/PhysRevLett.107.241801.
- [81] Planck Collaboration. Planck 2013 results. XVI. cosmological parameters. *Astronomy and Astrophysics*, under review.
- [82] J. Angrik et al. KATRIN design report 2004. Technical report, KATRIN Collaboration, 2005.
- [83] V. N. Aseev, et al. Upper limit on the electron antineutrino mass from the Troitsk experiment. *Phys. Rev. D*, 84:112003, Dec 2011. doi:10.1103/PhysRevD.84.112003.
- [84] Joachim Wolf. The KATRIN neutrino mass experiment. *Nuclear Instruments and Methods in Physics Research Section A: Accelerators, Spectrometers, Detectors and Associated Equipment*, 623(1):442 – 444, 2010. ISSN 0168-9002. doi:<http://dx.doi.org/10.1016/j.nima.2010.03.030>. 1st International Conference on Technology and Instrumentation in Particle Physics.
- [85] Joseph A. Formaggio. Year one: Direct neutrino masses post Planck. In *TAUP2013*. To be published by Elsevier.
- [86] J Beringer, et al. Review of particle physics. *PHYSICAL REVIEW D*, 86(1):1504, 2012. ISSN 1550-7998.
- [87] CUORE Collaboration, et al. Initial performance of the cuore-0 experiment, 2014.
- [88] Delia Tosi on behalf of the EXO Collaboration. The search for neutrino-less double-beta decay: summary of current experiments, 2014.
- [89] J.B. Albert et al. Search for Majorana neutrinos with the first two years of EXO-200 data. *To be determined*, 2014. Preprint available at <http://arxiv.org/abs/1402.6956>.

- [90] S. Umehara, et al. Neutrino-less double- $\beta$  decay of  $^{48}\text{Ca}$  studied by  $\text{CaF}_2(\text{Eu})$  scintillators. *Phys. Rev. C*, 78:058501, Nov 2008. doi:10.1103/PhysRevC.78.058501.
- [91] A.S. Barabash and V.B. Brudanin. Investigation of double-beta decay with the NEMO-3 detector. *Physics of Atomic Nuclei*, 74(2):312–317, 2011. ISSN 1063-7788. doi:10.1134/S1063778811020062.
- [92] J. Argyriades, et al. Measurement of the two neutrino double beta decay half-life of Zr-96 with the NEMO-3 detector. *Nuclear Physics A*, 847(34):168 – 179, 2010. ISSN 0375-9474. doi:<http://dx.doi.org/10.1016/j.nuclphysa.2010.07.009>.
- [93] J. Argyriades, et al. Measurement of the double- $\beta$  decay half-life of  $^{150}\text{Nd}$  and search for neutrinoless decay modes with the NEMO-3 detector. *Phys. Rev. C*, 80:032501, Sep 2009. doi:10.1103/PhysRevC.80.032501.
- [94] J. Kotila and F. Iachello. Phase-space factors for double- $\beta$  decay. *Phys. Rev. C*, 85:034316, Mar 2012. doi:10.1103/PhysRevC.85.034316.
- [95] J. Barea, J. Kotila, and F. Iachello. Limits on neutrino masses from neutrinoless double- $\beta$  decay. *Phys. Rev. Lett.*, 109:042501, Jul 2012. doi:10.1103/PhysRevLett.109.042501.
- [96] M Auger, et al. The EXO-200 detector, part I: detector design and construction. *Journal of Instrumentation*, 7(05):P05010, 2012.
- [97] E. Conti, et al. Correlated fluctuations between luminescence and ionization in liquid xenon. *Phys. Rev. B*, 68:054201, Aug 2003. doi:10.1103/PhysRevB.68.054201.
- [98] S. Herrin. *Double Beta Decay in Xenon-136: Measuring the Neutrino-Emitting Mode and Searching for Majoron-Emitting Modes*. Ph.D. thesis, Stanford University, 2013.
- [99] Josh Albert, et al. Neutron capture gamma tech note for  $0\nu\beta\beta$  analysis (summer 2013), 2013. Internal EXO Document 021.
- [100] Steven R Elliott and Jonathan Engel. Double-beta decay. *Journal of Physics G: Nuclear and Particle Physics*, 30(9):R183, 2004.
- [101] H. Ejiri and S. R. Elliott. The charged current neutrino cross section for solar neutrinos, and background to  $\beta\beta(0\nu)$  experiments, 2013.
- [102] M.R. Bhat. Evaluated nuclear structure data file (ENSDF). In SyedM. Qaim, editor, *Nuclear Data for Science and Technology*, Research Reports in Physics, pages 817–821. Springer Berlin Heidelberg, 1992. ISBN 978-3-642-63473-4. doi:10.1007/978-3-642-58113-7\_227. Data extracted using the NNDC On-Line Data Service from the ENSDF database, file revised as of February 24, 2014.

- [103] Arthur H. Compton. A quantum theory of the scattering of x-rays by light elements. *Phys. Rev.*, 21:483–502, May 1923. doi:10.1103/PhysRev.21.483.
- [104] M.J. Berger, et al. XCOM: Photon cross section database (version 1.5). [Online] Available: <http://physics.nist.gov/xcom> [Sunday, 23-Feb-2014 03:19:51 EST], 2010. National Institute of Standards and Technology, Gaithersburg, MD.
- [105] D.S. Leonard, et al. Systematic study of trace radioactive impurities in candidate construction materials for EXO-200. *Nuclear Instruments and Methods in Physics Research Section A: Accelerators, Spectrometers, Detectors and Associated Equipment*, 591(3):490 – 509, 2008. ISSN 0168-9002. doi: <http://dx.doi.org/10.1016/j.nima.2008.03.001>.
- [106] R. Neilson, et al. Characterization of large area APDs for the EXO-200 detector. *Nuclear Instruments and Methods in Physics Research Section A: Accelerators, Spectrometers, Detectors and Associated Equipment*, 608(1):68 – 75, 2009. ISSN 0168-9002. doi:<http://dx.doi.org/10.1016/j.nima.2009.06.029>.
- [107] E.-I. Esch, et al. The cosmic ray muon flux at WIPP. *Nuclear Instruments and Methods in Physics Research Section A: Accelerators, Spectrometers, Detectors and Associated Equipment*, 538(13):516 – 525, 2005. ISSN 0168-9002. doi: <http://dx.doi.org/10.1016/j.nima.2004.09.005>.
- [108] M Moszyski, M Szawlowski, M Kapusta, and M Balcerzyk. Large area avalanche photodiodes in scintillation and x-rays detection. *Nuclear Instruments and Methods in Physics Research Section A: Accelerators, Spectrometers, Detectors and Associated Equipment*, 485(3):504 – 521, 2002. ISSN 0168-9002. doi:[http://dx.doi.org/10.1016/S0168-9002\(01\)02117-9](http://dx.doi.org/10.1016/S0168-9002(01)02117-9).
- [109] R. Neilson. APD installation: Selection and ganging, 2009. Presented to the EXO collaboration at the February 2009 EXO week meeting.
- [110] Josh Albert, et al. Energy correction technote for  $0\nu\beta\beta$  analysis (spring 2013), 2013. Internal EXO Document 007.
- [111] EXO Monte Carlo Group. EXO 200 MonteCarlo documentation, 2013. Internal EXO Document 010.
- [112] EXO Reconstruction Analysis Group. Event reconstruction in EXO-200, 2013. Internal EXO Document 008.
- [113] Ryan Herbst. EXO electronics functional specification, draft revision 0.24, 2010. Internal EXO documentation.
- [114] L. Yang. EXO-200 electronics upgrade study report, 2013. Internal EXO Document 012.

- [115] L. Yang, R. Devoe, and K. Nishimura. EXO-200 electronics upgrade status and plans, 2013. Presentation at December EXO Week.
- [116] L. Yang and R. Devoe. EXO-200 electronics upgrade status and plans, 2014. Presentation at March 9 Analysis Meeting.
- [117] Sheldon Ross. *A First Course in Probability*. Pearson Prentice Hall, 2006.
- [118] M Szydagis, et al. NEST: a comprehensive model for scintillation yield in liquid xenon. *Journal of Instrumentation*, 6(10):P10002, 2011.
- [119] A. El Guennouni, K. Jbilou, and H. Sadok. A block version of BiCGSTAB for linear systems with multiple right-hand sides. *Electronic Transactions on Numerical Analysis*, 16:129, 2003.
- [120] L. S. Blackford, et al. An updated set of basic linear algebra subprograms (BLAS). *ACM Trans. Math. Soft.*, 28(2):135, 2002.
- [121] Kazushige Goto and Robert A. van de Geijn. Anatomy of high-performance matrix multiplication. *ACM Trans. Math. Softw.*, 34(3):12:1–12:25, May 2008. ISSN 0098-3500. doi:10.1145/1356052.1356053.
- [122] Intel. *Reference Manual for Intel Math Kernel Library*, 11.1 edition.
- [123] A. S. Barabash. Double beta decay: present status. *Phys. Atom. Nucl.*, 73:162, 2010.
- [124] Arthur H. Compton. A quantum theory of the scattering of x-rays by light elements. *Physical Review*, 21:483, 1923.
- [125] Matteo Frigo and Steven G. Johnson. The design and implementation of FFTW3. *Proceedings of the IEEE*, 93(2):216–231, 2005. Special issue on “Program Generation, Optimization, and Platform Adaptation”.
- [126] Clayton Davis. The daq et cetera, or, stuff you wish you could ignore, but are about to find out you cannot, 2013. Presentation at Spring analysis workshop before EXO Week.
- [127] C.E. Shannon. Communication in the presence of noise. *Proceedings of the IEEE*, 86(2):447–457, Feb 1998. ISSN 0018-9219. doi:10.1109/JPROC.1998.659497.
- [128] Mike Jewell. APD denoising noise correlations, 2013. Presentation to the energy group on July 29.
- [129] Josiah Walton. Environmental noise: Coherent noise, June 2013. An earlier version of this note was used as input to the electronics upgrade report [114].

- [130] Jens Keiner, Stefan Kunis, and Daniel Potts. Using NFFT 3—a software library for various nonequispaced fast fourier transforms. *ACM Trans. Math. Softw.*, 36(4):19:1–19:30, August 2009. ISSN 0098-3500. doi:10.1145/1555386. 1555388.
- [131] S.M. Ross. *Simulation*. Elsevier Science, 2012. ISBN 9780124159716.
- [132] Eckert and Ziegler Isotope Products. Certificate of calibration: Gamma standard source, 2009. Source strength measurement performed on behalf of the EXO-200 collaboration.
- [133] David W. Scott. *Multivariate density estimation : theory, practice, and visualization*. John Wiley and Sons, Inc., 1992.
- [134] S. Agostinelli, et al. Geant4a simulation toolkit. *Nuclear Instruments and Methods in Physics Research Section A: Accelerators, Spectrometers, Detectors and Associated Equipment*, 506(3):250 – 303, 2003. ISSN 0168-9002. doi: [http://dx.doi.org/10.1016/S0168-9002\(03\)01368-8](http://dx.doi.org/10.1016/S0168-9002(03)01368-8).
- [135] J. Allison, et al. Geant4 developments and applications. *Nuclear Science, IEEE Transactions on*, 53(1):270–278, Feb 2006. ISSN 0018-9499. doi:10.1109/TNS.2006.869826.
- [136] M Dressel. Geometrical importance sampling in Geant4: from design to verification. Technical Report CERN-OPEN-2003-048, CERN, Geneva, Sep 2003.
- [137] W. Shockley. Currents to conductors induced by a moving point charge. *Journal of Applied Physics*, 9(10):635–636, 1938. doi:<http://dx.doi.org/10.1063/1.1710367>.
- [138] Simon Ramo. Currents induced by electron motion. *Proceedings of the IRE*, 27(9):584–585, Sept 1939. ISSN 0096-8390. doi:10.1109/JRPROC.1939.228757.
- [139] D.O. North. An analysis of the factors which determine signal/noise discrimination in pulsed-carrier systems. *Proceedings of the IEEE*, 51(7):1016–1027, July 1963. ISSN 0018-9219. doi:10.1109/PROC.1963.2383. Reprint of original 1943 paper, which was classified.
- [140] Josh Albert, et al. Energy correction technote for  $0\nu\beta\beta$  analysis (august 2013), 2013 (revised February 2014). Internal EXO Document 018.
- [141] G.F. Knoll. *Radiation detection and measurement*. Wiley, 2000. ISBN 9780471073383.
- [142] Caio Licciardi. Calculation of the average energy resolution used in the search for  $\beta\beta0\nu$  with run-2 data, 2014. Internal EXO Document 019.

- [143] Igor Ostrovskiy. 0 2013. final analysis documentation, 2013. Internal EXO Document 015.
- [144] Glen Cowan, Kyle Cranmer, Eilam Gross, and Ofer Vitells. Asymptotic formulae for likelihood-based tests of new physics. *The European Physical Journal C*, 71(2):1–19, 2011. ISSN 1434-6044. doi:10.1140/epjc/s10052-011-1554-0.
- [145] Tomás R. Rodríguez and Gabriel Martínez-Pinedo. Energy density functional study of nuclear matrix elements for neutrinoless  $\beta\beta$  decay. *Phys. Rev. Lett.*, 105:252503, Dec 2010. doi:10.1103/PhysRevLett.105.252503.
- [146] J. Menndez, A. Poves, E. Caurier, and F. Nowacki. Disassembling the nuclear matrix elements of the neutrinoless decay. *Nuclear Physics A*, 818(34):139 – 151, 2009. ISSN 0375-9474. doi:<http://dx.doi.org/10.1016/j.nuclphysa.2008.12.005>.
- [147] Fedor Šimkovic, Vadim Rodin, Amand Faessler, and Petr Vogel.  $0\nu\beta\beta$  and  $2\nu\beta\beta$  nuclear matrix elements, quasiparticle random-phase approximation, and isospin symmetry restoration. *Phys. Rev. C*, 87:045501, Apr 2013. doi:10.1103/PhysRevC.87.045501.
- [148] H. V. Klapdor-Kleingrothaus and I. V. Krivosheina. Evidence for neutrinoless double beta decay. *Mod. Phys. Lett. A*, 21:20:1547, 2006.